
A rugged marine impact penetrometer for sea floor assessment

Vom Fachbereich Geowissenschaften
der Universität Bremen
zur Erlangung des Doktorgrades der
Naturwissenschaften

(Dr. rer. nat.)

genehmigte Dissertation von

Sebastian Stephan

München, November 2015

Gutachter

Prof. Dr. Heinrich Villinger

Universität Bremen
Fachbereich Geowissenschaften
Postfach 330 440
28334 Bremen

Prof. Dr. Achim Kopf

Universität Bremen
Marum - Zentrum für Marine Umweltwissenschaften
Postfach 330 440
28334 Bremen

Tag des Kolloquiums: 06. November 2015

Name: Sebastian Stephan
Anschrift: Postfach 901011
81510 München

Datum: _____

Erklärung

Hiermit versichere ich, dass ich

1. die Arbeit ohne unerlaubte fremde Hilfe angefertigt habe,
 2. keine anderen als die von mir angegebenen Quellen und Hilfsmittel benutzt habe und
 3. die den benutzten Werken wörtlich oder inhaltlich entnommenen Stellen als solche kenntlich gemacht habe.
-

München, den: _____

(Sebastian Stephan)

Abstract

The utilization of marine sediments, as well as the awareness of hazards originating from unstable sea floor conditions, has increased since the second half of the last century. Accordingly, testing methods and especially *in situ* tests have been developed to assess the geotechnical properties of marine sediments, with the static velocity Cone Penetration Testing (CPT) method being the most prominent testing technique. The values determined by CPT are the cone resistance, being the resistance of the sediment to the forced penetration of a measurement cone, and sleeve friction, being the friction between the sediment and the measurement. Pore water pressure during penetration may also be measured, in which case the testing is termed CPTu. However, the lower handling requirements of dynamic velocity impact penetrometers have led to investigations of their applicability for the determination of properties of marine sediments since the 1970s. Thereby, CPT instrumentation or alternate sensors were used within the impact penetrometers.

The aim of the research in this thesis is to investigate the applicability of an impact penetrometer – the Lance Insertion Retardation meter (LIRmeter) – for assessing geotechnical properties of marine sediments. The design of the LIRmeter needed to cover certain requirements regarding operating conditions, such as ruggedness, insensitivity to hydrostatic pressure, ability to cover a wide range of sediment types without retooling, and a fast measurement progress. To cover these requirements, a measurement approach has been chosen that uses solely acceleration sensors to determine geotechnical properties on the basis of the measured acceleration data.

Qualitative field trials in the German Bight (North Sea) successfully evaluated the instrument. These field trials were followed by a verification study in the Southern North Sea, where dynamic CPT measurements were taken simultaneously and additional data of a conventional, static velocity, CPT were available. During the verification study, it was shown that dynamically acquired cone resistance data was interchangeable with processed data from the acceleration sensors. Moreover, a correlation of dynamically acquired data with data from a nearby static velocity CPT station was established. This allowed for sediment classification on the basis of dynamic measurements by using common interpretation models.

The measurement approach was further investigated by conducting laboratory tests on dense sands with low amounts of cohesive fines. For this laboratory study, a model penetrometer was developed that, likewise, accommodates conventional sensors for measuring cone resistance and sleeve friction in addition to the acceleration during penetration. It was again shown that the acceleration data mimics the data of the cone resistance sensor to a high degree. Geotechnical testing on the mixed soil was undertaken to establish a correlation to the dynamically acquired data using the state parameter relationship. The laboratory study showed a good correlation between the reference data from geotechnical tests and the dynamically acquired data.

From the field validation and the laboratory study it was shown that the LIRmeter is able to deliver qualitative information about the hardness of marine sediments. Quantitative measures, such as cone resistance, bearing capacity, shear strength, or void ratio are deducible when data is further processed and information on the tested sediments is available from reference tests or may reasonably be assumed.

On the basis of the instruments performance during evaluation, validation, and laboratory studies the LIRmeter has been proven a valuable and reliable tool. Thus, allowing the instrument to be applied to address future geoscientific, geotechnical, or civil engineering questions as a supplementary tool to established investigation methods.

Zusammenfassung

In der zweiten Hälfte des letzten Jahrhunderts ist sowohl die Nutzung mariner Sedimente als auch ein steigendes Bewusstsein für die Gefahren, die von instabilen marinen Sedimenten ausgehen, zu verzeichnen. Aus diesem Grund wurden Methoden entwickelt, mit Hilfe derer sich die geotechnischen Eigenschaften mariner Sedimente bestimmen lassen. Insbesondere *in situ* Tests, wie das Cone Penetration Testing (CPT) Verfahren, werden seitdem vorwiegend zum Zweck der Charakterisierung mariner Sedimente eingesetzt. Die Parameter, die während des CPTs gemessen werden, sind einerseits der Spitzenwiderstand, als Widerstand, den das Sediment gegenüber der erzwungenen Eindringung einer Messspitze ausübt, als auch die Mantelreibung des Gestänges. Falls zusätzlich der Porendruck während des Eindringvorgangs gemessen wird, handelt es sich um einen CPTu test. Zusätzlich zu dem CPT Verfahren, das mit einer statischen Eindringgeschwindigkeit arbeitet, wurden seit den 1970er Jahren auch dynamische Verfahren (mit sogenannten Impaktpenetrometern) entwickelt. Diese Verfahren haben den Vorteil, dass sie weniger Handhabungsaufwand erfordern. Hierbei werden einerseits dieselben Sensoren wie beim statischen CPT, aber auch alternative Sensoren eingesetzt.

Die vorliegende Arbeit untersucht die Eignung eines Impaktpenetrometers – das Lance Insertion Retardation meter (LIRmeter) – mit dem Ziel, geotechnische Eigenschaften mariner Sedimente zu bestimmen. Hierbei lagen die Anforderungen an die Entwicklung des LIRmeters in einer einfachen Handhabung, Robustheit, Unempfindlichkeit gegenüber hydrostatischem Druck, einer Eignung für viele verschiedene Sedimenttypen ohne Umrüstung des Geräts, sowie in einem raschen Messfortschritt. Daher wurde ein Ansatz gewählt, bei dem die geotechnischen Eigenschaften nur auf der Grundlage von Beschleunigungsmessungen (kinematisches Messprinzip) bestimmt werden sollten.

Erprobungen in der Deutschen Bucht (Nordsee) zeigten, dass der Ansatz dazu geeignet ist, qualitative Aussagen hinsichtlich der geotechnischen Eigenschaften mariner Sedimente zu treffen. Eine weitere Kampagne in der Südlichen Nordsee brachte den Nachweis, dass die Beschleunigungsmessung mit einer parallel am selben Gerät durchgeführten konventionellen dynamischen Messung des Spitzenwiderstands austauschbar ist. Darüber hinaus konnte gezeigt werden, dass die dynamischen Messungen nach einer Datenbearbeitung eine Korrelation zu Referenzmessungen aufweisen, die mittels einer in unmittelbarer Nähe durchgeführten, konventionellen CPT gewonnen wurden. Somit konnten die vorliegenden Sedimente mittels etablierter Verfahren auf Grundlage der dynamischen Messungen klassifiziert werden.

Das kinematische Messprinzip konnte weiterhin durch Laborversuche an dichten Sanden mit geringem kohäsiven, feinkörnigen Anteil untersucht werden. Für die Laborversuche wurde ein Modell des LIRmeters entwickelt, das wiederum konventionelle Sensoren zur Messung der Spitzenwiderstands und der Mantelreibung neben den Beschleunigungssensoren aufwies. Es konnte auch im Rahmen der La-

borversuche gezeigt werden, dass sich der Spitzenwiderstand durch die Messung der Verzögerungsbeschleunigung während des Eindringens sehr gut abbilden lässt. Eine Korrelation zwischen Referenzmessungen, die mittels geotechnischer Laborversuche an den Mischsedimenten durchgeführt wurden und den dynamischen Daten des LIRmeters konnte mit Hilfe der *state parameter*-Beziehung hergestellt werden.

Durch die Feldmessungen und Laborversuche konnte gezeigt werden, dass mit dem LIRmeter qualitative Aussagen hinsichtlich der geotechnischen Eigenschaften mariner Sedimente getroffen werden können. Falls zusätzliche Informationen über die zu untersuchenden Sedimente durch Referenzmessungen oder durch begründete Annahmen vorliegen, können quantitative Aussagen wie z.B. Spitzenwiderstand, Tragfähigkeit, Scherfestigkeit oder Parameter wie die Porenzahl nach einer Auswertung der Impaktpenetrometerdaten getroffen werden.

Während der Feldmessungen und der Laborversuche konnte der Entwicklungsgrad des LIRmeters in ausreichender Weise für routinemäßige Feldeinsätze im Rahmen von geowissenschaftlichen, geotechnischen oder ingenieurgeologischen Fragestellungen eingesetzt werden. In Verbindung mit Referenzmessungen kann das LIRmeter als schnell einzusetzendes Gerät dienen, um die Aussagekraft punktueller Messungen z.B. in die Fläche zu erweitern.

Contents

1	Introduction	1
1.1	Motivation and objectives	1
1.2	Structure of the thesis	4
2	State of the art	9
2.1	Processing of dynamic penetration data	9
2.2	Geotechnical properties from CPT data	25
2.3	Static velocity penetrometers	29
2.4	Impact penetrometers	34
3	Instrument evaluation	79
3.1	Introduction	80
3.2	Design	82
3.3	Calibration, processing, tests	92
3.4	Results from field measurements	102
3.5	Summary	106
4	Field tests	109
4.1	Introduction	110
4.2	Geological setting	112
4.3	Materials and methods	116
4.4	Results	127
4.5	Discussion	134
4.6	Conclusions	141
5	Laboratory testing	145
5.1	Introduction	147
5.2	Laboratory study	149
5.3	Results	163
5.4	Discussion	168
5.5	Conclusions	178

6	Conclusions	181
7	Outlook	185
7.1	Laboratory analyses and field tests	185
7.2	Numerical modeling of penetration processes	189
	Acknowledgements / Danksagung	195
	References	197
A	Conference Paper OCEANS 2011	231
A.1	Introduction	234
A.2	Material and method	235
A.3	Results	240
A.4	Discussion	251
A.5	Conclusion	255

Chapter 1

Introduction

1.1 Motivation and objectives

Activities affecting the sea floor in shallow and deep water have increased since the second half of the last century due to expanding opportunities brought on by technological advances (Chakrabarti et al., 2005). The increased usage of the sea floor as a resource or foundation ground can be seen in such examples as the continual and increasing production of offshore oil and gas at ever-increasing water depths, dredging activities to harvest such resources as sand and gravel, the utilization of wind, wave or, tidal energy, and the laying of infrastructure, such as pipelines, communication, or power cables.

Anthropogenic interference changes sea floor conditions due to rearrangement of sediments, as observed in connection with, e.g., river deepening (e.g. Kerner, 2007), harbor construction (e.g. Winterwerp, 2005), or land reclamation (e.g. Flemming and Nyandwi, 1994). As a result of such activities, the sea floor is a target of interest with a concurrently emerging need for characterization of its physical and geotechnical properties.

The stability of submarine slopes is also of great importance for submarine infrastructure and bears, beyond that, a considerable risk for coastal areas. Submarine landslides can occur in a variety of settings ranging from continental slopes over island flanks to lake or fjord environments (Masson et al., 2006). The initiation of slope failure is linked to preconditions that enable failure. The preconditions may be special sedimentary sequences with weak layers or phenomena like the formation of gas hydrates. A change in environmental conditions (e.g., pressure or temperature changes) or external forcing (e.g., seismic shaking) trigger failure mechanisms, which are linked to the preconditions. Several techniques exist to assess the risk of slope failure

with geotechnical *in situ* testing being one of them (Vanneste et al., 2014).

The geotechnical characterization of sea-floor properties presents challenges related to differences in environmental conditions between onshore and subaqueous settings. The most important difference is the presence of fluids in the voids of sea floor sediments. Moreover, stress conditions are different due to superimposed hydrostatic stresses. If sea floor samples are investigated *ex situ*, undisturbed samples need to be retained and environmental conditions need to be reproduced. However, the extraction of undisturbed samples may be impeded by the sampling technique itself (Skinner and McCave, 2003).

To overcome these difficulties, offshore *in situ* testing has been established as an alternate method to obtain physical and geotechnical sea floor properties. The soil stability is predominantly assessed using the Cone Penetration Testing (CPT) method (Lunne and Kleven, 1981; Lunne et al., 1997), which measures the soil resistance to penetration of a measurement rod with a static insertion velocity. The technical realization for such offshore testing involves testing rigs with rods, movable parts, and delicate sensorial components (load cells) located in the tip of the penetrating rod, which is subjected to high mechanical loads during testing.

An alternate way to determine sediment resistance is the use of impacting penetrometers (e.g. Dayal and Allen, 1973). These penetrometers gather momentum during lowering through the water column and eventually impact the sea floor and penetrate dynamically up to a certain depth. This penetration depth, as well as the measurement of forces and/or kinematics during sea floor penetration, serves as a measure for sea floor strength.

The impact penetrometers available for such investigations range from lightweight devices for near-surface investigations (Stoll et al., 2007; Stark et al., 2009a) to huge penetrometers (Lieng et al., 2010). Impacting devices may carry similar sensors, such as the static velocity CPT, which are, to a certain extent, susceptible to catastrophic failure at peak loads during impact. Instruments that derive sea floor strength solely from kinematic properties, allow for a design and construction that is more sturdy due to greater freedom in choosing the sensor location and to the inherent robustness of the sensors.

However, only a few approaches exist on the quantification of sea floor properties solely from kinematic measurements with impact penetrometers (Stark et al., 2009b; Beard, 1985). This approach is presently used largely in combination with lightweight devices. Beyond that, huge devices, such as instrumented anchors, are seldom employed to investigate geotechnical soil properties. They are, rather, used for assessment of anchor performance (e.g., holding capacity) within the frame of site surveys (Lieng et al., 2010). The

gap between lightweight, dynamic devices with a kinematic measurement approach and well-established static velocity CPT motivated the development of an intermediately-sized penetrometer using the kinematic approach discussed herein.

The aim of this study is, therefore, to develop an impact penetrometer of intermediate size that overcomes the disadvantages mentioned above, especially regarding the robustness of conventional instrumentation. Such a device should be able to be deployed in a wide range of marine sediments without specific adaptations regarding technical rigging or sensors. The targeted intermediate depth range (< 10 m) is sufficient for the investigation of near-surface geotechnical properties and suffices for shallow foundations or slope stability assessment. The instrument should be deployable by winch and tether, but also suited to be triggered a few meters above the sea floor. With such deployment capabilities the targeted impact velocities between 1 and 5 m/s should be attainable. Additionally, analysis schemes have to be developed that allow for quantification of data from the different types of sediment typically encountered within coastal areas, such as sands, clays, and mixed sediments.

The choice of designing a robust instrument yields advantages regarding the handling procedure during deployment and measurement, and the on-site measurement progress (defined as the period of time between two deployments), and should allow for e.g., pogo-style measurements (Hyndman et al., 1979). However, following the robust measurement, exclusively kinematic, approach involves the abandonment of conventional instrumentation like load cells and pore pressure transducers. Therefore, it needs to be shown to what extent the kinematic data may be used for determination of geotechnical parameters.

The objectives arising from the motivation can be broken down into a set of tasks and milestones needed to attain the ultimate aim of having a robust impact penetrometer that can be used to determine geotechnical properties of marine sediments in a quantitative way.

- First, an instrument needs to be designed and constructed (see Figure 1.1 for a preview of the result) that is able to fulfil the requirements regarding targeted sediment penetration, robustness, and operating range, and should be easy to operate and handle.
- Second, field tests are required to evaluate the performance of the instrument. These field tests need to involve comparative measurements on samples, or incorporate established *in situ* testing methods regarding the applicability of the chosen sensors and the applicability of the dynamic measurement approach itself.

- Third, detailed investigations regarding the measurement principle and the performance under controlled conditions, such as laboratory tests, are needed to establish or verify relations between the acquired datasets and the properties of sediments.



Figure 1.1 – The LIRmeter and a suitable measurement lance aboard RV Planet. **a** The LIRmeter. The pressure tube containing all electronics, batteries, data storage, and sensors of the instrument for a self-sufficient operation; **b** The rod of the measurement lance. The length in this configuration is 4 m; **c** The weight stand of the lance. Additional weight plates may be mounted with nuts and bolts; **d** Mounting tubes for sensor packages, such as the LIRmeter; **e** Swivel to reduce twisting of the wire; **f** Holding brackets for the instrument. These are mounted within the mounting tubes; **g** Trolley for easy storage on deck.

1.2 Structure of the thesis

The milestones required for attaining the goal of the project are each covered by a published or submitted manuscript of this cumulative dissertation. An introductory part covers the motivation for this project, outlines the state of the art of existing testing techniques, and gives a comprehensive overview

on marine penetrometers. The manuscripts are introduced by bibliographic information (when applicable) and given in the published or submitted form with adaptations regarding layout. All references are consolidated within the references section. Where possible, digital object identifiers (DOIs) or uniform resource locators (URLs) were included for convenient access to the cited publications.

Chapter 1 is preceded by the thesis summaries in English and German. The chapter serves as an introduction into the thesis and addresses the motivation, as well as the therefrom derived objectives, which are addressed within this thesis. The introduction also contains this thesis outline.

Chapter 2 reviews the state of the art regarding Cone Penetration Testing, as well as impact penetrometer testing instrumentation and data processing techniques.

Chapter 3 gives a description of the measurement instrument that has been developed in the course of this thesis. This chapter comprises the first manuscript entitled:

The Lance Insertion Retardation Meter (LIRmeter). An instrument for in-situ determination of sea floor properties – technical description and performance evaluation

The article is authored by S. Stephan, N. Kaul and H. Villinger (all authors: Geoscience department, Universität Bremen). The main work reported within the manuscript was undertaken by S. Stephan. This comprises the conceptual design of the instrument, the selection, arrangement and calibration of sensors, and the design and programming of the data acquisition and user interface. The field evaluation was conducted in cooperation with T. Wever from FWG (WTD 71)¹ aboard R/V Planet and with support by FIELAX GmbH (Bremerhaven, henceforth: FIELAX). Grain-size data was been provided by Landesamt für Bergbau, Energie und Geologie (Hannover, henceforth: LBEG) and Bundesamt für Seeschifffahrt und Hydrographie (Hamburg, henceforth: BSH). The mechanical design of the lance was done by B. Heesemann (Geoscience department, Universität Bremen) in cooperation with FIELAX GmbH (Bremerhaven). The construction was done by Stahlbau Nord GmbH (Bremerhaven). Several smaller parts were

¹Forschungsbereich für Wasserschall und Geophysik (Wehrtechnische Dienststelle für Schiffe und Marinewaffen, Maritime Technologie und Forschung)

constructed by the mechanical workshops of the University of Bremen and the MARUM research center (University of Bremen, henceforth: MARUM).

The manuscript was written by S. Stephan. The co-authors N. Kaul and H. Villinger provided additional comments and suggestions on the first draft.

Chapter 4 gives a report on field tests and comparative measurements. This chapter comprises the second manuscript entitled:

Validation of impact penetrometer data by cone penetration testing and shallow seismic data within the regional geology of the Southern North Sea

The publication was authored by S. Stephan, N. Kaul and H. Villinger. The main work reported within the manuscript was undertaken by S. Stephan. This comprises the manufacturing of data acquisition units specifically for this purpose, execution of the field experiments, the background study on the regional geology of the working area, and the processing and interpretation of the data. The field trials were carried out in the frame of a cooperation with Fugro N.V. and Fugro Engineers B.V. (Netherlands, henceforth: Fugro) aboard their drillship D/V Markab. Staff from Fugro assisted during the deployment of the instrument. The design of the lance used in this study was done by D. Ruijtenbeek (Fugro). The adaptation of the cone sensor signals to the data acquisition was done by B. Heesemann and a modification on the digital filters was done by A. Schwab (Geoscience department, Universität Bremen). The modified data acquisition was calibrated by S. Stephan at the Fugro facilities in Leidschendam (Netherlands) with support from Fugro staff. The sediment echosounding data in Figs. 4.9, 4.11 and 4.12, as well as the CPT data in Fig. 4.10 were acquired, processed, and provided by Fugro.

The manuscript was written by S. Stephan. The co-authors N. Kaul and H. Villinger provided additional comments and suggestions on the first draft. J. Peuchen and J. Terwindt from Fugro revised the draft and provided further valuable comments.

Chapter 5 gives a report on systematical laboratory tests with a scaled model penetrometer. This chapter comprises the third manuscript entitled:

Laboratory impact penetrometer experiments in dense sand containing cohesive fines

The publication was authored by S. Stephan and S. Kreiter (MARUM). The main work reported within the manuscript was undertaken by S. Stephan. This comprises the manufacturing of a data acquisition unit specifically for

the laboratory tests, the design and manufacturing of the deployment apparatus, as well as the execution of the impact penetrometer tests with assistance by B. Heesemann, and the subsequent data analysis. The miniature cone has been loaned for use by Fugro for these tests. The data acquisition was adapted to the miniature cone with assistance by B. Heesemann. The geotechnical tests were conducted at the geotechnical laboratory at MARUM with assistance by D. Otto (MARUM). The grain-size analyses were conducted by N. Lampig (MARUM) and the abstract has been translated into French by Sylviane Stephan.

The manuscript was written by S. Stephan. The co-author S. Kreiter provided additional comments and suggestions regarding the interpretation of the geotechnical tests on the first and second draft of the manuscript.

Chapter 6 summarizes the main findings of the work presented within this thesis and **Chapter 7** gives an outlook on studies that could be conducted in the future to supplement findings from this thesis.

Appendix A is an extended abstract for the OCEANS '11 MTS/IEEE Kona conference, held at Waikoloa, Hawaii, USA on 19-22 September 2011. This chapter comprises another manuscript entitled:

*LIRmeter: A new tool for rapid assessment of sea floor parameters.
Bridging the gap between free-fall instruments and frame-based CPT*

The abstract was reviewed, whereas the conference paper was accepted without any further review. The publication was authored by S. Stephan, N. Kaul, N. Stark (presently at Virginia Tech, USA), H. Villinger and T. Wever. The main work reported within this manuscript was undertaken by S. Stephan. This comprises the data acquisition (see also the description for Chapter 3). S. Stephan also conducted the trials with R/V Heincke with support by N. Kaul and A. Schwab. The data analysis was done by S. Stephan. Grain-size analyses were carried out by A. Steiner. Additional grain-size data were provided by LBEG and BSH.

The manuscript was written by S. Stephan. The co-authors N. Kaul, H. Villinger and T. Wever provided additional comments and suggestions on the first draft. N. Stark provided the comparative data from the NIMROD penetrometer and contributed recommendations and comments on the manuscript.

Chapter 2

State of the art

The methods for acquisition, processing, and interpretation of penetration data are presented within this chapter with an emphasis on dynamic penetrometers. A description of the processing of dynamic penetration data acquired by, e.g., impact penetrometers, is followed by an introduction into the approaches for deduction of first-order sediment resistance parameters, e.g., penetration resistance (i.e., cone resistance q_c), which is presented in Section 2.1. The determination of geotechnical parameters from penetration testing requires the determination of penetration resistance. However, penetration resistance is nonlinearly back-coupled to penetration velocity (Casagrande and Shannon, 1949). Therefore, common rate correction approaches are presented in Section 2.1.3 for the correction of dynamically acquired penetration data.

The determination of second-order geotechnical properties, such as undrained shear strength, ultimate bearing capacity, or sediment state descriptors like void ratio is introduced in Section 2.2, followed by description of the testing equipment for static velocity testing (Section 2.3) and an extensive review on dynamic testing equipment (Section 2.4).

2.1 Processing of dynamic penetration data

2.1.1 Acceleration data for impact penetration testing: method and example

The penetration mechanism for different deployment options is shown in Figure 2.1. Penetrometers, which are deployed by tether, are susceptible to distortion by the vertical motion of the attachment point, which is influenced by the ships heave, pitch, and roll motion. The vertical motion transfers via

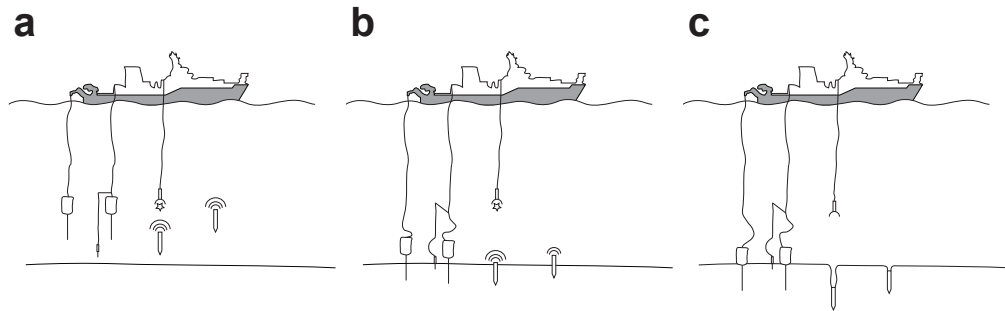


Figure 2.1 – Deployment of marine penetrometers. **a-d** sketch from left to right: tethered (e.g., LIRmeter (Fabian et al., 2008), see Section 2.4.17), triggered (e.g., instrumented corers (Preslan, 1969), see Section 2.4.12), propelled (e.g., ISP (James and Calloway, 1983), see Section 2.4.3) and free fall (e.g., XBP (Stoll and Akal, 1999), see Section 2.4.7); **a** The penetrometer is lowered through the water column; **b** The penetrometer is penetrating the sediment; and **c** The penetrometer is fully embedded.

the wire to the penetrometer and may be amplified depending on the tether length and its elastic properties (Lister, 1964). An additional particularity of tethered lowering is the elastic rebound of the tether, which occurs when the penetrometer enters the sea floor and the load on the wire diminishes. This may also occur with triggered deployment when the slack line length is dimensioned too tightly (Preslan, 1969). In absence of this issue, triggered devices are essentially free-falling devices.

With tethered instruments, it is advisable to conduct repetitive measurements at a single location. However, the loss of velocity during penetration in combination with high lowering velocities often suffices to generate enough slack to compensate for the elastic rebound and the forced motion of the wire. Tethered deployment is advantageous over free-fall or triggered deployments especially in deep waters, because the instrument does not need to be completely recovered in between two measurements (pogo-style deployment; Hyndman et al., 1979).

Embedment depth of lance-shaped devices is typically limited to the length of the rod, since the penetration resistance of the weight stand is too high due to its cross sectional area. However, for very soft soils, such as deep sea ooze or, e.g., harbor mud, weight stand penetration may be possible. Projectile shaped devices embed either completely or partially into the soil.

The kinematics of an impact penetrometer during soil penetration may serve as a proxy for soil strength. A penetration into a “hard” soil causes

a penetrator with a certain momentum to decelerate to zero velocity in a shorter time span, than into a “soft” soil. The momentum of an impact penetrometer is gathered either during free fall through the water column in the case of expendable or triggered devices, by a driving force in the case of propelled instruments, or through tethered lowering via winch.

When recorded, kinematic properties can be used to determine the embedment depth as a function of time, whereby data is sampled discretely with a certain sampling rate. This data is either obtained by measuring the relative distance between sea floor and instrument (e.g., with an altimeter), by measuring the velocity of the instrument (e.g., through the Doppler Effect), or by determining the acceleration of the instrument with acceleration sensors. The latter option is the most established method used in current devices.

No matter how the kinematics are sensed, it is possible to obtain displacement s , velocity v , or acceleration a through the equations of motion by integration or differentiation of one of these quantities, assuming constant conditions in time in between two data samples:

$$a(t) = \dot{v} = \ddot{s} \quad (2.1)$$

$$s(t) = \int v dt = \int \int a dt^2 \quad (2.2)$$

$$s(t) = at + v_0 = \frac{a}{2}t^2 + v_0t + s_0 \quad (2.3)$$

Since it is of interest to determine sediment properties as a function of soil depth (i.e., penetration depth), it is necessary to obtain a time series of displacement through measurement or calculation. Then it is possible to display acceleration, velocity, or other simultaneously acquired parameters as a function of penetration depth.

Fig. 2.2 shows exemplary data for three penetrations at a single location with a tethered penetrometer. The originally acquired data was a time series of acceleration (Figure 2.2a) that was acquired using a capacitive accelerometer.

The time t_0 indicates the time of impact on the sea floor. The instrument is lowered in the time span before t_0 . The variation around the value of gravitational acceleration $g = 9.81 \text{ m/s}^2$ may be ship-induced movement or a slight tilting of the instrument (see Section 3.3 for further information on inclination influences on acceleration measurement). Penetration takes place for times after t_0 (indicated by the dark colors above the acceleration-time diagram in Figure 2.2). These types of acceleration traces would be expected for all types of deployment, but with a difference in initial accel-

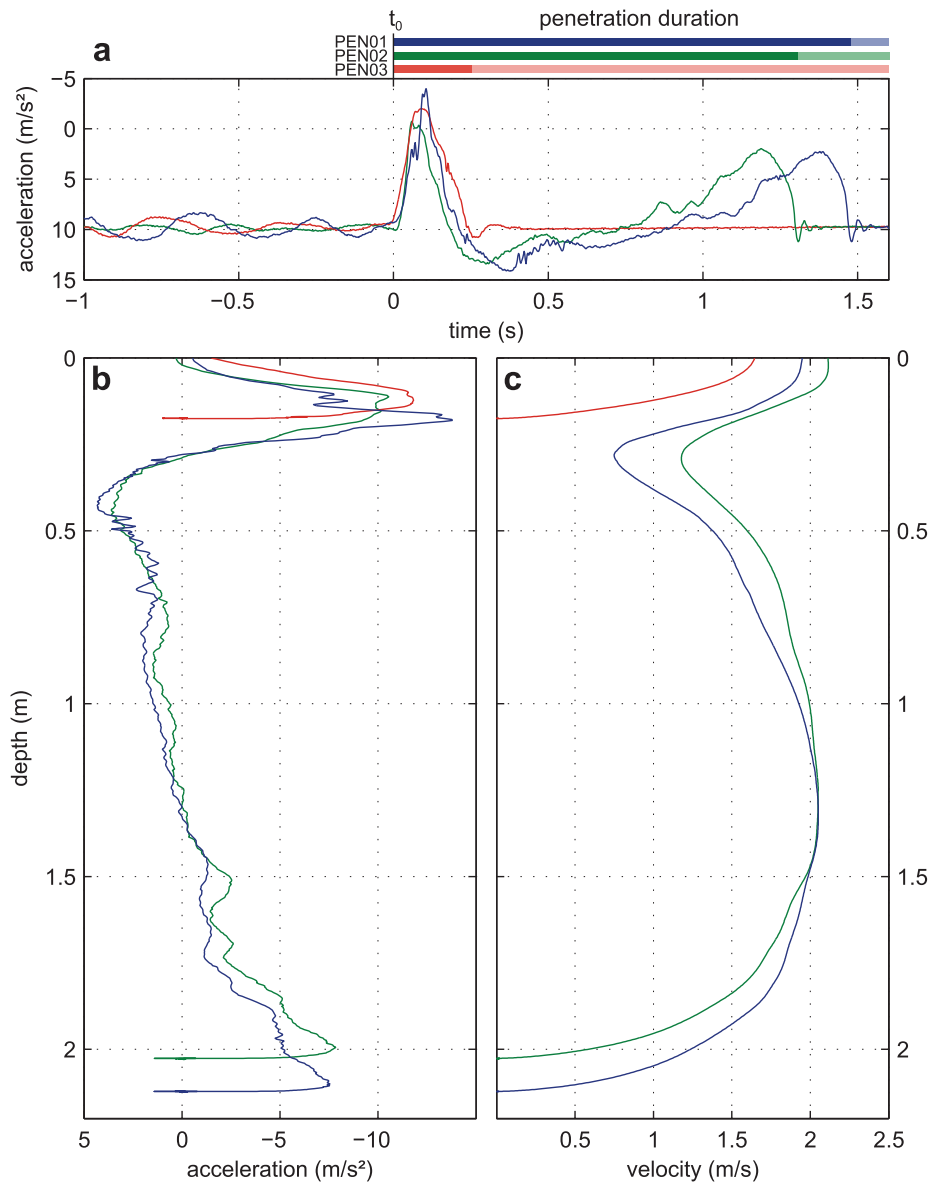


Figure 2.2 – **a** Acceleration-time series for PEN01-03. The durations of the respective penetration phases are indicated by dark colors above the plot, whereas the stall phase is indicated by light colors; **b** Acceleration-distance series for all three penetrations obtained by double-integration of the data in **a**; **c** Velocity-distance series for all three penetrations obtained by double-integration of the data in **a**.

ation, which would be less for free-falling devices. All three datasets show a reduction in acceleration because the penetrometer slows down (decelerates) within the sediment. The dataset PEN03 returns to gravitational acceleration at 0.25 s, while datasets PEN01 and PEN02 show an acceleration and subsequent deceleration (relative to g) after 0.25 s. The timespan where penetration is assumed to be complete (i.e., no change in acceleration, light colors above the acceleration-time diagram in Figure 2.2), is the longest for PEN03 (0.25 to 1.6 s) in this dataset.

Velocity and displacement are determined through integration (Equation 2.2). To solve the equation of motion resulting from the integration, additional information on the initial velocity v_0 and the initial displacement s_0 are needed. Considering the penetration process, a defined state exists within the timespan when the instrument is finally embedded in the sediment (stall phase). Then, $v := 0$ and $s := 0$. The discretely sampled acceleration may be integrated backwards from a point in time during this phase until the time of impact t_0 using an approximation technique, such as the trapezoidal rule.

Since the data is subjected to external, as well as electronically induced noise, it is important to select an optimal starting point for the integration because errors in acceleration propagate linearly into velocity and quadratically into displacement (see Eq. 2.3). This can be circumvented by application of a Monte-Carlo routine (Caffisch, 1998) to determine an optimal starting point for integration (see Section 3.3.3 for more information).

After integration, it is possible to represent acceleration (gravitational acceleration has been subtracted) and velocity during penetration as a function of penetrated distance (see Fig. 2.2b,c). It is now evident that the penetration depth reached during PEN03 (0.17 m) is only a fraction of PEN01 (2.12 m) and PEN02 (2.02 m). The velocities at impact range between 1.64 m/s (PEN03) and 2.11 m/s (PEN02), and the peak decelerations range between -10 m/s^2 (PEN02) and -13.8 m/s^2 (PEN03). The deeper penetration PEN02 and PEN03 have a phase of velocity increase between 0.3 and 1.4 m depth after the first deceleration between 0 and 0.3 m, which caused the lance to stop completely at 0.17 m for PEN03.

Considering that variations between penetrations may occur due to positioning uncertainties inhomogeneities of the sea floor, a very good reproducibility (characteristic features match within depth windows of 0.05 m) is shown for the three datasets. Considering that the data in Figure 2.2 originate from a single measurement for each respective penetration, a wealth of *qualitative* information can be already derived. The high decelerations in the first 0.3 m indicate a “hard” sediment, followed by a “softer” layer, which allows the lance to regain momentum. The softer layer seems to be uniform. The momentum of the lance during PEN03 (lowest impact velocity among

PEN01-PEN03) did not suffice to penetrate the upper harder layer.

2.1.2 Deduction of sediment resistance from kinematic data

Based on the consideration of forces acting on a non-driven penetrator (meaning no external forces applied) with projectile like shape are widely described by the Poncelet equation (Schmid, 1969; True, 1976). Thereafter, total resistance force acting on the penetrator is described as:

$$m \frac{d^2 z}{dt^2} = F_0 + W + F_H \quad (2.4)$$

with F_0 as plastic sediment resistance force, W as buoyant weight of the penetrator, and F_H as inertial drag acting on the penetrator. In the case of an object immersing completely into the sea floor, True (1976) derived the forces acting on the penetrator. Thereafter, F_0 is composed of F_{BE} , the bearing pressure force and F_{AD} , the side adhesion force. The inertial drag F_H is $-0.5(-A_F \rho v^2 \sin^2 \alpha)$, with α a nose half-angle v as penetration velocity and A_F as frontal area.

The bearing and adhesion forces F_{BE} and F_{AD} are calculated on the basis of bearing capacity theories for wedge-shaped foundations (Meyerhof, 1961; Durgonoglu and Mitchell, 1975) (cf. also Section 2.2.1 for the concept) with application of a strain-rate factor $S_{\dot{\epsilon}}$:

$$F_{BE} = -S_u S_{\dot{\epsilon}} N_c A_F \quad (2.5)$$

$$F_{AD} = \frac{S_u S_{\dot{\epsilon}} \delta A_s}{S_t} \quad (2.6)$$

with S_u as peak (undisturbed) static undrained soil strength, N_c as combined bearing capacity factor (see (True, 1976) for further details), A_s as side area, S_t as sensitivity (ratio between undisturbed (S_u) and remolded shear strength) and δ as side adhesion factor.

Empirical laboratory experiments (True, 1976) led to a formulation for the strain-rate and side adhesion factors $S_{\dot{\epsilon}}$ and δ , with δ being velocity dependent and ranging between 0 (low velocities) and 1 (high velocities) and $S_{\dot{\epsilon}}$ depending on sediment type and ranging between 1 and 10. This relationship has been applied in the analysis of Doppler penetrometer data (see Section 2.4.2) and in a modified form utilizing the rate factors presented in Section 2.1.3 for the assessment of deceleration behavior of dynamically

installed anchors with stabilizing fins during centrifuge tests (see Section 2.4.6):

$$m \frac{d^2 z}{dt^2} = W_d - F_\gamma - R_f (F_b + F_f) \quad (2.7)$$

$$= W_d - F_\gamma - R_f (F_{b,bA} + F_{b,bF} + F_{fA} + F_{fF}) \quad (2.8)$$

$$= W_d - F_\gamma - R_f (N_{c,bA} s_{u,bA} + N_{c,bF} s_{u,bF} + \alpha s_{u,sA} A_{sA} + \alpha s_{u,sF} A_{sF}) \quad (2.9)$$

$$R_f = 1 + \lambda \log_{10} \frac{v/D}{(v/D)_{\text{ref}}}; R_f \geq 1 \quad (2.10)$$

$$R_f = \left[1 + \eta \left(\frac{v/D}{(v/D)_{\text{ref}}} \right)^\beta \right] \frac{1}{1 + \eta}; R_f \geq 1 \quad (2.11)$$

with W_d as the anchor dry weight, F_γ as the buoyant weight of the soil, F_b as end bearing resistance, F_f as frictional resistance, $F_{b,bA}$ as end bearing resistance at the base of the anchor shaft, $F_{b,bF}$ as end bearing resistance at the base of the anchor fins, F_{fA} as frictional resistance along shaft, F_{fF} as frictional resistance along fins. The factor $N_{c,bA}$ is the bearing capacity factor at the base of the anchor shaft, $s_{u,bA}$ is the undrained shear strength at the base of the anchor shaft, $N_{c,bF}$ is the bearing capacity factor at the base of the anchor fins, $s_{u,bF}$ is the undrained shear strength at the base of anchor fins, and $s_{u,sA}$ is the average undrained shear strength over the embedded length of anchor shaft. A_{sA} is given as the embedded anchor shaft surface area, $s_{u,sF}$ as the average undrained shear strength over the embedded length of the anchor fins, A_{sF} as the embedded anchor fins surface area. Hossain et al. (2015) employed two rate formulae (see Section 2.1.3) for the rate factor R_f : (1) the log-relationship with a velocity measure (v/D), with D as the penetrometer diameter (Equation 2.10), and (2) a power-law relationship based on the Herschel–Buckley model (Eq. 2.11), modified for geotechnical applications (Zhu and Randolph, 2011). For more information, see Hossain et al. (2015) and Section 2.1.3.

Utilizing a finless penetrator and considering that side adhesion, buoyant and fluid drag are negligible (see, e.g., Stark et al. (2009b) or Steiner et al. (2012)), Equation 2.9 reduces to:

$$m \frac{d^2 z}{dt^2} = W_d - R_f F_b \quad (2.12)$$

Approaches based on energy balance

The depth of penetration of an impacting object is proportional to the energy it has at impact. Therefore, estimations on penetration behavior and penetration depth may be deduced considering energy balances.

O’Loughlin et al. (2013) presents an approach for predicting the embedment characteristics of dynamically installed anchors by using the “total energy”, which is the sum of the kinetic energy at impact and the potential energy upon placement of the anchor in the soil. For this purpose, 155 centrifuge model tests (O’Loughlin et al., 2004; Richardson et al., 2006; Richardson, 2008; Richardson et al., 2009; O’Loughlin et al., 2009) were reanalyzed, where, in total, 25 model penetrator configurations with different length to diameter ratios, fluke designs and masses were used (for further information, see O’Loughlin et al., 2013). The authors found an obvious dependency between velocity at impact and penetration depth, as well as a dependency between penetrator mass and penetration depth.

The concept of “total energy” is introduced to compare the variety of penetrators among themselves and with data from field trials:

$$E_{total} = 0.5mv_i + m'gz_e \quad (2.13)$$

with E_{total} as total energy, m as penetrator mass, m' as penetrator mass (corrected for buoyancy within the soil), v_i as impact velocity, g as gravitational acceleration, and z_e as final penetration depth. Note, that during the centrifuge experiments, the penetrator was falling through air prior to the impact into the saturated sediment. When corrected for the shear strength profile (k : gradient of shear strength with depth) and the different skin areas of the penetrators by a calculated (effective) diameter d_{eff} , which accounts for, e.g., fins, O’Loughlin et al. (2013) found a relationship between normalized anchor embedment depth and normalized total energy.

$$\frac{z_e}{d_{eff}} \approx \left(\frac{E_{total}}{kd_{eff}^4} \right)^{1/3} \quad (2.14)$$

with z_e as embedment depth. Eq. 2.14 predicts the embedment depth of the model penetrators, as well as the embedment depths of field-scale penetrating anchors.

The total energy approach has been adopted by Hossain et al. (2015) for the test data on calcareous silt and effectively accounts for differences in shear strength, mass, and dimensions, as shown by Hossain et al. (2015), where

results were compared with studies by Hossain et al. (2014). The authors found that the data fits to previous results (de Medeiros, 2002; Brandão et al., 2006; Zimmerman et al., 2009; Lieng et al., 2010; O’Loughlin et al., 2013; Hossain et al., 2014) with a modified exponent for tests in calcareous silt. Hossain et al. (2015) provide an alternate solution for the total energy approach accounting for the total surface area of the anchor, which produces a better fit to previous results (Hossain et al., 2014) for tests in calcareous silt (see Eq. 2.15):

$$\frac{d_{e,t}}{D_p} \approx q \left(\frac{E_{\text{total}}}{k A_s D_p^2} \right)^{1/r} \quad (2.15)$$

with $d_{e,t}$ as anchor tip embedment depth and D_p as anchor projected area equivalent diameter (including fins) and E_{total} as total energy and k as soil strength gradient and A_s as embedded anchor total surface area with q as first and r as second fitting parameter. For more information, see Hossain et al. (2015). Overall, normalized penetration depths are lower in silty sediments than in clayey sediments, which Hossain et al. (2015) attribute to the steeper shear strength gradient within the soil and to the general tendency of dilative behavior of silty sediments in contrast to the contractive behavior of clays.

Under the presumption that an impacting penetrometer has reached its terminal velocity before impact, dotOcean N. V. (2012) calculate density changes for very soft sediments based on a change in velocity during impact, assuming that the fluid sediment is considered to be a Newtonian fluid, following an energy-equilibrium approach:

$$E_{\text{kin}}(h_1) + E_{\text{pot}}(h_1) = E_{\text{kin}}(h_2) + E_{\text{pot}}(h_2) + \Delta E \quad (2.16)$$

with ($h_1 > h_2$) as two discrete heights. Since velocity does not change during fall through the water-column, the dissipated energy ΔE must account for the decrease in E_{pot} and is therefore attributed to the sum of buoyant- and fluid drag energy $E_{\text{buoy}} = \rho V g h$ and $E_{\text{drag}} = 0.5 \rho A C_d v^2 h$, with ρ as density of the medium, V as displaced volume, g as gravitational acceleration, h as difference between h_1 and h_2 , A as cross-sectional area of the penetrator, C_d as drag coefficient, and v as velocity. The drag-coefficient is material-specific and needs to be determined experimentally. Knowing the deceleration profile, ρ can be calculated.

2.1.3 Rate correction

The rate-dependent behavior of soils has been described by Casagrande and Shannon (1949). The authors found, that dynamic loads led to a high increase in the strength of clays, while the same conditions provoked only a slight increase in the strength of sands. Pile driving investigations by Geuze (1953) in sand revealed that the penetration resistance of piles were proportional to the logarithm of the penetration velocity. These findings were later confirmed by Kérisel (1961) and supported by a statistical-mechanical analysis of soil behavior by Mitchell (1964) considering the inter-grain contacts per unit area as a key parameter for soil strength and rate dependence.

The investigation of rate dependencies in soils is vital to assess the influences of rapid loading on the soil strength. Such rapid loading may occur when external forces are applied, e.g., in the course of building operations, during earthquakes, or soil penetration.

The dependency of soil strength on the deformation rate is thus also relevant to all fields of geotechnical testing, where deformation of soil samples is used to obtain strength parameters. Beyond the early studies, rate effects were investigated by, e.g., Sheahan et al. (1996), Soga and Mitchell (1996), and Chow and Airey (2013) for triaxial tests. Perlow and Richards (1977), Biscontin and Pestana (2001), Peuchen and Mayne (2007), and Schlue et al. (2010) investigated the rate dependence during vane shear testing. The rate-dependence during CPT is summarized in Lunne et al. (1997) and (Danziger and Lunne, 2012). In the case of full-flow penetrometers, rate effects were investigated by Lehane et al. (2009). For impact penetrometers, Dayal and Allen (1975) introduced a logarithmic dependency between penetration velocity and penetration resistance.

The term *rate* is often used in the context of the process described. Hence, a rate correction for triaxial tests relates to the strain rate $\dot{\epsilon}$ (Graham et al., 1983; Sheahan et al., 1996), whereas a rate correction for vane shear tests relates to the peripheral velocity or the rotational velocity of the vane (Biscontin and Pestana, 2001; Peuchen and Mayne, 2007). For penetrometer tests, *rate* is often used synonymously with penetration velocity v (Dayal and Allen, 1975) or a velocity measure, such as v/d (with d as diameter of the penetrometer) or normalized velocity V (Lehane et al., 2009; Steiner et al., 2014). However, if strains for the dynamic and reference condition are equal, strain may be substituted with velocity (Dayal and Allen, 1973). Rate corrections are applied to various geotechnical parameters, like undrained shear strength in the case of triaxial and vane shear tests (Sheahan et al., 1996; Schlue et al., 2010), or cone resistance in the case of penetrometer tests (Dayal and Allen, 1975). Therewith, the mathematical formulation of

the rate correction is consistent throughout the applications.

The assessment of rate effects is important during penetrometer testing, and especially during impact penetrometer testing, due to the dynamic nature of the penetration process. As shown in Table 2.2, penetration velocity (i.e., *rate*) can cover several orders of magnitude. In this context, three corrections are commonly used to correct for the non-uniform velocity during penetration:

- the log-relationship (Dayal and Allen, 1975)
- the power-law relationship (Biscontin and Pestana, 2001), and
- the arcsinh-relationship after Randolph (2004).

The log relationship in penetrometer testing

As pointed out above, several authors found, from observations (Geuze, 1953; Kérisel, 1961) and from systematic laboratory tests (Casagrande and Shannon, 1949), that the strength of soils may be described as a logarithmic function of strain rate or penetration velocity. Dayal and Allen (1973, 1975) introduced the log rate correction to marine impact penetrometer testing:

$$\text{RF}_{\log} = \frac{R_{\text{dyn}}}{R_{\text{ref}}} = 1 + K_L \log_{10} \left(\frac{r_{\text{dyn}}}{r_{\text{ref}}} \right) \quad (2.17)$$

$$= \frac{q_{c,\text{dyn}}}{q_{c,\text{ref}}} = 1 + K_L \log_{10} \left(\frac{v_{\text{dyn}}}{v_{\text{ref}}} \right) \quad (2.18)$$

with RF_{\log} as rate factor, R_{dyn} as dynamic resistance, R_{ref} as static (or reference) resistance, K_L as soil viscosity coefficient (Dayal and Allen, 1975), or simply: rate parameter, r_{dyn} as dynamic rate, and r_{ref} as static or reference rate. In the case of penetrometers, it is common to use cone resistance q_c or total cone resistance q_t as R and the penetration velocity v as r . The reference velocity v_{ref} is often set to 0.02 m/s, which is the standard penetration velocity of CPT (Lunne et al., 1997).

The rate factor increases by K_L for each 10-fold increase in penetration velocity. However, the mathematical formulation $\log_{10}(v_{\text{dyn}}/v_{\text{ref}})$ bears the effect that values for q_{dyn} become overcorrected, when $v_{\text{dyn}} < v_{\text{ref}}$. This occurs regularly during impact penetrometer testing, since the penetrator decelerates to $v_{\text{dyn}} = 0$. Consequently, RF_{\log} becomes ≤ 1 and even negative, while the rate corrected parameter $q_{c,\text{ref}}$ increases in the velocity range $v_{\text{dyn}} < v_{\text{ref}}$ (see Figure 2.3a,b).

Eq. 2.18 is the most popular rate correction and has been used to correct rate effects in sediments ranging from soft cohesive mud over calcareous silts and sands, to quartz sands and mixed sediments for a variety of marine impact penetrometers (see Table 2.1 for rate parameter values for the respective penetrometer, sediment type, and rate).

The power-law relationship in penetrometer testing

The power-law relationship originates in the treatment of soils considering rheological models (Šuklje, 1957; Jeong et al., 2009). Applying the rheological approach, it is unnecessary to consider drainage conditions because the soil is considered as a homogeneous, viscous volume (Lehane et al., 2009). The power-law approach has been adopted by Biscontin and Pestana (2001), Peuchen and Mayne (2007) and Schlue et al. (2010) for vane shear experiments, by Rattley et al. (2008) for triaxial extension experiments and by Briaud et al. (1984) for simple shear tests. The approach is formulated after, e.g., Biscontin and Pestana (2001) as follows:

$$\text{RF}_{\text{power}} = \frac{R_{\text{dyn}}}{R_{\text{ref}}} = \left(\frac{r_{\text{dyn}}}{r_{\text{ref}}} \right)^{\beta} \quad (2.19)$$

$$= \frac{q_{\text{c,dyn}}}{q_{\text{c,ref}}} = \left(\frac{v_{\text{dyn}}}{v_{\text{ref}}} \right)^{\beta} \quad (2.20)$$

with β as rate parameter, which is dependent on the rate range and the soil properties (Rattley et al., 2008; Chow, 2013). See Equation 2.18 for the designation of the other variables.

The power-law-relationship has been applied to dynamic penetrometers (Chow et al., 2014), such as deep penetrating anchors (O’Loughlin et al., 2009) or to dynamic CPT (Steiner et al., 2014).

The mathematical formulation of Eq. 2.20 leads to $\text{RF}_{\text{power}} < 1$ for $v_{\text{dyn}} < v_{\text{ref}}$, and hence to an overcorrection with excessive values for the rate corrected parameter $q_{\text{c,ref}}$ in this velocity range and especially when v_{dyn} converges to 0 (see Figure 2.3c). Table 2.1 gives rate parameter values for the respective penetrometer, sediment type, and rate.

The arcsinh relationship in penetrometer testing

Based on the theory of reaction rates (Glasstone et al., 1941; Eyring, 1936) and statistical mechanics, Mitchell (1964) and Kuhn (1987) deduct an expression describing sediment resistance to be proportional to the inverse hyperbolic sine of the strain rate based on the assumption that soil matter

follows processes analogously to the viscous flow of fluids and chemical reaction rates (Hazell, 2008). In terms of penetration problems, this relation is expressed as follows (Litkouthi and Poskitt, 1980):

$$\text{RF}_{\text{arcsinh}} = \frac{R_{\text{dyn}}}{R_{\text{ref}}} = 1 + \frac{K_L}{\ln 10} \operatorname{arcsinh} \left(\frac{r_{\text{dyn}}}{r_{\text{ref}}} \right) \quad (2.21)$$

$$= \frac{q_{\text{c,dyn}}}{q_{\text{c,ref}}} = 1 + \frac{K_L}{\ln 10} \operatorname{arcsinh} \left(\frac{v_{\text{dyn}}}{v_{\text{ref}}} \right) \quad (2.22)$$

Randolph (2004) favors Eq. 2.22 over Eq. 2.18 due to an inherent limitation for small rates. This is due to the mathematical formulation, which lets $\text{RF}_{\text{arcsinh}}$ converge to 1 for values of v_{dyn} converging to 0, which produces no excessive values as compared to Equations 2.18 and 2.20 in the velocity range $v_{\text{dyn}} < v_{\text{ref}}$ (see also Fig. 2.3). The rate parameter K_L has the same value as in Eq. 2.18. Randolph (2004), found, that setting $K_L/\ln 10$ produces rate factors matching those from the log relationship. However, discrepancies increase with increasing K_L (see next Section on that topic). Table 2.1 gives rate parameter values for the respective penetrometer, sediment type, and rate.

Comparison of rate formulae

As outlined above, some of the rate formulae have their peculiarities due to their mathematical formulations. Fig. 2.3b–d shows the outcome of the three rate corrections applied on a generic penetration profile (Figure 2.3a). The rate factors RF are given for minimum, mean, and maximum values of the rate parameter. The resulting band of rate corrected resistance (in this case: cone resistance q_t) is shown as a shaded area with the mean value as a solid line. The dynamic penetration resistance profile q_c (dash/dotted line) is given as a reference.

The rate corrections using the log and power-law approach lead to excessive values for rate corrected cone resistance. However, the effect occurs in the velocity range below the reference velocity, which is commonly set to 0.02 m/s for impact penetrometer testing. The distance, which is covered in the interval $0 < v_{\text{dyn}} \leq v_{\text{ref}}$ typically amounts to less than 1 % of the penetration depth for impact penetrometer testing (Steiner et al., 2014). Therefore, it is reasonable to discard the data in this depth interval, when rate corrections after Equation 2.18 or 2.20 are chosen to correct dynamic penetration data.

The arcsinh-relationship is shown as a function of the log-relationship in Fig. 2.4 with data from Figure 2.4, since they use the same rate param-

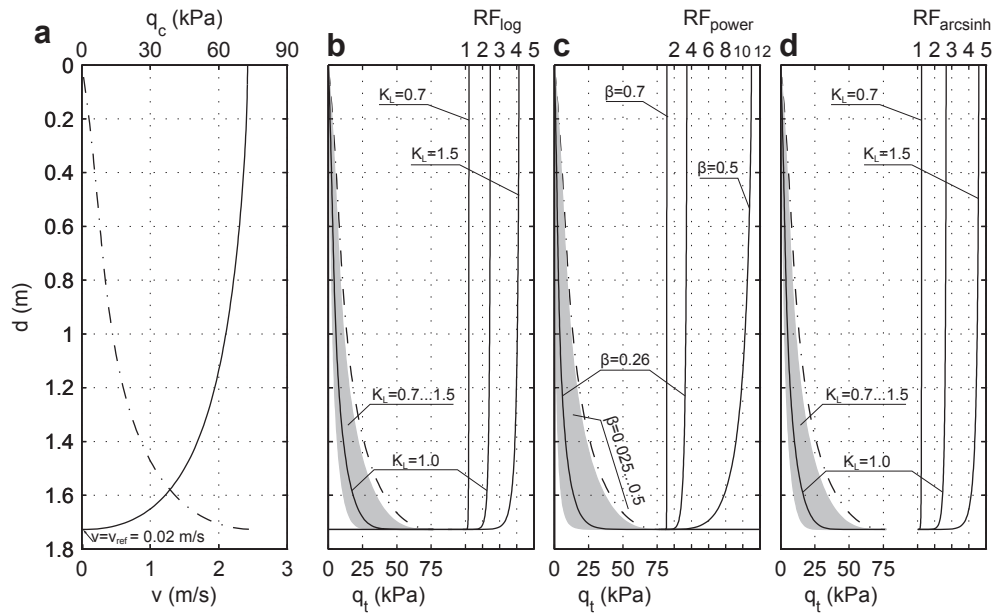


Figure 2.3 – Rate correction of a typical dynamic penetration dataset. **a** penetration velocity (solid line, lower axis) and dynamic cone resistance (dash-dotted line, upper axis) as a function of penetration depth; **b** rate corrected cone resistance data using the log relationship for a range of rate parameters K_L ; **c** rate corrected cone resistance data using the power-law relationship for a range of rate parameters β ; **d** rate corrected cone resistance data using the arcsinh relationship for a range of rate parameters K_L . The band of rate corrected data is given in **b-d** as a shaded area with a mean rate parameter as a solid line (lower axis). The dynamic resistance profile (dash-dotted line, lower axis) is given as a reference. The rate factors (upper axis) are given for a minimum, maximum, and mean value.

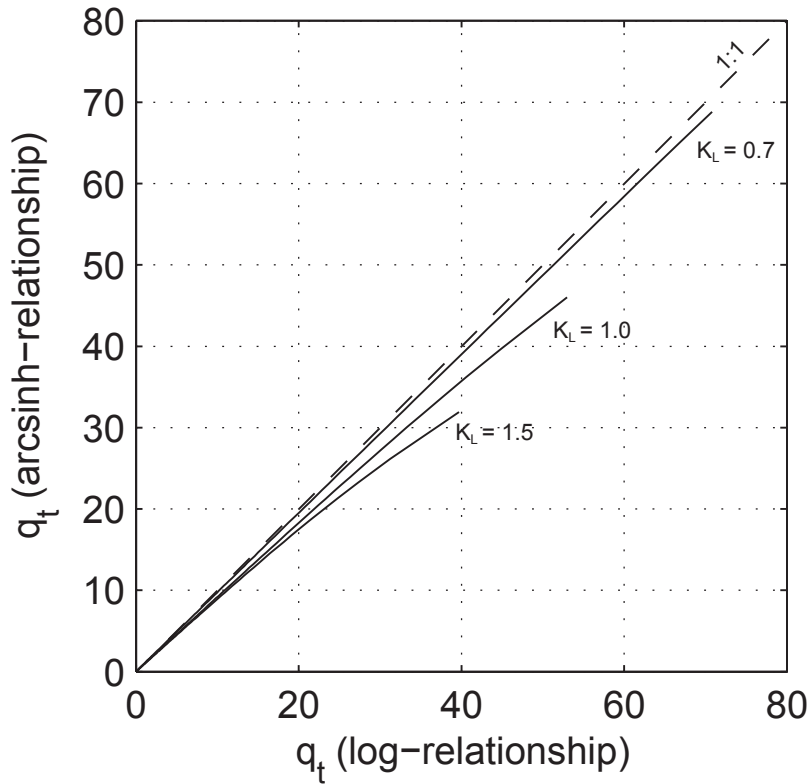


Figure 2.4 – Correlation between log and arcsinh relationships in dependency of the rate parameter K_L . Data is shown for $v_{\text{dyn}} > v_{\text{ref}}$.

eter K_L . The arcsinh-relationship produces lower values for rate corrected resistance than the log-relationship. This effect increases with decreasing penetration velocity (i.e., deeper penetration in this example) and is dependent on K_L with 3 % deviation for $K_L = 0.1$, 13 % deviation for $K_L = 1$ and 20 % deviation for $K_L = 1.5$.

The formulae produce qualitatively similar results for correction of penetration data in the considered velocity range. However, the uncertainty, which is connected to an assignment of a value to the rate parameter, has an influence on the results since the rate formulae are heavily dependent on their rate parameters β and K_L .

Table 2.1 – Rate parameters for different types of penetrometers, soil targets, penetration rate, and reference rate. PEN: dynamic penetrometer; cent.: centrifuge test with scaled gravity (scale factor for velocity in parentheses); backf.: backfitted.

Rate Parameter	Instrument	Max. Rate	Reference Rate	Citation
<i>log / arcsinh-relationship</i>				
0.105	PEN	10 m/s	0.02 m/s	(Buhler and Audibert, 2012)
0.13	PEN	6 m/s	0.02 m/s	(Steiner et al., 2012)
0 - 0.25	PEN	7.3 m/s	0.05 %/h	(Aubeny and Shi, 2006)
0.22 - 0.28 (0.43-0.59)	PEN (backf.)	4.7 - 12.2 m/s	0.011 m/s	(Chow and Airey, 2011a)
0.3-0.77	PEN	0.011 - 12.2 m/s	2.5 s ⁻¹	(Chow and Airey, 2011b)
0.2 - 0.5	DPA (cent.)	26 (· 200) m/s	0.2 s ⁻¹	(O'Loughlin et al., 2009)
0.13	PEN	6 m/s	0.02 m/s	(Steiner et al., 2012)
<i>calcareous silt</i>				
0.6 - 0.8	DPA (cent.)	21 (· 133) m/s		(Hossain et al., 2015)
<i>quartz sand</i>				
0.03 - 1.5	PEN	5.5 m/s	0.02 m/s	(Dayal and Allen, 1975)
1.0 - 1.5	PEN	10 m/s	0.02 m/s	(Stark et al., 2009b, 2012b)
1.0 - 1.5	PEN	6 m/s	0.02 m/s	(Stoll et al., 2007)
<i>carbonate sand</i>				
1.0 - 1.5	PEN	12 m/s	0.02 m/s	(Stark et al., 2009b, 2012b)
<i>power-law relationship</i>				
0.02 - 0.07	PEN	6 m/s	0.02 m/s	(Steiner et al., 2014)
0.05 - 0.1	PEN (cent.)	15.6 (· 100) m/s	0.1 s ⁻¹	(Chow et al., 2014)
0.06 - 0.12	DPA (cent.)	26 (· 200) m/s	0.2 s ⁻¹	(O'Loughlin et al., 2009)
0.19	DPA (cent.)	29 (· 200) m/s	0.17 s ⁻¹	(Gaudin et al., 2013)
<i>calcareous silt</i>				
0.15	DPA (cent.)	21 (· 133) m/s		(Hossain et al., 2015)

2.2 Geotechnical properties from CPT data

2.2.1 Theoretical models for penetration tests

Theoretical approaches to determine the shear strength of sediments were established by several authors. Three approaches are commonly applied to penetration testing.

The bearing capacity theory

The bearing capacity theory approach has been introduced by Terzaghi (1943) based on the plasticity approach developed by Prandtl (1921). The bearing capacity theory is widely accepted for the determination of maximum stresses a soil can bear prior to failure. Consequently, failure occurs, if the bearing capacity is exceeded by the loading mechanism. The bearing capacity method has initially been formulated for a strip footing and has been widened to be applicable to deep foundations, inclined loads, and wedge or cone-shaped foundations by Meyerhof (1951, 1953, 1961) and Durgonoglu and Mitchell (1975). Transferred to penetration problems, the cone resistance measured during penetration is assumed as the incipient failure load (i.e. bearing capacity; Lunne et al., 1997) of plastic, rigid material. Depending on the geometry, plastic zones are described differently and the mathematical formulations differ (cf. Fig. 2.5a for the strip foundation and Fig. 2.5b for a deep, wedge, or cone-shaped foundation).

The ultimate bearing capacity for the strip foundation q_u is formulated as follows (Das, 2001):

$$q_u = q_c + q_q + q_\gamma = cN_c + qN_q + \frac{1}{2}\gamma BN_\gamma \quad (2.23)$$

with N_c , N_q , and N_γ as bearing capacity factors, γ as unit weight, c as cohesion and B as width of the foundation. The bearing capacity for deep, wedge-shaped foundations q_r is formulated as follows (Meyerhof, 1961):

$$q_r = cN_{cr} + p_0N_{qr} + \frac{\gamma B}{2}N_{\gamma r} \quad (2.24)$$

with N_{cr} , N_{qr} , and $N_{\gamma r}$ as bearing capacity factors for a cone-shaped foundation and p_0 as equivalent stress (Meyerhof, 1951).

The bearing capacity theory is dependent on the soil stiffness and the failure geometry in the plastic zone (Lunne et al., 1997). However, due to the simplicity and the broad empirical background, it is a widely applied method to determine sediment properties from cone resistance measurement.

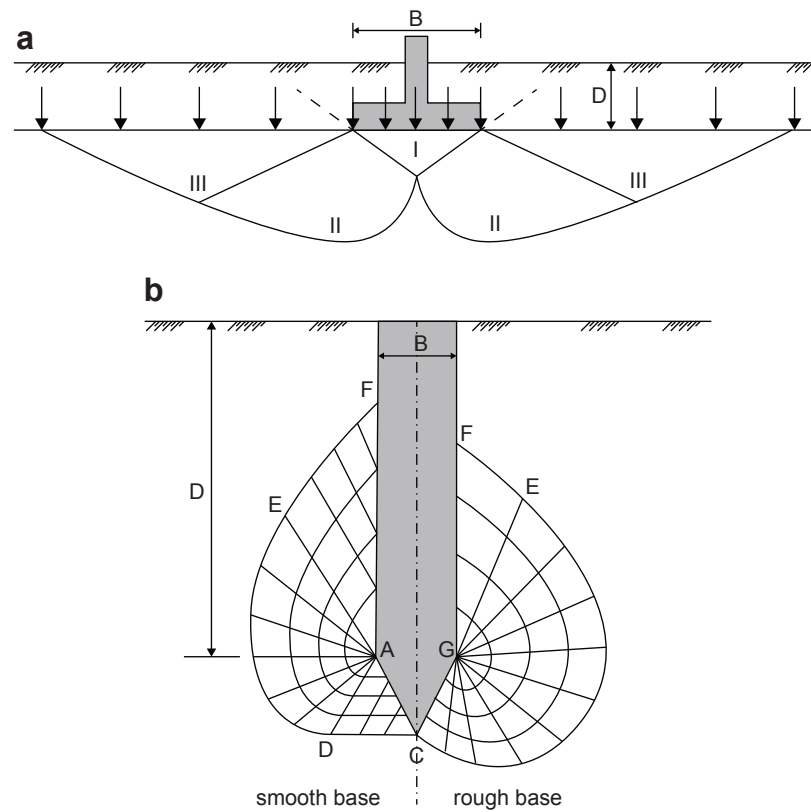


Figure 2.5 – Failure mechanism and plastic zones. **a** Deformation zones under a strip footing with width B and depth D after the ultimate bearing capacity theory of Terzaghi (1943). Zone I is an elastic zone. Zones II are radial shear zones. Zones III are the Rankine passive zones. The rupture lines are the solid lines at the bottom described by a logarithmic spiral. Sketch modified after Das (2001); **b** The deformation zones of a deeply immersed, wedge or cone-shaped foundation: Zone ACD: plane shear zone; Zone ADE or BDE: radial shear zone; Zone AEF or BEF: plane shear zone. Sketch modified after Meyerhof (1961).

The cavity expansion theory

The cavity expansion theory assumes, that the resistance to penetration is proportional to the pressure needed to expand a spherical cavity of the same volume within an infinite elastoplastic soil (Bishop et al., 1945; Vesic, 1975; Lunne et al., 1997). Based on energy balance considerations, Baligh (1975) assumes that the work required to push a cone at a constant rate into the soil medium is proportional to the work required to expand a cylindrical cavity of the same volume (Lunne et al., 1997). In order to use the cavity expansion approach on cone resistance, two steps are necessary: development of limit pressure solutions for the cavity expansion and the relation of the cavity expansion limit pressure to cone resistance. The cavity expansion model can be further improved, e.g., by considering a cylindrical cavity (Carter et al., 1986), the incorporation of large strains within the plastic region (Yu and Houlsby, 1991), or the inclusion of friction and dilation angles around the cavity (Salgado et al., 1997).

2.2.2 Empirical relationships

The undrained shear strength of cohesive sediments from (total) cone resistance

In applied and research practice, empirical correlations are often used to obtain values for shear strength from cone resistance measurements since theoretical approaches are not able to describe the heterogeneity of soils regarding, e.g., anisotropies, sensitivity, or ageing (Lunne et al., 1997). The empirical correlations are obtained from laboratory tests where sediment properties and environmental conditions are known or controlled. The undrained shear strength of cohesive sediments is related to the cone resistance in the general form:

$$s_u = \frac{q_c - \sigma}{N_k} \quad (2.25)$$

$$s_u = \frac{q_t - \sigma}{N_{kt}} \quad (2.26)$$

with q_c as cone resistance, q_t as total cone resistance, which has been corrected for the unequal area effect, σ as *in-situ* total pressure (or vertical (effective) pressure σ_v), and N_k or N_{kt} as the theoretical cone factor depending on the physical properties of the soil and the characteristics of the penetrator (typically ranging between 11 and 19; Lunne and Kleven, 1981).

The state parameter relationship for cohesionless sediments

All empirical relationships involving cone factors N_k (cf., e.g., Equation 2.25), have a limited applicability to non-cohesive samples (Lunne et al., 1997). As void ratio (or porosity) is the controlling variable for soil behavior, Been et al. (1987) established a relationship between cone resistance, void ratio, mean normal stress, and the steady state parameters by introducing the state parameter ψ (Been and Jefferies, 1985; Been et al., 1986). The relationship is established based on laboratory calibration chamber tests on a variety of model sands:

$$\frac{q_c - p}{p'} = ke^{-m\psi} \quad (2.27)$$

$$k = 8.1 - \ln \lambda \quad (2.28)$$

$$m = 8 + \frac{0.55}{\lambda - 0.01} \quad (2.29)$$

$$\psi = e_c - e_{ss} \quad (2.30)$$

with q_c as cone resistance, p as mean *in situ* stress, p' as mean effective *in situ* stress, λ as the slope of the steady-state line, e_c as void ratio of the sample, and e_{ss} as void ratio at a steady state corresponding to p' . The concept of the state parameter is shown in Fig. 2.7, whereas the relationship between k , m , and soil type is shown in Fig. 2.6. The steady state line is the state in which a soil under shear stress flows continuously under constant shear stress and constant effective confining pressure at constant volume and constant velocity (Kramer, 1996). The steady state is represented as a curve in e - p' - q -space and may be projected as a line in p' - q -space and e - $\ln(p')$ -space, respectively.

Soils with a state above the steady state line (positive ψ) show compressive behavior during undrained shearing at constant horizontal stresses, whereas soils below the steady-state line (negative ψ) show dilative behavior (Been and Jefferies, 1985). Under undrained conditions (i.e., constant void ratio), no volume changes occur. Therefore, pore pressure increases during application of deviatoric stress q . Consequently, effective stress p' is reduced (see inset in Fig. 2.7c). For dilative samples, pore pressure decreases under undrained conditions (see inset in Fig. 2.7a) and, therefore, contributes to the strain-hardening behavior of the soil. Inset (b) describes an intermediate behavior with initial weakening due to increasing pore water pressure and subsequent hardening during shear, which is described as limited liquefaction behavior (Castro, 1969).

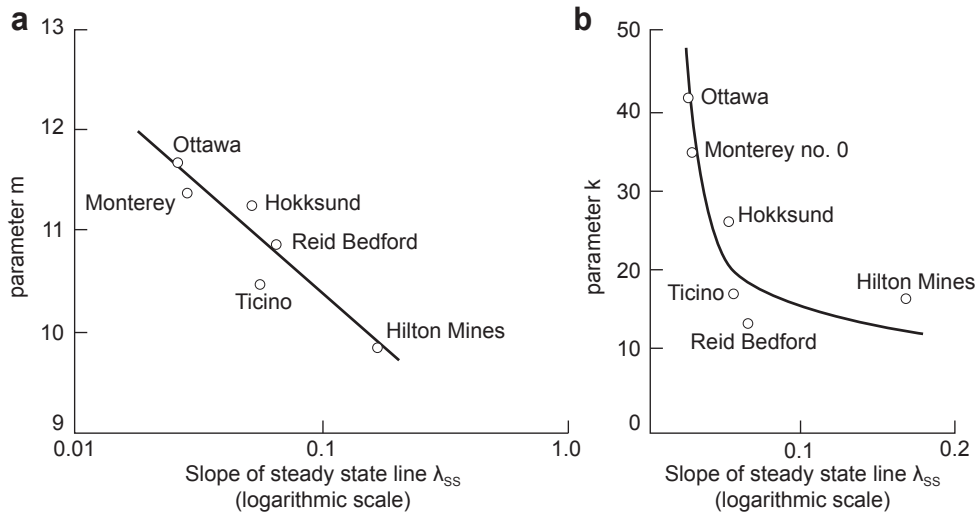


Figure 2.6 – **a** Slope m of normalized tip resistance – ψ -relationship; **b** Normalized cone resistance at $\psi = 0$, k . Plots modified after Been et al. (1987).

2.3 Static velocity penetrometers

Commonly, static velocity penetrometers are used for cone penetration testing. Cone penetration with static velocity measures, opposed to dynamic velocity testing with impact penetrometers, determines the soil resistance to the penetration of a cone with a constant velocity. This velocity is typically 0.02 m/s (Lunne et al., 1997). Under marine conditions, three deployment scenarios are common (Lunne, 2012): (i) operation in seabed mode, (ii) operation in down-hole or drilling mode and (ii) operation in down-hole mode deployed from the seabed. The three modes have different concepts regarding the push mechanism and the location of the driving gear.

2.3.1 Sensors for CPT

Cone penetration testing is conducted nearly exclusively with electric sensors (henceforth: cones), where cone and frictional loads q_c and f_s act on the cone tip and the sleeve, respectively, and are directly measured through load cells with strain gauges. Piezocones additionally measure the pore pressure in the tip (U1 position), behind the conical part (U2 position), or behind the friction sleeve (U3 position). See Fig. 2.8 for pore pressure sensor locations. Modern cones accommodate additional sensors, e.g., for temperature or inclination.

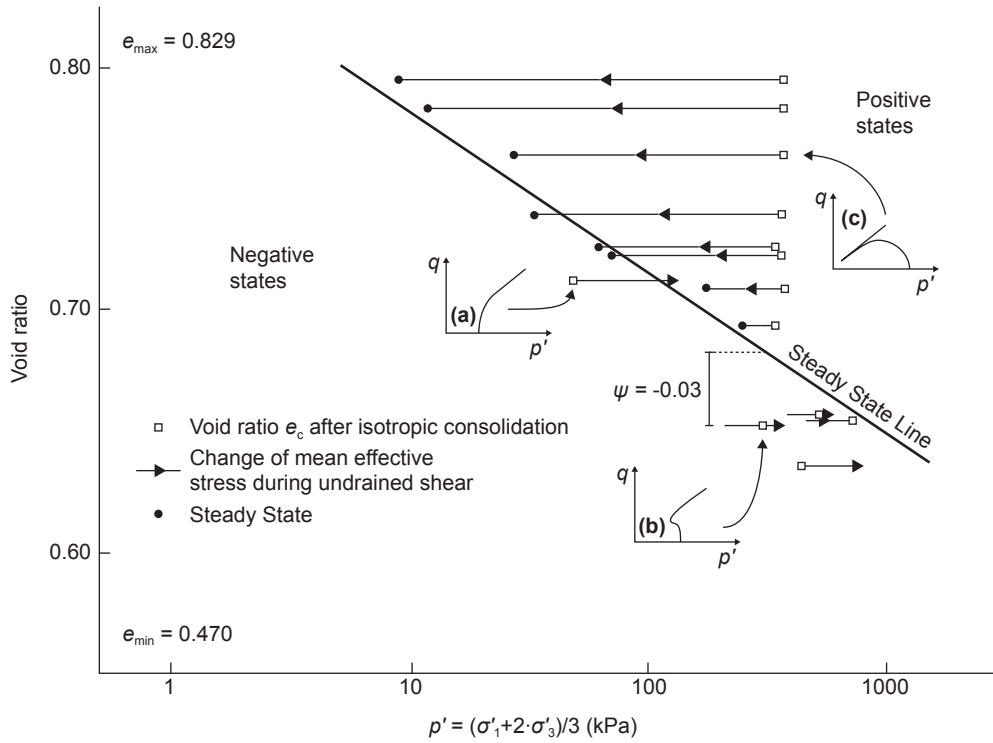


Figure 2.7 – The behavior of loose and dense sand under undrained shear. The isotropically consolidated samples lie in the p' - e -space above (loose) or below (dense) the steady state line (open squares). The horizontal lines with arrows indicate the change in effective stress during undrained shear. Closed circles indicate the steady state. Insets (a-c): Illustrative effective stress paths for the different initial states and shear behavior. Modified after Been and Jefferies (1985). Data from Kogyuk 350/2 sand (Been and Jefferies, 1985).

The cones exist in different measurement assemblies and are termed, compression, tension, or subtraction cones, which depends on the configuration of load cell arrangement (see Fig. 2.9). Load cells are sensors that produce electrical signals proportional to the applied force. Strain gauges, which change their electrical resistance upon deformation, are the common sensing elements within load cells. The pore pressure in piezocones is measured with one or more pore pressure transducers, which use piezoelectric sensing elements. The cones typically have an apex of 60° (Lunne et al., 1997). Although, other shapes exist, such as ball- or T-bar penetrometers. These so-called full-flow penetrometers (Stewart and Randolph, 1991; Watson et al., 1998) allow the determination of remolded soil properties. The diameter and hence the cross-sectional or projected area is different and depends on the application. Typical cross-sectional areas for cones are 10 and 15 cm² (Lunne, 2012), whereby 1, 2, 5, and 33 cm² cones are also used (Lunne, 2012; Hefer et al., 2005). Small cones are used in general for small loads and detailed investigations where a high vertical resolution is required or for coiled tubing instruments (Lunne, 2010). Larger cones tend to be used where mechanical robustness is required (e.g., down-hole CPT) (Lunne, 2010).

Measurements in deep water at high hydrostatic pressures have an effect on the cone resistance measurement q_c , thus reducing the sensitivity of the measurement due to the requirement of a larger measurement range. Therefore, pressure compensated load cells were developed (e.g. Jorat et al., 2014a).

Due to the volume changes of the soil matrix during penetration, the equilibrium pore pressure of the sediment is affected by the measurement. During CPTu testing, pore pressure is registered. However, changes in pressure affect also the measurement of cone resistance. This effect can be compensated by calculation of the total cone resistance q_t by taking the pore water pressure during penetration into account (Lunne et al., 1997):

$$q_t = q_c + u \left(1 - \frac{A_c}{A} \right) \quad (2.31)$$

with u as pore water pressure, A_c as cross-sectional area of the load cell exposed to the pore water pressure and A as cross sectional area of the cone.

2.3.2 CPT in seabed mode

Devices following the operational concept of seabed mode were among the first designs for marine use. In seabed mode, a CPT device is lowered through the water column and placed at the desired location on the sea floor. Then, a

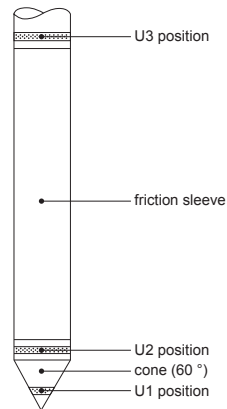


Figure 2.8 – Locations for measurement of pore pressure in the tip (U1), behind the tip (U2) and behind the friction sleeve (U3). Cone resistance and sleeve friction are measured over the indicated areas. Image modified after Bayne and Tjelta (1987); Lunne (2012).

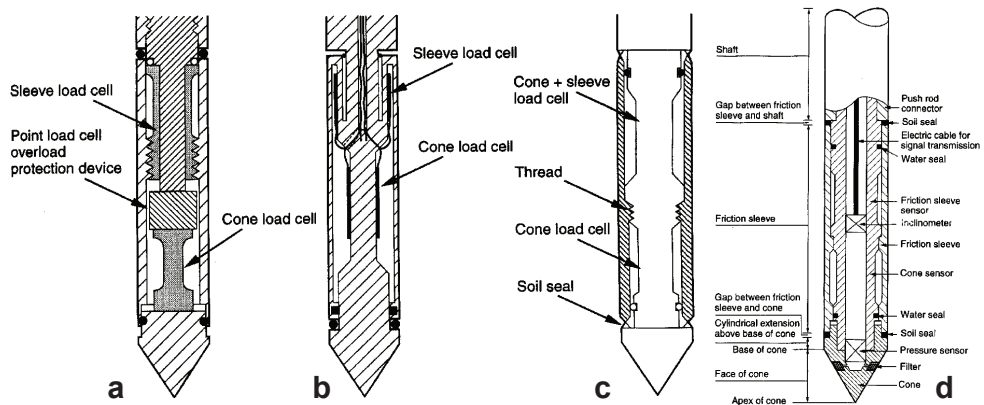


Figure 2.9 – **a** Electric cone penetrometer with compression load cells for cone resistance and sleeve friction; **b** Electric cone penetrometer with compression load cell for cone resistance and tension load cell for sleeve friction; **c** Electric cone penetrometer in subtraction-type configuration; **d** Electric piezocone with pore pressure measurement in the U1 position (within the cone tip). All drawings modified after Lunne et al. (1997).

sensor is inserted into the sediment by using pushrods until a predetermined sounding depth is reached or constraints are met (Lunne, 2010). The main constraints for devices in seabed mode are (i) the maximum water depth where operation is possible, (ii) the maximum length of the push-rods, and (iii) the buoyant weight of the instrument itself as it serves as the reaction force to the penetration resistance (Lunne, 2012).

The first devices were developed by Fugro in the early 1970s with the *Seabull* (Zuidberg, 1972) and the *Seacalf* (Zuidberg, 1975a). The devices pushed an instrumented cone through a hydraulic actuator into the sediment, whereby the penetration is discontinuous because the travel distance of the actuator is limited.

An instrument with roller wheels has been introduced by A.P. van den Berg (Netherlands) to drive the pushrods and the cone into the soil yielding an uninterrupted penetration. The continuous driving mechanism has been adopted by Fugro for the *Seacalf* (Richards and Zuidberg, 1985) and is state of the art for seabed mode rigs.

Seafloor rigs exist in various dimensions depending on the investigation target. The *Seacalf* has a mass of up to 20000 kg (Zuidberg, 1975b). Even stackable devices exist (Fugro, pers. comm.) to enlarge the reaction force. Lighter devices, such as the Geotechnical Offshore Seabed Tool (GOST, Jorath et al., 2014b) of MARUM are more suited for detailed, rapid investigations.

The above mentioned devices use straight rods to attain the desired or anticipated penetration depth, which limits the maximum penetration depth due to handling problems. To overcome such issues, seabed rigs with coiled rods, such as the TSP (Power and Geise, 1994), Penfeld (Meunier et al., 2004), or the Neptune system (Datem, United Kingdom) were developed.

2.3.3 CPT in down-hole mode

Down-hole systems require a drill vessel. The penetrometer is located in the tip of the drill string, which allows the sampling of undisturbed sediments before drilling (Lunne, 2010). The WISON system by Fugro (Zuidberg, 1972) is shown in Fig. 2.10d. Due to the limited travel distance of the cone penetrometer and the required drill phases to attain deeper penetration, down-hole type systems are discontinuous. Moreover, the data quality depends on the stabilization of the platform as vessel movement transfers over the rigid drill string directly to the penetrometer. This can be mitigated by using heave compensation or, in shallow water depths, jack-up rigs (Lunne, 2012).

2.3.4 CPT in combined seabed and down-hole mode

Seafloor drill-rigs are not susceptible to vessel movement because they rest like seabed-CPTs on the seafloor and are, therefore, decoupled from the platform (Lunne, 2012). The Portable Remotely Operated Drill (PROD, Kelleher and Randolph, 2005) has a magazine that allows for the selection of drills for different materials and the CPT instruments. The measurement concept is similar to the down-hole mode CPTs.

2.4 Impact penetrometers

This section gives an overview on the state of the art regarding impact penetrometers with a description of several devices comprising their dimensions, sensorial configuration, and deployment technique, as well as selected cases, where such penetrometers were applied for investigative purposes. The section begins with the description of free-falling expendable devices (Section 2.4.1–2.4.5), such as the Marine Sediment Penetrometer (MSP), the Expendable Doppler Penetrometer (XDP), the Instrumented Seabed Penetrometer (ISP). These devices were for the greater part developed at Sandia National Laboratories (Albuquerque) as pilot studies within the frame of potential disposal of radioactive waste in deep waters. Another application of penetrometers for anchoring purposes emerged from these studies. Following the description of free-falling expendable devices, lightweight devices are introduced (Section 2.4.7–2.4.10). Intermediately-sized penetrometers, such as the FF-CPT, the CPT-Stinger or the LIRmeter are introduced in the end of this Chapter (Section 2.4.12–2.4.17). Table 2.2 gives an overview on the instruments described in the following sections.

Table 2.2 – Dimensions, characteristics, and references for marine impact penetrometers. Tip shapes: hemispherical (h), conical (c, with apex in °), sting (s) tangent ogive (to, with caliber, cal), open barrel (ob), cylindrical (flat). Sensors: acceleration (a), acoustic (ac) pressure (u), cone resistance (q), sleeve friction (f), optical (o), and inclination (i). Water depth: wd. Deployment: free-fall (ff), tethered (t), umbilical (u), expendable (x), and propelled (p). Typical embedment: partial (p) or full (f).

penetrometer	m	l	d	v_i	tip	sen- sors	wd	de- ploy- ment	em- bed- ment	citation
	kg	m	m	m/s			m			
XDP	173	2,45	0.09	< 30	h	ac	< 6000	ff, x	f	(Beard, 1976)
XDP MK-II	141	1,95	0.09	< 30	h	ac	< 6000	ff, x	f	(Beard, 1984)
XDP (Sonatech)	30	0,97	0.09	10-25	h, s	ac		ff, x	f	(Douglas and Wapner, 1996)

Table 2.2 (continued)

penetrometer	m kg	l m	d m	v_i m/s	tip	sen- sors	wd m	de- ploy- ment	em- bed- ment	citation
XBP	0,74	0.215	0.052	< 7		a	< 200	ff, u, x	f	(Stoll and Akal, 1999)
FFCPT	52	1.8	0.088	< 8	c (60°)	a, u, o	< 660	ff, t	f	(Melton et al., 2000)
FF-CPT (SW)	40-170	1-6	0.044	< 10	c (60°)	a, q, f, u, i	< 200	ff, t	p	(Stegmann et al., 2006b)
FF-CPT (DW)	500-550	4-7	0.044	< 10	c (60°)	a, q, f, u, i	< 4000	ff, t	p	(Stegmann, 2007)
Migliore penetrometer	78	< 3	0.025	< 4,5	c (45°) d:0.058 m	a	< 400	ff, t	p	(Migliore and Lee, 1971)
MSP	45	1.5	0.076	< 28	6.0 cal, to	a	< 1500	ff, u, x	f	(Colp et al., 1975)
Newcastle penetrometer	7	1	0.036		c (60°)	a, q	lab	ff	f	(Denness et al., 1981)
ISP MK-1 and MK-2	320	2.4	0.2	< 100	6.0 cal, to	a	< 6000	ff, p, x	f	(James et al., 1981)
ISP MK-3	468	3.4	0.203	< 55	6.0 cal, to	ac	< 1700	ff, x	f	(Hickerson et al., 1988)
ISP MK-4	2360-2665		0.032	< 55	6.0 cal, to	ac	< 6000	ff, x	f	(Freeman and Burdett, 1986)
Nantes penetrometer	2.3		0.05	0	c (60-90°)	a	lab	ff	f	(Levacher, 1985)
Ballistic Penetrator	2000	3.6	0.36	< 55	c (60°)	a, c, f, u, i	< 6000	ff, u, x	f	(Hembise et al., 1990)
Lake penetrometer	3	0.3	0.06	0	h	a	< 15	ff, t, u	f	(Spooner et al., 2004)
GraviProbe	7-10	0.9	0.05	6-7	c	a, u	0	ff, t	f	(ITelegance BVBA, 2010a)
STING / PROBOS	10	> 1 (ex- tend- able)	0.19	6	c (90°), h, flat	a	< 300	ff, u	p	(Lott and Poeckert, 1996; Stoll, 2004)
DPA	75000	13	0.8-1.2	20-25	c		300-3000	ff, x	f	(Lieng et al., 1999)
Torpedo Anchors	24500-97000	12-15	0.76-1.07	12-15	c		1000	ff, x	f	(de Medeiros, 2001)
OMNI-Max anchor	38000	9.7	width: 3.0	23	special		1646	ff, x	f	(Shelton, 2007)
Preslan-Scott-corer	81-499	3-9	0.053-0.076	0,3-9	ob	a	1000-2000	ff, t	p	(Preslan, 1969; Scott, 1970)
Burns-corer	25.4-29.8	0.35-2.45	0.038-0.081	6	ob	t	lab	ff	p	(Burns, 1966)
Heffler-corer	1000-2000	3-30	ID: 0.1	var	ob	a	< 6000	ff	p	(Heffler, 1991)
Seyb-corer	1255	var	var	var	ob	a, i, o	< 4600		p	(Seyb et al., 1977)
Villinger-corer	2000	12	ID 0.09-0.125	6-8	ob	a	< 6000	ff, t	p	(Villinger et al., 1999)
HARPOON	> 110	> 1.2	0.168	var	c	a, u	3400	ff, t	p	(Mosher et al., 2007)
NIMROD	11-15	0.81	0.11	< 12	c, flat, h	a, u	200	ff, t	p, f	(Stark et al., 2009a)
EU waste carriers	1800	3,25	0.325	46-51	c (60°)	ac	< 5400	ff, x	f	(Freeman et al., 1984)
MIP	453	4.75-15	0.076	< 8.5	c (60°)	a, c, f	300	ff, t	p	(Dayal and Allen, 1973)

Table 2.2 (continued)

penetrometer	m	l	d	v_i	tip	sen- sors	wd	de- ploy- ment	em- bed- ment	citation
	kg	m	m	m/s			m			
CPT-Stinger	3200- 3400	23.3- 34.6	0.16	0.02-2	ASTM D5778	a, c, f, u	< 2100	ff, t	p	(Young et al., 2011)
LIRmeter	typ: 500- 2000	typ: 1-6	typ: 0.036- 0.063	typ: < 6	c (60°)	a	< 5000	ff, t	p	(Fabian et al., 2008)

2.4.1 The Marine Sediment Penetrometer

The Marine Sediment Penetrometer (MSP-1, MSP-2; Colp et al., 1975; Trabant, 1984) is a projectile-shaped impactor (see Fig. 2.11), instrumented with accelerometers. The tip is designed following ballistic principles (6.0 caliber tangent ogive nose; Colp et al., 1975) and has an apex of $\sim 20^\circ$. Acceleration data is transmitted via a thin wire to a recording unit. The instrument weighs about 45 kg, has a diameter of 7.62 cm, and a length of 1.5 m. It is rated to a water depth of 1800 m and reaches terminal velocities around 28 m/s.

2.4.2 The Expendable Doppler Penetrometer

The Expendable Doppler Penetrometer (XDP), see Fig. 2.12 is a hydrodynamically shaped lead-filled device, intended to determine sediment strength for the assessment of anchor installations (Beard, 1976). The device has a mass of 173 kg, a diameter of 90 mm (3.5 in) and a length of 2.45 m (cf. Beard (1977) for further details). The system free falls through the water column and reaches impact velocities of up to 30 m/s. During the fall, it emits sound of a certain frequency, which is recorded using a deck unit. Through the frequency shift, it is possible to calculate the velocity of the penetrator (Beard, 1976). The instrument has been evaluated in a series of tests (Beard, 1977, 1981). Further tests (Beard, 1984, 1985; Cyr, 1990) involved a slightly modified embodiment with a length reduced by 0.5 m and less weight. In total, around 50 tests in water depths of up to 5430 m are published using these versions of the XDP by the latter authors. The penetration depths reach up to 12 m (Beard, 1981).

Later studies (Douglas and Wapner, 1996; Orenberg et al., 1996; Thompson et al., 2002) utilize an instrument, also called XDP, which is manufactured by Sonatech. The penetrator also has a diameter of 90 mm (3.5 in), but is shorter (length: 97 cm) and lighter (30 kg; Thompson et al., 2002). The Sonatech XDP can be equipped with a hemispherical tip or a 0.6 m long

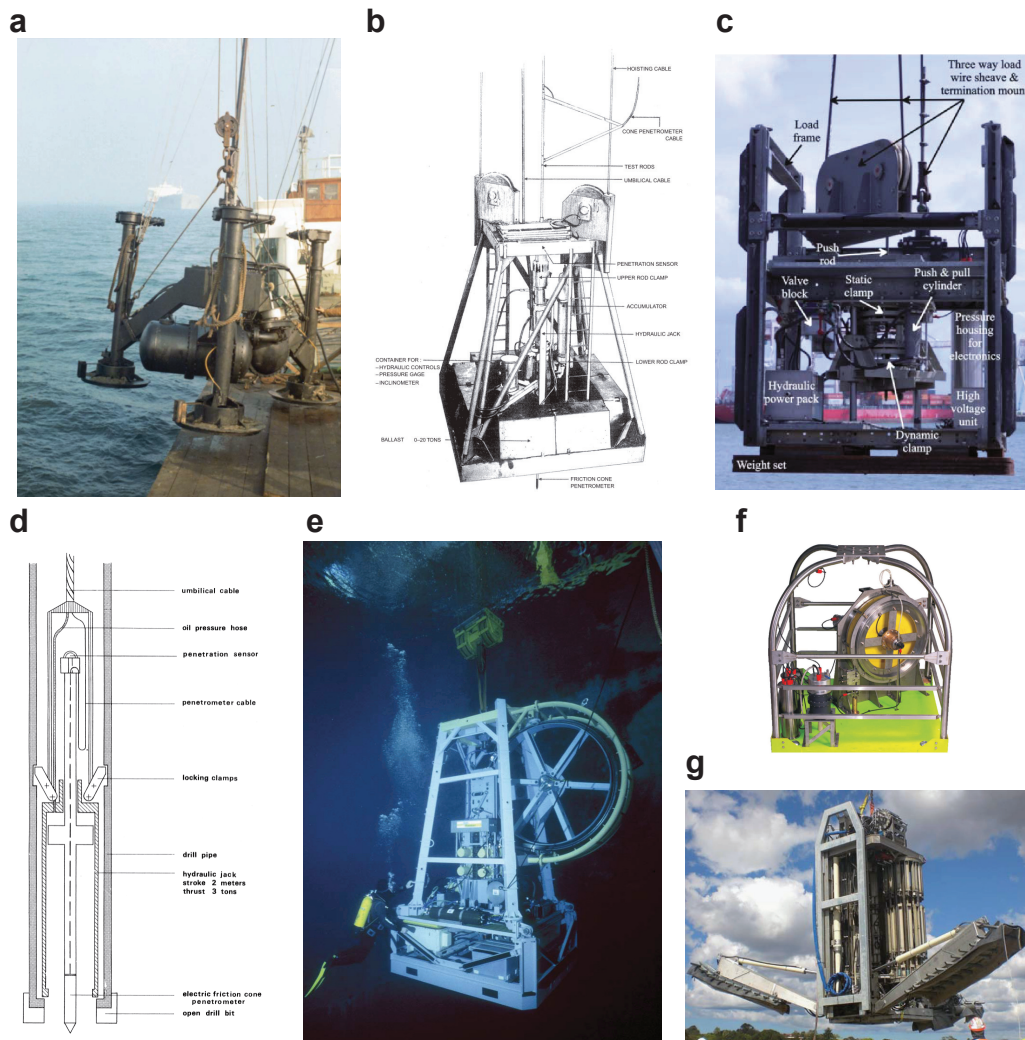


Figure 2.10 – **a** The Seabull seabed system (Fugro, Lunne, 2012); **b** The Seacalf seabed system (Fugro, Zuidberg, 1975b); **c** The GOST seabed system (MARUM, Jorat et al., 2014b); **d** Sketch of the WISON down-hole system (Fugro, Zuidberg, 1975b); **e** The Penfeld coiled tubing penetrometer (Ifremer, Meunier et al., 2004); **f** The Neptune coiled tubing system (Datem, Lunne, 2010); **g** The PROD seabed rig (BenthicGeotech, Randolph et al., 2011).

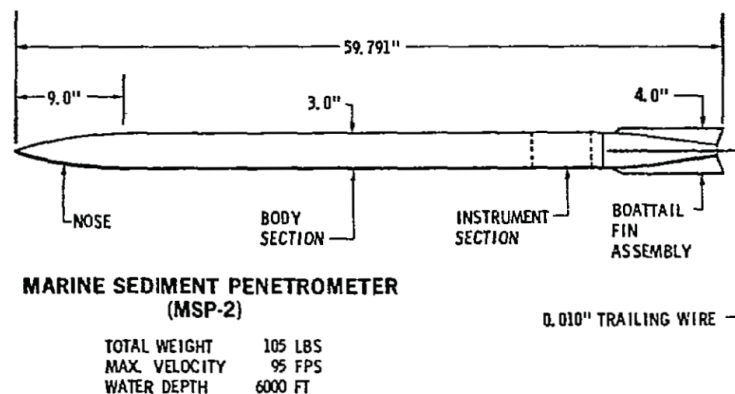


Figure 2.11 – The Marine Sediment Penetrometer (MSP), here as MSP-2 design. Modified after (Colp et al., 1975).

stinger (diameter: 0.0254 m) for stiff sediments (Douglas and Wapner, 1996). With this type of XDP, penetration depths between 0.16 m (Orenberg et al., 1996, using the stinger in dense sands) and 1 m (Douglas and Wapner, 1996, soft clay) have been reported.

The kinematic (velocity) data is processed following the force-based approach by True (1976) (see also Section 2.2.2 for details) with adaptations for the XBP (Beard, 1985).

2.4.3 Instrumented Seabed Penetrometer

The Instrumented Seabed Penetrator (ISP) has been developed at Sandia National Laboratories (James et al., 1981) and successfully tested during field trials (James and Calloway, 1983; Hauser and Hickerson, 1988). The aim of the project was to develop a penetrometer for radioactive waste disposal at sea, which could operate in water depths ranging from 30 to 6000 m and reach up to 50 m penetration into the sediment (James et al., 1981). The authors found, that an impact velocity of 100 m/s would be needed to reach such an embedment depth for typical ocean sediments. Therefore, an approach of an impelled impactor was chosen. The system should incorporate acceleration sensors to measure the embedment characteristics, and e.g. vane shear devices or acoustical sources or provisions to determine geotechnical or acoustical properties of the sediment (James et al., 1981).

Field trials were conducted between 1981 and 1983 at water depths of 22 m with two designs of the Instrumented Seabed Penetrator: ISP-1 and ISP-2 (see Fig. 2.13a,b). The devices had a mass of 320 kg, a diameter of

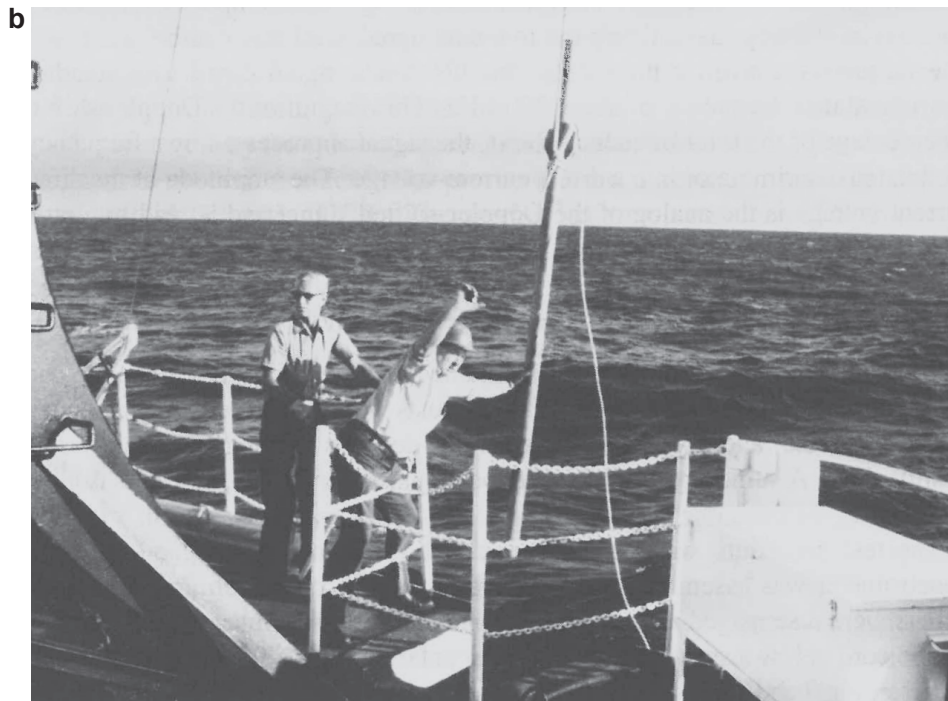
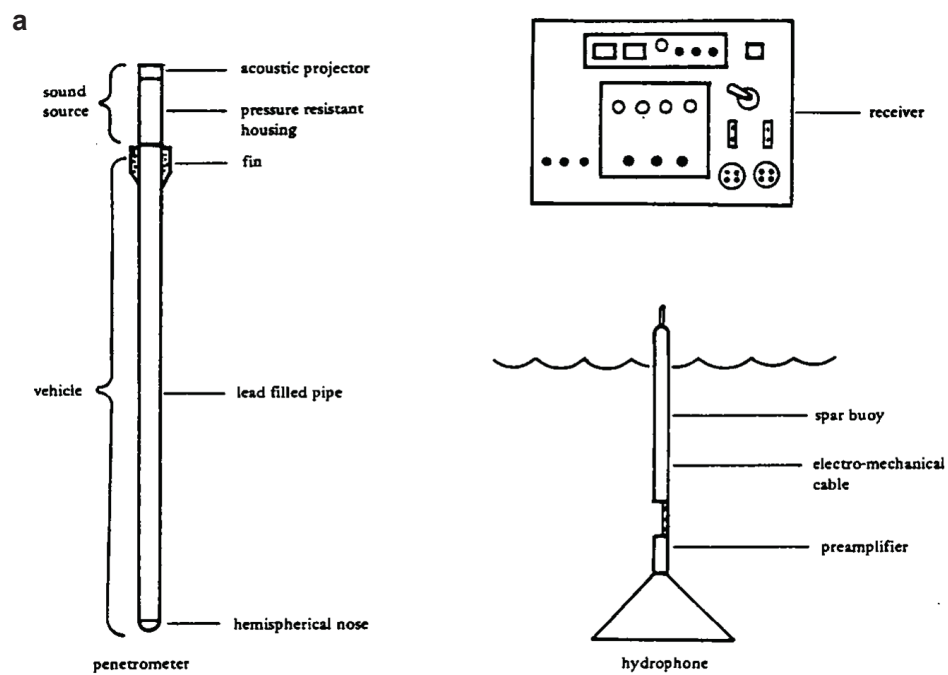


Figure 2.12 – **a** Schematic of the XDP instrument and data acquisition (Beard, 1985); **b** Deployment of the penetrometer (Beard, 1985).

0.2 m, and a length of 2.4 m. The devices were launched by a gun (mass 1950 kg, barrel length: 2.4 m, burn-chamber volume: 0.026 m³, propellant charges up to 4.8 kg James and Calloway, 1983). The nose of the ISP is ballistically shaped (see Sec. 2.4.1) and has an average opening angle between 25 and 35 °.

The ISP-1 system reached an embedment depth of 28 m using 1.6 kg propellant charge, whereas the ISP-2 system reached 36 m depth using 3.2 kg propellant charge (James and Calloway, 1983). The difference between both systems lies within the data acquisition for the kinematic data.

The penetration velocity and embedment depth are calculated within ISP-1. Then, the final embedment depth is transmitted via modulated signal pulses to a receiving unit (James and Calloway, 1983). This transmission system can also be used to determine acoustical properties of the sediment (Edrington and Calloway, 1984).

The ISP-2 system is likewise deployed using the gun. However, acceleration is continuously recorded within the instrument. The instrumentation package is recovered using a wire, to which it is attached to. The continuous dataset of acceleration can be used to generate shear strength profiles (James and Calloway, 1983) according to the approach of Beard (1981), see Section 2.2.2.

Hauser and Hickerson (1988) reports further developments regarding the ISP. Two designs with significantly higher mass and better data transmission capabilities were developed and tested between 1983 and 1988 in the context of nuclear waste disposal. Two models of the ISP-3 design (mass: 468 kg, length 3.4 m, diameter: 0.203 m; Hickerson, 1988) were launched in water depths of 1700 m in 1984. Four deployments of the ISP-4 (mass: 2360 - 2665 kg, diameter: 0.324 m) in water depths of 5840 m are reported by Freeman and Burdett (1986) and Hickerson (1988). These penetrators (see Fig. 2.13c,d) were deployed in free-fall mode and reached impact velocities around 55 m/s, and embedment depths around 30 m (Freeman and Burdett, 1986).

2.4.4 The Ballistic Penetrator

Hembise et al. (1990) presents the design of the Ballistic Penetrator (BP, Fig. 2.14) and results from field trials. The BP is intended for seabed investigation. The whole device has an alternating diameter (max. diameter: 0.36 m), a length of 3.6 m, and a mass of 2000 kg and is rated up to 6000 m water depth. The system is equipped with an inertial platform, a tail-force sensor, a tip-force sensor, a side-friction sensor, inclinometers, and pressure gauges. The penetrometer internally stores the data (A/D resolution: 12 bit)

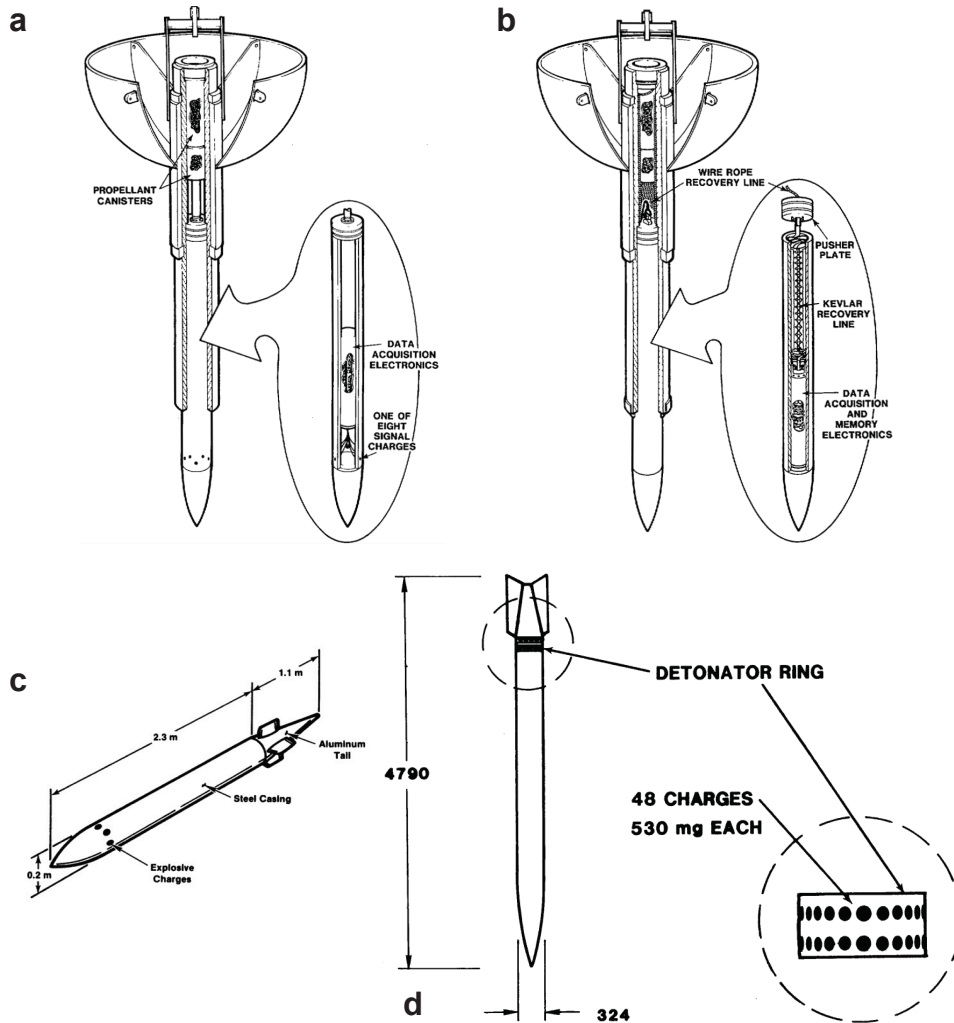


Figure 2.13 – **a** ISP-1 with data acquisition, mounted in the gun launcher apparatus. Note the detonator ring in the bottom part of the shaft. Image modified after James et al. (1981); **b** ISP-2 with data acquisition and storage, mounted in the gun launcher apparatus. Note the kevlar tether to retrieve the data storage. Image modified after James et al. (1981); **c** The ISP-3 penetrometer with detonator telemetry. Image modified after Hauser and Hickerson (1988); **d** The ISP-4 penetrometer with detonator telemetry. Image modified after Hauser and Hickerson (1988).

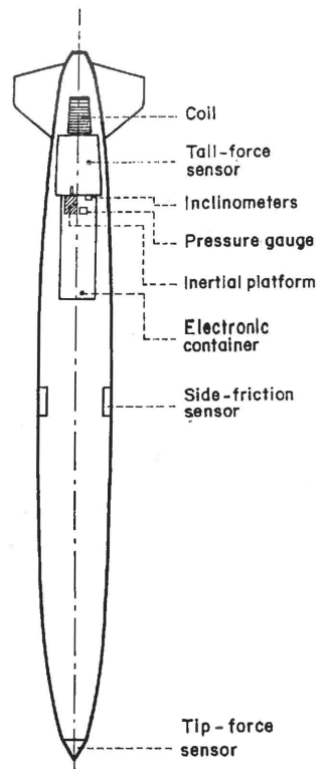


Figure 2.14 – The Ballistic Penetrator with annotations of relevant parts. Modified after (Hembise et al., 1990).

and transfers data to an external acquisition by a thin umbilical wire.

During field trials at water depths of 5300 m, five deployments yielded results which were suitable for interpretation. The instrument reached terminal velocities of ~ 55 m/s and penetration depths between 30 and 40 m (Hembise et al., 1990).

Based on an inverse model (Hembise et al., 1990), shear strength can be calculated as a function of penetration velocity with depth (or acceleration with depth). The model is valid for cohesive soil targets only, i.e. interparticle friction yields errors in analysis.

2.4.5 Radioactive waste disposal at sea

The disposal of high-level radioactive wastes (being e.g. nuclear waste created by the reprocessing of spent nuclear fuel) into the deep ocean has been investigated starting in the 1970ies (Talbert, 1980) and continued through

the 1980ies. The feasibility has been evaluated by two groups being (i) the United States in cooperation with Sandia National Laboratories and (ii) the European Union with its Joint Research Centre (Richards and Zuidberg, 1985).

The disposal of radioactive waste into the seabed offers the advantage, that potentially emergent radiation is absorbed within the surrounding sediments (typically clay) and within the water column. Typical deep-sea sediments moreover behave plastically and can therefore seal potential fissures (Talbert, 1980; Winters, 1987). However, eventual retrieval and monitoring of the disposal is complicated due to the environmental conditions. The International Maritime Organization (IMO) enacted a ban on the disposal of radioactive wastes in 1993 (IMO, 1993; IAEA, 1999). Investigations in this field stopped at that point.

Different methods were proposed to emplace radioactive waste into the seabed, where placement in pre-drilled holes and direct emplacement with penetrators were the most advanced investigations (Talbert, 1980; Winters, 1987). The EU and US programmes nurtured a wealth of investigations within the context of sediment penetration studies and the behavior of projectile-like penetrators. The penetrators should carry the waste containers during the fall through the water column, protect them during the penetration into the sediment, and shield the environment from the radiation of their payload (Hickerson et al., 1988). Different concepts were developed in the US and in the EU (Hickerson et al., 1988), yielding standard penetrator designs: The EU penetrator has a length of 8.5 m, a diameter of 0.65 m, and a mass of 18000 kg. The US penetrator have a diameter of 0.56 m, a length of 6.75 (7.99) m, and a mass of 8200 (11000) kg. Values in parentheses are for the fuel carrier, other values for the reprocessed waste carrier. Predicted burial depth (tail) for the EU penetrator is 66 m, and for the US models 46 (57) m at the Nares Abyssal Plain (NAP) site (see below, Hickerson et al., 1988). See also Fig. 2.15a–c for dimensions and penetrometer shapes.

The penetrator performance has been evaluated within field trials (i) in two areas in the Atlantic Great Meteor East (GME) area, which lies in the southwestern area of the Madeira Abyssal Plain, (ii) in an area in the Pacific (PAC area: lying 2000 km east of Japan, and 200 km east of the Shatsky Rise near DSDP hole 576; Hickerson et al., 1988), and (iii) in the NAP, which lies off the Greater Antilles, respectively (Talbert, 1980). The performance has been assessed through drops of prototype penetrators, yielding impact velocities between 46 and 51 m/s (EU, Freeman et al., 1984) and penetration depths between 27 and 31 m (EU, Freeman et al., 1984) in clay at water depths of 5400 m. The prototypes had a mass of 1800 kg, a diameter of

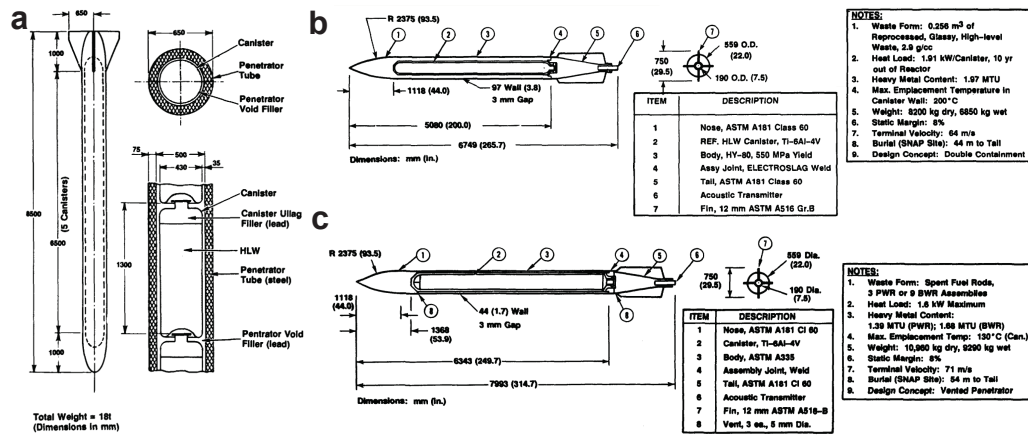


Figure 2.15 – **a** The EU reference penetrator. Schematic with dimensions and annotations of relevant parts; **b** the US reference penetrator design for the reprocessed waste carrier; **c** the US reference penetrator design for the spent fuel carrier. All schematics modified after Hickerson et al. (1988).

0.325 m and a length of 3.25 m. Further tests were done in the GME area involving penetrators with a mass of 3200 kg. These penetrators reached depths of 58 m (Freeman and Schüttenhelm, 1990). The prototype penetrators were equipped with different types of sensors and systems to obtain their velocity. The data acquisition systems for the US penetrators originated in the developments of the MSP/ISP (see Sec. 2.4.1 and 2.4.3), as well as in the technology developed for the XDP (see Section 2.4.2). The data acquisition for the EU penetrator is comparable to the XDP approach, but uses a lower frequency of the signal source (Freeman et al., 1984; Richards and Zuidberg, 1985).

Several studies were conducted concerning the embedment characteristics of the penetrators. The approach followed within US studies (as summarized in Hickerson et al., 1988) was a force-based approach after Beard (1976) and True (1976), where penetration depth is estimated from the penetrator design, soil characteristics, and the impact velocity. The EU studies also used the force based approach, as well as an upper-bound approach after Hembise et al. (1987), which treats the soil as newtonian fluid. The approaches reproduced field data in an acceptable way (Freeman et al., 1984). Knowing the penetrator characteristics and design, soil parameters can be back-calculated from these data (Hickerson et al., 1988; Freeman and Schüttenhelm, 1990).

2.4.6 Penetrating anchors

Penetrating anchors are used to tether floating platforms to the sea floor using mooring lines. These anchors, often termed as “Torpedo Anchors” or “Deep Penetrating Anchors (DPA)” (Lieng et al., 1999; de Medeiros, 2001), feature a projectile-shaped tip and penetrate marine sediments vertically due to the momentum they gathered during free fall. The anchors are cylindrically shaped and have dimensions of ~ 12 m to 15 m in length and ~ 0.75 m to 1.2 m in diameter (Lieng et al., 1999; de Medeiros, 2001) with a mass of 51000 to 102000 kg (Randolph et al., 2011). The anchors are equipped with fins to ensure hydrodynamic stability and to increase the holding capacity due to an increased contact area between soil and anchor. A mooring line is attached to a pad-eye on the upper end of the anchor (de Medeiros, 2002; Lieng et al., 1999), or to a special fixture on the body (Shelton, 2007). The anchors are released 50 to 100 m above the sea floor and penetrate up to 45 m (\sim three times their length), depending on sedimentary conditions (Randolph et al., 2011). During penetration, soil gets remolded and pore pressures build up, affecting the short-term holding capacity of the anchor. The regain of undisturbed anchor capacity is a function of soil properties and can take up to months (Richardson et al., 2009).

The concept of free-falling anchors was introduced by Atturio and Valent (1977) for mooring of floating offshore platforms. The water depth anticipated for deployment is 6000 m. The authors, discussing several lowering techniques, found the free-fall lowering as most practical. Colliat (2002) summarizes the use of anchoring solutions for offshore production projects. The author presents free falling anchors as solution for mooring of Floating Production Units, Mobile Drilling Units, and Floating Production Storage and Off-loading units. However, it has been highlighted, that the assessment of pullout capacity of such anchors is coupled with complicated offshore tests. However, it is discussed to assess the anchor capacity by determination of a soil strength profile, which can be acquired during anchor installation. Ehlers et al. (2004) summarized the developments in the field of penetrating anchors to that date. The authors introduce the deployment principle and highlight the advantages of penetrating anchors. The main advantages are:

- simple fabrication and installation
- cost advantages during production and installation
- no limitation in water depth regarding operation
- greater ductility of the soil/structure interface due to deeper placement depth (lower susceptibility to a sudden failure)

However, the authors state, that among other anchoring concepts, penetrating anchors were to that point not yet at the desired level of maturity. The most critical points to be addressed were after Ehlers et al. (2004) the analytical study of anchor penetration, the development of a framework for anchor design regarding dimensions and fin layout, small-scale and field tests regarding holding capacity and penetration characteristics.

Randolph et al. (2011) reviews anchor concepts and analytical studies comprising model tests in geotechnical centrifuges. The authors highlight the geotechnical problems connected with anchor penetration and anchor holding capacity. The former is governed by the anchor mass, shape and impact velocity. Since high velocities are present, the authors indicate, that a rate-correction is needed for the shear resistance term in formulae predicting the embedment depth. For penetrating anchors, the increase in shear resistance with strain rate is found to be higher than typically encountered in laboratory experiments (Randolph et al., 2011). The assessment of anchor capacity is presented as a further field of research. The anchor capacity of penetrating anchors is dependent on the inclination of the mooring line, where at a load inclination of 30° , anchor capacity is governed by the vertical capacity component (Randolph et al., 2011).

Deep Penetrating Anchor (DPA)

Lieng et al. (1999) introduces the concept of a Deep Penetrating Anchor (DPA). These DPAs (see Fig. 2.16b) permit a cost- and time-effective anchoring of floating platforms in deep water depths (300-3000 m, Lieng et al., 1999, 2000). The penetrators are dropped from 20 to 24 m above the mud line (Lieng et al., 1999, 2000) and penetrate up to 30 m into the sediment. During the falling phase, they reach terminal velocities of 20 to 25 m/s (Lieng et al., 1999, 2000). See Fig. 2.16a for the deployment procedure. The anchors are designed to ensure a deep embedment and a high holding capacity. Thus, they have a mass of 75000 kg, a diameter of 0.8 to 1.2 m (Lieng et al., 1999, 2000) and a length of 13 m (Lieng et al., 2000). The tips of the anchors are conically shaped, and the shaft is equipped with flukes to ensure a vertical penetration and to enlarge the holding capacity (Lieng et al., 1999). Scaled model (1:25) drop tests were carried out for design optimisation purposes (Lieng et al., 2000) and were followed by offshore model tests with scaled (1:3) penetrators at the Troll field (Norway, Sturm and Andresen, 2010). The 1:3 DPAs had a length of 4.4 m length, a shank diameter of 0.4 m, and were equipped with four fins (Sturm and Andresen, 2010).

Full-sized anchors were deployed at Gjøja field in a water depth of 360 m, where they reached penetration depths of 24 and 31 m (Lieng et al., 2010).

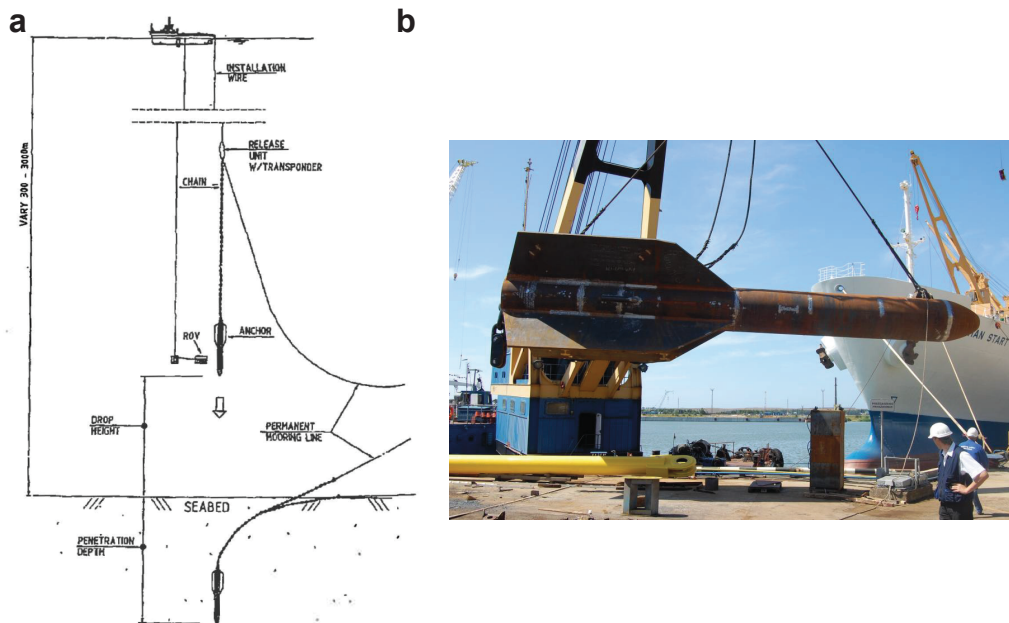


Figure 2.16 – **a** Deployment procedure of the DPA. Schematic modified after Lieng et al. (2000); **b** Full-scale DPA. Image retrieved from <http://www.deepseaanchors.com>

The impact velocities ranged from 25 to 27 m/s at fall heights of 50 and 75 m (Lieng et al., 2010). These penetrators were equipped with retrievable accelerometers and data acquisition to verify the penetration depth and the verticality of the installed anchors (Lieng et al., 2010).

Sturm and Andresen (2010) analyzed the penetration behavior of the 1:3 model penetrators numerically and determined stress states straight after anchor installation and after consolidation. The authors also found, that the remolded zone in the sediment extends to $\sim 2/3$ of the shaft radius radially from the penetrometer.

Torpedo Anchor

The concept of Torpedo Anchors is presented by de Medeiros (2001). Torpedo anchors are huge projectile-shaped devices, typically equipped with fins, which serve as anchors for floating platforms (de Medeiros, 2001). Torpedo anchors (see Fig. 2.17) exist in different designs having a length of 12 m, a diameter of 0.76 m, and a mass of 24500 kg (type I: with fins, type Ia: without fins) or a length of 15 m, a diameter of 1.07 m, and a mass of 97000 kg

(type II: with fins) (de Medeiros, 2001, 2002; de Araujo et al., 2004; Brandão et al., 2006). The anchors are deployed at heights of 30 to 150 m above the sea floor and reach impact velocities between 10 and 22 m/s (de Medeiros, 2001, 2002). In normally consolidated clays, the tip penetration ranges between 22 and 37 m.

Full scale field tests of the type I and type II design (type II with a mass of 63200 kg) are presented by de Medeiros (2001) for different sedimentary settings ranging from normally consolidated clay, overconsolidated clay, fine sand to calcareous sand, while water depth ranged between 200 and 1000 m. During the tests, impact characteristics were monitored (de Medeiros, 2001). For the type Ia anchors, a penetration of 29 m was reached in normally consolidated clay, while the penetration depth amounted to 13.5 m in overconsolidated clays. In uncemented calcareous sand, 15 m penetration depth was reached and in a two-layer system (13 m fine sand, followed by normally consolidated clay), 22 m were reached (de Medeiros, 2001, 2002).

Raie and Tassoulas (2009) compared results from numerical Computational Fluid Dynamics (CFD) modeling with results from field trials reported by de Medeiros (2002) and found that the numerically predicted and observed penetration depth matched within the uncertainty of the shear strength gradient within the sediment.

Numerical studies were also conducted regarding the assessment of the holding capacity of torpedo anchors. The undrained load capacity of a torpedo anchor, which has been embedded in cohesive soil using 3D finite element modeling is assessed by de Aguiar et al. (2009). Later, the effect of a tilted anchoring and inclined loads on the holding capacity of a torpedo anchor were assessed by de Aguiar et al. (2011), while de Sousa et al. (2011) assessed the long term undrained load capacity of a torpedo anchor in cohesive soil.

Torpedo Pile

Audibert et al. (2006) presents an US project at The University of Texas (Austin) for performance-evaluation of finless torpedo piles. The project was planned to comprise laboratory, as well as (scaled) field tests. Audibert et al. (2006) present data from initial laboratory experiments with model anchors penetrating clay targets. Gilbert et al. (2008) presents further findings from these experiments (62 tests) in a report. Penetration behavior and pullout capacity were analyzed. The achieved penetration depth matched well with predicted values following the approach of True (1976). However, publication activity within the project stopped at this point.



Figure 2.17 – Torpedo Anchors. Images showing conical tip, flukes and pad-eye, used for deployment and mooring. Modified after de Aguiar et al. (2009).

OMNI-Max anchor

The OMNI-Max anchor is a small-size, recoverable gravity-installed anchor for mooring of mobile offshore drilling units in the Gulf of Mexico developed from 2004 to 2007. The concept was introduced by Shelton (2007). The OMNI-Max anchor (see Figs. 2.18a,b) is not pile-shaped and has a mass of 38000 kg, a length of 9.7 m and a width of 3.0 m (fins fully extended; Shelton, 2007). The anchor needs to penetrate at least to its full length. A special tethering system with two separate ropes for mooring and recovery allows the anchor to dig itself into the sediment, when loads are applied on the mooring line (see Shelton (2007); Zimmerman et al. (2009) for a detailed description). The load needed to recover the anchor is $\sim 50\%$ of the maximum mooring tensions (Shelton, 2007).

Shelton (2007) conducted laboratory experiments and field tests. The penetrators used during laboratory experiments were 245 mm, 305 mm, 813 mm and 1.5 m in size. Prior to testing, performance characteristics were estimated based on the design. For a fall height of 45 m above the sediment level, the authors estimated a terminal velocity of 23 m/s, and a penetration depth of up to 23 m (tip penetration) assuming typical Gulf of Mexico sediment properties ($s_u=2.4$ kPa at the surface, gradient: $s_u/m = 0.34$ kPa Shelton, 2007).

The laboratory model tests were done on a Laponite (synthetic, relatively clear layered silicate) soil target. The tests were primarily done to evaluate the movement of the anchor penetrator within the sediment once loads are applied on the mooring line. See Shelton (2007) for a description of the testing set-up.

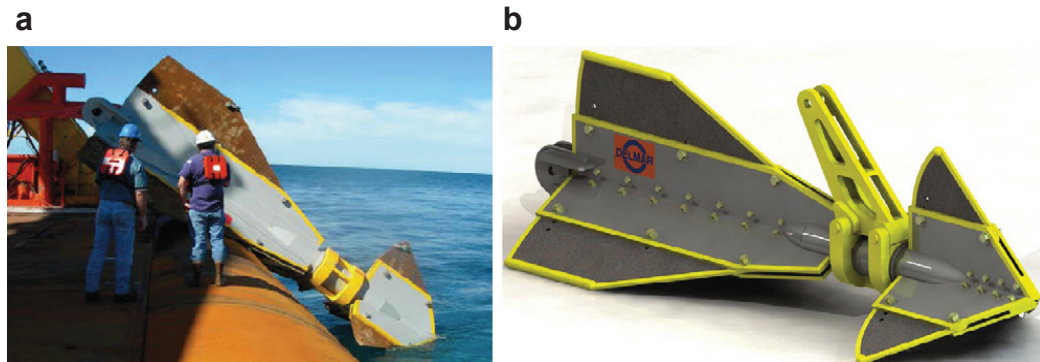


Figure 2.18 – **a** OMNI-max anchor during deployment; **b** Rendering of an OMNI-max anchor. Note the freely-rotating mooring arm and the pad-eye for recovery at the tail. Images modified after Randolph et al. (2011).

Field scale tests were conducted in the Gulf of Mexico at water depths of 1646 m at a drop height of ~ 76 m. The anchor achieved its full terminal velocity. The tip penetration reached 12 m depth and the inclination of the anchor was less than 10° in the soil (Shelton, 2007).

Zimmerman et al. (2009) reports 54 installations of the OMNI-Max anchors in slightly overconsolidated kaolin. The anchors reached terminal velocities of 19 m/s, when dropped 30 m above the seabed. In total, 96 % of the anchor deployments reached the critical embedment depth.

Zimmerman (2010) summarizes 120 OMNI-Max anchor installations as of 2010. All installed anchors performed as expected. One anchor reached twice its original installation depth after deployment (Zimmerman, 2010).

The OMNI-Max anchor performance has also been assessed for calcareous silt (Gaudin et al., 2013) using model tests in centrifuges (see Section 2.4.6 for information on centrifuge tests with penetrators). The authors conducted a total of 13 tests, whereby 7 were done with a kaolin target and 6 were done in calcareous silt. A total embedment is required for this anchor type to ascertain the designed holding capacity. The authors found, that an impact velocity of 25 m/s or more would be needed to achieve the needed embedment depths in calcareous silt.

Centrifuge experiments

Starting from 2004, laboratory centrifuge tests were conducted at the University of Western Australia to evaluate the penetration behavior of model penetrometers under fully scaled conditions (see Fig. 2.19a,b for model an-

chors and a centrifuge setup).

O'Loughlin et al. (2004) presents 1:200 model centrifuge experiments in kaolin clay and compares the results (especially penetration characteristics) to the approaches of True (1976); Freeman and Burdett (1986). Moreover, the prediction of penetration characteristics on the basis of True (1976) is modified by application of alternate formulations of the strain rate dependency (log-relationship: e.g. Dayal and Allen, 1975) and estimations of inertial drag during penetration. O'Loughlin et al. (2004) presents results from three model anchors with different fluke designs (4 flukes with 90 ° alignment, 3 flukes with 120 ° alignment, and a pile-like design with no flukes). The models with flukes had a diameter of 6 mm and a length of 75 mm and a mass of 0.0125 kg while the finless model had a mass of 0.01675 kg (O'Loughlin et al., 2004). See Fig. 2.19 for images of the model penetrators. The impact velocities ranged from 0 to 34 m/s and achieved penetration depths ranged between 110 and 220 mm (i. e. 22-44 m in full scale). Due to the accelerated environment in within the centrifuge, prototypes were scaled down by the amount of relative centrifugal force (RCF, e.g.: 200), loads were scaled down by the square of RCF and masses by RCF^3 . See Fig. 2.19b for an image of the beam centrifuge.

O'Loughlin et al. (2009) further discusses the strain-rate dependency of soil resistance by application of the logarithmic and power-law correction (see Section 2.1.3) to experimentally acquired data. The results are discussed within the context of measured and predicted penetration depth, as well as measured and predicted penetration velocity as function of penetration depth.

Richardson et al. (2009) presents results of anchor installation and assessment of anchor capacity using laboratory centrifuge tests (scale 1:200). The utilized anchors were dropped from 200 mm height and directly above the soil target, which consisted of kaolin clay. The anchors were designed with four and zero flukes and had different mass configurations: 0.0082 kg and 0.0062 kg for the zero-fluke (~ 6 mm diameter, ~ 65 mm length) and 0.0096 kg and 0.0127 kg for the four-fluke model (~ 6 mm diameter, ~ 75 mm length). The penetration depth ranged from 101 mm to 110 mm, while impact velocities between 0 m/s and 16.2 m/s were achieved. Compared to the results from O'Loughlin et al. (2004), the lower embedment depths are related to the lower mass of the penetrators (Richardson et al., 2009).

O'Loughlin et al. (2013) employed the anchor embedment model, based on the total energy approach (cf. Section 2.1.1 and Eq. 2.14) on the 155 model tests, as well as on data from field tests with waste carriers. After correction for rate effects using the log or power law relationship and calibration of the bearing capacity factor N_c and the adhesion factor α , the authors found, that

the anchor embedment model predicts the measured velocity profiles with penetration depth to a high degree. The achieved penetration depth could be reproduced within a variation of 4 %. However, strain rate coefficients exhibited a velocity dependency, additionally to the discrepancy between model penetrometer strain rates compared to the strain rates in field (factor 200, owing to the centrifuge environment).

Hossain et al. (2013) presents a study regarding anchor embedment and performance in clay and calcareous silt using centrifuge experiments and numerical modeling. Hossain et al. (2014) presents detailed results from laboratory centrifuge penetration experiments in clay and calcareous silt (as well as anchor capacity estimations). Hossain et al. (2015) presents results from laboratory centrifuge tests in calcareous silt in detail and discusses the difference to penetrations in clay targets. The model penetrometers used in these studies resemble the penetrometers employed by Richardson et al. (2009). The dimensions are 75 mm length, 6 mm diameter, and 0.01916 kg mass (four rectangular fins; Hossain et al., 2013, 2014); 81 mm length, 6 mm diameter, and 0.02201 kg mass (four butterfly fins; Hossain et al., 2014); 127.50 mm length, 8.03 mm diameter, and 0.052 kg mass (four rectangular fins; Hossain et al., 2015). The tests were likewise performed in a beam centrifuge under accelerations of 200 g for (Hossain et al., 2013, 2014) and 133.3 g (Hossain et al., 2015).

The penetration characteristics of the model anchors in kaolin clay were qualitatively analyzed in Hossain et al. (2013) with penetration depths ranging from 142 to 151 mm at impact velocities between 15 and 19 m/s for the 71 mm anchor model. Hossain et al. (2014) discusses results from tests in both calcareous silt regarding their embedment depth, where penetration characteristics (d_{\max} from 142 to 154 mm at v_i between 15 and 19 m/s for clay and d_{\max} from 88 to 117 mm at v_i between 15 and 22 m/s for calcareous silt) were estimated using the force-based approach of True (1976). Both publications are focussed on the anchor capacity rather than impact characteristics.

O’Loughlin et al. (2014) uses a model of the OMNI-Max anchor (see Section 2.4.6), which has been instrumented with a ± 500 g MEMS accelerometer. The accelerometers performance was evaluated using the constant acceleration of the centrifuge, as well as during anchor embedment. Therefore, the authors used a reference accelerometer and measured the travel distance during the acceleration of the anchor using photo emitter receiver pairs (PERPS, O’Loughlin et al., 2004). Twofold integration of the accelerometer data yielded a penetration depth resolution of 0.82 mm (O’Loughlin et al., 2014).

Hossain et al. (2015) presents a comprehensive study of impact char-

acteristics and anchor capacity in soil targets consisting of calcareous silt. The model penetrometers had larger dimensions due to the lower acceleration within the frame of the centrifuge (133 g Hossain et al., 2015). The model penetrometers were constructed to meet the designs of de Araujo et al. (2004); Brandão et al. (2006) (T-98 torpedo anchor, rectangular fins) and were equipped with MEMS accelerometers (O’Loughlin et al., 2014; Hossain et al., 2015), which allowed to acquire kinematic data over the whole penetration process. Previous studies (Hossain et al., 2013, 2014) used PERPS, which were located on the guidance rail. In these cases, free-fall velocity was extrapolated from PERP data, and kinematics during penetration were estimated using the force-based approach.

Hossain et al. (2015) presents 15 model penetration tests. The impact velocities ranged between 16.6 and 21.2 m/s with embedment depths ranging between 124 and 140 mm. This results in anchor embedments of 0.97 to $1.1 \cdot L_A$, with L_A being the anchor length.

Hossain et al. (2015) adopts the force-based approach (see Section 2.2.2) with some modifications (see Eq. 2.9) to describe the penetrators movement within the soil. The strain-rate correction (as applied by O’Loughlin et al., 2013) is replaced by a term after (Zhu and Randolph, 2011). The constants were back-figured to meet the experimental data. Hossain et al. (2015) also found the drag term neglectable due to the high strength of the soil. Moreover, results are discussed in context to model anchor tests in clay (O’Loughlin et al., 2013) using the log and power law strain rate correction with back-figured values for the respective rate parameters.

After a modification of the total energy approach (O’Loughlin et al., 2013), it yielded reasonable results for calcareous silts. See Section 2.2.2 for details.

During tests in calcareous silt (Hossain et al., 2014, 2015), insertion holes stayed at least partly open during and after penetration (see Fig. 2.19c), while O’Loughlin et al. (2004, 2013); Hossain et al. (2014), as well as Shelton (2007) observed surficially closed holes in clayey targets. However, it has not been possible to observe, whether the insertion holes were open or closed, or if backflow of soil occurred during the penetration of the model penetrators. Hole closure has an effect on the calculation of anchor movement using the force-based approach, since reverse end bearing on the upper shaft and the fins are dependent on the soil density. Studies (O’Loughlin et al., 2013; Hossain et al., 2015) assumed, that, during penetration, the hole stays open right behind the penetrator based on previous work by Aubeny and Shi (2006) and Poorooshasb and James (1989).

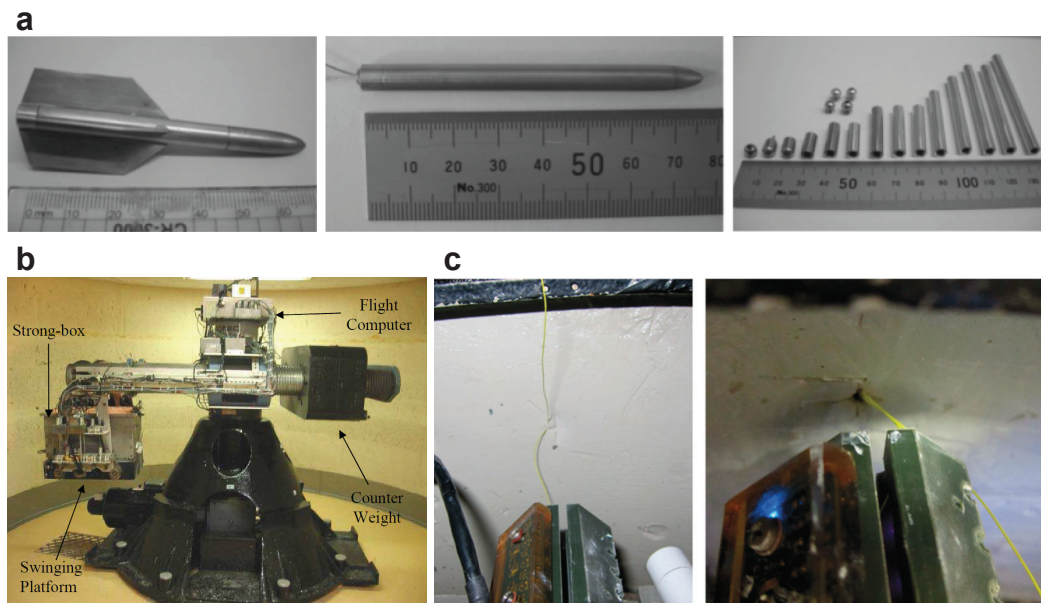


Figure 2.19 – **a** Different shapes and configuration possibilities of the model penetrators. Image after O’Loughlin et al. (2013); **b** Beam centrifuge at the University of Western Australia. Image from Richardson (2008); **c** Hole closure for clayey targets (left) and targets consisting of calcareous silt (right) with the guidance rail in the lower parts of the images. Images from Hossain et al. (2014).

2.4.7 The Expendable Bottom Penetrometer

The Expendable Bottom Penetrometer (XBP; Ingram, 1982) follows the concept of the Expendable Bathythermograph (XBT) probe, which has a length of 0.215 m, a diameter of 5.2 cm and weighs 0.74 kg in air (Green, 1984). The XBP (see inset in Fig. 2.20) is a modified XBT with an accelerometer instead of a temperature sensor. The sensor data is transferred via an umbilical to the on-deck data acquisition. The penetrometer falls free through the water column. The XBP can be used in water depth ranging from 3 to 200 m (Stoll and Akal, 1999). The instrument reaches terminal velocities around 7 m/s (Stoll, 2004). However, the penetration depth is limited to the very surficial sediments (Akal and Stoll, 1995), while peak deceleration of more than 60 g can be reached (Aubeny and Shi, 2006; Stoll and Akal, 1999). The XBP is used in naval applications, and as well in research (e. g. Stark and Wever, 2009). Different approaches exist for data analysis. Stoll and Akal (1997); Stoll (2004) present a classification approach based on the deceleration behavior of the lance (see Fig. 2.20). Aubeny and Shi (2006) investigated the results of XBP deceleration numerically regarding undrained shear strength and applied a logarithmic rate correction (see also Section 2.1.3).

2.4.8 The STING penetrometer

The Seabed Terminal Newton Impact Gradiometer (STING penetrometer) is described in Lott and Poeckert (1996) and Mulhearn (2002). The probe consists of a body, which houses the data acquisition and the sensors. The probe measures the deceleration during penetration, has a length of 1 m (extendable) and a mass of 10 kg (see Fig. 2.21a for a drawing). The rod has a diameter of 19 mm, to which interchangeable tips can be attached. The tips can be of hemispherical, flat or conical design. The base diameters of the tips are 25, 35, 50 and 70 mm (Mulhearn, 2002). The conical tip has an apex of 90°. STING can be operated in water depths of up to 300 m.

Lott and Poeckert (1996) presents a comparison of XDP (see Section 2.4.2) and STING deployment data after a normalization against impact velocity in the context of mine burial prediction. The authors found, that there is a good agreement between the two methods.

Mulhearn (2002) reports seven deployments in context of mine burial predictions located in Sydney Harbour (Australia) in water depths of 8 to 16 m. The penetration depth ranged between 0.5 and 0.8 m. See Mulhearn (2002) for more information.

The STING penetrometer or modified designs based on its design have been applied in both laboratory and numerical studies, where several authors

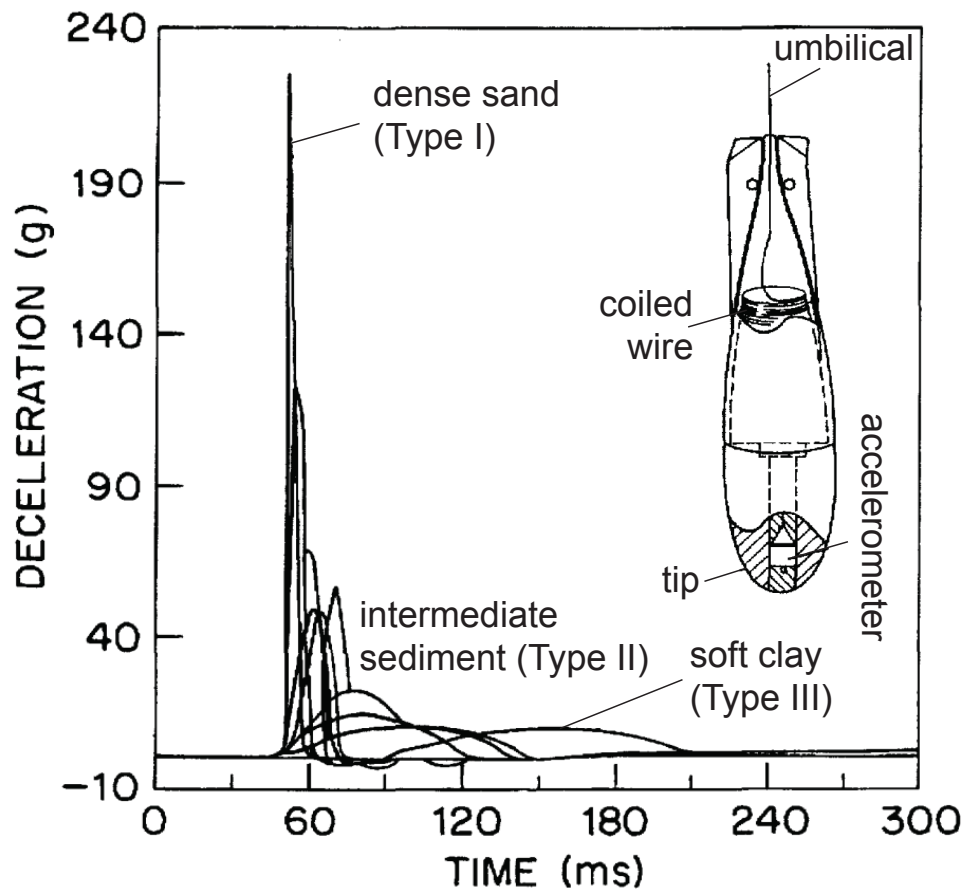


Figure 2.20 – Classification of XBP time series into sediment types I, II, and III after (Stoll and Akal, 1999). The inset shows a schematic of the XBP with relevant parts. Modified after Stoll and Akal (1997).

address strain rate effects and the determination of undrained shear strength from STING measurements.

Allan et al. (2007) presents laboratory investigations (73 tests) with a model penetrometer based on the STING design (shaft diameter is 5 mm and mass between 70 and 470 g). The soil targets consisted of uniform clay. The maximum impact velocity was 6 m/s. Allan et al. (2007) found, that the rate dependency of the penetrometer is only sensitive to the diameter of the penetrometer, when undrained shear strength values were determined after Vesic (1975).

Abelev et al. (2009a,b) numerically investigated the penetration behavior of the STING penetrometer with using finite element and finite difference approaches. Shear strength is derived from the numerical experiments using cone factors and by application of a strain-rate correction (Abelev et al., 2009b). The numerical data is compared with field data from STING deployments and reference datasets of undrained shear strength.

Chow and Airey (2013) present an empirical model based on 52 model penetrometer tests and reference triaxial tests to determine undrained shear strength of clay targets from penetrometer tests. Therefore, model penetrometer tests were carried out using the model penetrometer described by Allan et al. (2007) (see Fig. 2.21b for a drawing and test set-up). Based on the findings, rate and cone factors are developed, which allow the reproduction of the reference data through penetrometer measurements.

Chow and Airey (2014) presents systematic laboratory experiments of a model STING penetrometer (56 tests), where the influence of mass, tip diameter, tip shape, impact velocity, and undrained shear strength were investigated regarding their influence on the strain rate effect. The authors conclude, that mass, tip diameter and shape have a negligible influence on the rate effects during the tests (see Fig. 2.21c for model configurations). Chow and Airey (2014) also found, that rate effects change up to a limiting penetration velocity of 5 m/s.

2.4.9 The PROBOS penetrometer

The PROBOS (short for proboscis) penetrometer has been introduced by Stoll (2004). The penetrometer is very similar to the STING regarding its dimensions (Stoll, 2004; Stoll et al., 2007). However, the PROBOS is instrumented with force sensors in the tip in addition to the acceleration sensors in the body of the probe. The shaft is extendable (1 or 2 m in length). The PROBOS is connected to a data acquisition system via an umbilical, which also serves as a tether for recovery (Stoll et al., 2007). Strain rate correction is carried out following the approach of Dayal (1974) using a logarithmic

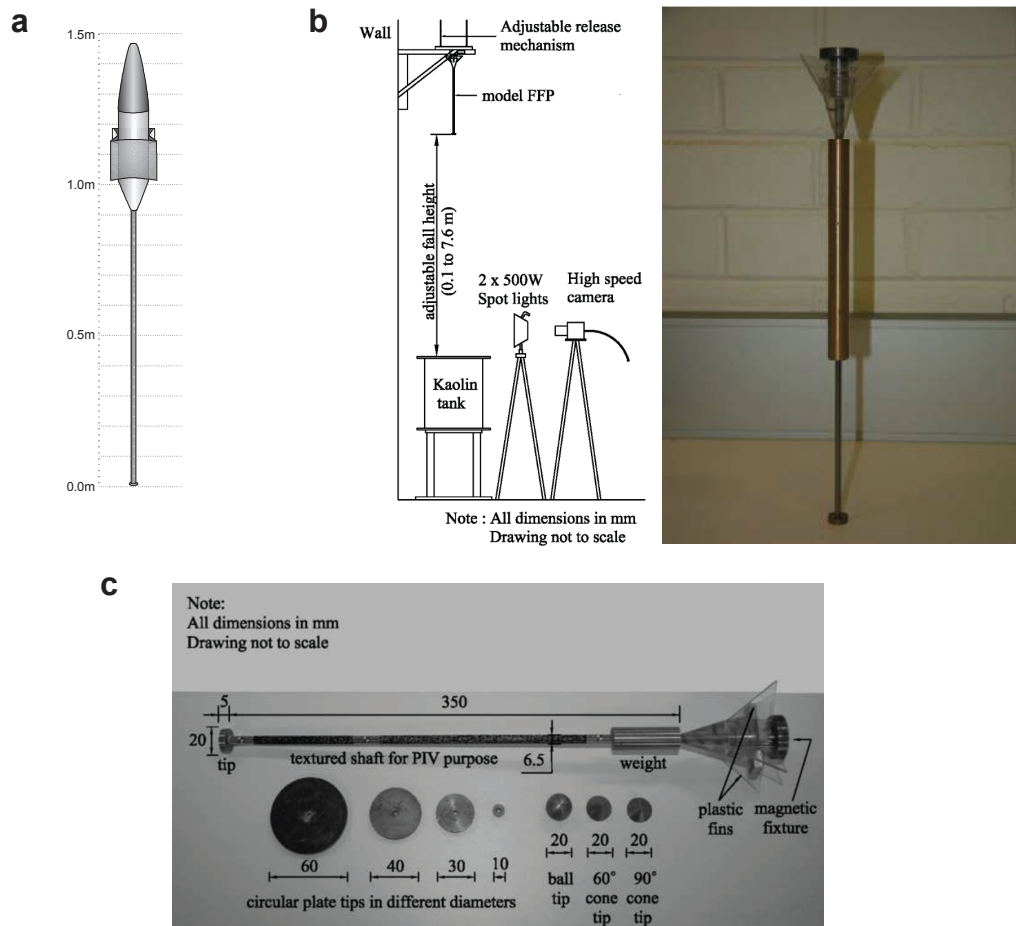


Figure 2.21 – **a** Schematic view of the STING penetrometer with dimensions. Modified after [Mulhearn \(2002\)](#); **b** The model embodiment of the STING penetrometer and set-up of laboratory experiments. Modified after [Chow \(2013\)](#); **c** Dimensions and configuration options of the model STING penetrometer. Modified after [Chow and Airey \(2014\)](#).

strain rate correction (Stoll, 2004; Stoll et al., 2007). See also Section 2.1.3 on that topic.

2.4.10 The NIMROD penetrometer

The NIMROD penetrometer (Stark et al., 2009a) is a lightweight free-fall penetrometer (see Fig. 2.22a for a schematic). The device has a length of 0.81 m, a diameter of 0.11 m, a mass of 11–15 kg (Stark et al., 2009b, depending on tip configuration), is rated to a water depth of 200 m (Stark et al., 2009a), and reaches terminal impact velocities of 13 m/s in shallow waters (Stark et al., 2012b), 2 m/s in deep waters (≥ 100 m; Stark and Kopf, 2011), and 3 m/s when deployed near the sea floor from submersible platforms, or by divers (Stark et al., 2013, 2012a). The impact velocity is dependent on fall height, hydrodynamic conditions and the drag of the retrieval tether (Stark and Kopf, 2013). See Figs. 2.22a,b,c for deployment and the attachment of the retrieval tether. The system penetrates up to 3 m in very soft, muddy sediments (Stark et al., 2013), usual penetration depths range between 0.05–0.24 m (dense sand) and up to 0.34 m (loose carbonate sand), see Stark et al. (2012b).

The NIMROD records acceleration with different sensitivities, temperature (Stark and Kopf, 2011), and water/porewater pressure (Stark et al., 2009b, U2 position). The tip is interchangeable and of different shape (60° conus, cylinder, hemispherical; Stark et al., 2011). The acceleration data are used to determine penetration depth and impact velocity. The acceleration-depth series are further processed to determine bearing capacity using a force-based approach (see Section 2.1.1), a strain rate correction to correct for the nonlinear backcoupling of the non steady penetration velocity (see Section 2.1.3), and the equation for ultimate bearing capacity (Stark et al. (2009b), see also Section 2.2.2)

The system has been deployed in different settings to investigate a variety of near-surface processes. Stark et al. (2009b) investigated sediment remobilization in a tide-dominated estuary, remobilisation under open marine conditions, and near shore sediment mobilisation and erosion. Stark et al. (2011) investigated sediment remobilisation along active subaqueous dunes, while scouring and deposition as effect of soil-structure interaction were investigated by Stark and Kopf (2011). A study on the penetration behavior in quartz vs. carbonate sands can be found in Stark et al. (2012b). The NIMROD has also been used to study high-energy regimes, such as the sorted bedforms in Stark et al. (2012b) and the strong current areas in Stark et al. (2014b). Fine-scale observations were made in lake sediments (Stark et al., 2013) and investigations in harbor sediments were done in Stark et al.

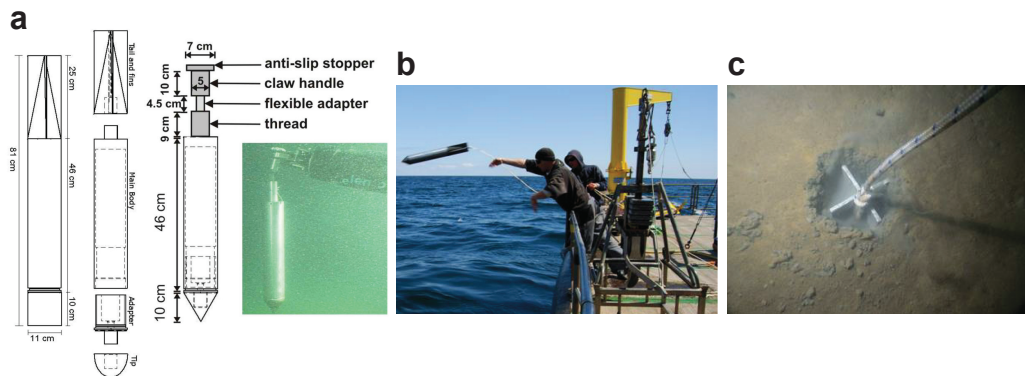


Figure 2.22 – **a** Schematic of the NIMROD penetrometer with different tip and tail configuration. The handle-tail is used for deployment from submersible vehicles, such as ROVs or manned submersibles (see photograph for deployment from a submersible). Images modified after Stark et al. (2012b, 2013); **b** deployment of the NIMROD penetrometer from a vessel. The penetrometer is recovered via tether. Image modified after Stark (2010); **c** final embedment of the penetrometer into soft sediments. Image modified after Stark et al. (2014b).

(2014b). Recently, geotechnical assessment for renewable energy projects using the NIMROD penetrometer is presented in Stark et al. (2014a).

2.4.11 Other penetrometers

Several impact penetrometers were developed in the 1970s and 1980s. However, a literature research yielded, that development has been discontinued on these penetrometers or ended up in other projects. Developments with little scientific publication activity (such as the dotOcean penetrometer, see Sec. 2.4.11) are also grouped in these sections.

Accelerometer-instrumented penetrometer

Migliore and Lee (1971) presents a penetrometer (see Fig. 2.23a), which is instrumented with an accelerometer after Scott (1967), see Fig. 2.23b. The penetrometer has an interchangeable shaft (rod with conical tip and corer pipe). The rod has a diameter of 0.0254 m, the conical tip has a diameter of 0.058 m and an opening angle of 45° , while the corer has an inner diameter of 0.076 m and an outer diameter of 0.083 m and a mass of 78 kg (Migliore and Lee, 1971). The authors present four deployments with the

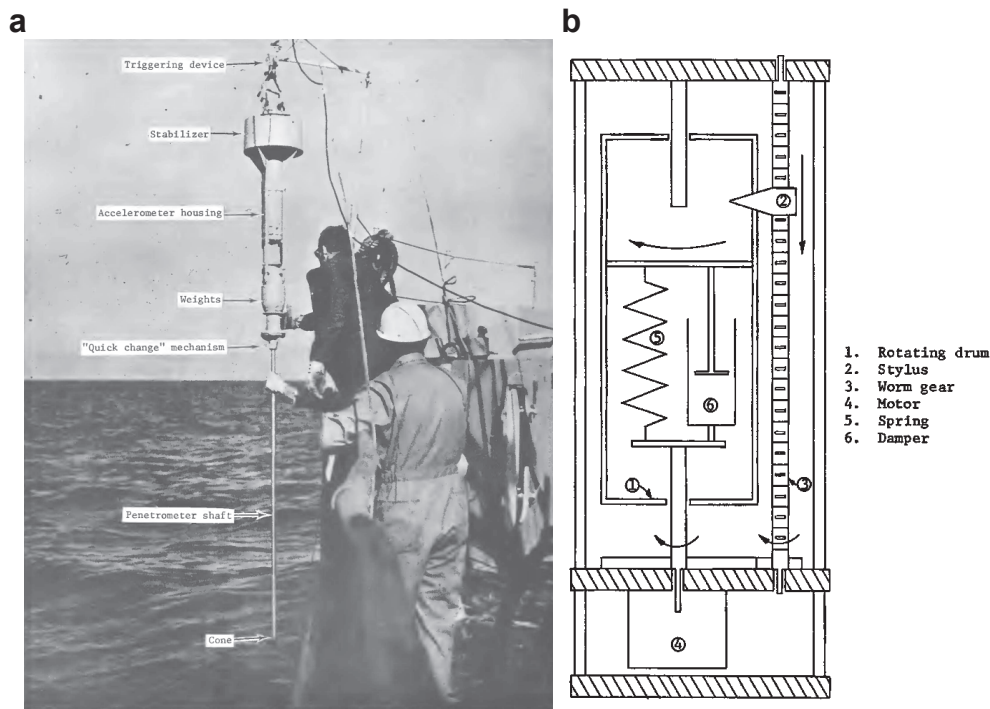


Figure 2.23 – **a** Deployment of the penetrometer instrumented with an accelerometer. Relevant parts are annotated; **b** schematic of the accelerometer. Images modified after Migliore and Lee (1971).

conically tipped rod and six deployments with the corer pipe. The acceleration data are processed and yield acceleration over penetration distance, as well as a velocity-depth profile. Migliore and Lee (1971) present a force-based approach to predict the penetration behaviour under assumption of soil strength profiles.

Model penetrometer at Newcastle University

The Newcastle University developed a model free-fall penetrometer (Denness et al., 1981) to investigate strain rate effects, predict pile driveability, and to deter geotechnical properties, such as undrained shear strength from the measurements. The penetrometer (see Fig. 2.24) has a length of 1 m (extendable), a mass of 7 kg (at 1 m length), and a diameter of 36 mm. The system is equipped with accelerometers to determine the kinematics during penetration. A possibility to mount a standard cone (10 cm^2) is announced (Denness et al., 1981). The authors present results from laboratory testing in clay for free-fall and impelled experiments.

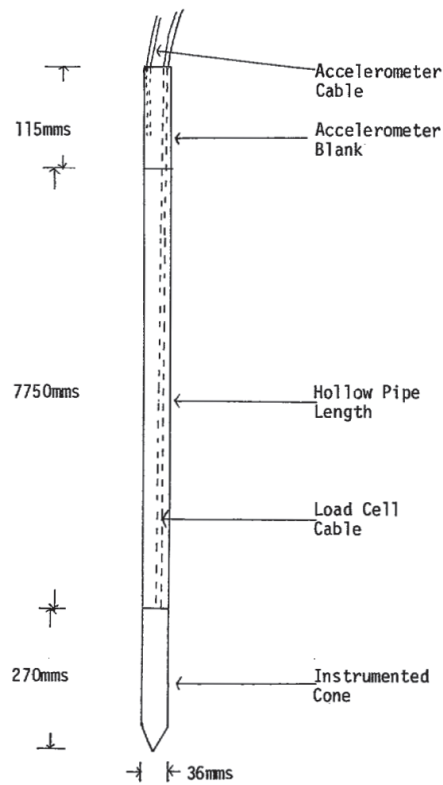


Figure 2.24 – The model penetrometer at Newcastle University with dimensions and annotations of relevant parts. Modified after Denness et al. (1981).

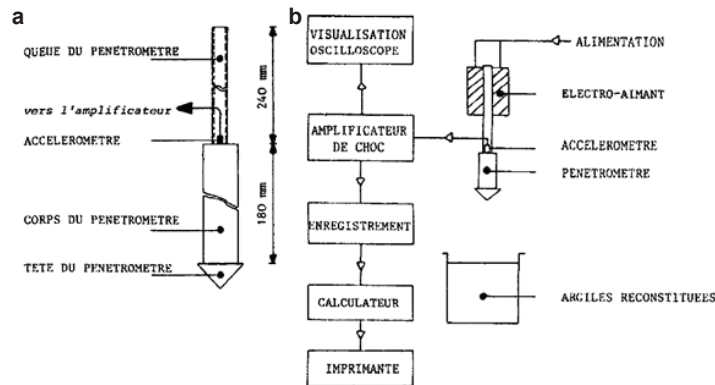


Figure 2.25 – **a** Schematic of the model penetrometer at Université de Nantes; **b** Data acquisition process for the model penetrometer. Modified after (Levacher, 1985).

Penetrometer at Université de Nantes

Levacher (1985) describes a model penetrometer, which is equipped with an accelerometer (see Fig. 2.25). The penetrometer has a mass of 2.3 kg, a diameter of 50 mm. Levacher (1985) presents two cone designs (60° and 90° apex). The cones have at their widest side a 10 mm larger diameter than the rod. The acceleration data is transferred via an umbilical wire to a data acquisition. The system is mounted in a launching apparatus.

The author shows acceleration-time series from laboratory experiments on reconstituted clay samples. The dynamic penetration resistance is determined by using a force-based approach (see Section 2.2.2), neglecting side friction.

The free-fall lake sediment penetrometer

Spooner et al. (2004) presents a lightweight penetrometer (see Fig. 2.26) for rapid investigation of lake sediments to determine ideal locations for geologic sampling. The system has a mass of 3 kg, a diameter of 60 mm and a length of ~ 30 cm. The tip is hemispherically shaped with a radius of 30 mm. The deceleration during penetration is sensed with a 25 g accelerometer. Data is transferred with an umbilical wire to a data acquisition system. The penetrometer is rated to water depths of up to 15 m.

Spooner et al. (2004) presents results from field trials in lake sediments, which show good reproducibility. The data are analyzed qualitatively regarding the shape of the acceleration-time record.

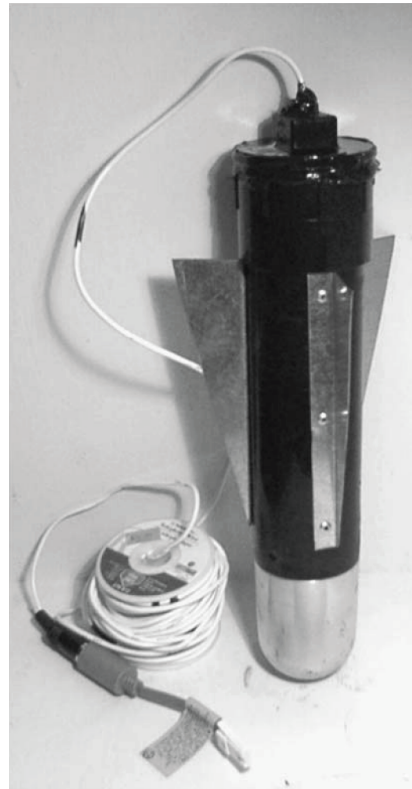


Figure 2.26 – The free-fall lake sediment penetrometer with spherically shaped tip, stabilizing fins, and tether / data transmission cable. Image modified after Spooner et al. (2004).

GraviProbe penetrometer

The Belgian company dotOcean N.V. developed a free-falling penetrometer called GraviProbe (Geirnaert et al., 2014), which is similar to the NIMROD penetrometer (Section 2.4.10) in size, shape and deployment (see Figs. 2.27a,b). Several patent applications have been filed for this penetrometer (Geirnaert et al., 2011; ITelegance BVBA, 2010b; dotOcean N. V., 2012; ITelegance BVBA, 2010a), revealing details about application and data analysis. The GraviProbe has a length of 0.9 m, a diameter of 0.05 m, a variable mass of 7–10 kg, a conical tip and reaches terminal velocities between 6 and 7 m/s (Geirnaert et al., 2014). The GraviProbe is instrumented with accelerometers and pressure sensors (Geirnaert et al., 2014).

The penetration resistance, as well as shear strength and fluid density are derived from acceleration data considering energy relations: Once the penetrometer reaches terminal velocity in water, the kinetic energy stays constant. However, potential energy decreases due to the downward motion of the penetrometer. This is caused by fluid drag (in water) and by drag or shear stress within the sediment. See dotOcean N. V. (2012) and Section 2.2.2 for further details.

The instrument has been used to determine the navigable water depth (shear stress >100 Pa) in ports (Geirnaert et al., 2014). There, penetration depths between 2.5 m and 3.5 m were reached in soft harbor sediments (counting from the 100 Pa transition). The system and has been calibrated in a sediment column with known sediment characteristics (Stark et al., 2014b).

Penetrometers for extraterrestrial use

The properties of granular materials in remotely accessible regions, such as the (deep) ocean can be evaluated with penetrometers or penetrators. Likewise, penetrometers can be applied in space to assess such properties. Some arbitrary selected studies and projects are presented within this section.

McCarty and Carden (1962) conducted low- and high velocity tests with accelerometer-instrumented projectiles to assess the properties of several granular materials. The aim of the study was to assess the penetrability of lunar surface material with an empirically determined database of analog materials. The authors evaluate the acceleration-time histories for different impact mechanisms and target materials. Empirical relationships were formulated, based on the dimensions and kinematics of the impactor. The penetrometers had conically (60°) and hemispherically shaped tips, a diameter of 0.076 m, a length between 0.076 and 0.23 m and a mass of 0.44 to 3.57 kg. This study was continued in 1986 (McCarty and Carden, 1968) with a wider



Figure 2.27 – **a** The GraviProbe Penetrometer. Image modified after <http://www.oceanologyinternational.com>; **b** the GraviProbe during deployment. Image modified after <http://www.nauticexpo.de>

range of target materials and the explicit intention to use penetrometers in extraterrestrial vehicles to assess conditions of potential landing sites for manned and unmanned missions, as well as for the assessment of material properties for scientific use.

Roddy et al. (1963) evaluated the penetrability of loose and densely packed granular material under vacuum and atmospheric conditions with the aim to provide a framework for the assessment of the bearing strength of lunar materials by penetrometer tests.

Lorenz et al. (1994) describes the development of piezoresistive sensors (accelerometer and force sensors), which were attached to the Cassini-Huygens probe, which landed on Titan, Saturn's largest moon. The probe accelerations and forces recorded during the landing and hence the penetration of Titan's surface yielded strength, which are also encountered during penetration of e.g. wet clay, lightly packed snow and wet or dry sand (Zarnecki et al., 2005).

The Rosetta lander "Philae" (see Fig. 2.28), which landed on comet 67P/Churyumov-Gerasimenko ("Chury") on November, 12 2014 includes the multi purpose sensor package (MUPUS; Spohn et al., 2007), which has been developed to measure the mechanical strength of the surface among other parameters by two techniques. First, the anchoring procedure with harpoon-type anchors would be monitored by accelerometers, which are sampled at very high rates (50 kHz) due to the high anchor impact velocity (100 m/s) caused by a pyrotechnical launch. Second, mechanical strength would also be determined while driving (hammering) a probe into the comet's surface. However, the anchor deployment failed due to unknown reasons and the penetration experiment did not attain the desired penetration depth (Spohn et al., 2015). Though, from the penetration data, it could be assumed, that the surficial mechanical strength of the landing site lies in the range of 4 MPa (Spohn et al., 2015).

2.4.12 Instrumented corers

Lister (1964) instrumented a piston corer with an acoustical source. The study aimed on the vertical movement of equipment lowered to deep water depths. The study showed, that the system consisting of vessel, wire, and equipment acts as a harmonic oscillator with possible amplification of the excitation amplitude (Lister, 1964).

Open barrel or piston corers can easily be equipped with passive piggy-back instrumentation to acquire data on their movement during penetration, thus enhancing the information which can be drawn from a corer deployment. This has been done by Preslan (1969) and Scott (1970) with a purpose-built

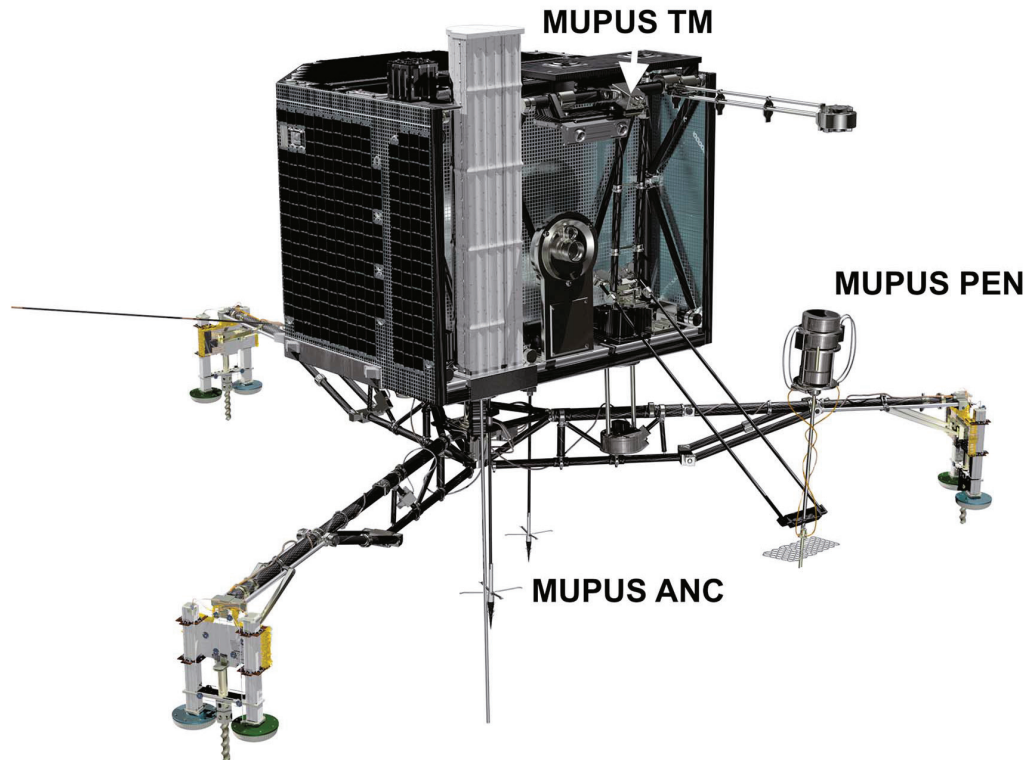


Figure 2.28 – The Philae lander with investigation equipment for the determination of the mechanical strength of the comets surface. MUPUS ANC: pyrotechnically launched anchors, which are equipped with accelerometers. MUPUS PEN: Hammered penetration device, which delivers strength estimates through the applied energy for each blow. Modified after [Spohn et al. \(2015\)](#).

accelerometer and data registration (Scott, 1967). See Fig. 2.29a for the acquisition device and the setup of the corer.

The aim of the first studies using accelerometers (Preslan, 1969; Scott, 1970) was to gather information on the corer performance and the in-place properties of ocean-bottom sediments. In total 36 corer deployments were conducted with piggy-back instrumentation. The corers were both triggered corers (i.e., piston corer in this study) and non-triggered (i.e., open barrel corers in this study). The corers had masses ranging between 81 and 499 kg, and inner diameters ranging between 0.076 and 0.053 m (Preslan, 1969). Especially, it has been of interest to determine the disturbance of samples, which may occur during coring.

The disturbances may be caused by a neglectfully designed trigger set up (in case of piston corers; Preslan, 1969), or by excessive corer motion (Lister, 1964) in case of tethered corers without trigger. The disturbances were described as double penetration (Preslan, 1969), sediment inflow (due to partly penetration of piston corers; Bouma and Boerma, 1968; McCoy, 1985), core shortening (e.g. McCoy and Von Herzen, 1971; Buckley et al., 1994), selective coring (especially of plastic lithologies Weaver and Schultheiss, 1983; Parker and Sills, 1990), or core stretching (Scott, 1970; McCoy, 1985; Buckley et al., 1994). Skinner and McCave (2003) also reviews disturbances encountered during coring operations. These disturbances may not be evident, when cores are visually inspected and may thus lead to misinterpretation of the sedimentary sequence (Preslan, 1969). Correction (e.g. linear) for these effects cannot be applied since it cannot be known without additional measurements if and where disturbances occur.

However, double integration of acceleration records yields distance over time, which can serve as a continuous, second measure of penetration depth. This can be used to compare it to the retrieved core length (Preslan, 1969) or mud marks on the outer shell of the corer pipe (Preslan, 1969; McCoy, 1980).

Scott (1970) determines the sediment resistance force from accelerometer measurements accounting for other forces occurring during the penetration (i.e. hydrodynamic drag and cable force). The cable force has found to be a critical parameter, since the wire behaves elastically (e.g. Lister, 1964) and may rebound once the load of the penetrator disappears (Scott, 1970) due to triggering or diminishes during penetration (in case of tethered corers). Scott (1970) outlines the use of the accelerometer in combination with solid, tipped rods to assess geotechnical properties of the sediments. This approach has been adopted by Migliore and Lee (1971), see Sec. 2.4.11.

Burns (1966) conducted 21 deployments with lightweight gravity corers (mass between 25.4 and 49.8 kg, inner diameter between 0.038 and 0.081 m,

and length between 0.35 and 2.45 m) in a large-scale tank. See Fig. 2.29b for schematics of the employed corers. There, the dependency of impact velocity from the fall height was investigated under consideration of hydrodynamic drag. The author found, that the optimal fall height for a triggered corer lies between 2 and 3 m, when terminal velocity is reached. The corer dynamics were investigated by timing known distances during free-fall.

Seyb et al. (1977) used an accelerometer, inclinometers, a camera, and a compass to determine penetration depth and orientation of piston corers (mass: 1255 kg). Fig. 2.29c for the acquisition instrument. The data analysis of the acceleration data from 2 deployments follows the concept of Preslan (1969) and Scott (1970) with double integration and representation of acceleration and velocity as a function of penetration distance.

Heffler (1991) presents an acceleration monitoring system for piston corers, where acceleration sensors (in addition to tilt and pressure sensors) are mounted on the corer pipe and on the piston. See Fig. 2.29d for both devices. Said author presents data from a single deployment for both sensor locations, indicating, that the rebound of the wire (Scott, 1970) severely affects the motion of the piston. Thus effects like core stretching or sediment inflow are promoted due to pressure gradients between the sediment and the piston. The piston corer had a mass of 1000 kg, a length of 12 m, and an inner diameter of 0.1 m (Heffler, 1991).

Villinger et al. (1999) equipped the core heads of open-barrel and piston corers with accelerometers and pressure transducers. The corers had a weight stand with a mass of 2000 kg, and inner diameters of 0.125 m (open-barrel) or 0.09 m (piston corer), and a length of 12 m. The piston corer reached impact velocities of over 8 m/s (Villinger et al., 1999). The acceleration data (see Fig. 2.29e for time series of piston- and open-barrel corer penetrations) was used to assess corer motion during penetration. The authors reveal, that retrieved core length and penetration depth determined from acceleration measurements differ by up to 30 % (where difference is more severe for open-barrel corers) for the 13 measurements taken. Correlations of peak decelerations with bulk density data from core logging reveal, that the most loss of core material (owed to compaction or selective coring) occurs in the lowermost part of the measurement (i.e., at the greater depths).

Mosher et al. (2007) uses a modified version of the FFCPT (Osler et al. (2006a), see Section 2.4.14) in combination with coring equipment. The device (HARPOON) is mounted at the cutting edge of the corer. See Fig. 2.29f for a system ready for deployment. Thus, obtainment of cores is not possible while this device is used. The HARPOON device is rated up to 3400 m water depth, has a length of 1.2 m, a diameter of 0.168 m and a mass of 110 kg, which adds to the mass of the coring device (Mosher et al.,

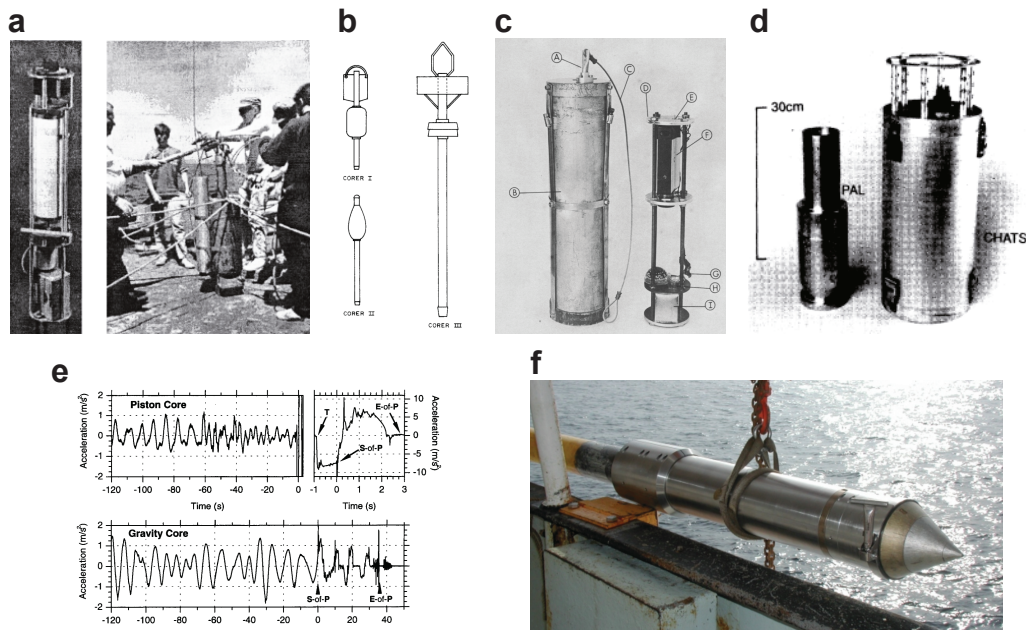


Figure 2.29 – **a** left: acquisition of acceleration data, right: vetting of the trigger mechanism. Image modified after Scott (1970); **b** schematics of different gravity corers. Image modified after Burns (1966); **c** Orientation monitoring system. Modified after Seyb et al. (1977); **d** Monitoring system for piston corers: PAL monitors the piston movement and CHATS monitors the corer pipe. Image modified after Heffler (1991); **e** Acceleration-time series of corer penetration for open-barrel and piston corers. Modified after Villinger et al. (1999); **f** HARPOON device mounted at the end of a corer. Image modified after <http://www.brooke-ocean.com>

2007). The authors present data from seven deployments, where depths of up to 12 m were reached. After processing, acceleration data can be used to determine dynamic undrained shear strength of cohesive sediments by application of a cone factor (Mosher et al., 2007).

2.4.13 The Marine Impact Penetrometer

The Marine Impact Penetrometer has been envisaged and developed by Dayal and Allen (1973); Dayal et al. (1975) at the Memorial University of Newfoundland (St John's, Canada). The penetrometer is a lance-shaped device with a rod length of 4.57 m (extendable up to 15 m), a rod diameter of 0.076 m, a conical tip (60° apex) and a mass of 453 kg. The Marine Impact

Penetrometer is rated to water depths of up to 300 m (Dayal et al., 1975). Dayal (1974) presents extensive tests with a model penetrometer in different sediments (loose sand, dense sand, clay and layered sediments). The model penetrometer has the same dimensions regarding diameter and cone design as the Marine Impact Penetrometer and has a variable mass of 6.8 to 29.5 kg and a rod length of 0.6 m (Dayal, 1974). See Fig. 2.30a for the model penetrometer. Both instruments are equipped with an acceleration sensor and strain gauges measuring cone resistance and sleeve friction. The data acquisition of the full-scale instrument is self-contained within the weight stand in a casing resistant to water pressure (Dayal et al., 1973). The full-scale instrument has been tested in both laboratory and field settings (Dayal et al., 1975). The impact velocities ranged between 3.8 and 6.1 m/s for laboratory tests (Dayal, 1974) and around 8.5 m/s for field tests (Dayal et al., 1975). The system is designed to achieve its terminal velocity through a triggering device (see Fig. 2.30b for a schematic of the full-scale instrument). Shear strength data can be deduced from the penetration data (cf. Dayal (1974); Dayal and Allen (1975); Dayal (1981) for details) by application of a strain-rate correction and a force-based processing approach based on the bearing capacity theory by Meyerhof (1961).

Field tests were conducted in soft harbor sediments (Dayal et al., 1975), where a penetration depth of 1.8 m (impact velocity: 8.4 m/s) could be reached. Chari et al. (1978, 1981) modified the penetrometer regarding its dimensions and data acquisition. The new design of the Marine Impact Penetrometer had a cone diameter of 0.075 m, a rod diameter of 0.0635 m, a mass of 159 kg with a total rod length of 3.7 m (Chari et al., 1981). See Fig. 2.30c for the modified penetrometer. The impact velocity was ~ 10 m/s for a fall height of 15 m and the penetration depth in medium stiff clay reached the rod length of 3.7 m (Chari et al., 1978; Dayal, 1980). The data from acceleration sensors were transmitted via an umbilical wire to a tape recorder on the vessel (Chari et al., 1978).

2.4.14 The Free-Fall Cone Penetrometer (FFCPT)

The Free-Fall Cone Penetrometer (FFCPT; Melton et al., 2000) is a commercially available probe (ODIM Brooke Ocean Inc., Canada), which measures pore and hydrostatic pressure, optical backscatter, electrical resistivity, and acceleration. The pressure and acceleration records are used to deliver depth information or to classify sediment (Osler et al., 2006a). This is done within the sediment classification scheme of Robertson (1990) based on the dynamic data without the application of a rate correction.

The FFCPT (see Fig. 2.31) has a diameter of 88 mm (3.5 in), a length

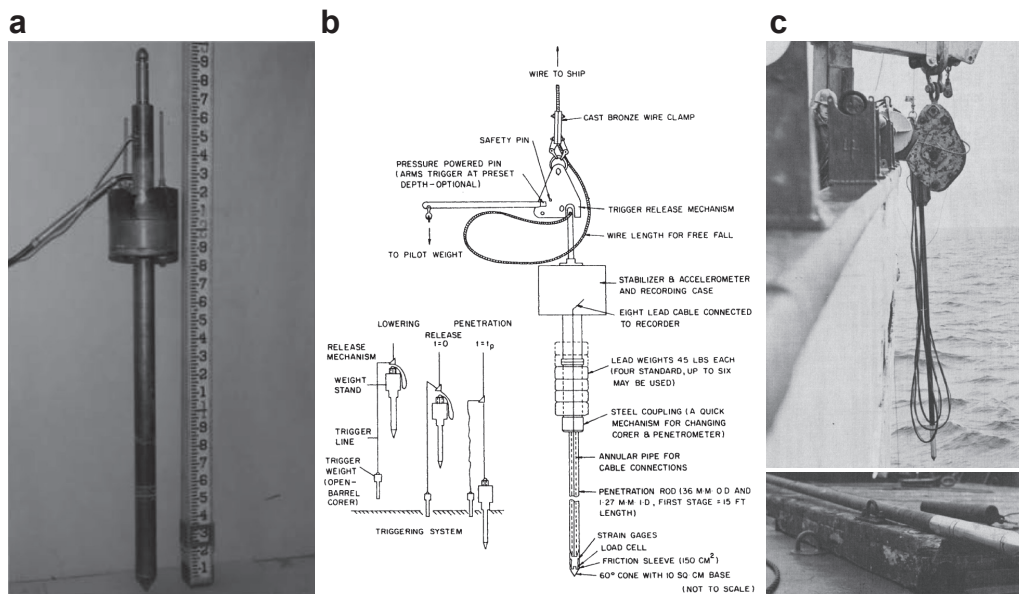


Figure 2.30 – **a** Laboratory model penetrometer. Diameter and cone dimensions are identical to the field penetrometer. Images modified after Dayal (1974); **b** Schematic of the field penetrometer (36 mm design) relevant parts and dimensions are annotated within the figure. Inset: trigger procedure. Schematic modified after Dayal et al. (1975); **c** Upper image: deployment of the 75 mm outer diameter embodiment of the marine impact penetrometer. Lower image: rod with sensor-equipped cone. Images modified after Chari et al. (1978).

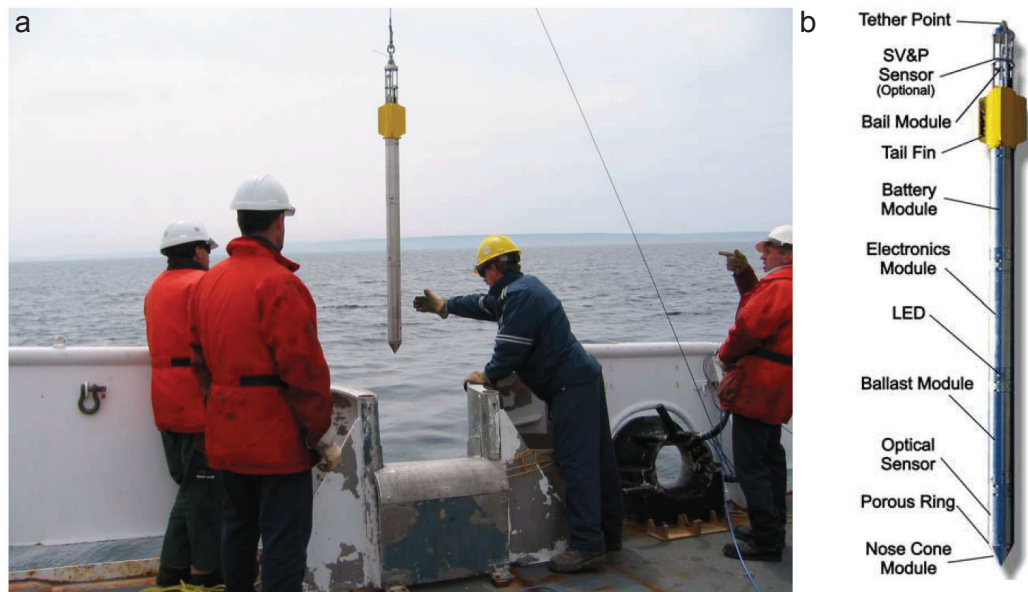


Figure 2.31 – **a** Deployment of the FFCPT instrument; **b** FFCPT instrument with annotations regarding sensors and other components. Image modified after Furlong et al. (2006).

of 1.8 m, and a mass of 52 kg (115 lbs) (Furlong et al., 2006). The system can be used in combination with the Moving Vessel Profiler (MVP; Furlong et al., 2006; Osler et al., 2006b,c) e.g. to obtain frequent measurements along profiles. A free-fall operation is also possible. However, the system is not expendable. In free-fall mode, it reaches terminal velocities around 8 m/s. For higher water depths, the drag of the tether diminishes the terminal velocity (Osler et al., 2006a).

Tests in water depth ≤ 100 m (the instrument is rated up to 660 m) are reported by several studies (MVP; Osler et al., 2006a,b,c). Mulukutla et al. (2011) used a FFCPT to classify sediments based on the embedment characteristics.

2.4.15 The Free-Fall Cone Penetrometer (FF-CPT)

The FF-CPT has been developed at the MARUM institute at Bremen University and exists in two different versions: a shallow water instrument (SW FF-CPT: Stegmann et al., 2006a,b) and a deep water instrument (DW FF-CPT: Stegmann and Kopf, 2007). The SW FF-CPT has a rod length ranging between 1 to 6 m and a mass of 40 to 170 kg (Stegmann et al., 2006a). The

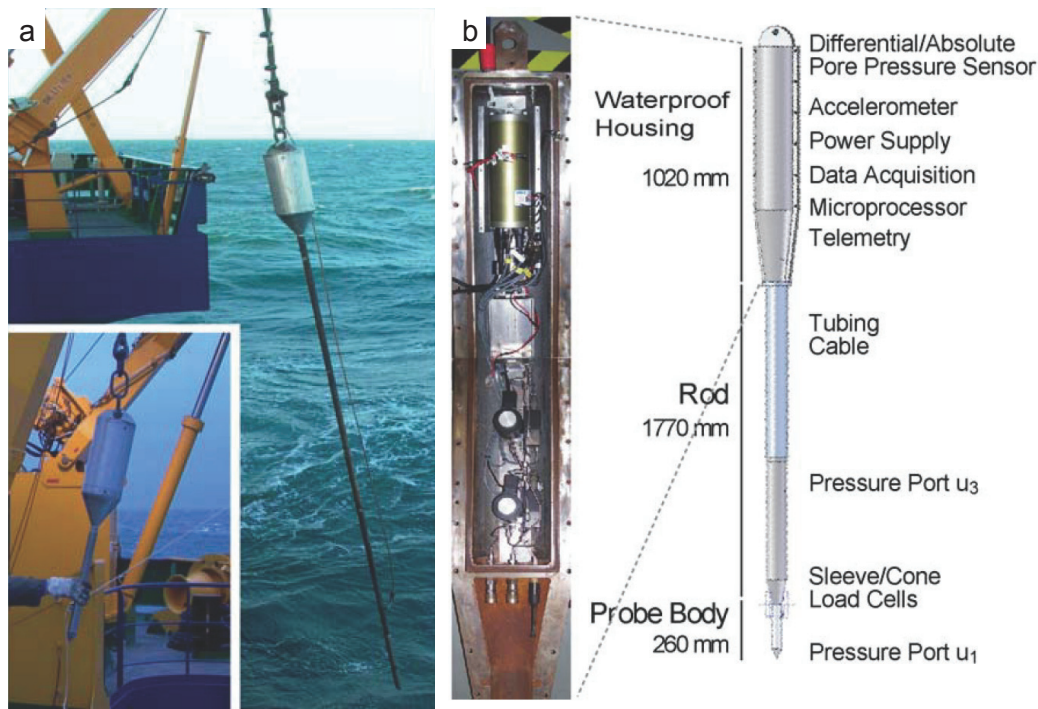


Figure 2.32 – **a** Shallow-water FF-CPT during deployment (inset: short version), modified after Stegmann (2007); **b** Deep-water FF-CPT electronics and schematic with annotations of sensors and parts. Modified after Stegmann and Kopf (2007).

SW FF-CPT (Fig. 2.32a) can be deployed in free fall (terminal velocity: 6 m/s) or in winch mode (Stegmann et al., 2006a). The instrument records time series of acceleration, cone resistance, sleeve friction and pore pressure. The cross sectional area of the cone is 15 cm² and it is rated to 200 m water depth (Stegmann et al., 2006b).

The DW FF-CPT (Fig. 2.32b) has a length of 4 to 7 m, a mass of 500 to 550 kg (Steiner, 2013) and a cross-sectional area (cone) of 15 cm² with increasing diameter of the rods. Additional to cone resistance, sleeve friction and acceleration, (differential) pore pressure is recorded (Stegmann and Kopf, 2007). Data analysis comprises strain rate correction (cf. e.g. Steiner et al. (2014) and Section 2.1.3 for a discussion of several approaches).

Both instruments have been used extensively for scientific investigations of different problems: e.g. subaquatic slope stability (Stegmann et al., 2007; Strasser et al., 2007; Steiner et al., 2012), landslide characterisation (Kopf et al., 2007), and mud volcanoes (Kopf et al., 2009).

2.4.16 The CPT Stinger

The CPT Stinger (Young et al., 2011) is a hybrid device between a free-fall lance-shaped penetrometer and a static cone penetrometer. The CPT Stinger is a modified Jumbo Piston Corer (JPC), which houses a CPT driving unit instead of core liners and the piston. The CPT sensor acts as the furthestmost element at the tip of the device, hence being always subjected to undisturbed sediment. See Fig. 2.33a for a schematic and Fig. 2.33b for the cone sensor arrangement. The measurement is carried out in two phases: (i) the free fall phase. There, the piston corer is released with using a trigger system. The corer gains momentum during the free-fall through the water column and the first sedimentary layers (Buhler and Audibert, 2012). At a certain point, the corer has reached its final embedment depth. (ii) the embedded piston corer has a holding capacity, which is large enough (2680–3570 kN Young et al., 2011) to drive the cone sensor further into the soil with a static velocity of 0.02 m/s. During both phases, cone resistance sleeve friction, pore pressure and corer acceleration are acquired (Young et al., 2011). See Fig. 2.33c for the deployment of the CPT Stinger.

The JPC has a mass ranging between 2300 and 3400 kg, depending on configuration (Caruthers et al., 2014). The outer diameter of the coring pipe is 0.14 m (Young et al., 2011) and 0.16 m at transitions between segments (Jeanjean et al., 2012). The extendible CPT rod is a standard configuration after ATM D5778 (Caruthers et al., 2014). The length of the corer pipe is variable (11.6 and 17.7 m Young et al., 2011). Likewise, the length of the CPT rod varies between 9.1 and 15.2 m, resulting in a total extended rod length with a rod of 23.3 to 34.6 m (Young et al., 2011).

The results of field tests are presented by several authors (Young et al., 2011; Buhler and Audibert, 2012; Jeanjean et al., 2012). The instrument has been deployed at water depths of 2100 m in the Gulf of Mexico, in hemipelagic sediments which are underlain by a debris flow deposit (Buhler and Audibert, 2012). The CPT Stinger has been triggered ~ 1 m above the sediment level, reached an impact velocity between 1 and 2 m/s and accelerated throughout the sediment up to 10 m/s (Jeanjean et al., 2012). A total penetration depth (with extended CPT rod) of 35 m could be reached.

Penetration data of static penetrations are processed and interpreted like conventional static-velocity CPT (Young et al., 2011). The dynamic stage of penetration requires strain-rate correction. The data processing (Jeanjean et al., 2012) incorporates a force-based penetration model after True (1976) and strain-rate correction using log, power, and square root relationships (Buhler and Audibert, 2012). It has been shown (Young et al., 2011; Jeanjean et al., 2012), that the static velocity data from the post-embedment

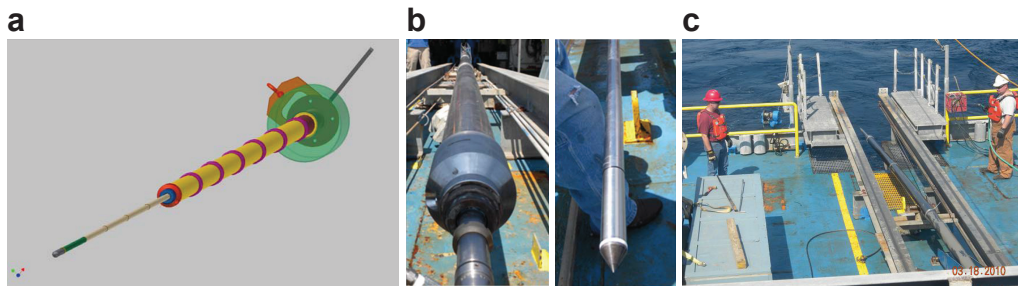


Figure 2.33 – **a** Schematic of the JPC with the integrated CPT driving unit. See the extended cone and the transition pieces between the core barrel sections. Schematic modified after Young et al. (2011); **b** Close-up photographs of the transition between core barrel and cone section (left), as well as the cone section (right). Images modified after Young et al. (2011); **c** CPT Stinger during deployment. Image modified after Young et al. (2011).

phase satisfactorily match to the processed dynamically acquired data of the first penetration phase. The whole CPT-Stinger dataset moreover matches a reference dataset, acquired using conventional CPT equipment (Jeanjean et al., 2012).

2.4.17 The Lance Insertion Retardation Meter (LIR-meter)

Development of a penetration monitoring device started in 2007 at Bremen University. The Bremen Lance Insertion Retardation Meter (Fabian et al., 2008) is a self-contained device capable of acquiring acceleration data as a function of time at a sampling rate of 500 Hz and a A/D resolution of 16 bit for durations of up to 48 hours (Fabian et al., 2008). See also Fig. 2.34 for the LIRmeter electronics. The LIRmeter can be used in combination with any marine lance (e.g., open-barrel corers, piston corers, heat-flow probes, pore pressure probes). When used with non-triggered lances, a pogo-style operation (Hyndman et al., 1979). Thus, it is possible to enable a time efficient characterisation of marine sediments especially in deep waters. The only factor limiting the operating depth is the design of the pressure casing (Fabian et al., 2008).

The LIRmeter was envisioned to be a fast and easy to use tool for the investigation of near-surface sediments. Especially with attention to the lately developed field of offshore wind energy, the measurement concept appeared suitable to rapidly map areas of interest without having to perform exten-



Figure 2.34 – **a** Electronics of the LIRmeter. Relevant parts are annotated within the figure; **b** Deployment of the LIRmeter within the Bremen Heat Flow Probe (Villinger et al., 2010c). Images modified after Fabian et al. (2008).

sive geotechnical surveys. This new field of application revived the robust and simple kinematic approach, which has been widely used in the 1970s and 1980s with the MIP and the MSP/XDP/ISP instruments, respectively. The robustness is needed, especially in near-shore environments, due to a high lateral variability in sedimentary conditions.

Field tests at a water depth of 6000 m (Fabian et al., 2008) showed, that the acceleration records during penetration can be used to determine layering of marine sediments. Comparisons of penetration depth to penetration data of the carrier lance (in this case: the Bremen Heat-Flow Probe: Villinger et al., 2010c) showed an excellent fit. The lance has a mass of ~ 1400 kg, a rod diameter of 0.13 m and a rod length of 5.52 m. Several structural components are welded on the rod (see Fig. 2.34b) However, the authors found, that the data record may be disturbed by the ships motion. Additional prototype evaluation in deep water (> 3000 m) has been carried out during research cruises MSM11/1 (Villinger et al., 2010b), SO-207 (Villinger et al., 2010a) by the author. Recent testing was carried out during cruise SO-240 (Villinger, pers. comm.) in the German manganese nodule license area (Pacific).

Chapter 3

Instrument and performance evaluation

The Lance Insertion Retardation Meter (LIRmeter). An instrument for in-situ determination of sea floor properties: Technical description and performance evaluation

Stephan, S¹ ✉ and Kaul, N¹ and Villinger, H¹

Published in: *Marine Geophysical Research*; Received: 26 March 2012 / Accepted: 25 May 2012 / Published online: 12 June 2012

Citation: Stephan, S, Kaul, N, Villinger, H (2012). The Lance Insertion Retardation Meter (LIRmeter). An instrument for in-situ determination of sea floor properties – technical description and performance evaluation. *Marine Geophysical Research*, 33(3):209–221.

The final publication is available at Springer via <http://dx.doi.org/10.1007/s11001-012-9156-2>

¹Universität Bremen
Department of Geosciences
28359 Bremen, Germany
sstephan@uni.bremen.de

Abstract Within this paper we present the Lance Insertion Retardation Meter (LIRmeter) as an instrument to determine the strength of marine sediments by a measurement of the deceleration of a probe during penetration into the sea floor. The instrument has been designed for the penetration of the upper 4 m of marine sediments and is therefore suitable for site investigation applications such as cable route surveys. The LIRmeter can be easily deployed from a floating platform in water depths of up to 4500 m. The system is suitable for long lasting missions (more than 12 hours) with pogo style measurements due to a rugged design and a special selection of sensors and electronics. The LIRmeter provides a custom data acquisition software and a web interface for acquisition setup, data download and system administration. An adaption of the instrument to specific problems (e.g., extremely soft sediments) is possible due to interchangeable tips and adjustable weights of the lance. The specifically developed user interface and the rugged design make the instrument very easy to handle and to maintain. The sensors and the data acquisition were tested in the laboratory as well as in the field. Field measurements took place in the North Sea, where numerous measurements were performed. This paper gives an extensive description of the design of the LIRmeter (mechanics, electronics and data acquisition) supplemented by a description of data analysis and results of field- and laboratory-tests.

3.1 Introduction

Knowledge of sea floor parameters, especially the sediment strength in terms of bearing capacity (Das, 2001), shear strength (Terzaghi, 1943) or sediment type (in terms of grain size or porosity) are essential parameters for a variety of fields like geotechnical research (Stegmann and Kopf, 2007), the offshore industry (Duncan, 1969) or even military purposes (Chu and Chenwu, 2007). Once these stability parameters are known i.e. through a direct or indirect measurement, they can be used to assess the seabed stability.

Sediment strength parameters are measured routinely *ex situ* on samples or half split sediment cores with various methods, such as the Vane Shear Test (standard D-4648 by the ASTM (2000)) or by Fall Cone Penetrometers (Hansbo, 1957). The *ex situ* techniques are well established and cost efficient. Commonly used instruments are easy to handle and to transport. Notwithstanding these advantages, there are severe shortcomings: (1) Transportation after recovery as well as temperature and pressure changes can alter the sediment properties and structure prior to the measurement, (2) coring operation can alter the sediment structure (Parker and Sills, 1990) or even destroy or change the sedimentary sequence (Parker and Sills, 1990; Weaver

and Schultheiss, 1983), (3) highly permeable sediments as sands will drain completely and (4) contents of gas or gas hydrates in the sediment may not be recovered due to the pressure release while recovering, unless an autoclave corer is used.

To overcome these disadvantages, devices have been developed with which *in situ* determination of geotechnical sea floor parameters is possible. The *in situ* measurement is generally done by using penetrating devices with a static (Lunne et al., 1997) or dynamic penetration behavior (Beard, 1981; Chari et al., 1981; Ingram, 1982; Akal and Stoll, 1995; Villinger et al., 1999; Spooner et al., 2004; Osler et al., 2006a; Stegmann et al., 2006b; Fabian et al., 2008; Stark and Wever, 2009). Other approaches, like *in situ* Vane Shear Tests exist (Richards et al., 1972), but are rarely applied.

Dynamic penetrometers are used to measure a range of parameters like water pressure, temperature, pore pressure, deceleration, inclination, turbidity, side friction and cone resistance. The parameters relevant to the determination of sediment strength are, on one hand, the conventional CPT parameters (side friction, cone resistance, pore pressure) or, on the other hand, the deceleration of a probe during a penetration process into the seafloor (Stoll et al., 2007).

The *in situ* determination of sediment strength by deceleration measurements yields, in contrast to *ex situ* measurements on samples or split cores or *in situ* tests with static penetrometers, non standardized and instrument specific results (Mulukutla et al., 2011). Up to now, empirical relationships are used to convert deceleration to target parameters like bearing capacity or shear strength (Stark et al., 2009b). These conversions are only possible on the basis of assumptions and by using empirically determined scale factors (Dayal and Allen, 1975; Beard, 1981; Stoll et al., 2007).

Nevertheless, qualitative estimates of sediment properties can directly be deduced from the deceleration depth behavior (Stoll and Akal, 1999; Stark and Wever, 2009). This can be used to complement established measurements on cores or to supplement *in situ* geotechnical measurements as conventional sea floor CPT surveys and also help to interpret geophysical measurements like seismic or sediment echo sounding surveys.

The Lance Insertion Retardation Meter (LIRmeter, see Fig. 3.1) was developed to infer sediment strength information from deceleration measurements by dynamic penetration of the upper four meters of the sediment. It started out as a fairly simple system (Fabian et al., 2008) and continued to evolve to a technically mature and reliable measurement system for routine sea floor measurements. The system consists of a lance with a length of four meters, a weight stand and a pressure housing for the electronics. The system was developed in cooperation with Fielax Gesellschaft für wissenschaftliche

Datenverarbeitung mbH (Bremerhaven, Germany <http://www.fielax.com>) and is primarily intended to provide supplementary sediment strength data for the planning process of submarine cable routes (cf. also de Lange, 2011).

In this paper, we present the construction of the mechanical system and the design of the electronics, as well as first measurements in the German Bight (North Sea) as a performance evaluation of the developed system.

3.2 Design

3.2.1 Design strategy

The spectrum of possible applications for the LIRmeter ranges from near shore shallow water surveys (e.g., mapping of sea floor sediments for shallow foundations) (Seifert et al., 2008; Raie and Tassoulas, 2009; Stark et al., 2011) to deep sea applications (e.g., properties of pelagic sediments for scientific investigations or deep sea mining operations) (Stegmann and Kopf, 2007). Therefore, the design of the measurement system should allow operations in various depth regimes. A vital requirement of the industry on the specifications and usability of the system was that it can be deployed and maintained by non specialist operators on ships of opportunity, where penetrometer measurements are not routinely executed. Thus, the design of the mechanics and the electronics has to be as simple as possible, robust and shock resistant and has to withstand also high peak accelerations when the instrument hits hard ground (Stoll and Akal, 1999). If the system is deployed in deep water, pressure housings for the electronics and special types of sensors are required due to high ambient pressure. The system is designed to work autonomously i.e. it can be operated in a pogo like fashion (Hyndman et al., 1979) with mission lengths of up to 12 hours. In that way, profiles of several kilometers can be surveyed in less than a day. In conclusion, the main factors crucial for the successful design of the instrument were:

- robustness,
- simplicity in operation and maintenance,
- variable depth rating, and
- autonomous operation.

Contrary to static-velocity Cone Penetration Tests (CPT) (Lunne et al., 1997) we do not measure pore pressure. Two main reasons were responsible for this decision: (1) Cohesive sediments tend to clog the ports of pore

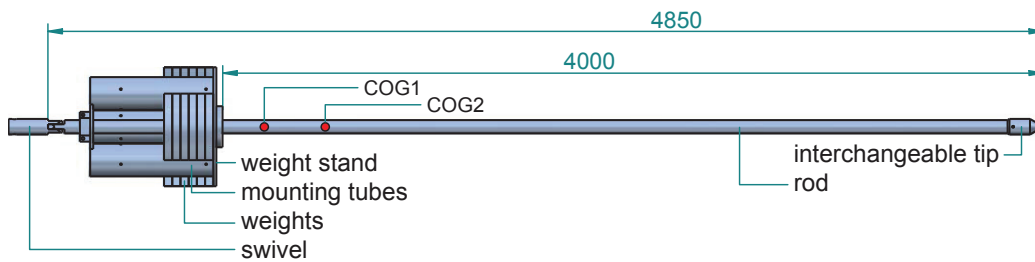


Figure 3.1 – Technical drawing of the LIRmeter lance. All lengths are in mm. Main features are annotated within the figure. The center of gravity (COG) depends on the amount of weights and lies between 3.5 m (COG2) and 3.8 m (COG1) measured from the tip.

pressure sensors, which would preclude the pogo style operation and (2) a complicated installation of hydraulic tubing would be necessary to connect pressure ports at different locations with differential pressure sensors. The incorporated sensors are chosen based on these design constraints. Studies on the direct measurement of sediment properties by observing a penetration processes using acceleration sensors instead of pore pressure transducers or conventional CPT sensors are common (Dayal and Allen, 1973; Chari et al., 1981; Akal and Stoll, 1995; Villinger et al., 1999; Osler et al., 2006a; Stoll et al., 2007; Stark and Wever, 2009) and yield qualitative estimations or quantitative relationships based on empirical assumptions.

Mechanical design

The LIRmeter was designed to be very robust with rigid connections and few moving parts as vibrations can cause oscillations of structural components and hence generate noise in the acceleration measurement during penetration. Therefore, a two component design was chosen consisting of the lance (solid rod) and the weight stand Fig. 3.1.

The coring wire is either attached directly to the rod or by using a swivel, which is the recommended way of operation. The rod has a diameter of 65 mm and a length of 4 m (bottom to mounting plate) with interchangeable tips of various shapes and diameters resulting in different cross sectional areas (see Table 3.1). The length of the fully assembled LIRmeter is such, that it fits easily in a 20' container for shipping. The diameter of the tips is by design always larger than the diameter of the rod (65 mm) to reduce the friction during penetration. This design resembles a full flow penetrometer layout (Chung and Randolph, 2004). The rod as well as the tips are made out

of stainless steel, which reduces the risk of corrosion and therefore ensures a consistent penetration behavior.

The weight stand can house three pressure cases and an adjustable load of max. 245 kg of additional weights. The weights are placed between the mounting tubes for the pressure cases (see Fig. 3.1) and mounted with solid bolts, which allows an exact trimming of the lance. The weight stand and the additional weights consist of zinc coated steel. This material was chosen to minimize corrosion and to reduce the costs of material and manufacturing. Technical specifications of the lance are shown in Table 3.1.

Table 3.1 – Mechanical parameters of the LIRmeter. Values in parentheses are for a configuration with all additional weights.

Property	Unit	Value
length over all	m	4.850
diameter weight stand	m	0.580
length of rod	m	4.000
tip geometry	deg	60
cross sectional area of tip	cm ²	45 / 60
net weight	kg	285
max. weights (18 pieces)	kg	245
volume	m ³	0.037 (0.070)
mounting tubes		3
length of mounting tubes	m	0.6
COG from tip	m	3.5 (3.8)

The housing for the electronics has been designed to withstand pressures of at least 50 MPa (\sim 5000 m water depth) with a safety factor of 2. The pressure tube contains the electronics, the sensors, the batteries and connections for communication and battery charging. The case is installed into the mounting tubes of the weight stand with sleeves which are made of Polyoxymethylene (POM). The POM sleeves secure the pressure case in an upright position and are tightened to the mounting tubes with set screws. The use of thermoplastic sleeves provides an electrochemical separation of the stainless steel housing from the zinc coated mounting tubes which minimizes corrosion.

The internal setup of the electronics (see Fig. 3.2) is aligned vertically beginning with the sensors, which are mounted to the bottom end lid of the tube (layer 1: L_1). The next layer (L_2) hosts the data logger and the mass storage device. The batteries and the signal conditioning circuit (L_3 , L_4) are

mounted on top of this layer. The pressure sensor and the connectors are mounted in the top end lid of the pressure housing. The layers, consisting of POM discs, are connected to each other with through mounted hexagonal spacers. This design allows to make very good use of the available volume in the pressure case and has been proven to be rigid and robust.

The center of gravity (COG) of the whole system (lance and installed electronics) lies at approximately 3.8 m of the full length of 4 m measured from bottom to top, which is right before the weight stand (see Fig. 3.1). Additional weights will shift the COG towards the weight stand. Despite the unfavorable COG, observations during the lowering of the device show a stable lowering behavior with only slight rolling.

3.2.2 Sensors

The sensors incorporated in the electronics housing of the instrument are (a) three accelerometers with different measurement ranges (b) one sensor for ambient pressure and (c) two auxiliary sensors like a temperature sensor and gyroscopes. Our description focuses on the sensors relevant to the deceleration measurement, specifically the accelerometers. Accelerometers are used in a wide variety of applications and environments, where high peak accelerations occur and precise measurements are necessary (e.g., the automotive industry as described by Gogoi and Mladenovic (2002)). These sensors are now available as micro electro mechanical systems (MEMS) (Ghodssi and Lin, 2011), which makes them ideal for the incorporation in underwater instruments (see Section 3.2.2 for details). Within the LIRmeter, the accelerometers are located in the pressure tube next to the data acquisition (DAQ) and fixed to the pressure case which, in turn, is rigidly mounted in the weight stand of the lance. The accelerometers are the main sensors, delivering time series of the momentary acceleration (or deceleration) the probe is subjected to, especially during penetration into the sea floor. Gyroscopes are used to monitor the rotation of the instrument in the water column before penetration. Furthermore, a pressure sensor determines the water depth as an auxiliary parameter while temperature is measured to assess the temperature dependency of the accelerometers and gyroscopes.

Accelerometers

For sensing the acceleration, we use analog sensors of the “iMEMS low g” accelerometer product line of AnalogDevices, Inc. (see Table 3.2 for models used). The design of the MEMS sensors is similar to conventional capacitive accelerometers, however, the mechanics is produced on a single piece of sil-

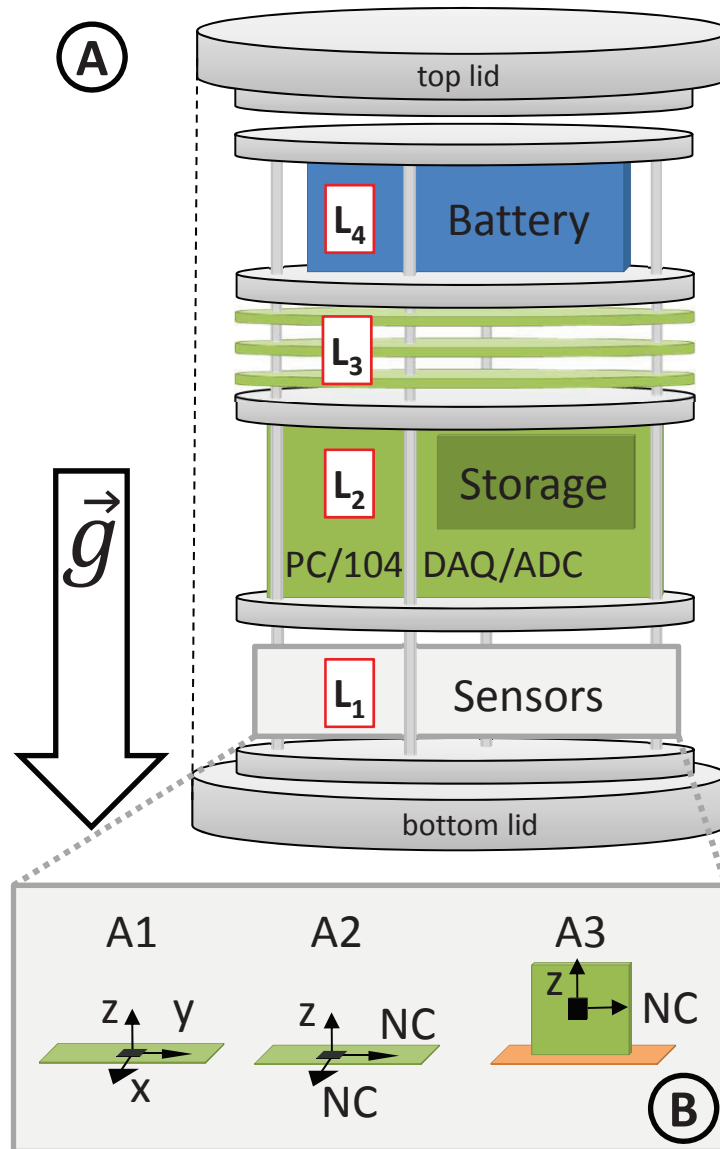


Figure 3.2 – A: Conceptual sketch of the electronics inside the pressure housing. L₁: Sensors, L₂: DAQ circuitry and data storage, L₃: Anti Alias filtering and power supply, L₄: LiPo battery. B: Closeup of the sensor setup in L₁ showing the alignment of the accelerometers and axis directions. The labeled axes are sampled by the DAQ, NC means “not connected”, and therefore not sampled.

icon (Ghodssi and Lin, 2011) with a size of the sensor package of less than 25 mm². Typically, the sensors are delivered in a SMD (surface mounted device) package. Due to the fact that the sensors are capacitive type accelerometers, they sense dynamic acceleration on top of static gravity (Beliveau et al., 1999). Details of the sensor specifications can be found in Table 3.2. All accelerometers used have a resonant frequency of 5500 Hz (Analog Devices, 2010a,b,c).

The vertical axes of the acceleration sensors are mounted parallel to the axis of the lance and their positive z-orientation is opposite to the penetration direction. This allows a higher measurement range in deceleration due to a partly compensation of the sensor DC Offset. For a sketch of the sensor setup and the recorded axes see Fig. 3.2B. The sensor A3 is a two axis sensor with one of the two axes orientated in the vertical direction, whereas A1 and A2 are three axis devices, measuring vertical acceleration (A1, A2) and horizontal acceleration (A1). The sensors (A1, A2, A3) have different full scale ranges to cover high peak decelerations ($a_{\text{dec}} > 30 \text{ m/s}^2$), as well as small decelerations caused by soft sediments ($a_{\text{dec}} < 10 \text{ m/s}^2$).

Assuming a typical impact velocity of 2 m/s, a steady deceleration and a sampling rate of 500 Hz, the device can resolve depth via double integration of the acceleration with a resolution of 0.004 m and better. The depth resolution of the probe is primarily dependent on the momentary penetration velocity and the sampling rate. The higher the deceleration at the beginning of a penetration event, and thus a reduction of velocity, the more measurements will be taken in a following depth interval. For an overview of sensor specifications and sensor resolution see Table 3.2.

Pressure transducer

Ambient pressure is sensed by an analog pressure sensor (series 21-G, Keller Druckmesstechnik AG, Switzerland) with a measurement range depending on the maximum water depth in the survey area. In shallow water, a sensor with a range from 0 ... 10×10^5 Pa (0 ... 100 m) is typically selected. The error in linearity of the sensor readings is typically 0.25 % of the full scale range, which is adequate for depth estimates in shallow water. A deployment of the instrument in deeper water depths requires a high precision pressure sensor with a larger range and better precision over the full pressure range. The pressure sensor is mounted to the top end lid of the pressure case which makes a replacement of the sensor very easy.

Table 3.2 – Technical specifications of the accelerometers used in the LIR-meter. Resolution is calculated for a voltage conversion with an accuracy of 16 bits ± 3 LSB (DiamondSystems, 2011). The conversion from units of gravity (g) to m/s^2 is done by using $1 g_n = 9.80665 \text{ m/s}^2$ as conversion factor (BIPM, 2006).

Property	Value		
	A1	A2	A3
Sensor			
Sensor Name	ADXL335	ADXL325	ADXL203
Sampled Axes	z, (x, y)	z	z
Range m/s^2	43.3	49	16.7
Sensitivity $\text{V}/(\text{m/s}^2)$	0.034	0.018	0.102
Resolution m/s^2	0.001134	0.00215	0.000374
Noise Density $\mu\text{g}/\text{s}\sqrt{\text{Hz}}$	300	250	130
Bandwidth Hz	550 (1600)	550	2500
Supply Current A	0.0035	0.0035	0.007
Power Consumption mW	11	11	21

3.2.3 Data acquisition

The data acquisition system needs to fulfill several demands arising from (a) high resolution and high speed data acquisition (b) handling and operation (easy to set up and operate) and (c) size and power consumption. A market survey of currently available data loggers fulfilling these demands resulted in the choice of a low-power PC/104 microcomputer with integrated data acquisition (DAQ by DiamondSystems).

Data logger

The selected logger provides a fully functional x86, low power, 32-bit computer system with an on-board high speed analog to digital converter (ADC). The system is produced in the PC/104 form factor with very compact dimensions (90 by 96 mm) well suited for the installation inside of a pressure housing. The CPU of the microcomputer is a low power Vortex86 processor. The system provides 256 MB RAM and interfaces like Ethernet, IDE, RS232, VGA, PS/2 and digital I/Os. The total power consumption of the microcomputer with integrated DAQ is on average 5 W.

The advantage of this system lies in the combination of microcomputer based logging and analog to digital conversion combined in an all-in-one system. Programming libraries and drivers for the analog to digital converter (ADC) are provided by the manufacturer for various operating systems. Debian GNU/Linux was chosen as operating system with a modified kernel (ver. 2.6.23) to support the hardware of the microcomputer. Using a standard distribution of a Linux OS offers a wide range of public domain software providing interfaces like web-, ftp-, ssh-servers to control the system. The development of DAQ specific software is facilitated by the possibility to use non specialized tool chains like the commonly available GNU tool chain with its C Compiler gcc.

The on-board ADC features a 16 channel, 16 bit analog to digital conversion circuit and can operate at a combined sampling rate of up to 250 kHz. High sampling rates are achieved with a field programmable gate array (FPGA) controller on the hardware side for buffering and storage of samples. The FPGA is read out in the kernel space on the software side of the DAQ process (see Fig. 3.3 for a schematic). Data is gathered by interrupt routines and stored on a 4 GB CompactFlash (CF) card. The OS and application software is stored on a solid state flash drive (2 GB), which is, as well as the CF-card, connected to the IDE interface of the PC/104.

In the current configuration, the sampling rate is typically set to 500 Hz per channel, whereas the bandwidth of the acceleration signal is limited to 100

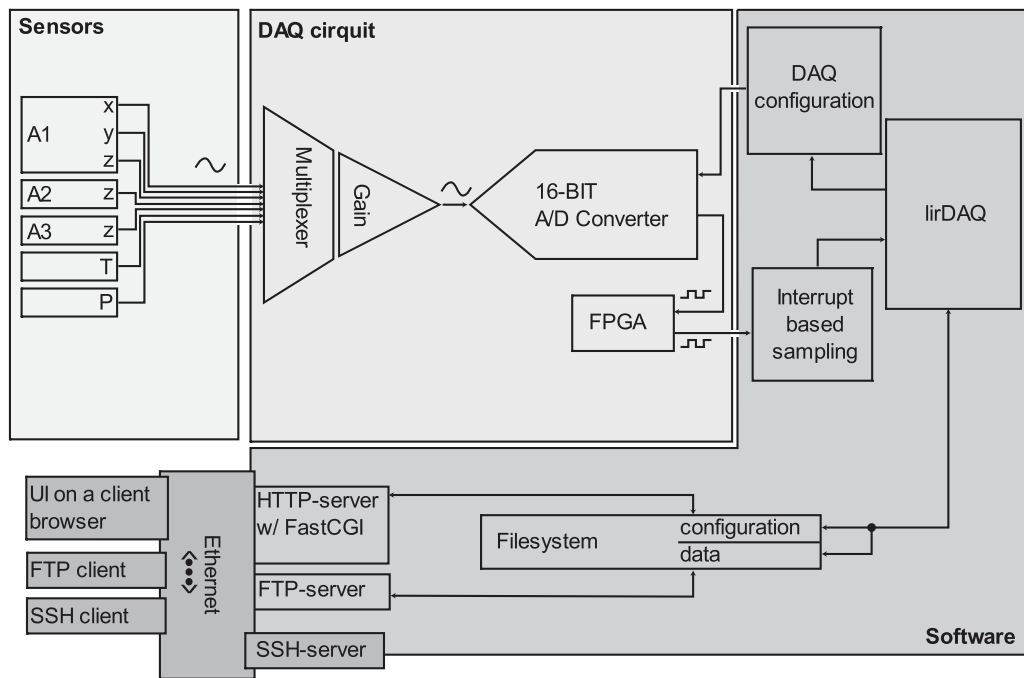


Figure 3.3 – Schematic of the data acquisition setup both on the hardware- and software side. Data is delivered by the sensors, digitalized by the A/D circuitry, acquired with the lirDAQ routine, stored in the file system, and provided to the user via various interfaces.

Hz prior to digitalization with an analog low-pass filter. The digitalization with a resolution of 16 bit and nonlinearity of 3 LSB (DiamondSystems, 2011) yields an accuracy of $38 \mu\text{V}$ at a measurement range of $0 \dots 2.5 \text{ V}$. The system can operate at different input ranges ($1.25 \dots 10 \text{ V}$) in an either unipolar (16 inputs) or bipolar setting (8 inputs). The current setup uses a unipolar input with a range of 2.5 V , which meets the output characteristics of the chosen sensors and anti-aliasing filters.

Signal conditioning

The analog sensor data is filtered before digitalization to prevent aliasing effects. The employed filters are switched capacitor 8th order low pass Butterworth filters (MAX7480), (Maxim Integrated Products, 1999). The Butterworth filters are characterized by a damping of 3 dB at the corner frequency f_c and a steep increase in damping at higher frequencies (damping at $3 f_c = 76 \text{ dB}$). Their f_c can be adjusted by application of a certain clock frequency or by using their internal clock. The corner frequency can be set to a value ranging from 1 Hz to 2 kHz and is currently preset to 100 Hz . Anti-alias filtering is done for all channels of the ADC.

DAQ process

The DAQ is controlled by a user interface (UI) which allows the user to:

- schedule DAQ tasks,
- check the status of running, scheduled or completed DAQ processes,
- download data, and
- maintain the system.

The UI is accessible via a web server running on the microcomputer. The operational status of the system can be monitored externally with a LED, which is embedded in the on/off connector of the device. The DAQ is controlled by an in house developed C routine (lirDAQ) which incorporates interrupt based sampling and auto calibration functions of the conversion circuits. These high level routines are provided by the manufacturer of the ADC. The DAQ is controlled by simple ASCII files which are passed as arguments. They are auto generated by the UI or generated by the user. See Fig. 3.4 for a flowchart of the main elements in the lirDAQ routine. Converted data is fed to the FPGA hardware buffer and then transferred to a ring buffer using an interrupt function. The size of the ring buffer

depends on the sampling rate and the number of sampled channels. It is big enough to gather the incoming data during time intensive steps like writing operations on the CF-drive. The lirDAQ routine operates in an one second cycle to check the ring buffer for new data, distribute the sampled data to stacks for each channel and eventually write out files if a size threshold is reached. The binary files are labeled with a hexadecimal timestamp of the Unix time of the first sample in the file as filename. The suffix represents the channel where the data came from. Data is stored in the IEEE little endian format as 16 bit signed integer values, starting with the first value of the data chunk and ending with the last one. Header information is provided in the configuration file which is passed to the routine.

3.3 Calibration, data processing and laboratory tests

The measurement system was calibrated statically to determine the misalignment of the sensors and the sensor specific sensitivity by conducting inclination measurements. A standard scheme is presented for the processing of acceleration data and is applied to a laboratory experiment to demonstrate the performance of the measurement system under controlled conditions.

3.3.1 Sensor calibration and sensitivity

An empirical calibration of the complete data acquisition circuitry was conducted to evaluate both the misalignment and sensitivity of the vertical axes of the accelerometers incorporated in the LIRmeter. An Applied Geomechanics 756 (Applied Geomechanics, 2000) sensor with a resolution of $1 \mu\text{rad}$ was used as reference sensor. The accelerometers were mounted in a slanted fashion on precisely manufactured brackets with angles between $0 \leq \varphi \leq 90^\circ$ in 10° steps, whereas the inclination sensor had to be mounted horizontally leveled due to the limited measurement range ($\pm 10^\circ$) of the sensor (see Fig. 3.5 for the calibration setup). The inclination sensor was used to precisely level the bracket.

The measured acceleration (or sensor output voltage) of the vertical z-axis can be converted to an inclination angle using the following equation

$$\alpha = \arccos\left(\frac{U}{U_{1g}}\right) \quad (3.1)$$

with α as measured inclination angle, U as measured voltage and U_{1g} as voltage, when exactly horizontal. The deviation of measured angles α from

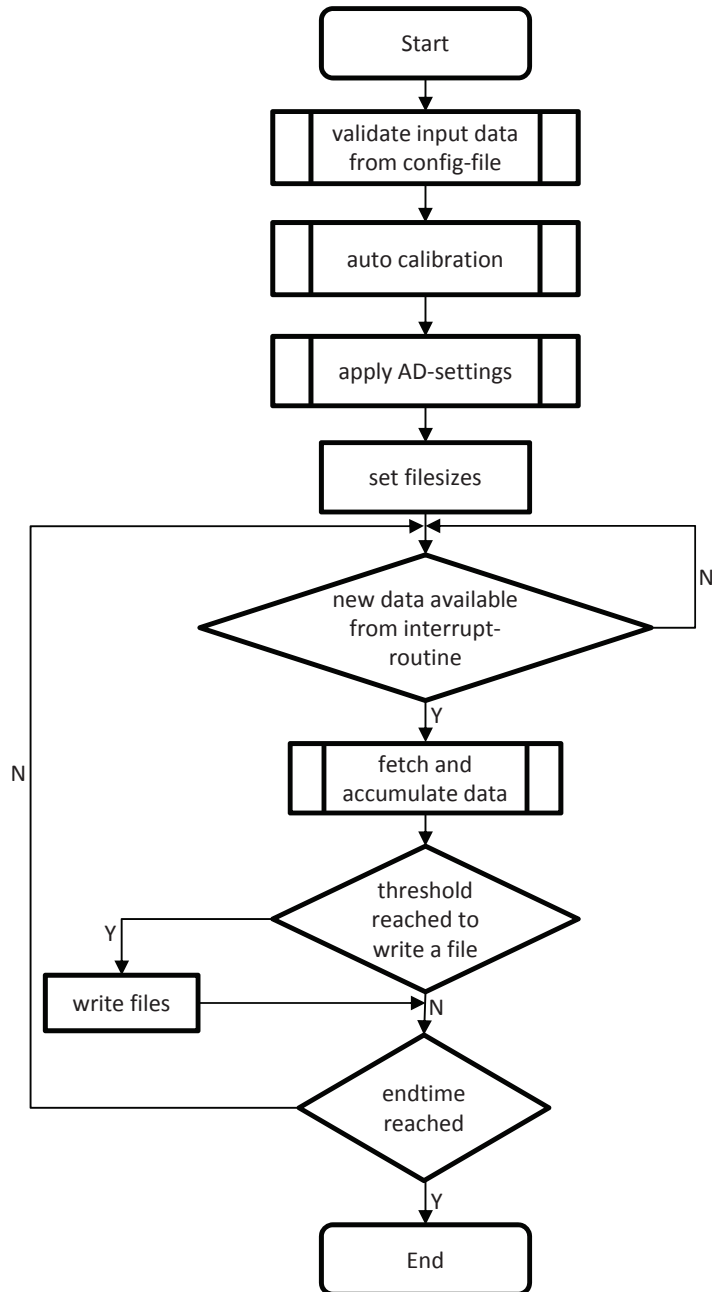


Figure 3.4 – Simplified flowchart of the data acquisition routine (lirDAQ) showing the main procedural components.

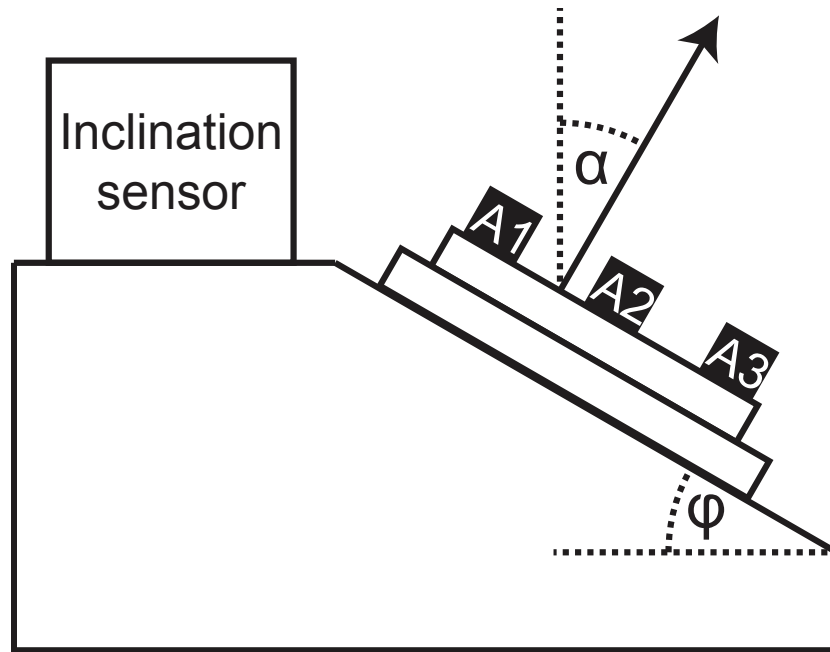


Figure 3.5 – Scheme of the calibration setup with acceleration sensors A1, A2, A3 and Applied Geomechanics Tilt sensor (yellow cylindrical sensor). The acceleration sensors are mounted on the bottom lid of the pressure tube, which resides on a precisely manufactured POM holder (white ring). The holder is mounted on a calibration bracket with an inclined and a horizontal plane. The inclination angle ranges from 0° to 90° on different brackets. The precision of the leveling of the horizontal plane is given by the tilt sensor. α : inclination of the measurement axis of the accelerometer, φ : angle of the inclined plane.

the reference and true angles φ is shown in Fig. 3.6, where a series of 100 measurements for each inclination step is presented in the box plot. The results show an offset between the two sensor orientations: measurement axis in direction of gravity (left column) and in opposite direction to gravity (right column). The offset between the two orientations is produced by (a) a misaligned mounting of the sensor and (b) an inherent misalignment of the vertical measurement axes. The inclination during field measurements is certainly in the range between 0° and 20° . Penetrations with higher inclinations would most likely mean that the lance does not penetrate completely and the measurement would not be usable. Hence, correction factors will be calculated based on the calibration values between 0° and 20° .

The sensor sensitivity of accelerometers can be expressed as sensor output voltage U per fraction of gravitational acceleration g (V/g) as a function of inclination angle. The result of the sensitivity calibration is shown for sensor A1 in Fig. 3.7.

An average sensitivity can be calculated for each sensor. This sensor sensitivity can be used to convert the sensor output voltage to engineering units (m/s^2). The sensitivities for the z-axes of sensor A1 to A3 are shown in Table 3.3. The determined sensitivities for sensor A1 and A2 lie in the range given by the manufacturer. The sensitivity for sensor A3 differs from the datasheet value, because the output voltage of sensor A3 is reduced (from $0 \dots 5$ V to $\sim 0 \dots 2.5$ V) using a voltage divider to meet the input characteristics of the ADC.

Table 3.3 – Sensitivity of acceleration sensors A1 to A3 as a result from calibration measurements compared to datasheet values.

Sensor	Sensitivity V/g	Sensitivity (Datasheet) V/g
A1	0.312	0.300 ± 0.03
A2	0.182	0.174 ± 0.018
A3	0.542	1.000 ± 0.04

3.3.2 Processing of deceleration data

Acceleration-time series can be integrated once to obtain velocity vs. time and twice to obtain distance vs time and can hence be expressed as a function of distance (see Eqs. 3.2, 3.3). In the application of the LIRmeter, deceleration (which is negative acceleration) will be expressed as a function

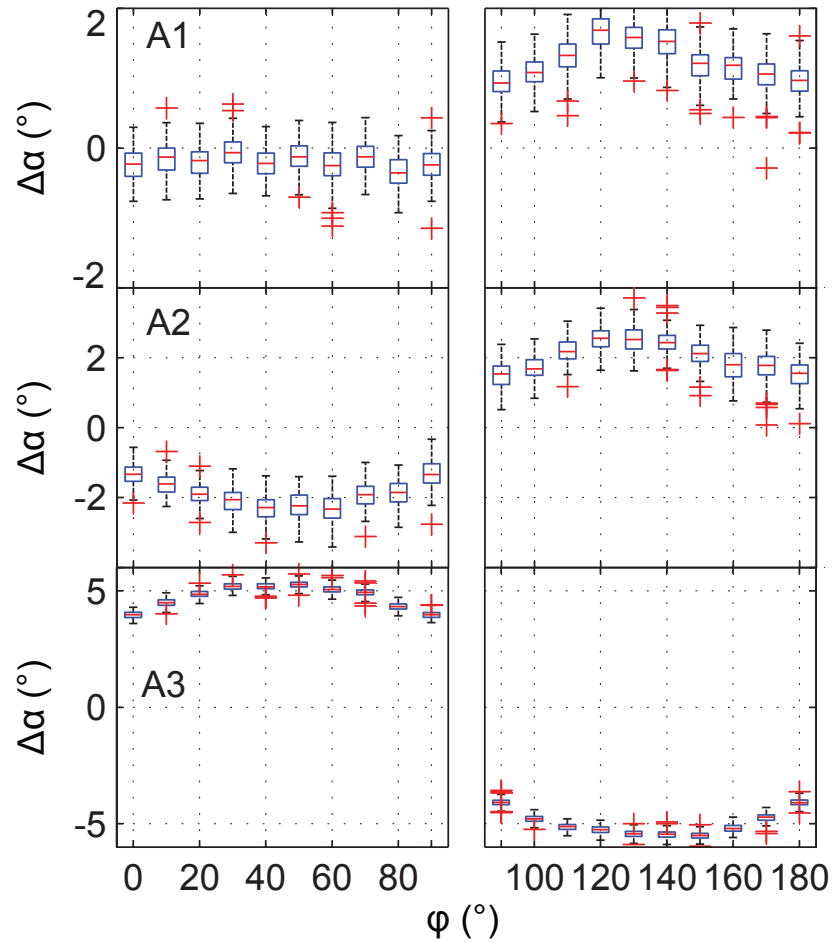


Figure 3.6 – Result of the inclination calibration of sensors A1, A2 and A3 showing the deviation from the adjusted angle. The angle 90° appears two times, because of two orientation possibilities of the sensor in the horizontal setup. The axis misalignment can also be seen in the offset between these two values.

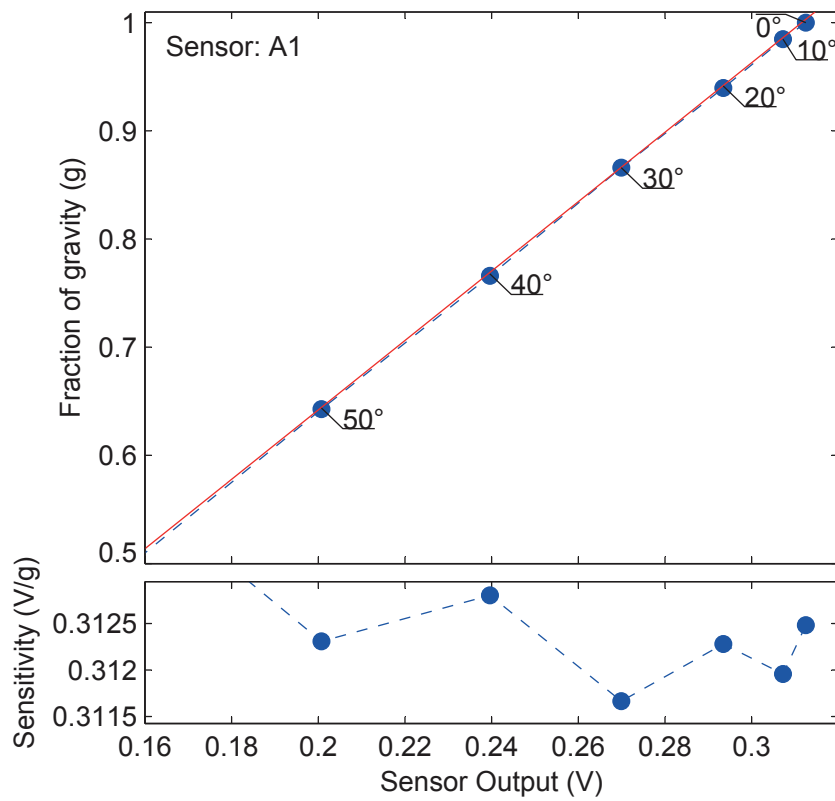


Figure 3.7 – Sensor calibration and sensitivity for sensor A1. $1 g_n = 9.80665$ m/s^2 . Inclination angles are annotated within the figure, the static (DC) offset of the sensor has been removed from the data.

of sediment depth. Hence revealing zones of high or low deceleration, a proxy for stiff or soft sediments.

$$v(t) = \int_0^t a(t)dt = at + v_0 \quad (3.2)$$

$$d(t) = \int_0^t v(t)dt = \frac{a}{2}t^2 + v_0t + d_0 \quad (3.3)$$

The integration is always performed backwards, starting in a phase (stall phase) of constant acceleration and no movement ($a = const, v_0 = 0$). This is the case, once the lance has reached its full penetration depth and came to rest in the sediment. The integration of the acceleration in this phase should result in zero velocity, because the lance has reached its final position in the sediment. The backward integration of the acceleration-time series is performed numerically using the trapezoidal rule for each time step. However, if a wrong starting value was selected for the integration due to noise in the measured data, integration leads to linear (or quadratic) errors in the first (or second) step. Therefore, a randomly chosen subset of values in the stall phase is chosen and averaged. The data from the stall phase is integrated after this average has been subtracted. This procedure is repeated several (100) times. The average, whose removal produced the integration result yielding the smallest linear trend in velocity, is chosen as acceleration offset, which is subtracted prior to the whole integration process. This procedure is in essence a very simple implementation of a Monte Carlo Integration (Caflish, 1998). The processing scheme is applied to both field data (Section 3.4) and experimental data (Section 3.3.3).

3.3.3 Elevator ride experiment

Accelerations in cabled elevators in buildings are assumed to lie in the range of less than 10 m/s^2 . Therefore we should be able to record the accelerations during an elevator ride. The accelerometer should measure two acceleration and two deceleration phases during a round trip between two levels. Double integration of the acceleration-time series yields travelled distance during the elevator ride which should amount to twice the distance between floors (see Fig. 3.8). Differences between the starting and ending distance reveal inaccuracies in the double integration algorithm and/or problems of the data acquisition. The different stages of the elevator ride as shown in Fig. 3.8 are delimited by vertical lines in the time series in Fig. 3.9, which shows a typical example of the recorded acceleration during an elevator ride from the 4th to

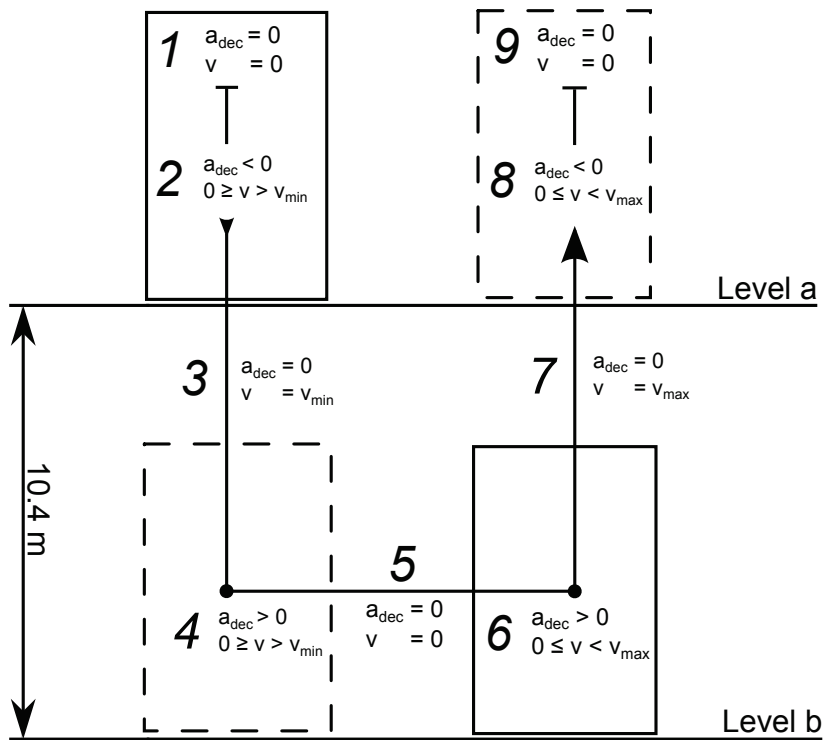


Figure 3.8 – Sketch of the deceleration phases during the elevator roundtrip. For time series see Fig.3.9.

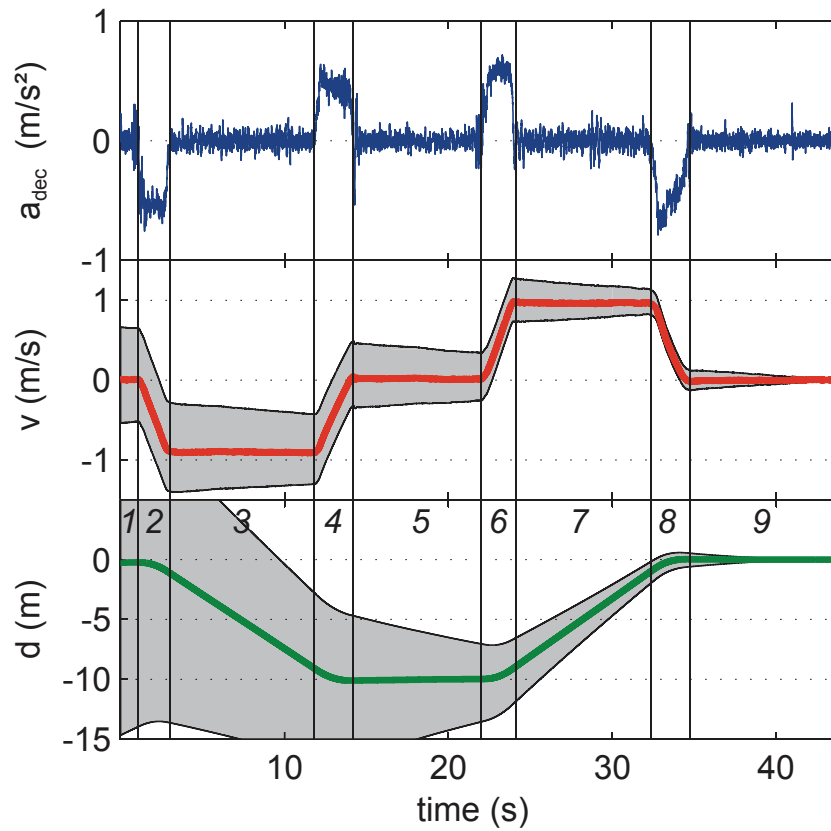


Figure 3.9 – Recorded acceleration time series (blue) and calculated travelling velocity (red) and distance (green). Shaded area marks the boundaries of possible integration results with varying starting offsets (see Section 3.3.2). Vertical lines denote the phases of elevator movement (see Fig. 3.8).

1st and back to 4th level in the Geoscience Faculty building at the University of Bremen. The distance between the two levels (1st and 4th floor) is 10.4 m.

Fig. 3.9 shows the recorded accelerations during an elevator ride with peak values up to 1 m/s². Integration starts at a known stage (i. e. phase 9: final stop, where no dynamic acceleration occurs and velocity is 0 m/s) and is executed backwards twice to obtain velocity and distance (see previous Section). Fig. 3.9 shows the upper and lower boundaries double integration result for 100 starting values which were calculated by randomly chosen values within the phase 9. The red and green lines show the integration result with the optimal offset determined from the random integration. The results of the elevator ride are presented in Table 3.4 and show a very good consistency between start- and end value. The calculated travelled distance is 10.1 m, 0.3 m less than the value of 10.4 m from building plans.

Table 3.4 – Values of velocity and distance from starting point at three distinct phases during the experiment as evaluation of the data processing scheme, using an elevator ride as an approximation to the conditions of field experiments.

Integration step	Start (Phase 9)	Intermediate (Phase 5)	End (Phase 1)
Velocity (m/s)	0	0	-0.001
Distance form start (m)	0	-10.1	-0.014

3.3.4 Implications for field measurements

The calibration of the acceleration sensors yielded values for the sensor specific sensitivity, which is needed to convert sensor data to engineering units. The axis misalignment could be determined and will be used to correct measured values. The elevator ride demonstrates the very good performance of the measurement system and the processing scheme. The test results show a very good stability of the backwards integration routine with very low offsets in velocity and distance after the integration. The accelerations during an elevator ride are assumed to reproduce the acceleration (or deceleration) behavior of a lance penetrating extremely soft sediments ($a_{\text{dec}} < 1 \text{ m/s}^2$). Hence, the very good performance of the measurement system could be evaluated at a low signal to noise level promising even better results under field conditions.

3.4 Results from field measurements

Layering and bearing capacity are the main factors controlling the deceleration behavior of a lance penetrating marine sediments. The layer thickness can range from a fraction of centimeters to several meters depending on sedimentation rate and alternation frequency of sedimentary properties. Additionally, the bearing capacity can vary from very low values (e.g., highly water saturated clays) to high values (compact fine sand or bedrock). Hence, penetration behavior can be classified into two main scenarios (see also Fig. 3.10):

- Single layer penetration: the lance is decelerated within a single layer, which is very thick or very hard.
- Multiple layer penetration: the lance is not completely decelerated within the first layer and is capable to penetrate a second, or even further layers.

Here, we show typical examples for the two important cases. The data were recorded in the German Bight (North Sea) in December 2010 during a campaign in cooperation with the German Navy research institute “Forschungsanstalt für Wasserschall und Geophysik” on the naval research vessel “WFES PLANET”. The investigation area is located near the island Helgoland. See Fig. 3.11 for a map with penetration- and sample locations as well as a classification of surficial sediments.

The sediment is classified by the content of silt and mud (which is the fraction $\leq 63 \mu\text{m}$) in the coarser matrix (fraction $> 63 \mu\text{m}$), for details, see Figge (1981). Measurements were carried out along a profile (see Fig. 3.11B) starting with fine sands containing different amounts of silt and mud ranging from 5 to more than 50 %. The transect ends at locations with medium sand to predominantly gravelly sediments. The processed data of selected penetrations are shown in Fig. 3.12. The double backwards integration (Section 3.3.2) of the recorded acceleration data was done in the same way as in the performance evaluation (Section 3.3.3). Each location shows multiple penetration events marked by different colors. Each penetration of these repetition measurements has a different starting velocity due to the dynamic character of the measurement, which has to be taken into account when absolute values for deceleration are compared.

The location STAT1 lies in an area of fine sand with an amount of 20 to 50 % mud and silt and is located close to an area with even higher amounts of a fine grained fraction. A penetration depth of 3.5 to 4 m has been reached in all three repetition measurements. During penetration, the

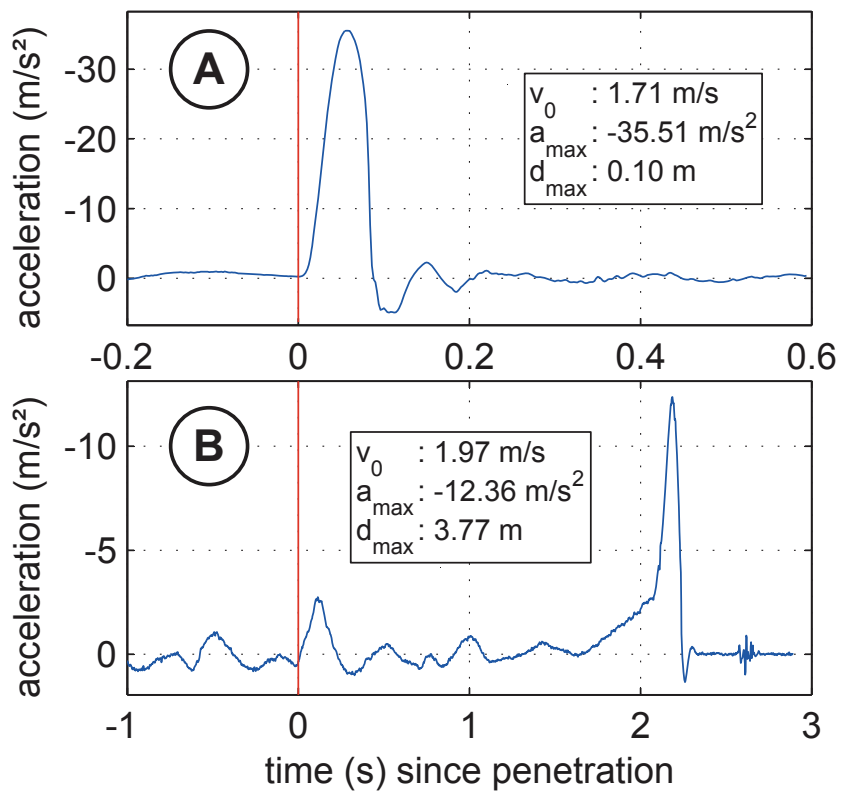


Figure 3.10 – Acceleration-time series for A: Single layer penetration type, and B: Multi layer penetration type. The penetration duration of type A is significantly shorter than type B. Both penetration events show a damped oscillation effect prior to final arrest (Stoll and Akal, 1999).

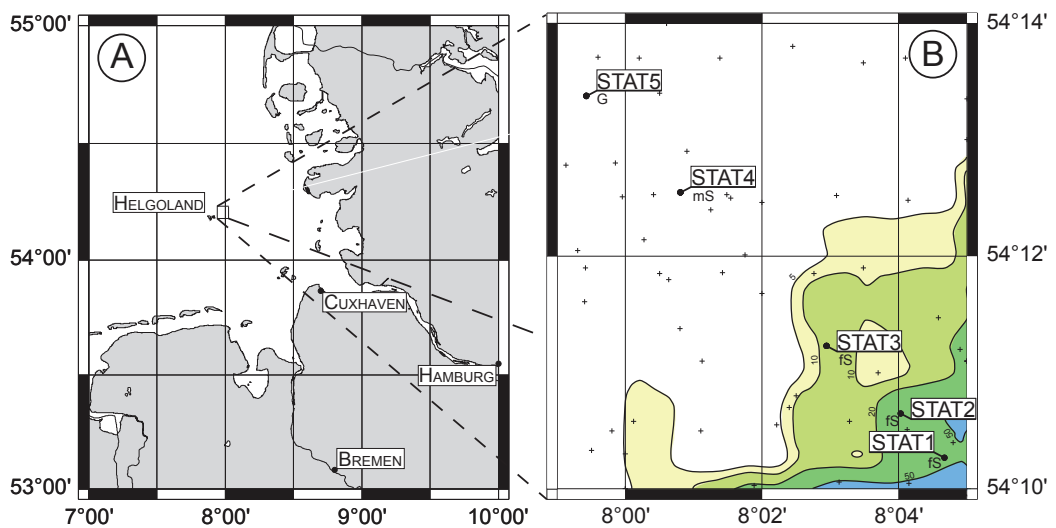


Figure 3.11 – A: location of the investigation area, where field tests were carried out. B: test location and location of the measurements. Color coding indicates the amount of fine grains ($< 63 \mu\text{m}$) in the matrix of coarser grains ($> 63 \mu\text{m}$), after Figge (1981). Supplemental data is kindly provided by the database “Geopotenzial Deutsche Nordsee”. The contours are calculated from grain size analyses at the locations indicated by the small crosses.

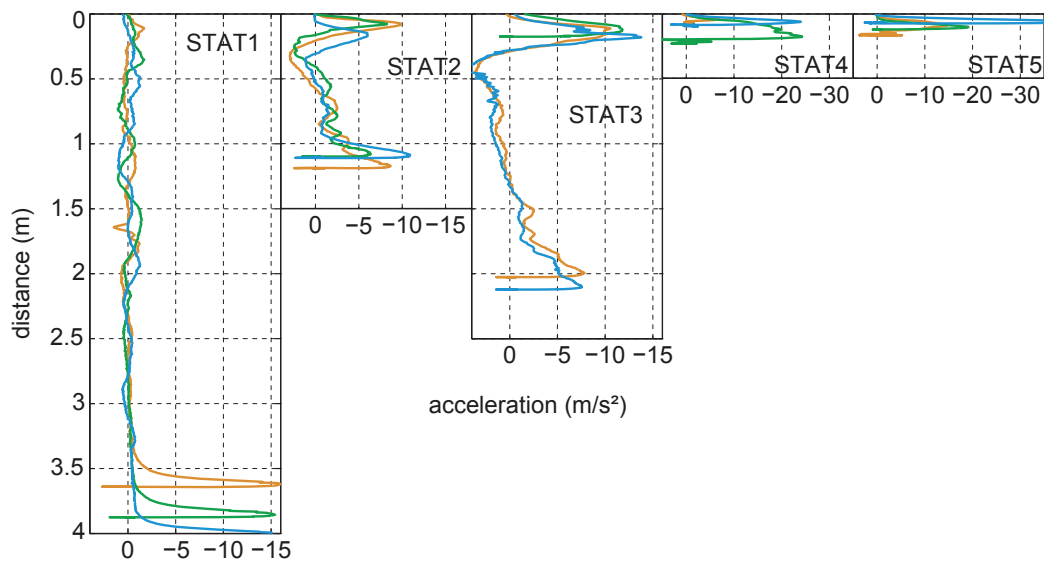


Figure 3.12 – The depth scale was deduced from the recorded acceleration data. The acceleration data has been corrected for static offsets like gravity and sensor offsets. Colored lines show repetition measurements at each location. Note the inverted x-axis with negative values of acceleration (deceleration) plotting to the right and acceleration events plotting to the left.

maximum deceleration does not exceed 2 m/s^2 . These light deceleration events reproduce at similar depth between the repetition measurements. After some of the slight deceleration events, an acceleration of the probe is observed, which is assumed as a sagging like motion due to the weight and momentum of the probe. The last peak (15 m/s^2) results from a high rate in velocity decrease due to increased friction between sediment and rod and the approach of the weight stand to the sediment surface.

The station STAT2 is in the same region as STAT1, but is close to an area with fine sand and a fine fraction (mud, silt) ranging from 11–20 %. The total penetration depth lies about 1 m and is reproduced by the repetition measurements. This location indicates a stronger surficial layer yielding peak decelerations between 10 and 15 m/s^2 between 0 and 0.25 m depth. After this layer, the deceleration increases steadily again to 10 m/s^2 until the final arrest of the probe at a penetration depth of 1 m. The two layer penetration behavior is observable at all three repetition measurements and can be correlated at similar depths.

The penetrations at the location STAT3 show a similar penetration depth behavior to location STAT2. The initial deceleration of all penetration events in the uppermost layer lies above 10 m/s^2 , which is higher than station STAT2. One penetration (Fig. 3.12, STAT3, green) even comes to rest in this layer, the other two achieved 2 m penetration depth. After the first layer, an decrease in deceleration is observed, which is higher as observed at station STAT2. The deceleration rate with depth after the first layer is slightly lower, than observed at station STAT2, suggesting a weaker second layer.

The penetrations at station STAT4 and STAT5 show ultimate penetration depth of less than 0.25 m and peak decelerations of 15 m/s^2 and higher. The sediments in the region of station STAT4 consist of medium sand with a fine fraction of less than 5 %. The sediment at station STAT5 consists of gravel.

3.5 Summary

The aim was to build a measurement system to determine the stiffness of marine sediments. Therefore, we developed a Lance Insertion Retardation Meter (LIRmeter) which measures deceleration during a penetration process into marine sediments. The deceleration vs. time can be converted to deceleration vs. depth by double integration of deceleration and then related to sediment physical properties like bearing capacity. We developed a lance equipped with a high speed, high precision data acquisition system. Acceleration (or deceleration) is measured by using MEMS sensors. The

measurement system has an operation range from shallow waters to 4500 m water depth, can be deployed in a pogo style fashion and operate continuously up to 14 hours. The LIRmeter is easy to handle (one person operation / two person deployment) and easy to maintain and operate. The incorporated sensors are off the shelf MEMS sensors, which are used in a variety of instruments ranging from scientific instrumentation (Bhattacharya et al., 2012) to consumer electronics (Hollocher et al., 2009). The sensors deliver a good performance for our application and are easy to obtain and replace in case of a malfunction.

The developed data acquisition performs very well at the targeted sampling rates and delivers a resolution which is high enough to register a penetration process allowing further analysis and calculations. The advantages of the developed system lie in the envisioned operational environment (pogo style missions along profiles lasting from half a day to one day), the comparatively high precision DAQ and the user friendly operability with a well designed and convenient user interface.

Calibration and laboratory experiments show a very good performance of the sensors and data acquisition system. The measurement system, consisting of data acquisition electronics and the measurement lance, has proven its robustness and maturity on several sea trials, from one of which results are presented within this paper. Datasets which were taken at a single location show excellent repeatability. The data show significant changes in the sedimentary sequence allowing first qualitative interpretations based on this raw data. The development of the LIRmeter has now reached a level, which allows the user to perform highly reproducible measurements on a routine basis in a fast and easy way.

Acknowledgements This project is supported with funding from the program “Angewandte Umweltforschung” of the Bremen State (Senator für Umwelt, Verkehr, Bau und Europa) in the frame of the “European Fund for regional development 2007-2013”. European Union: investments in your future. European funding for regional development. The cooperation with T. Wever from Forschungsanstalt der Bundeswehr für Wasserschall und Geophysik for the field trials of the instrument was a big opportunity for us and is very much appreciated. Also we would like to thank the captain and crew of WFES PLANET for their tireless efforts and support during the measurement campaign in Dec. 2010. Further we would like to thank Fielax Gesellschaft für wissenschaftliche Datenverarbeitung mbH for the good and inspiring cooperation during the project. The work for and dedication to this project by our engineer B. Heesemann and by our student A. Schwab is greatly appreciated. The preceding experiments by M. Fabian and T. Gmeinder

were very helpful and contributed to the successful development of the LIRmeter. Also support from M. Naumann (LBEG), C. Thürnagel (BGR) and W-U. Laurer (BSH) from the project Geopotenzial Deutsche Nordsee is appreciated.

Chapter 4

Field tests

Validation of impact penetrometer data by cone penetration testing and shallow seismic data within the regional geology of the Southern North Sea

Stephan, S¹ ✉ and Kaul, N¹ and Villinger, H¹

Published in: *Geo-Marine Letters*; Received: 16 September 2014 / Accepted: 5 March 2015 / Published online: 19 March 2015

Citation: Stephan, S, Kaul, N, Villinger, H (2015). Validation of impact penetrometer data by cone penetration testing and shallow seismic data within the regional geology of the Southern North Sea. *Geo-Marine Letters*, 35(3):203–219. doi:10.1007/s00367-015-0401-y

The final publication is available at Springer via <http://dx.doi.org/10.1007/s00367-015-0401-y>

¹Universität Bremen
Department of Geosciences
28359 Bremen, Germany
sstephan@uni.bremen.de

Abstract This study presents the assessment of total cone resistance from *in situ* deceleration measurements using the Lance Insertion Retardation meter (LIRmeter) in the Southern North Sea. The penetrometer is equipped with a measurement lance that is up to 6 m in length. The aim was to validate LIRmeter data interpretation within the regional geological context by comparison with static velocity cone penetration testing and sub-bottom profiles. In total, 13 measurements could be taken in addition to preexisting hydroacousical, and static velocity CPT datasets. The dynamically acquired data are processed and compared to the static velocity data, which serve as a reference dataset. The validation encourages the use of acceleration based dynamic penetration tests, since a high degree of agreement could be demonstrated within this study between independently acquired dynamic, and static cone resistance data. Moreover, results reveal evidence of two successive formations with different geotechnical properties, consistent with existing knowledge on the regional setting. Additionally, there is novel indication of an incised glacial valley with muddy low-permeability sediments extending much further than reported to date, which would necessitate updating of older maps. The main advantage of penetrometer-based deceleration measurements lies in the robustness of the method and the reliability of the sensors. However, penetration depth is, for dimensioning reasons, limited to the order of a few meters. Additionally, data processing includes the dependency of knowledge about the soil type to correct the dynamic data. These limitations can be satisfactorily outweighed by combination with reference data from static velocity tests, as demonstrated by integrating these data into a soil classification scheme.

4.1 Introduction

Knowledge of near-surface geotechnical properties (e.g., bearing capacity and undrained shear strength) of marine sediments is critical for civil engineering projects, including building operations in shallow waters that require the safe deployment of jack-up rigs on a load-bearing seafloor. Today, *in situ* testing techniques such as Cone Penetration Testing (CPT) are well advanced to meet these challenges. Indeed, geotechnical measurements in intact sediments unaltered by sampling (cf. Weaver and Schultheiss, 1983; Parker and Sills, 1990) or transportation can be achieved only by using *in situ* testing. This circumvents the confounding effects of, for example, sampling-induced degassing, selective coring, or strong drainage in highly permeable sediments (e.g., sands) during core recovery. Nevertheless, laboratory testing techniques have the advantage of controlled test conditions, so that commonly

both approaches are used in combination.

The routine *in situ* method for determining soil-bearing capacity and undrained shear strength in both on- and offshore settings is CPT, the key parameters being the cone resistance (q_c), sleeve friction (f_s), and pore pressure (u) at (or behind) the cone. Measurements are taken in discrete intervals as a function of soil depth while maintaining a constant (static) penetration velocity. Correction and interpretation of these data are well assured by a broad theoretical (Baligh, 1985; Teh, 1987) and empirical background (see Lunne et al. (1997) for review). Modern CPT instruments are equipped with strain gauges, and pore pressure is typically measured by means of pressure transducers. Today, seafloor CPT rigs penetrate down to 60 m using coiled or straight rods, and to more than 100 m in combination with drilling techniques (Lunne, 2010).

Other methods are based on a non-steady (dynamic) penetration velocity, as in the case of impact penetrometers (Dayal and Allen, 1973). These typically lance- or projectile-shaped devices penetrate the seafloor due to the momentum they gather either during free fall (e.g. Stoll et al., 2007; Stark and Wever, 2009) or during rapid, tethered lowering with a winch (e.g. Preslan, 1969; Villinger et al., 1999; Osler et al., 2006a; Stephan et al., 2011). In addition to the CPT parameters q_c , f_s and u , they measure kinematic parameters such as acceleration to obtain depth information during penetration. Indeed, advances in sensor technology, data acquisition, and data storage in recent years have stimulated the development of a variety of impact penetrometers (Osler et al., 2006a; Stegmann et al., 2006b; Stoll et al., 2007; Fabian et al., 2008; Stark and Wever, 2009; Stephan et al., 2011; Jeanjean et al., 2012). Their primary advantage is that a measurement requires only seconds. Therefore, tests can be performed in rapid succession in space and time, rendering *in situ* testing more time- and hence cost-efficient. However, penetration depth is usually limited (on the order of a few meters) due to the small dimensions of most of these instruments. Furthermore, data corrections are required (Dayal, 1974) to enable comparison with static velocity testing.

Another key challenge in the development of new generation dynamically impacting penetrometers is to ensure that the sensors are sufficiently robust for high-rate testing. Indeed, CPT sensors may be significantly disturbed or even damaged by hydrostatic pressure, temperature, and mechanical loads during the penetration process, especially when the testing is conducted at high penetration rates. This mechanical fragility renders the utilization of CPT sensors, designed for static velocity testing, questionable for dynamically impacting penetrometers.

Within this context, the present study evaluates the performance of a dy-

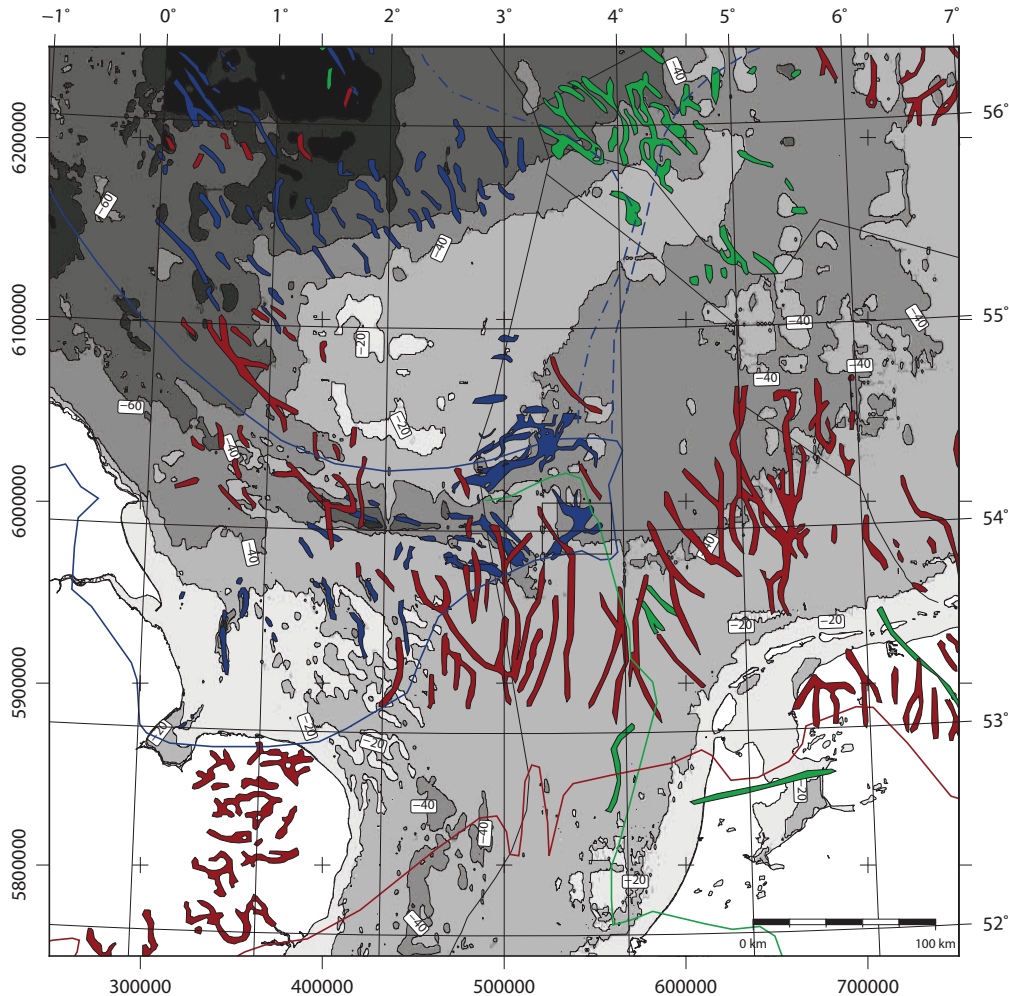
namically operating impact penetrometer, the Lance Insertion Retardation meter (LIRmeter, Fabian et al., 2008; Stephan et al., 2011), during a 2013 site inspection survey for building operations in a sector of the Southern North Sea characterized by fine-grained and slightly muddy sediments. The lance was equipped with a conventional CPT cone in addition to the acceleration sensors of the LIRmeter, enabling simultaneous data acquisition. The basic concept behind the measurement strategy with accelerometers is that the deceleration during impact can be taken as a proxy for some geotechnical parameters. The ultimate aim was to validate LIRmeter data interpretation with independent evidence based on both static and dynamic cone resistance measurements within the regional geological context, as well as with reference to shallow sub-bottom profiler data. Results show excellent performance of the kinematic measurement approach while achieving a good reproducibility of the independently acquired penetration data. However, due to limitations inherent to the measurement principle and data processing, LIRmeter cone resistance measurements are here considered as supplementary to conventional static CPT seafloor tests.

4.2 Geological setting

The study area lies in the Dutch sector of the Southern North Sea in water depths ranging between 40 and 50 m (Fig. 4.1). The younger sedimentary regime is influenced primarily by the last two Pleistocene glacial stages, and a change from deltaic to full marine conditions (Cameron, 1992). The Pleistocene formations reach an overall thickness of more than 800 m (Cameron et al., 1986; Jeffery et al., 1989), and are overlain by Holocene sediments with thicknesses ranging from 1 to more than 20 m (Harrison et al., 1987; Jeffery et al., 1988).

Glacial valleys are filled with cohesive, mechanically weak sediment that is potentially gas-charged (Bowen, 1999; Schroot and Schüttenhelm, 2003). The thickness and geotechnical properties of the overburden, as well as the properties of the valley infill are of particular interest to engineers. Cameron (1992) uses the term “scaphiform” to describe the three-dimensional, boat-like shape of these incised valleys excavated by meltwater discharge (Cameron et al., 1987; Huuse and Lykke-Andersen, 2000; Janszen, 2012). Valley infilling is dependent on the formation time during a glacial stage: during advancing stages, the infill is dominated by subglacial deposits such as basal tills. Retraction phases, by contrast, promote deposition of proglacial outwash, and diamict sediments (Janszen, 2012).

The Quaternary geology of the Southern North Sea is well known from



extensive mapping in the late 1970s and early 1980s by the British Geological Survey (BGS) and the Dutch Rijks Geologische Dienst (RGD; Cameron et al., 1986; Harrison et al., 1987; Jeffery et al., 1988, 1989; Cameron, 1992). The Quaternary succession can be subdivided into (1) early Pleistocene deltaic sediments, (2) late Pleistocene nondeltaic sediments, and (3) Holocene sediments (Cameron, 1992). The deltaic sediments, which were supplied by the Rhine and Meuse rivers, form part of prograding deltas deposited until the late middle Pleistocene (Zagwijn, 1974). The nondeltaic sediments are characterized by thin, climate-influenced sedimentation events (Cameron, 1992). From the middle to late Pleistocene, the regional sedimentation was influenced by the Elsterian, Saalian, and Weichselian glacial stages. Deposits of at least the Elsterian and Weichselian glacial stages have been identified in the study area (Cameron, 1992; Carr, 1999; Huuse and Lykke-Andersen, 2000; Carr et al., 2006).

4.2.1 Late Pleistocene

For this study, relevant information was obtained from sediments adjacent to, superimposed on, or underlying the stratigraphic interface between the Holocene and Pleistocene. In addition, the underlying infill of glacial valleys may be relevant within the context of penetrometer measurements. In Fig. 4.2, the late Pleistocene successions are grouped with the non-deltaic formations, along with the thickness of the Holocene overburden.

The Well Ground (WLG) formation consists of poorly sorted fine to very fine micaceous sand with intercalations of silt and clay (Cameron et al., 1989b; Jeffery et al., 1989; Carr, 1999; Fitch et al., 2005). It can reach thicknesses of 6 m, and is commonly overlain by the Boulders Bank and Dogger Bank formations (Cameron et al., 1986). WLG sediments were deposited under fluvial influence in a proglacial setting of the late Weichselian (van der Meer and Laban, 1990; Cameron, 1992; Rijdsdijk et al., 2005; Stoker et al., 2011).

Incised valleys formed during the Weichselian glacial stage are up to 80 m deep, 8 km wide, orientated mainly N–S, and filled with proglacial sediments classified as the Botney Cut (BCT) formation (Creutzberg and Postma, 1979; Cameron et al., 1986, 1987, 1989b,a; Jeffery et al., 1989; Cameron, 1992; Kusters et al., 1992; Scourse et al., 1998; Carr, 1999; Rijdsdijk et al., 2005; Diesing et al., 2009; Graham et al., 2011). The valleys are generally smaller than their Elsterian counterparts, which are filled by sediments of the Swarte Bank formation. The sediments were deposited under glaciolacustrine to glaciomarine conditions during the late Pleistocene prior to the Holocene marine transgression. Two members have been described in terms

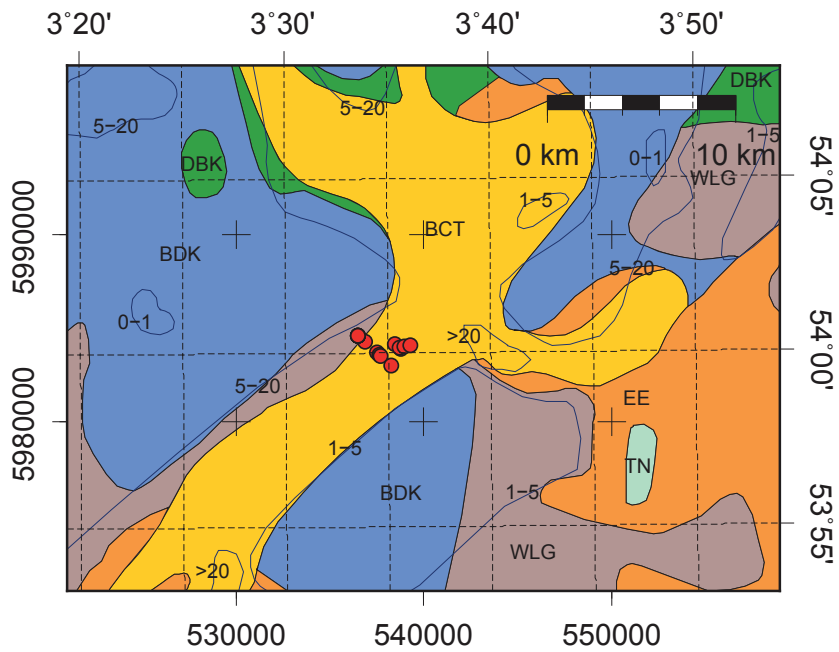


Figure 4.2 – Formations at the Holocene/Pleistocene interface in the study area (modified after Cameron et al., 1986; Jeffery et al., 1989). *Yellow* Botney Cut (BCT), *blue* Boulders Bank (BDK), *grey* Well Ground (WLG), *light green* Twente (TN), *green* Dogger Bank (DBK), *orange* Eem (EE). *Red circles* Locations of penetration stations, contour lines thickness of overlying Holocene sediments or depth below seafloor. For more information, see Fig. 4.1.

of sedimentary and acoustic facies.

The lower member shows chaotic reflections in acoustic datasets, and reaches thicknesses of approx. 15 m (Cameron et al., 1986; Diesing et al., 2009). It consists of poorly sorted, gravelly coarse sand diamicts, which are often difficult to identify on seismoacoustic records (Jeffery et al., 1989; Bowen, 1999; Carr, 1999; Stoker et al., 2011).

The upper member is strongly stratified, and consists of occasionally pebbly glaciolacustrine and glaciomarine clays (Bowen, 1999; Carr, 1999) locally charged by small amounts of gas (contents <1%), as inferred from blanking zones in acoustic datasets (Cameron et al., 1989b; Schroot and Schüttenhelm, 2003). The upper member is always present in seismoacoustic datasets or samples, and can reach thicknesses of 35 m (Jeffery et al., 1989).

4.2.2 Holocene

The upper few meters of the sedimentary cover are dominated by Holocene sediments deposited under open marine conditions (see Jelgersma et al. (1979) and Fig. 4.3), generally consisting of sands ranging from 100–400 μm in median grain size (Jansen et al., 1979). Of these, the sequence known as the Terschellinger (TER) Bank member is an open marine deposit containing a fully marine mollusk fauna (Fitch et al., 2005; Rijdsdijk et al., 2005). It reaches thicknesses of 1–10 m, and consists of slightly muddy fine-grained sands and silts with median grain sizes of 100–220 μm and mud contents of < 10 % (Harrison et al., 1987; Cameron, 1992; Fitch et al., 2005). The sediment is of periglacial provenance, and interpreted as being derived from reworked Pleistocene deposits (Cameron et al., 1989b; Fitch et al., 2005). The TER member is associated with the Southern Bight Formation within the revised stratigraphy of the Southern Bight proposed by Rijdsdijk et al. (2005).

4.3 Materials and methods

The measurements were conducted in late February 2013 in cooperation with Fugro aboard their RV Markab. The study area had been investigated by Fugro using sub-bottom profilers as well as static velocity CPT to, for example, locate glacial valleys (cf. Fig. 4.4 for track lines). During the campaign, measurements were taken in the area where previous investigations (Cameron et al., 1986; Jeffery et al., 1989) identified a Weichselian glacial valley (BH1–10) filled with the BCT formation. The locations were planned on previously recorded sub-bottom profiler transects. Other dynamic measurements were

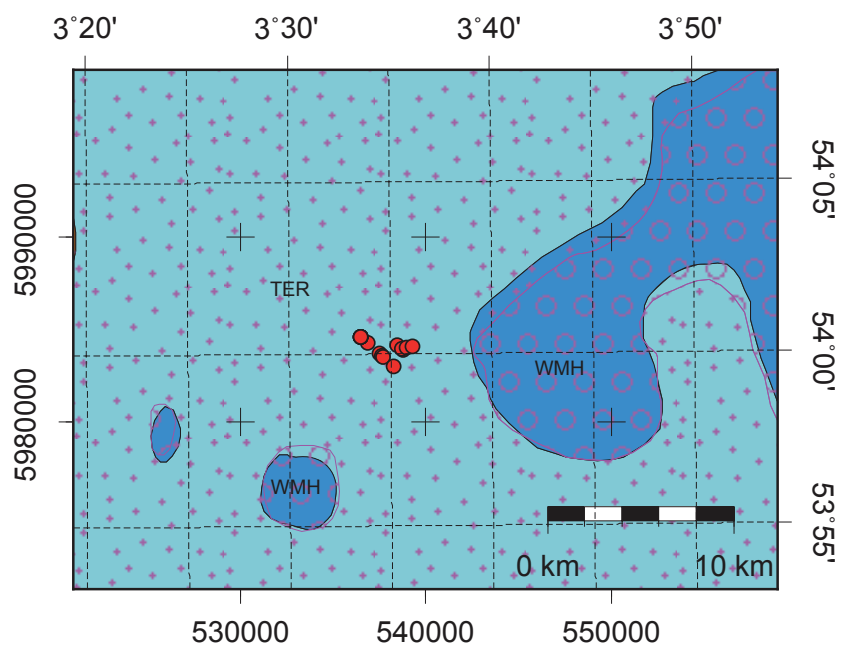


Figure 4.3 – Holocene sediments in the study area (modified after Harrison et al., 1987; Jeffery et al., 1988). *Light blue* Terschellinger (TER) Bank member, *dark blue* Western Mud Hole (WMH) formation. Sediment composition: *crosses* sand (mud $\leq 10\%$), *open circles* muddy sand ($50\% \leq \text{mud} < 100\%$); gravel content $\leq 1\%$ throughout. *Red circles* Locations of penetration stations. For more information, see Fig. 4.1.

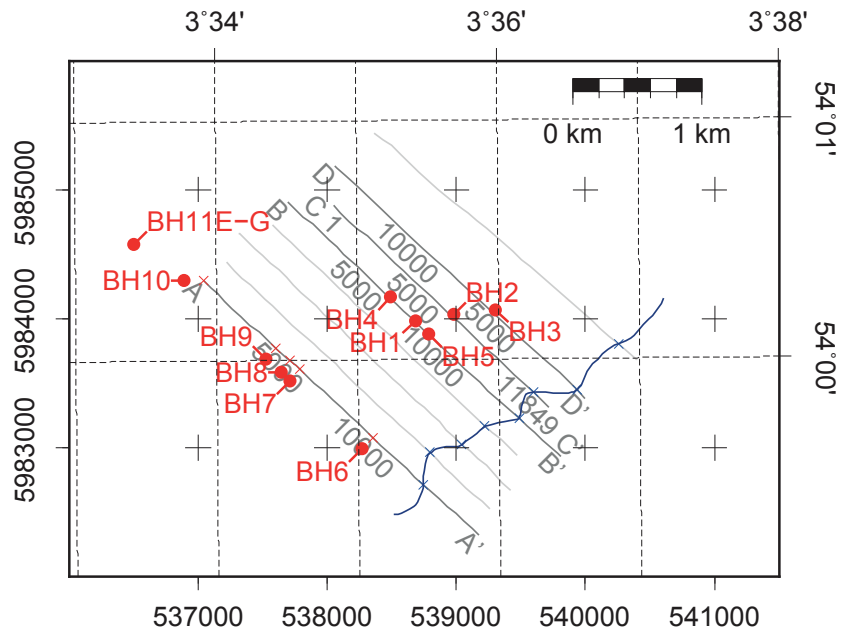


Figure 4.4 – Locations of sub-bottom profiler transects (*grey lines*) and penetration stations (*red circles*) in the study area (data provided by Fugro with kind permission of GDF Suez E&P Nederland B.V.). *Blue line* Weichselian glacial valley. For more information, see Fig. 4.1.

made in the vicinity of an existing static velocity CPT station (BH11E–G; cf. Fig. 4.4 for locations). The location of each penetration was determined using a positioning device attached to the lance, assuring an uncertainty in positioning of approx. 10 m. In all, 13 successful measurements were made at 11 stations. The southeasterly outline of a Weichselian valley (inferred from the subbottom profiler data) is shown in Fig. 4.4. The penetration depths and impact velocities for each station are reported in Table 4.1.

4.3.1 LIRmeter impact penetrometer

The LIRmeter (cf. Stephan et al., 2011, 2012) in combination with a measurement lance measures a kinematic quantity such as acceleration (a) or deceleration ($-a$) as the lance penetrates into sediment. Tip resistance vs. depth is derived from this kinematic dataset. The main advantages of this approach lie in the insensitivity to ambient hydrostatic pressure, and the robustness of the sensors. In addition, and for validation purposes, the tip load was directly measured using strain gauges to obtain an independent,

Table 4.1 – Results for penetrations at stations BH1 to BH11 in the Weichselian glacial valley: impact velocity v_i , penetration depth d , peak deceleration a_{\min} , cross-sectional area A , buoyant weight w_b

	v_i	d	a_{\min}	A	w_b
	(m/s)	(m)	(m/s ²)	(cm ²)	(kN)
BH1	4.37	2.06	-14.46	15	2.781
BH2	4.49	2.70	-14.20	15	2.781
BH3	3.70	1.80	-21.08	15	2.781
BH4	4.35	1.98	-18.84	15	2.781
BH5	4.60	1.65	-21.65	15	2.781
BH6	4.62	2.36	-17.68	15	2.781
BH7	4.00	1.88	-24.69	15	2.781
BH8	3.74	1.71	-17.67	15	2.781
BH9	4.22	1.98	-18.57	15	2.781
BH10	3.89	1.62	-16.44	15	2.781
BH11E	3.74	1.25	-16.84	15	2.157
BH11F	4.15	1.59	-19.67	15	2.781
BH11G	4.64	1.89	-19.05	15	2.781

synchronously recorded dataset.

The LIRmeter, described in detail in [Stephan et al. \(2012\)](#), consists of a lance that is up to 6 m in length and a weight stand that contains the instruments for data acquisition (i.e., the actual LIRmeter). The accelerometers have different sensitivities and measurement ranges (see Table 4.2), which enables the LIRmeter to cover a wide range of sedimentary conditions without having to change the sensors. The system can be deployed either by a winch, which results in typical penetration velocities of 1–2 m/s and allows pogo-style measurements (cf. [Hyndman et al., 1979](#)), or by a trigger system with penetration velocities of 3–5 m/s.

The cone sections employed for the first time within this study were incorporated for comparative dynamic measurements. The cones have a cross-sectional area of 15 cm² and a standard conical tip with an apex angle of 60 ° (Fig. 4.5). The cones, which were manufactured and provided by Fugro for use in the lance of the dynamic penetrometer, are designed as subtraction cones ([ASTM \(2012\)](#); see Fig. 4.6). Electrical signals and power supply were guided through the rod. Technical data of the LIRmeter, the mechanics of the lance, and the instrumented cones are shown in Table 4.2.

The system was deployed from the vessel using a winch and tether while fitted with a Kullenberg-type trigger system ([Kullenberg, 1947](#)), which al-

Table 4.2 – Technical data of the LIRmeter, the mechanics of the lance and the employed sensors. The accelerometers have different measurement ranges (multiples of gravitational acceleration g). RMS root mean square, DAQ data acquisition

Property	Unit	Value
Mechanical dimensions		
Cross-sectional area of tip	cm ²	15
Tip apex	°	60
Max. length overall	m	7.5
Rod diameter	m	0.063
Net weight (max.)	kg	240 (350)
Mounting tubes	-	3
DAQ characteristics		
Sampling frequency (max.)	Hz	500 (4000)
Resolution	bit	16
Battery capacity	Ah	23
RMS noise performance		
3g accelerometer A1	m/s ²	0.133
5g accelerometer A2	m/s ²	0.054
2g accelerometer A3	m/s ²	0.182
Cone resistance	kN	0.085
Sleeve friction	kN	0.044
Pore pressure	kPa	11



Figure 4.5 – LIRmeter and measurement lance configured with one rod extension and an instrumented 15 cm^2 cone (total length: 2.5 m), in a deployment sledge onboard the research vessel. Rods are extendable in steps of 1 m.

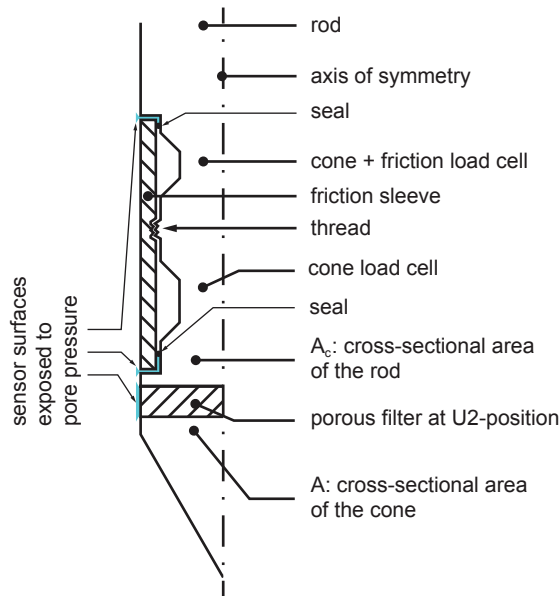


Figure 4.6 – Schematic of a cross-section of a subtraction cone (not to scale, modified after Lunne et al., 1997). The cone is symmetric along the vertical axis. The friction sleeve is sealed with O-rings.

lowed impact velocities greater than 3 m/s. A sketch of the relevant parts of the lance and the deployment strategy is shown in Fig. 4.7.

All data were collected using a 15 cm² cone, which required the installation of a transition piece between the cone and the extendable rod (see Fig. 4.5). The transition piece has a higher cross-sectional area than the cone and the rod. An increase in cross-sectional area requires the penetrometer to displace more sediment during penetration, and amplifies the force acting on the penetrometer. This results in an increase in deceleration at a penetration depth of approx. 0.8 m (location of the transition piece), and consequently an increased deceleration due to the amplified sediment resistance. Deployments BH11F and BH11G were performed using the same configuration as for the measurements on the subbottom profiler transects (w_b : 2.781 kN). The instrument was slightly lighter for station BH11E (see Table 4.1).

4.3.2 Processing of impact penetrometer data

Processing of the impact penetrometer data starts with a twofold integration of the deceleration time series, resulting in time series of velocity and penetration depth. During the second step, the deceleration time series is

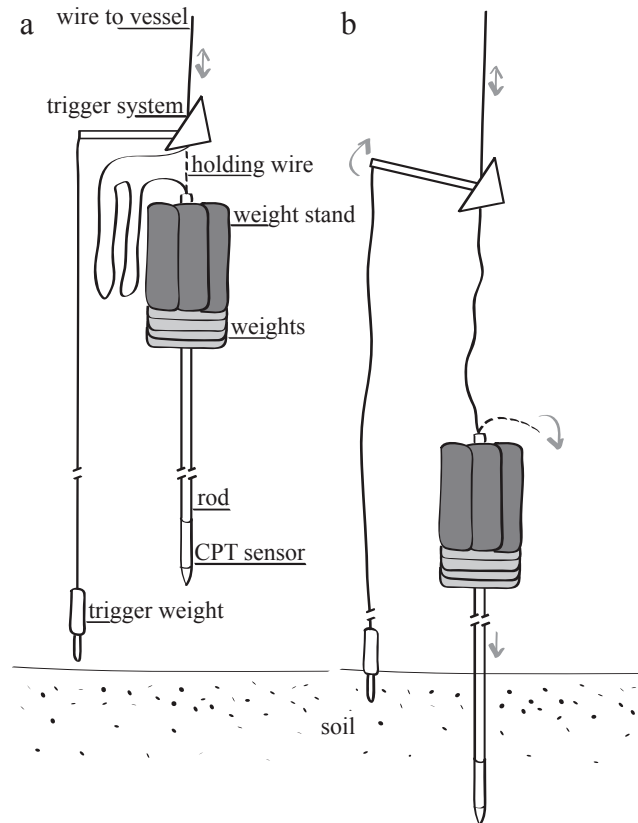


Figure 4.7 – Sketch of lance deployment. **a** Pre-penetration. The lance is lowered at a winch speed of typically 1–2 m/s, and oscillates vertically in response to the heave motion of the vessel. **a** After triggering and during penetration. The wire continues to be fed at winch speed after the release of the holding wire, the lance gaining velocity before impact because it is now decoupled from vessel movement. During penetration (after impact), the lance decelerates due to friction.

converted to a deceleration vs. depth profile. Details of the acceleration data processing sequences are described in [Stephan et al. \(2012\)](#).

The force F that acts on the penetrometer during penetration is, under consideration of the buoyant weight, calculated using Newton's second law of motion:

$$F = (m_1 - V_1\rho_w)a = \frac{w_b}{g}a \quad (4.1)$$

where m_1 is the mass of the LIRmeter, ρ_w the density of water, V_1 the volume of the LIRmeter, a the acceleration, g the gravitational acceleration, and w_b the buoyant weight of the instrument.

Because the acceleration of the whole instrument is sensed by the acceleration sensors, it is considered that the penetrometer is decelerated solely by stresses acting on the interface between the soil and the conical tip. Thus, friction along the rod would be negligible, and the cone resistance $q_{\text{dyn}}^{\text{acc}}$ can be calculated on the basis of accelerometer data from the determined force F by dividing with the cross-sectional area A of the penetrating lance:

$$q_{\text{dyn}}^{\text{acc}} = F/A \quad (4.2)$$

This approach is justifiable for non-cohesive soils or sediments, which typically exert low friction on penetrometers ([Dayal, 1974](#)). For cohesive sediments such as soft clays, either friction along the rod needs to be taken into account, or the penetrometer needs to be designed (e.g., as full-flow penetrometer, or by the incorporation of friction reducers) to minimize friction at the interface between rod and soil (cf. [Lunne et al., 1997](#); [Randolph, 2004](#); [Chung and Randolph, 2004](#)). At peak deceleration of 20 m/s^2 , the buoyancy of the rod immersed in the sediment amounts to approx. 2 % (at 6 m penetration depth) of the derived cone resistance, and is therefore considered as negligible in this study. When very soft soils (deceleration $< 5 \text{ m/s}^2$) are tested, however, the buoyancy can amount up to 10 % of the measured cone resistance at full penetration. Then, a correction of $q_{\text{acc}}^{\text{dyn}}$ as a function of penetration depth z is needed:

$$q_{\text{dyn}}^{\text{acc}} = F/A - \Delta q_{\text{rod}}^{\text{buoy}} \quad (4.3)$$

with

$$\Delta q_{\text{rod}}^{\text{buoy}} = \frac{(\rho_s - \rho_w)\pi R^2 z g}{A} \quad (4.4)$$

where $\Delta q_{\text{rod}}^{\text{buoy}}$ is the effect of the rod's buoyancy on the tip resistance as a function of penetration depth, ρ_s the bulk density of the soil, and R the radius of the rod.

4.3.3 Correction of cone resistance data

Due to the mechanical design of the cone, the cone resistance measured by the instrumented tip of the impact penetrometer $q_{\text{dyn}}^{\text{cone}}$ needs to be corrected for the unequal area effect (Lunne et al. 1997) to obtain the corrected total cone resistance:

$$q_{\text{t,dyn}}^{\text{cone}} = q_{\text{dyn}}^{\text{cone}} + u \left(1 - \frac{A_{\text{c}}}{A} \right) \quad (4.5)$$

where A_{c} is the cross-sectional area of the load cell exposed to pore pressure (see Fig. 4.6). The correction of the unequal area effect accounts for the smaller effective area of the cone due to an exposed area behind the tip. The area ratio and sensitivity of the load cells were determined in a calibration vessel prior to the field trials for hydrostatic pressures up to 2.5 MPa and tip loads up to 10 kN. During the data analysis, hydrostatic pressure was used as the pore pressure u for the data correction. The measured cone resistance at the instrumented tip $q_{\text{t,dyn}}^{\text{cone}}$ is not affected by the increased area of the transition piece (see above), because the measurements are taken through the strain gauges.

Because the acceleration sensors are not affected by pressure, the total dynamic cone resistance $q_{\text{t,dyn}}^{\text{acc}}$ (derived from the deceleration measurement) can be calculated directly from Eqs. 4.2 or 4.3 following the aforementioned arguments:

$$q_{\text{t,dyn}}^{\text{acc}} = q_{\text{dyn}}^{\text{acc}} \quad (4.6)$$

4.3.4 Correction for rate effects

To compare the total cone resistance from dynamic measurements $q_{\text{t,dyn}}^{\text{acc}}$ with the total cone resistance from a constant velocity (static) CPT q_{t} , the LIR-meter data need to be corrected for strain rate effects. Geuze (1953) found that soil resistance is dependent on the strain rate (or penetration velocity), and Kérisel (1961) formulated a logarithmic relationship (Eq. 4.7) to correct for this effect. The relationship has been applied to impacting penetrometers by Dayal (1974) as well as Dayal and Allen (1975) for a velocity range of 0.13–5.50 m/s, and subsequently widely adopted for dynamically penetrating impactors such as small penetrometers (Stoll et al., 2007; Stark et al., 2009b, 2012b), model penetrometers (O’Loughlin et al., 2004), and lance-shaped impact penetrometers (Steiner et al., 2014):

$$\frac{q_{\text{t,dyn}}}{q_{\text{t,ref}}} = 1 + \lambda \log_{10} \left(\frac{v_{\text{dyn}}}{v_{\text{ref}}} \right) \quad (4.7)$$

where λ is the soil- and stress state-specific viscosity coefficient, v_{dyn} the momentary velocity of the penetrometer, v_{ref} the reference velocity, and $q_{t,\text{ref}}$ the total cone resistance of a reference penetrometer. A soil viscosity coefficient of 1.5 denotes a 1.5-fold increase in dynamic cone resistance $q_{t,\text{dyn}}$ if velocity increases by one order of magnitude with reference to v_{ref} . The strain rate correction after Dayal (1974) and Dayal and Allen (1975) is meaningful only where $v_{\text{dyn}} \geq v_{\text{ref}}$, because of the logarithmic term in Eq. 4.7. Typically, a reference velocity of 0.02 m/s is chosen to compare impact penetrometer data with static velocity CPT measurements.

The soil viscosity coefficient has been applied for dynamic penetrations with penetrometers in clayey sediments, where it ranges between 0.04 and 1.50 (Dayal and Allen, 1975; Dayal, 1980; Randolph, 2004; O’Loughlin et al., 2004, 2013; Einav and Randolph, 2005; Aubeny and Shi, 2006; Low et al., 2008; Zhou and Randolph, 2009; Young et al., 2011; Nazem et al., 2012; Steiner et al., 2012, 2014; Chow and Airey, 2013, 2014). Applications of the strain rate correction on silty sediments yield a soil viscosity coefficient between 0.13 and 0.36 (Perlow and Richards, 1977; Biscontin and Pestana, 2001). Several authors employing lightweight dynamic penetrometers penetrating sands at high rates have used values of 0.7–1.5 for the soil viscosity coefficient λ , although Dayal (1974), Dayal and Allen (1975), and Lunne et al. (1997) concluded from laboratory observations that the strain rate correction is applicable only to cohesive sediments.

4.3.5 Drainage conditions during penetration

Drainage of sediment during penetration affects the deceleration behavior of penetrometers under undrained conditions at high penetration rates and/or low sediment permeability (e.g., Danziger and Lunne, 2012), and the normalized velocity V can be used to delimit drained from partially drained or undrained conditions. This dimensionless measure is defined as (Finnie and Randolph, 1994):

$$V = \frac{v \cdot d}{c_v} \quad (4.8)$$

where v is the velocity, d the penetrometer diameter, and c_v the coefficient of consolidation.

According to Finnie and Randolph (1994), undrained conditions occur above $V=30$ and drained conditions below $V=0.01$. Drainage conditions for high-rate penetrations can be considered to be undrained for penetration rates exceeding 0.5 m/s (Fig. 4.8). Even for highly permeable, poorly consol-

idated sediments, it is possible to assume at least partially drained conditions at penetration velocities in the range of a few cm/s.

4.3.6 Static velocity CPT data

Soil classification in classes of “soil behavior types” based on pre-processed static velocity CPT data was conducted following the approach of Robertson (1990) using the normalized cone resistance Q_t , normalized friction ratio F_r , and pore pressure ratio B_q :

$$Q_t = \frac{q_t - \sigma_{v0}}{\sigma'_{v0}} \quad (4.9)$$

$$F_r = \frac{f_s}{q_t - \sigma_{v0}} \cdot 100 \quad (4.10)$$

$$B_q = \frac{u_2 - u_0}{q_t - \sigma_{v0}} \quad (4.11)$$

where σ'_{v0} is the (effective) vertical overburden pressure, f_s the sleeve friction, u_2 the pore pressure measured at the U2 position behind the cone tip, and u_0 the hydrostatic pressure. Processed CPT data from a static velocity Wison-type downhole CPT tool (cf. Sanglerat, 1972) were collected on an earlier cruise in December 2012, and kindly provided by Fugro. For the purposes of the present study, several figures were generated using the Generic Mapping Tools (GMT) by Wessel and Smith (1991), and Wessel et al. (2013).

4.4 Results

4.4.1 Sub-bottom profiler transects, stations BH1–5

For stations BH1–5 along sub-bottom profiles B–B', C–C', and D–D', penetration depths range between 1.7 and 2.7 m (Fig. 4.9a) with impact velocities of 3.7–4.6 m/s (see Table 4.1). The sub-bottom profiler data show prominent divergent reflectors (dashed lines) tracing a v-like structure from a depth of 1.5 m to over 10 m below seafloor (mbsf). The depth interval between 0 and 1 mbsf is masked by reverberations. However, parallel to subparallel horizontal layers are visible just below the masked depth interval. The unit characterized by divergent layers has a thickness of more than 10 m in the NW, diminishing to the SE.

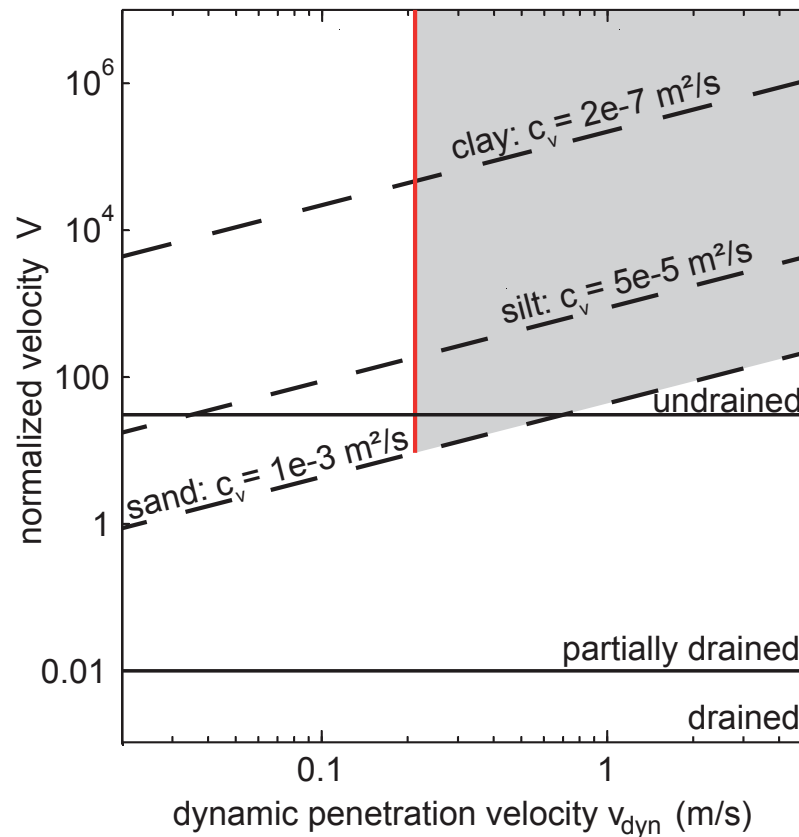


Figure 4.8 – Drainage conditions as a function of normalized velocity V and sediment type. Values of c_v for sand and silt are from Finnie and Randolph (1994), for clay from Randolph (2004). Normalized penetration velocity was calculated for a 15 cm^2 penetrometer. Border conditions for V at 0.01 and 30 are after Finnie and Randolph (1994). *Shaded area* Range for most LIRmeter penetrations, *red line* normalized velocities for penetration rate of 0.02 m/s as a function of sediment type.

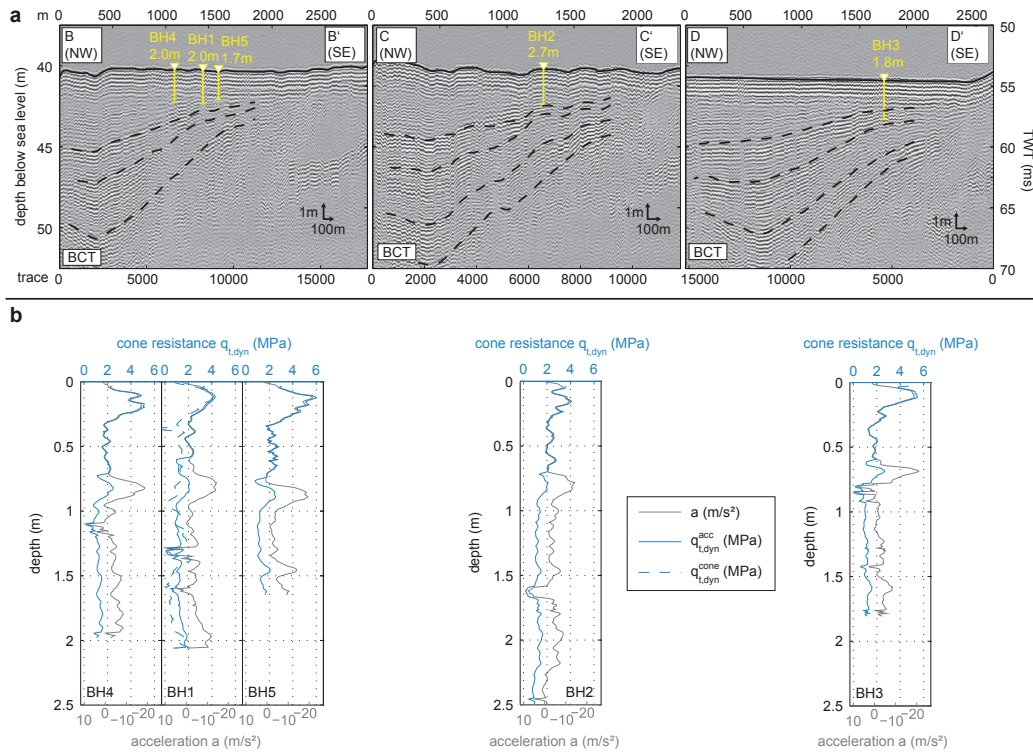


Figure 4.9 – **a** Sub-bottom profiler data and interpretation of formations along profiles B–B’, C–C’, and D–D’ (processed data provided by Fugro with kind permission of GDF Suez E&P Nederland B.V.; vertical exaggeration approx. 100:1; depth calculated assuming a constant sound velocity of 1500 m/s). *Yellow triangles and bars* Locations and depths of penetrations. **b** Corresponding depth profiles of dynamic penetration data (i.e., without strain rate correction) recorded by the LIRmeter (cf. locations in a): acceleration a (grey), dynamic cone resistance $q_{t,dyn}^{acc}$ (blue) and $q_{t,dyn}^{cone}$ (dashed blue). Negative a values denote deceleration.

Depth profiles of acceleration a and dynamic cone resistance $q_{t,\text{dyn}}$ at stations BH1 to BH5 (without rate correction; cf. Eq. 4.7) reveal a ranging from 9 to -21 m/s^2 , with high values of deceleration in the depth interval of 0–0.3 m and again at 0.8 m (Fig. 4.9b), where the friction reducer passes the boundary between water and sediment (e.g., see Fig. 4.9b, BH3). The penetration depths differ between stations BH1 to BH5, as a consequence of different impact velocities (cf. Table 4.1). At station BH5, the instrument penetrated 1.6 m into the seafloor while experiencing high decelerations in the upper 0.3 m (-21 m/s^2). At station BH2, however, with a similar impact velocity, 2.5 m penetration depth was reached with lower peak decelerations in the upper 0.3 m (-10 m/s^2).

The calculated and measured values of $q_{t,\text{dyn}}$ (dynamic cone resistance for both acceleration and tip sensor) show very similar patterns in the 0–0.8 m depth interval (see station BH1 in Fig. 4.9b). The cone resistance $q_{t,\text{dyn}}^{\text{acc}}$ was calculated from the acceleration a (see Eq. 4.2), accounting for the increase in cross sectional area caused by the transition piece. Throughout stations BH1 to BH5 $q_{t,\text{dyn}}$ is greater than 4 MPa in the depth interval between 0 and 0.3 m, and reaches a peak value of 6 MPa at station BH5. As the penetration depth increases, values for $q_{t,\text{dyn}}$ decrease. In particular, at penetration depths greater than 0.7 to 1 m, the cone resistance shows substantially lower values and less variation compared to the upper meter of penetration (Fig. 4.9b).

4.4.2 Static velocity CPT, station BH11

At neighboring sites E–G of station BH11 (see Fig. 4.4 for location), repeated LIRmeter-based measurements of penetration velocity show decreasing penetration velocities with depth (Fig. 4.10a). The impact velocities ranged between 3.7 and 4.6 m/s, whereby the lowest impact velocity occurred during the deployment with the lighter instrument (site BH11E; cf. Section 4.3). Higher impact velocities are associated with deeper penetration of the LIRmeter. The deceleration during penetration and inferred values (dynamic and total cone resistance) are shown in Fig. 4.10b for stations BH11E to BH11G. The acceleration data were processed using the same strategy as for locations BH1 to BH5, accounting for the influence of the transition piece. The strain rate correction (Eq. 4.7) was applied to the dynamic cone resistance $q_{t,\text{dyn}}$ using a value of 1.5 for the soil viscosity coefficient λ . The value of the soil viscosity coefficient was chosen within the limits of published values. The acceleration records of the penetrations BH11E to BH11G show a similar pattern throughout the three deployments. The upper 0.3 m are characterized by high deceleration values of more than -10 m/s^2 . Higher decelerations (up to -20 m/s^2) occur again at 0.8 to 1 mbsf.

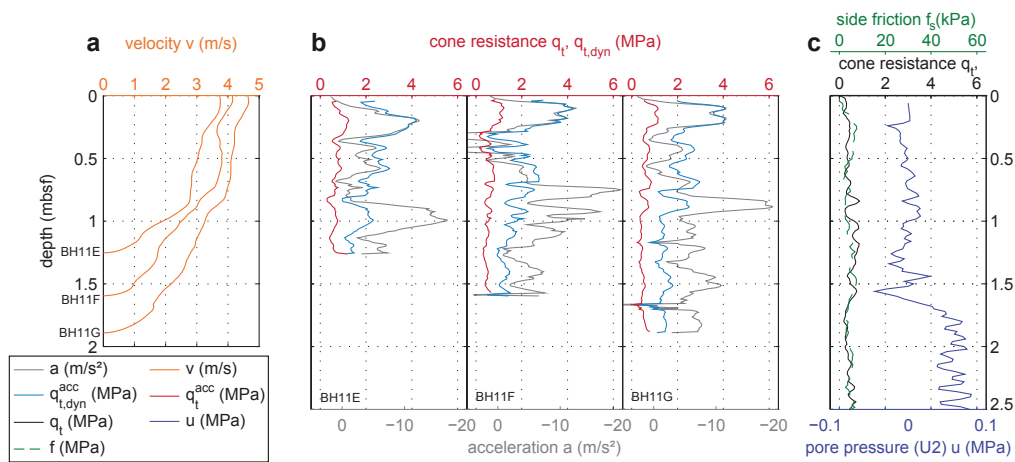


Figure 4.10 – **a** Dynamic penetration data from the LIRmeter: penetration velocity v . **b** Penetration resistance data from the LIRmeter: acceleration a (grey), calculated dynamic cone resistance ($q_{t,dyn}$ light blue), and rate corrected cone resistance q_t (red). **c** Static velocity penetration data from a frame-based CPT: total cone resistance q_t (black), sleeve friction f_s (green), and pore pressure u at U2 position (dark blue). Static velocity data provided by Fugro with kind permission of GDF Suez E&P Nederland B.V.

The dynamic cone resistance inferred from acceleration data $q_{t,\text{dyn}}^{\text{acc}}$ shows likewise high values (up to 4 MPa) in the depth interval of 0 to 0.3 m. The high decelerations occurring at greater depths do not transfer into high cone resistance values, since the increase in cross-sectional area has been considered during data processing. Generally, below 1 mbsf, $q_{t,\text{dyn}}^{\text{acc}}$ shows values below 2 MPa.

The rate-corrected total cone resistance from acceleration data q_t shows values around 1.3 MPa in the upper 0.3 m of stations BH11E to BH11G, and values below 0.5 MPa for penetration depths greater than 1 mbsf. The intermediate depth interval (0.3–0.7 mbsf) is characterized by values between 0.5 and 1 MPa.

Values of the static test (BH11) are shown in Fig. 4.10c. Here, total cone resistance, sleeve friction, and pore pressure are given for a depth interval of 0–2.5 mbsf. The cone resistance from the static test (see Fig. 4.10c) behaves similarly with values around 1.2 MPa in the near-surface interval (0–0.3 mbsf), and intermediate values for q_t ranging around 0.5 MPa in depths between 0.3 and 1.5 mbsf. The drop below 0.5 MPa occurs at a depth of 1.5 mbsf for the static tests at station BH11. The sleeve friction at a depth of 2.5 m amounts to 4.7 kPa, where the total cone resistance for the corresponding depth lies in the range of 400 kPa.

In the depth interval between 0 and 1 m, hydrostatic pressure (i.e., 0 MPa in Fig. 4.10c, because hydrostatic pressure has been subtracted) can be observed for u , while the data show a sharp increase to 50 kPa above hydrostatic pressure at a depth of 1.6 m. The depth interval between 1.6 and 1.8 m is characterized by increasing pore pressure up to 90 kPa.

4.4.3 Sub-bottom profiler transect, stations BH6 to BH10

Data from location BH11 (see above for a description) are shown along with the deployments of the impact penetrometer (BH6 to BH10 and BH11E, BH11EG) near the sub-bottom profile A in Fig. 4.11. The profile with five penetrometer stations begins approx. 500 m to the SE of station BH11. The penetration locations BH6 to BH10 (see Fig. 4.12 for penetration depths and sub-bottom profiler data) were planned in the proximity of the hydroacoustic profile. The actual locations of the penetrations were projected onto the sub-bottom profiler transect (see Fig. 4.4). The deployments of the impact penetrometer at station BH11 (BH11E, BH11G) and BH6 to BH10 were corrected with a strain rate factor λ of 1.5 yielding q_t on the basis of acceleration measurements.

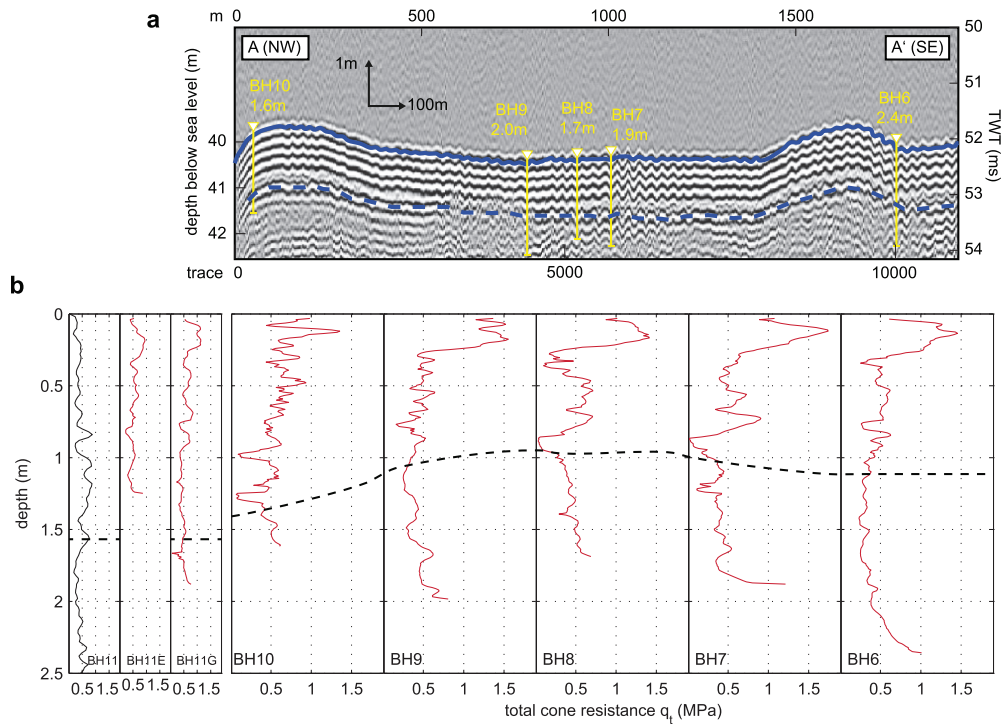


Figure 4.11 – **a** Sub-bottom profiler transect A–A' with seafloor reflector (*solid blue*) and subparallel to parallel sedimentary features (*dashed blue*) attributable to Holocene sediments (processed data provided by Fugro with kind permission of GDF Suez E&P Nederland B.V.). *Yellow triangles and bars* Locations and depths of penetrations. Water depth calculated from TWT assuming a sound velocity of 1500 m/s. **b** Measurements at CPT station BH11 (left) showing q_t recorded by static (*black*) and dynamic penetrometer (*red*), aligned with corresponding data at stations BH10 to BH6 along profile A–A'. *Dashed line* Interface between Holocene and Pleistocene formations.

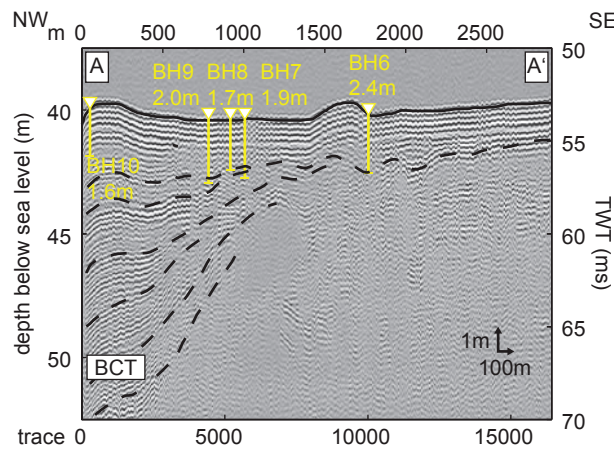


Figure 4.12 – Expanded sub-bottom profiler transect A–A’ spanning stations BH6–10 (processed data provided by Fugro with kind permission of GDF Suez E&P Nederland B.V.). Station BH11 lies approx. 500 m NW of station BH10. *BCT* Botney Cut formation.

Stations BH6 to BH 9 show high values of q_t up to 1.5 MPa in the upper 0.3 mbsf. The penetration depths correlate with impact velocity (see stations BH6 to BH9 in Fig. 4.11b, and Table 4.1 for impact velocities). However, the surficial area of high cone resistance is not well resolved at station BH10 (see Fig. 4.11b), but still observable in that depth interval. All stations show a decrease of total cone resistance in the depth range of 1–1.5 mbsf from values ≥ 0.5 MPa to values below 0.5 MPa. The sub-bottom profiler data (Figs. 4.11a and 4.12) show parallel to subparallel reflectors below the reverberation of the seafloor reflector. Deeper reflections of profile A are characterized by divergent lamination starting at 55 ms TWT in the SE. These reflectors show a thickness of more than 10 m in the NW, diminishing to the SE.

4.5 Discussion

4.5.1 Reproducibility and validation

Penetrometer measurements at a single location are very well reproducible. The features presented above appear in a similar magnitude and depth range in between repetitive measurements (e.g., see repeated measurements E–G at station BH11 in Figs. 4.10 and 4.11). The high level of reproducibility is also a consequence of the ability to ascertain a low spatial scatter of mea-

surements due to the positioning control during the campaign (see Materials and methods).

The dynamic cone resistance from the deceleration measurement $q_{t,\text{dyn}}^{\text{acc}}$ and the dynamic cone resistance from the tip measurement $q_{t,\text{dyn}}^{\text{cone}}$ match up to a penetration depth of 0.7 m (see BH1 in Fig. 4.9b). The friction reducer (cf. Fig. 4.5) enlarges the diameter of the penetration rod, and hence amplifies the sediment resistance force by the increased diameter. Processing of $q_{t,\text{dyn}}^{\text{acc}}$ accounted for that effect. However, when the friction reducer is fully immersed into the sediment (i.e., below 0.7 mbsf), two signals are recorded by the accelerometer: first, the passage of the tip through a given layer, and second, the passage of the friction reducer through the same layer. If more than one layer is present within the sediment column, then these deceleration signals may overlap and blur the information retrieved from these data. Therefore, qualitative and quantitative discrepancies between $q_{t,\text{dyn}}^{\text{acc}}$ and $q_{t,\text{dyn}}^{\text{cone}}$ increase below a penetration depth of 0.7 m (see BH1 in Fig. 4.9b). For the interval between 0 and 0.7 m, a linear transfer function is expected between these two parameters. The dynamic cone resistance from acceleration measurement reproduces the simultaneously acquired but independently measured cone resistance from the tip sensor to a high degree with a slope of 0.95 ± 0.05 of the linear regression. Fig. 4.13 shows $q_{\text{dyn}}^{\text{acc}}$ as a function of the simultaneously acquired $q_{\text{dyn}}^{\text{cone}}$ for discrete intervals of cone resistance at station BH1.

For measurements at station BH11, the static velocity data q_t^{cpt} (station BH11) and dynamically acquired, rate-corrected data q_t^{acc} (station BH11E to BH11G) can be evaluated regarding their agreement as a function of penetration depth. The data lie in a good agreement for the depth interval between 1.0 and 1.7 m, whereas for shallow depths the cone resistance is overestimated by q_t^{acc} in reference to q_t^{cpt} (see Figs. 4.10b, 4.14, 4.15). This overestimation can be attributed to a change in sedimentary conditions, since the rate correction is carried out with a sediment-specific soil viscosity coefficient λ . As outlined above, a uniform λ of 1.5 was chosen for all dynamic penetrations. This factor fits well for depths below 1.0 m, where cohesive sediments of the BCT formation are suspected. However, for penetration depths above 1.0 m, Holocene sands of the TER formation are indicated by the sub-bottom profiler data and the results of the static velocity CPT at station BH11. The strain rate effect for penetrometers impacting at high rates is not as well investigated for noncohesive sediments as it is for cohesive sediments (see above). Therefore, the observed mismatch is taken as indicator for the sandy sediments of the TER formation.

The high values of dynamically acquired cone resistance in the upper interval (between 0 and 0.3 m for q_t^{acc}) reproduces throughout the impact

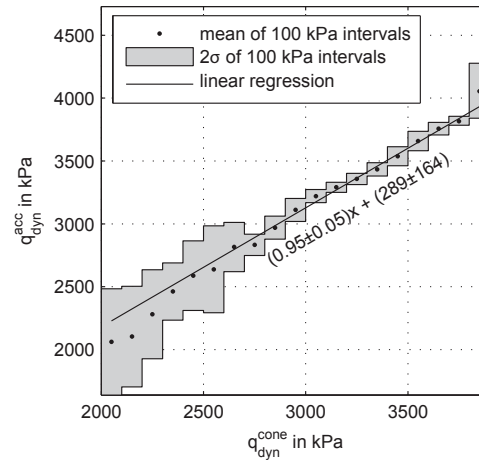


Figure 4.13 – Directly measured cone resistance $q_{t,dyn}^{cone}$ versus inferred cone resistance based on acceleration measurement $q_{t,dyn}^{acc}$ at station BH1 for the 0–0.7 m depth interval.

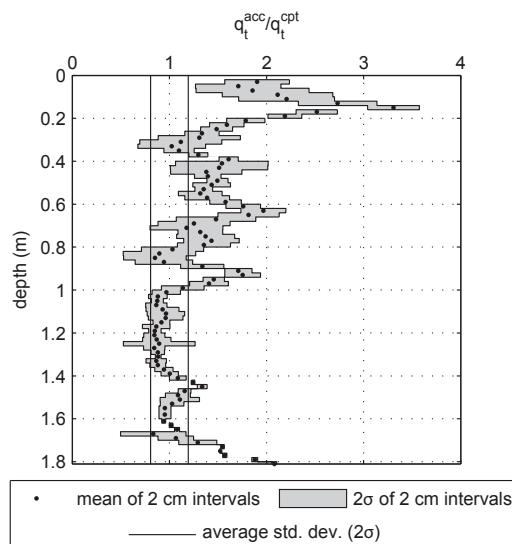


Figure 4.14 – Relation between averaged rate-corrected cone resistance data from the acceleration sensors q_t^{acc} at stations BH1E–G, and the static velocity CPT data q_t^{cpt} (the latter resolved at 0.02 m).

penetrometer measurements BH11E to BH11G (see Fig. 4.10b and the correlation in Fig. 4.13). However, these elevated cone resistance values are not well represented in the static velocity data (Fig. 4.10c and discrepancy in Fig. 4.14). This may be attributed to the fact that these surficial sediment layers might have been altered during testing by the static velocity CPT. Additionally, the TER member is described to feature a rich mollusk fauna. The presence of shells or shell fragments has an effect on impact penetrometer measurements. As reported by Stark and Wever (2009) and Stephan et al. (2011), shells provoke high deceleration of impacting penetrometers, which is influenced by abundance and orientation of the shells. This may also serve as an explanation for the high near-surface amplitude of deceleration and tip resistance obtained with the impact penetrometer.

4.5.2 Combining static and dynamic testing

The concept of determining the cone resistance from acceleration measurements follows the notion that deceleration due to friction along the rod of the penetrometer plays a minor role compared to that exerted by the sediment resistance force and transferred over the cross-sectional area of the lance. This is because accelerometers sense the acceleration of the entire instrument in relation to the gravitational acceleration.

The sleeve friction of the Holocene sediments can be determined from static velocity testing. The friction ratio is a commonly employed measure for sleeve friction assessed by cone penetrometers (see Eq. 11). For the considered depth interval of 0 to 2.5 m, the measured values of sleeve friction amount to a fraction of the cone resistance q_t , resulting in friction ratios F_r lying in the range between 0.5 and 2 %, which is typical for sandy sediments (see also Fig. 4.10).

Following Robertson (1990), the friction ratio is plotted against the normalized cone resistance (see Eq. 4.9), which allows a classification of the sediment. This has been done for the static velocity CPT data in Fig. 4.15, together with the relationship between the normalized pore pressure and normalized cone resistance (see Eqs. 4.9, 4.11). For the purpose of interpretation, two units were defined in the dataset, the first unit ranging from 0–1.56 mbsf and the second unit for all measurements below 1.56 mbsf. The upper unit lies in classes five and six, which are described as clean sand to sand mixtures (silty sand to sandy silt) in accordance with the description of the TER formation (Fig. 4.15, blue), while the lower unit is classified as silt mixture to clay in accordance with the description of the upper layer of the BCT formation (Fig. 4.15, red).

Additionally, the normalized cone resistance was calculated for the cone

resistance deducted from the deceleration of the LIRmeter. Because Q_t is the only parameter (of the parameters Q_t , F_r and B_q) that can be inferred from deceleration data, the dataset is one-dimensional and therefore shown in Fig. 4.15 as a frequency distribution (i.e., number of measurements within specific Q_t intervals). The normalized cone resistances of the LIRmeter lie in the range of classes four and five for the lower unit, and five to seven for the upper unit. Additionally, the Q_t inferred from deceleration data is presented as a function of the friction ratio from the static velocity test (Fig. 4.15, light colors). Both one-dimensional impact penetrometer data and static velocity CPT data match regarding the discrimination of the two sedimentary layers based on Q_t and the occurrence of measurements in the respective classes. Some overlap can be observed at the interface between classes 5 and 6 for both dynamic and static testing. For both measurement approaches, the majority of samples lie in class five for the lower unit, where the majority of samples for the upper unit lie in class six. The present approach shows that, if reasonable presumptions on interface friction between penetrometer and soil or F_r can be drawn or made based upon measurements, then sediment classification using impact penetrometers such as the LIRmeter is possible on the basis of the determination of the tip resistance q_t^{acc} .

4.5.3 Extending the spatial coverage of static velocity CPT

Because dynamic penetrometer measurements conducted using the LIRmeter lack side friction and pore pressure data, quantitative geotechnical interpretation is limited to the derived q_t^{acc} . Moreover, the parameter λ for the strain rate correction is sediment-specific, which requires knowledge of the sediment properties. Such properties can be determined at a reference location by sampling and *ex situ* laboratory tests or by *in situ* measurements. Using station BH11 as reference station, information from BH11 can be extended by the use of dynamic penetrometer measurements. The thickness of the Holocene sand layer (TER formation) can be determined from the corrected cone resistance q_t^{acc} in combination with data from the BH11 reference station. At station BH11, the q_t of static velocity CPT shows a decrease at a penetration depth of approx. 1.5 m (see Fig. 4.11b) along with an increase in pore pressure (see Fig. 4.10c). The change in sediment response to the penetrometer tests can be attributed to a transition from Holocene sedimentation (TER) to the infill of Weichselian glacial valleys (BCT). This interpretation is supported by seismoacoustic structures in sub-bottom profiler data, static velocity CPT measurements, and the regional geologic context described by various authors

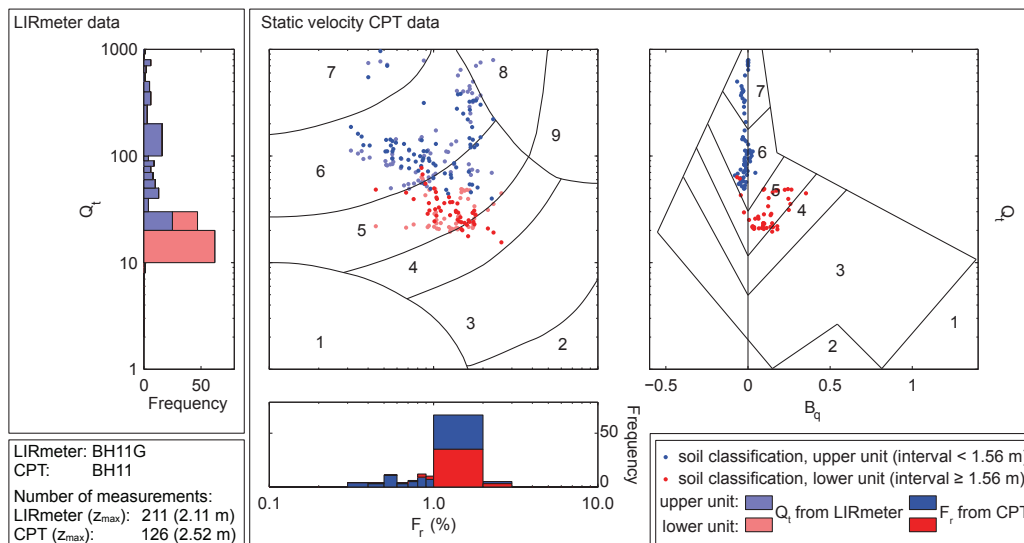


Figure 4.15 – Soil classification incorporating normalized cone resistance Q_t , normalized friction ratio F_r and pore pressure ratio B_q (cf. Robertson, 1990), with dynamic LIRmeter-based Q_t distribution supplemented by static CPT data. Soil behavior types: 1 fine-grained, 2 organic-rich, peat, 3 clay to silty clay, 4 silty clay to clayey silt, 5 sandy silt to silty sand, 6 silty sand to sand, 7 sand to gravelly sand, 8 clayey sand to very stiff sand, 9 very stiff fine-grained. Depth interval at station BH11: blue dots 0–1.56 m, red dots 1.56–2.50 m. Light colors Impact penetrometer (LIRmeter) data, dark colors CPT data.

(e.g., see Cameron (1992) for compilation). This inferred border is continued through profile A of dynamic penetrometer measurements and the observed decrease in cone resistance (see Fig. 4.11b). Additionally, the lower boundary of occurrence of parallel to subparallel reflectors (see Fig. 4.11a) in the hydroacoustic dataset supports the interpreted transition from Holocene to Pleistocene sediments.

Indeed, the uniform correction of strain rate seems to overestimate the cone resistance of the Holocene formations (cf. higher ratio in Fig. 4.14 for the upper depth interval) resulting in a higher contrast in q_t^{acc} of the two sedimentary units. The transition between Holocene and Pleistocene formations with the expressed decrease in cone resistance around 1 mbsf is likewise observable in the more distant profiles B, C, and D (see Fig. 4.9b for penetrometer records). The overlying Holocene sediments are not well resolved in the acoustic data due to the masking effect. It is therefore not possible to identify the depth of the transition from mechanically resistant fine-grained sand of the Holocene TER formation to the mechanically weaker glaciolacustrine to glaciomarine clays of the Pleistocene BCT formation solely on the basis of the sub-bottom profiler data. However, the combination of hydroacoustic datasets and dynamic penetrometer measurements in combination with a static CPT enhances the ability to interpret these partially masked intervals in the hydroacoustic datasets.

4.5.4 Pleistocene formations, Weichselian glacial valley

For Pleistocene sediments at the interface between the Holocene and Pleistocene, geological maps postulate two formations in the study area. Stations BH1 to BH10 lie within a sector where the BCT formation has been identified. Station BH11 lies in a sector where the WLG formation has been identified (see Fig. 4.2). Data from measurements carried out within the context of this field trial show in both hydroacoustic and penetrometer datasets that the glacial valley extends beyond station BH11. Since the WLG formation is described as fine-grained sand with thicknesses of up to 6 m (see Section 4.2), it should demonstrate both acoustically and mechanically stronger characteristics than the overlying TER member of Holocene age. The incising glacial valleys of the Weichselian glaciation are seismostratigraphically younger than the depositions forming the WLG formation (Cameron, 1992). The expected characteristics of the WLG formation are found in neither the hydroacoustical nor the penetrometer datasets. Moreover, the presence of WLG depositions is extremely unlikely in combination with the erosional

formation of Weichselian valleys.

Data from both static velocity and impact penetrometer testing show that the resistance decreases with depth (see Fig. 4.11). From the pore pressure data (Fig. 4.10c), a reduction in sediment permeability may be derived at a depth of 1.5 m. Therefore, on the basis of both static and dynamic penetrometer measurements (see Figs. 4.9, 4.11), it is suggested that the glacial valley with its muddy low-permeability infill extends much further to the NW, beyond station BH11 (see hydroacoustics in Figs. 4.9a and 4.12). This interpretation necessitates updating of maps reported by Cameron et al. (1986) and Jeffery et al. (1989).

4.5.5 Drainage conditions

The drainage capacity of the tested sediments plays a role in the interpretation of the penetration data because the penetration speeds are high and the hydraulic conductivity of the sediment is limited. The drainage conditions have been estimated using the concept of normalized velocity (see Fig. 4.8). The penetration velocities are shown in Fig. 4.10 as a function of depth. The penetration velocity ranges above 0.5 m/s for nearly the whole penetration interval, with a sharp decrease in velocity over the last few centimeters, which results in undrained conditions assuming best case conditions (i.e., sandy sediment). Thus, parameters such as shear strength calculated on the basis of the measured cone resistance yield conservative estimations due to the pore overpressure generated during penetration, causing an apparent weakening of the soil. Consequently, penetrometer measurements solely qualify to derive undrained parameters such as undrained shear strength (as found by Danziger and Lunne, 2012; Steiner et al., 2014).

4.6 Conclusions

A processing scheme has been applied to the dynamically acquired acceleration data of a free-fall lance, resulting in a depth profile of cone resistance q_t^{acc} . It could be demonstrated that:

- Acceleration-based measurements with the LIRmeter are coherent with dynamically acquired cone resistance data.
- Dynamically acquired data (either directly measured or inferred from deceleration) are, under certain presumptions, both qualitatively and quantitatively suitable to determine cone resistance.

This encourages the future application of acceleration based impact penetrometer testing of marine sediments. The benefits of the suggested measurement principle can be summarized as follows:

- The acceleration measurement is insensitive to external influences such as hydrostatic pressure, and extreme and rapidly changing mechanical loads. Therefore, this method was demonstrated to be a robust and reliable method for geotechnical *in situ* testing.
- The high level of reproducibility of acceleration-based penetrometer measurements encourages the future use of the measurement method to obtain results that are comparable to standard geotechnical tests.
- Following the combined approach of dynamic and static penetrometer testing, it is possible to extend the results from static velocity CPT over a wider area using dynamic penetrometer tests.

The cone resistance determined from impact penetration testing can be used, after data processing, in the same way as static velocity data for common soil classification schemes, such as those given by Robertson (1990). However, given the discussed inherent limitations of the measurement strategy, a stand-alone use of acceleration-based penetrometer testing is a challenge for interpretation when unknown sediments are tested. Therefore, knowledge about the depositional context, as outlined within this study, is crucial for the interpretation of the dynamically acquired data. The following limitations on the measurement principle persist and need to be taken into account when impact penetrometer testing is performed:

- The assumption that the lance is decelerated solely by stresses acting on the interface between soil and the conical tip only holds true when slender penetrometers with non alternating rod diameters are used (e.g., full-flow penetrometers, where the diameter of the tip is greater than the rod diameter). Non-uniform diameters and complex geometries require further processing, and may complicate data interpretation.
- Soil-specific parameters (soil viscosity coefficient λ) or knowledge about the sediment (amount of shaft friction and bulk density for cohesive, soft sediments) are required for data processing, based on additional testing or estimations from other sources.
- Drainage conditions may alter the sediment response, in most cases resulting in measurement parameters that will yield “undrained” geotechnical quantities.

Based on the experience gathered so far, impact penetrometers such as the LIRmeter are robust and easily deployable instruments whose deceleration records during penetration provide reliable and robust data. These data can be interpreted as cone resistance, and thus supplement existing conventional marine geotechnical *in situ* tests. Additionally, results from dynamic penetration testing (in combination with static velocity CPT data and hydroacoustic records) in the study area indicate the presence of a glacial valley filled with low permeability sediments, in accordance with published datasets. However, this study revealed that the northwesterly border of the valley extends much further to the northwest than previously documented.

Acknowledgements We greatly appreciate cooperation with Fugro that enabled the field trials and comparative measurements, as well as generous access to sub-bottom profiler and static velocity CPT data granted by Gaz de France Suez E&P Nederland B.V. and provided by Fugro. We would like to thank the captain and crew of Fugro's vessel Markab for their tireless support during the measurement campaign in February 2013, as well as D. Ruijtenbeek of Fugro and our engineer B. Heesemann for their help. The paper benefited from external assessments by J. Terwindt and E. Tervoort (both Fugro), journal reviews by N. Stark and V. Moon, and feedback from the editors.

Chapter 5

Laboratory testing

Laboratory impact penetrometer experiments in dense
sand containing cohesive fines

Stephan, S¹ ✉ and Kreiter, S²

Submitted to / under revision: *Géotechnique*; Received: 31 July 2015 /
Under Revision: 28 September 2015

¹Universität Bremen
Department of Geosciences
28359 Bremen
sstephan@uni.bremen.de

²Universität Bremen
MARUM - Zentrum für Marine Umweltwissenschaften
28359 Bremen, Germany

Abstract Cone penetration tests (CPT), and even more impact penetrometer tests are difficult to interpret for mixed sediments. This study investigates sensor performance of a marine dynamic impact penetrometer, as well as the suitability of such a penetrometer for testing of dense sands with low amounts of cohesive fines. Such sediments are prominent in coastal areas, where utilization and exploitation of the sea floor is prevalent, due to shallow water depth and the proximity to the shore. To investigate the sensor performance, laboratory experiments were set-up involving a deployment apparatus for the penetrometer, the construction of remolded dense soil targets, and geotechnical tests to obtain reference values, which were determined using the state parameter relationship with cone resistance. It was shown, that acceleration sensors are virtually interchangeable with conventional strain gauge sensors in the cone. However, factors influencing the acceleration measurement are discussed. It has been found, that the dynamic penetration data needed a correction for the impact velocity. Therefore, a model was chosen, where a rate parameter was back-fitted. In this manner, a high degree of correlation between the rate-corrected cone resistance data and the established state parameter relationship for the dense sand targets was established.

Résumé Il est difficile d'interpréter les épreuves du pénétrömètre statique et en particulier les mesures du pénétrömètre-impact dans des sédiments mixtes. Cette étude examine d'une part l'efficacité de capteurs placés dans les pénétrömètres-impact marins et d'autre part leur aptitude à des analyses dans des sables à faible proportion de granité fine et cohésive. De tels sédiments se trouvent en particulier dans les régions proches de la côte, où le fond marin est travaillé du fait de la proximité de la côte et du peu de profondeur de l'eau. Pour analyser l'efficacité des capteurs, on a entrepris des expériences en laboratoire. Dans le cadre des expériences on a mis au point des instruments, effectué des échantillons et entrepris des essais géotechniques afin d'obtenir des valeurs de référence sur la base du paramètre d'état. On a pu démontrer que les jauges de déformation conventionnelles dans le cône sont interchangeables avec les capteurs d'accélération. Toutefois la discussion porte aussi sur les facteurs qui ont un impact sur les mesures d'accélération. On a constaté que les données de la pénétration dynamique requièrent une correction en ce qui concerne la vitesse de pénétration. C'est pourquoi on a choisi un modèle correctif adéquat et calculé ensuite sur cette base un paramètre de taux. De cette manière on a pu établir une concordance très satisfaisante entre la résistance au cône avec correction de vitesse et la résistance au cône avec emploi du paramètre d'état.

5.1 Introduction

Geotechnical testing of marine sediments is widely conducted in research and commercial applications. Especially near-surface geotechnical properties are of interest for e.g. cable burial or the installation of pipelines. However, testing of surficial marine sediments is challenging: retaining of undisturbed samples and subsequent laboratory testing is difficult and requires extra precautions for sandy sediments (Sanglerat, 1972; Frost and Park, 2003). Moreover, coring may disturb or even alter or mix up the sedimentary fabric (Skinner and McCave, 2003). Therefore, *in situ* testing is established as favorable method to obtain the geotechnical properties of marine sediments.

In situ testing is often done using the cone penetration testing (CPT) method, where cone resistance q_c and sleeve friction f_s are measured during the penetration of a conical tip into the soil. Most modern systems measure additionally the pore pressure u and are called piezocone testing or CPTu. Marine CPT is done either maintaining a steady penetration velocity with devices resting on the sea floor (Lunne et al., 1997), by downhole CPT from a drill vessel (Sanglerat, 1972), or by utilizing so-called dynamic or impact penetrometers (Dayal, 1974; Stephan et al., 2012).

In contrast to conventional frame-based CPT, dynamic penetration testing (DPT) offers the advantage that no unwanted stresses are exerted on the surficial sediments by the measurement apparatus, since dynamic penetrometer immerse into the sediment due to the momentum they have gathered during the lowering or free fall through the water column. Due to this measurement approach, DPT devices are time- and hence cost efficient in deployment and recovery. Different types of impact penetrometers are utilized for DPT. These penetrometers are either rapidly lowered by winch and tether, or fall free through the water column. Generally, two different measurement approaches are followed: direct measurement of at least one parameter of q_c , f_s , and u (e.g. by Dayal and Allen, 1973; Osler et al., 2006a; Stegmann and Kopf, 2007), and determination of q_t or s_u from kinematic quantities such as acceleration a and/or velocity v (e.g. by Stark et al., 2009b; Mulhearn, 2003; Beard, 1981; Stephan et al., 2011; Stoll et al., 2007). Impact penetrometers exist in a variety of sizes and are – to some extent – purpose-specific designs. Small and lightweight devices, such as the expendable bottom penetrometers XBP (Stoll et al., 2007) or the NIMROD device (Stark et al., 2009a) usually penetrate in the order of centimeters, have a projectile-like shape, and are used to investigate surface processes in detail.

Intermediately sized devices are typically lance-shaped, such as the marine impact penetrometer (Dayal and Allen, 1973), the expendable Doppler penetrometer (Beard, 1981; Orenberg et al., 1996), instrumented gravity cor-

ers (Preslan, 1969; Villinger et al., 1999), the STING penetrometer (Mulhearn, 2003), the PROBOS lance (Stoll et al., 2007), the FFCPT (by Osler et al., 2006a), the FF-CPT (Stegmann et al., 2006a; Stegmann and Kopf, 2007) and the Lance Insertion Retardation meter (LIRmeter: Fabian et al., 2008; Stephan et al., 2012). These devices immerse deeper, and in some cases even completely, into the sediment. Thereby attaining penetration depths in the order of 1 to 10 m.

Huge penetrometers are mainly used for anchor and mooring purposes. Such deep penetrating anchors DPA (Lieng et al., 1999), torpedo anchors (de Medeiros, 2001) or nuclear waste carriers (Freeman and Schüttenhelm, 1990) gain high impact velocities during free fall and reach substantial penetration depths up to 40 m while having considerable dimensions (15 m) in length and mass (50 – 100 t). Penetration of these anchors is monitored as well (Lieng et al., 2010; Hembise et al., 1990), and subsequently used for soil investigation purposes.

Laboratory investigations of lance-shaped impact penetrometers were carried out by Dayal (1974) in clay and sand mixtures and later for the PROBOS-type lance by Stoll et al. (2007). Chow and Airey (2013) and Chow and Airey (2014) investigated the penetration behavior of a model STING penetrometer immersing into clay targets.

Soils behave rate-dependent (Casagrande and Shannon, 1949) and since dynamic penetration testing includes deformation rates of three or more magnitudes, the analysis of these tests needs to take rate effects into account (Lehane et al., 2009). The penetration velocity of DPT is initially high and subsequently discontinuously decreasing as the probe gets decelerated during sediment penetration. A widely applied logarithmic rate correction (Eq. 5.1) has been found by Kérisel (1961) and applied to correct velocity effects associated with impact penetrometer testing by Dayal (1974) and later studies in a variety of applications:

$$\frac{q_{t,\text{dyn}}}{q_{t,\text{ref}}} = 1 + K_{\text{rate}} \log_{10} \left(\frac{v_{\text{dyn}}}{v_{\text{ref}}} \right) \quad (5.1)$$

This relationship applies analogously to sleeve friction f_s (Dayal and Allen, 1975). Strain rate corrected cone resistance from DPT is used like cone resistance from common static velocity testing (CPT) to derive undrained shear strength s_u using an instrument and sediment-specific empirical cone factor N_k (Lunne et al., 1997), when clayey soils are tested (cf. e.g. Low et al., 2010). For non-cohesive soils, sediment state is often deducted from cone resistance measurement (Been et al., 1986, 1987) or relative density is estimated after Baldi et al. (1986) or Kulhawy and Mayne (1990). Moreover,

ultimate bearing capacity is calculated on the basis of bearing capacity theory (Meyerhof, 1961; Terzaghi, 1943) from shallow DPT and non-cohesive sediments (Stark et al., 2009b).

Within this study, we present systematic laboratory experiments with a recently designed, scaled version of the LIRmeter, which has a shaft length of 0.5 m (mLIRmeter). The original device has been developed at the University of Bremen (Stephan et al., 2012) and is used in combination with penetration lances with lengths of up to 6 m (Stephan et al., 2011, 2015). With this penetrometer, the kinematic approach of deriving cone resistance from deceleration measurement during penetration is followed.

This study is conducted en route of the development of the impact penetrometer “LIRmeter”, which is used to assess the strength of a variety of marine soil types under a broad range of environmental and deployment conditions. Mixed sediments in particular occur in coastal areas, such as the German Bight area of the North Sea (Zöllmer and Irion, 1996). Due to the proximity to shore and the shallow water depths, the utilization and exploitation of the sea floor is fostered e.g. for building or dredging operations, which need estimates on the seabed strength. The LIRmeter uses rugged sensors, which are less susceptible to external influences such as temperature, water pressure, shock loads, or excessive pore pressure (Stephan et al., 2012). However, due to simplifications and assumptions inherent to the penetrometer design, LIRmeter measurements are to be considered as supplementary measurements to established methods, such as CPT or laboratory tests (Stephan et al., 2015).

The aims of this study are to reveal

- whether impact penetrometer measurements are suited to assess cone resistance in dense sands with low contents of cohesive fines,
- whether conventional resistance sensors are substitutable by acceleration sensors to measure the cone resistance within impact penetrometers through their deceleration during impact, and
- to assess whether a rate correction is applicable to soil targets consisting of remolded, uncohesive sediments of high density with low amounts (10–15 %) of cohesive fines.

5.2 Laboratory study

To investigate the penetration behavior of the model penetrometer in remolded sand with varying content of Kaolin clay, laboratory experiments

were set up involving the model penetrometer and soil targets T . Isotropically consolidated, undrained triaxial tests were carried out to obtain reference values for the critical state parameter M . The CIU tests were conducted on reference samples R_1 to R_3 of each sediment type, which were composed and constituted using the same methods employed for the large scale soil targets. One-dimensional compression testing has been carried out on reference samples R_4 of each sediment type to determine critical-state parameters λ , κ , and e_Γ , and to obtain an estimate on the coefficient of consolidation c_v , and the hydraulic conductivity k_f of the soil targets.

5.2.1 Impact penetrometer

The mLIRmeter penetrometer has a standard tip geometry with a cone angle α of 60° and a cross sectional area of 1 cm^2 . Additional data on the penetrometer, which is equipped with acceleration sensors to measure the deceleration during the lance penetration into the soil target, are shown in Table 5.1, a schematic of the cone is shown in Fig. 5.1A. Sediment resistance force F_{res} , penetrometer velocity v and embedment depth d are calculated from the deceleration data. The data processing is described in detail in Stephan et al. (2012) and Stephan et al. (2015). Additionally, the tip is instrumented with strain gauges to obtain an independently measured dataset of q_c and f_s , acquired synchronously with the deceleration of the penetrometer. The instrumented miniature cone has been kindly provided by Fugro (Netherlands) for this study.

5.2.2 Testing apparatus and cone resistance from acceleration measurement

To ensure a controlled penetration and lowering phase, a guide has been designed to exclusively allow a defined vertical movement of the instrument during free-fall and penetration (see Fig. 5.1B). The instrument is suspended over pulleys by a nearly inelastic tether and is guided with rails. The model penetrometer is balanced using counter masses, which are likewise attached to the tether, allowing the control of uniform acceleration a during the lowering phase in air, which is dependent on the ratio of counter mass m_1 , mass of the penetrometer m_2 , and gravitational acceleration g . Neglecting frictional forces, inertial force of the deflection rollers and air resistance, a is described as follows:

$$a = g \frac{m_2 - m_1}{m_2 + m_1} \quad (5.2)$$

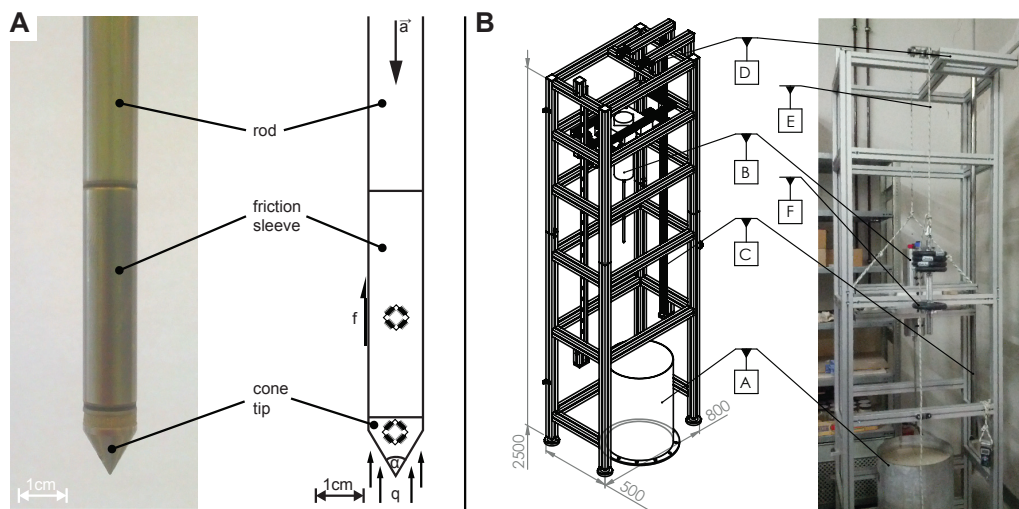


Figure 5.1 – A: Photograph and schematic of the instrumented cone. Tip and frictional loads q_c , f_s are sensed using strain gauges. Signals are fed through wires within the hollow rod into the mLIRmeter data acquisition. During fall, the mLIRmeter is accelerated with acceleration a . B: Schematic drawing and photograph of the experimental setup. All dimensions in mm. A: Bucket with soil specimen; B: mLIRmeter with attached 1 cm^2 cone; C: guides for vertical movement; D: deflection rollers to guide the tether which connects guidance frame and counter weights; E: tether; F: countermass.

Table 5.1 – Mechanical and sensorial penetrometer characteristics. RMS: root mean square. DAQ: data acquisition.

Property	Unit	Value
Mechanical dimensions		
A_{tip}	10^{-4} m^2	1
α	$^\circ$	60
Total length (rod length)	m	1 (0.5)
Rod diameter	10^{-3} m	11.28
Surface of friction sleeve	10^{-3} m^2	1.56
Net mass	kg	13.7
DAQ		
Sampling Frequency (max)	Hz	500 (4000)
A/D Resolution	Bit	16
Battery capacity	Ah	23
RMS resolution		
A1 (ADXL335)	10^{-3} m/s^2	0.133
A2 (ADXL325)	10^{-3} m/s^2	0.054
A3 (ADXL327)	10^{-3} m/s^2	0.182
q_c	kPa	0.316
f_s	kPa	0.038

Once the instrument penetrates the soil specimen, a sediment resistance force F_{res} causes a change in acceleration of the penetrometer. Since acceleration is measured within the reference frame of the penetrometer, it is possible to obtain F_{res} from acceleration measurements by reformulation of Equation 5.2 to:

$$F_{\text{res}} = m_2(g - a) - m_1(a + g) \quad (5.3)$$

Assuming that the penetrometer is solely decelerated by the force acting on the conical tip, thus neglecting friction on the rod, it is possible to calculate dynamic total cone resistance: $q_{\text{t,dyn}}^{\text{acc}} = F_{\text{res}}/A_{\text{tip}}$. The load sensor in the tip of the penetrometer delivers, after correction for the unequal area effect (Lunne et al., 1997) total dynamic cone resistance from cone measurement $q_{\text{t,dyn}}^{\text{cone}}$:

$$q_{\text{t,dyn}}^{\text{cone}} = q_c + u_2 (1 - a_{\text{cone}}) \quad (5.4)$$

with a_{cone} being the cone area ratio. The total dynamic cone resistance from acceleration measurement $q_{\text{t,dyn}}^{\text{acc}}$ does not need to be corrected for the unequal area effect, since the acceleration sensors are not affected by pressure differences. The cone sensor measurements are used as independently acquired dataset for the validation of accelerometer data. The dynamic sleeve friction $f_{\text{s,dyn}}$ is used to assess whether the friction on the rod is negligible.

5.2.3 Soil components

The sand fraction consisted of a well-sorted, medium sand with subrounded, pure quartz particles. The sand component is commercially available from Schlingmeier Quarzsand GmbH & Co. KG (Schwülper, Germany), Type: G20T. To vary penetration resistance, pure kaolin (pottery) clay was added at relative mass contents of 10 % (SED I) and 15 % (SED II). The grain size of the fines ranged from clay ($< 2 \mu\text{m}$) to silt. The pottery clay is commercially available from Sibelco Deutschland GmbH (Ransbach-Baumbach, Germany). The grain size distributions of the samples, as well as the distribution of the clean sand, given as reference, are shown in Fig. 5.2.

5.2.4 Sample constitution

To obtain reproducible soil states, the sediment targets were compacted to their maximum dry density at their respective optimal water content for compaction w_{opt} by moist tamping using the Proctor technique DIN18127 and (Howell et al., 1997). The w_{opt} had been determined with a series of pretests after DIN18127. The minimum and maximum void ratio e_{min} and

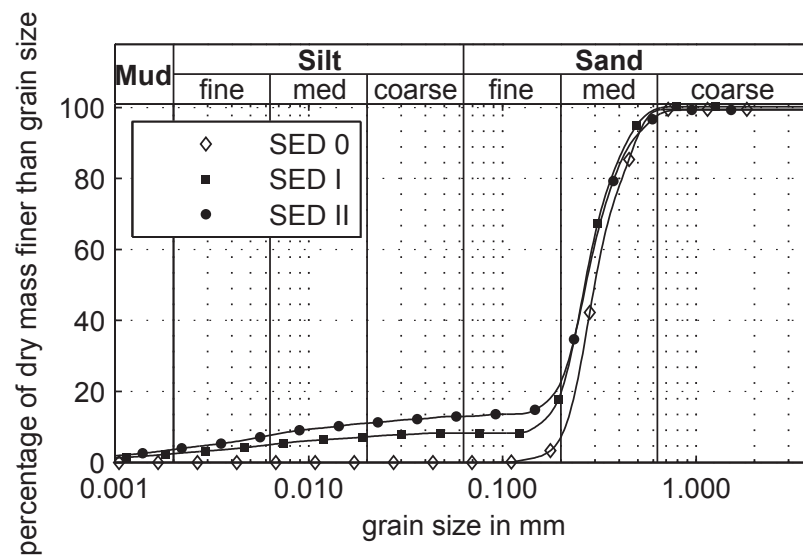


Figure 5.2 – Grainsize analyses of constructed soil specimen (SED I and SED II), as well as the grain size distribution of the pure sand (SED 0). The grain size distribution has been determined using a laser diffraction particle size analyzer (Coulter LS 13 320 series).

e_{\max} were likewise determined with a series of pretests after DIN18126, which is applicable to mud contents of up to 15 %. Before compaction, the soil components were thoroughly dry-mixed, watered to their w_{opt} and let cure for 24 hours before constitution. Compaction was carried out layer wise (5 layers), while maintaining a standard compaction effort of 0.6 MNm/m^3 for T and R_1 to R_4 . The soil targets were composed in a large-scale mold of 0.38 m diameter, 0.6 m height (see Fig. 5.1B) using a rammer of 0.38 m diameter and a mass of 31 kg. The reference samples were constructed in a mold with 0.1 m diameter and 0.12 m in height after DIN18127, P100-Y or analogously ASTM D698-07, 4 in mold, manual rammer. The desired height of the soil targets was around 0.5 m, the height of the reference samples was determined by the height of the mold (0.12 m). To compensate for overcompaction of the soil targets due to the repeated treatment of the lower layers, the undercompaction method (Ladd, 1978) has been applied with an initial undercompaction (u_1) of 4 % (Germaine and Germaine, 2009). Subsequent undercompaction u_n is calculated for each layer i by

$$u_n = u_1 \cdot \frac{j - i}{j - 1} \quad (5.5)$$

with j being the total number of layers. After compaction, a hydraulic gradient was applied to the targets T over a permeable interface below and around the soil specimen for a duration of at least 24 hours, which is a multiple of the required time by the hydraulic conductivity of the sediment (see Table 5.2). Samples R_1 to R_4 were extracted from the small scale mold using cylindrical cutters. Saturation of R_1 to R_3 has been carried out during sample installation in the triaxial testing cell by application of a vacuum and subsequent saturation with de-aired water. Samples R_4 were submerged in de-aired water within the oedometer apparatus.

5.2.5 Sample state

Sediment properties after compaction are shown in Table 5.3, i.e. the soil targets T and reference samples R_1 to R_4 , which were used for triaxial and oedometer testing. Table 5.3 also denotes the errors in the parameters resulting from propagation of errors resulting from weighting accuracy in the sample preparation technique. The dry densities ρ_d were determined from the mass of the soil components and the volume of the sample after compaction. The dry densities have tolerances around 2 % for the big soil target (T in Table 5.3) and the reference samples (R_1 to R_4 in Table 5.3).

Table 5.2 – Results of geotechnical testing of samples R_1 to R_1 . Remolded specimen R_1 to R_3 were constructed for triaxial testing, samples R_4 were constructed for one-dimensional testing. See Table 5.3 for physical properties and sample state. E_s (oedometer modulus), c_v (coefficient of consolidation) and k_f were calculated for a loadstep of 100–200 kPa.

		SED I			SED II		
property	unit	R_1	R_2	R_3	R_1	R_2	R_3
Triaxial CIU testing (DIN18137)							
p'_c	kPa	22	201	269	87	153	164
e_c	-	0.470	0.438	0.434	0.405	0.398	0.396
B	-	0.9	0.94	0.93	0.99	0.84	0.89
BP	kPa	399	299	299	399	399	299
M	-		1.41			1.38	
ϕ'	°		34.7			34.3	
K_o	-		1.88			2.36	
One-dimensional compression testing (DIN18135)							
		R_4			R_4		
C_c	$1/\log_{10}(\sigma'v)$	0.0325			0.0332		
C_s	$1/\log_{10}(\sigma'v)$	0.0087			0.0081		
λ	$1/\ln(p')$	0.0141			0.0144		
κ	$1/\ln(p')$	0.0038			0.0035		
e_Γ	-	0.528			0.474		
e_N	-	0.535			0.481		
ψ	-	-0.015			-0.004		
E_s	kPa	10700			9700		
c_v	m^2s^{-1}	$2 \cdot 10^{-5}$			$3 \cdot 10^{-6}$		
k_f	ms^{-1}	$2 \cdot 10^{-5}$			$4 \cdot 10^{-6}$		

Table 5.3 – Physical properties and sediment state for soil targets and reference samples. The dry density is given by ρ_d , the content of fines by c_c and the initial void ratio after compaction by e_i .

SED I						
		T	R_1	R_2	R_3	R_4
ρ_d	kg m ⁻³	1750±24	1750±9	1750±9	1750±9	1760±9
c_c	-	0.100±0.001		0.100		
w_{opt}	-	0.103±0.002		0.103±0.001		
e_{max}	-			0.91		
e_{min}	-			0.77		
e_i	-	0.51±0.01	0.51±0.007	0.51±0.007	0.50±0.007	0.50±0.007
SED II						
		T	R_1	R_2	R_3	R_4
ρ_d	kg m ⁻³	1840±23	1840±9	1850±9	1850±9	1850±9
c_c	-	0.150±0.001		0.150		
w_{opt}	-	0.107±0.002		0.107±0.001		
e_{max}	-			0.92		
e_{min}	-			0.73		
e_i	-	0.44±0.01	0.44±0.007	0.42±0.007	0.43±0.007	0.42±0.007

5.2.6 FFP testing campaign

In total, 21 penetrations were conducted with the model penetrometer. The fall height h , mass configuration m_{bal} (as difference between instrument mass and mass of the counter weights), impact velocities v_i and observed penetration depths d_{max} are shown in Table 5.4. Some combinations of m_{bal} and h were omitted, since penetration depth would have exceeded the height of T . The impact location has been positioned using a printed template, which could be attached to T and a laser pointer fixed to the shaft of the model penetrometer. The penetrometer was lifted to the desired height h and released either by removing a retention pin or by hand. The soil container was adjusted after each penetration. The penetration locations were spaced at least 9 rod diameters D apart from each other and 4 D from the border of the container., concordant to assumptions made for other model free-fall penetrometer (FFP) studies by e.g. Chow and Airey (2014) and FFP simulations (Abelev et al., 2009a; Lu et al., 2004). The drainage conditions during penetration depend on the velocity of the cone and the hydraulic conductivity of the sediment. High strain rate at low hydraulic conductivity yields undrained conditions. To assess drainage conditions, Finnie and Randolph

(1994) introduced the concept of normalized velocity, which is given as:

$$V = \frac{v_{\text{dyn}} \cdot D}{c_v} \quad (5.6)$$

with c_v as coefficient of consolidation. Finnie and Randolph (1994) and later authors (Jaeger et al., 2010; Kim et al., 2008) define a normalized velocity of 0.01 to 0.05 as boundary between completely drained and partially drained conditions and a normalized velocity of 10 to 30 as boundary between partially drained and undrained conditions for uncohesive, sandy sediments. Fig 5.3 shows, how c_v , V and v_{dyn} are connected.

5.2.7 Rate correction of penetration data

Dynamic penetration data needs correction for the penetration rate. A formula for rate correction is given in Eq. 5.1, where K_{rate} is a soil-specific rate factor, v_{dyn} is the penetration velocity, and v_{ref} is a reference velocity. For penetration tests, v_{ref} is typically set to the rate of a reference test, or to the standard rate of CPT (0.02 m/s). For rate corrections of penetration tests in non-cohesive sediments, the rate factor K_{rate} typically ranges between 0.6 and 1.5 (Stoll et al., 2007; Hossain et al., 2015; Stephan et al., 2011), whereas for cohesive sediments K_{rate} ranges between 0.05 and 0.5 (O’Loughlin et al., 2009; Zhou and Randolph, 2009). See also Table 5.5 for a non-exhaustive compilation of K_{rate} values in dependency of sediment type and penetrator. Beneath the log-relationship, other approaches exist to correct penetrometer data, as e.g. the arcsinh-approach (e.g. Randolph, 2004), the power-law relationship (e.g. O’Loughlin et al., 2009), and a rate correction following the concept of viscous fluids (Hossain et al., 2015; Zhu and Randolph, 2011). Steiner et al. (2014) assessed the performance of strain rate corrections with regard to dynamic penetration testing and showed, that the log- and arcsinh-relationships produce similar results. The log-relationship is the most established method, especially in the case, when non-cohesive sediments are tested (Stoll et al., 2007; Stark and Wever, 2009; Hossain et al., 2015; Stephan et al., 2011). Therefore, it has been used within this study. However, due to the mathematical formulation, Equation 5.1 causes unreasonably high values for penetration below the reference velocity. Therefore, data within that velocity range are omitted. Besides, they account for a very low fraction $< 1\%$ of the total penetration data (see Fig. 5.3B).

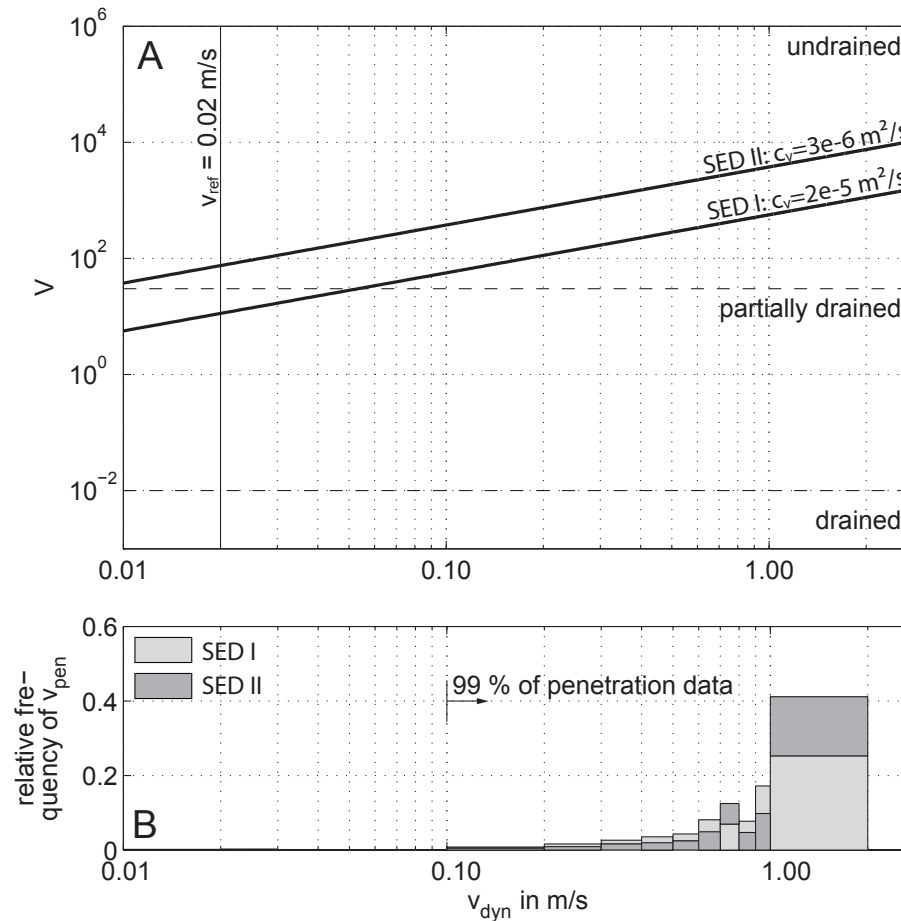


Figure 5.3 – A: Normalized velocity in dependency of insertion velocity and sediment type. Boundaries between drained, partially drained and undrained conditions from Finnie and Randolph (1994). B: Relative frequency of all velocities in dependency of sediment type. Penetration velocities have been averaged over constant depth intervals.

Table 5.4 – List of penetrometer deployments with impact velocities, kinetic energy at impact and penetration depth for sediment types SED I and SED II in dependency of fall height and mass configuration.

SED I										SED II				
h	m_{bal}	v_i	name of	E_{kin}	d_{max}	a_i	m_{bal}	v_i	name of	E_{kin}	d_{max}	a_i		
m	kg	m/s	penetration	J	m	m/s ²	kg	m/s	penetration	J	m	m/s ²		
0.3	7.41	0.71	PEN01	11.84	0.236	1.30	7.41	0.67	PEN01	10.55	0.200	0.85		
	9.84	0.93	PEN04	19.27	0.351	1.54	9.84	0.90	PEN04	18.05	0.282	0.91		
	12.26	1.12	PEN07	26.43	0.410	2.35	12.26	1.07	PEN07	24.12	0.390	1.44		
	12.26	1.10	PEN10	25.49	0.392	1.72	12.26	1.08	PEN08	24.58	0.398	1.94		
	12.26	1.12	PEN11	26.43	0.433	2.14	12.26	1.06	PEN09	23.67	0.391	1.65		
	12.26	1.10	PEN12	25.49	0.403	1.97								
0.5	7.41	0.94	PEN02	20.76	0.300	0.89	7.41	0.89	PEN02	18.61	0.262	1.02		
	9.84	1.20	PEN05	32.08	0.377	1.15	9.84	1.16	PEN05	29.98	0.358	1.40		
0.7	7.41	1.10	PEN03	28.43	0.324	0.70	7.41	1.06	PEN03	26.40	0.289	0.97		
	9.84	1.41	PEN06	44.29	0.417	1.48	9.84	1.37	PEN06	41.81	0.380	0.71		
	9.84	1.43	PEN08	45.56	0.419	2.14								
	9.84	1.43	PEN09	45.56	0.424	1.04								

Table 5.5 – Factors K_{rate} for the strain rate correction after Equation 5.1 in dependency of soil type and testing method.

Soil type	K_{rate} (log-relationship)	Testing method	Study
Sand	1.0 ... 1.5	Dynamic penetrometers	Stoll et al. (2007)
	1.25 (Quartz and Calcite)		Stark et al. (2009b)
Calcareous silt	1.5	Dynamic anchors (centrifuge tests) Full-flow penetrometer (pushed)	Stephan et al. (2011)
	0.6 ... 0.8		Hossain et al. (2015)
	0.05 ... 0.2		Einav and Randolph (2005)
	0.01 ... 0.3		Biscontin and Pestana (2001)
Cohesive sediments	0.13 ± 0.03	Laboratory vane tests	Peuchen and Mayne (2007)
	0.09 ... 0.19	Triaxial tests	Graham et al. (1983)
	0.13	Dynamic penetrometer	Steiner et al. (2012)
	0.1 ... 1.0	Dynamic anchors (centrifuge tests)	O'Loughlin et al. (2013)

5.2.8 Geotechnical Soil Testing

Undrained, monotonic triaxial compression tests have been carried out on R_1 to R_3 of each sediment type under different isotropic confining stress (CIU tests). Testing has been carried out according to DIN18137 using the MARUM (University of Bremen) dynamic triaxial testing device (Kreiter et al., 2010). The device has been operated in velocity controlled mode with a rate of 0.1 mm/min. Strain has been registered using external laser displacement sensors. Deviatoric stress is measured using a pressure compensated submersible load transducer within the testing cell with a force limit of 1 kN, whereas cell pressure is sensed externally. See Table 5.2 for the testing program and parameters.

The behavior of dense sands during CIU tests depends on the relative density of the tested sediment and the amount of fines. During CIU tests, dense sands are expected to show dilative behavior, or limited liquefaction behavior, reaching a *steady state of deformation* after large strains. This state is defined by the steady state line (SSL). For the determination of the SSL, concepts of critical state theory (Schofield and Wroth, 1968) can be applied analogously, when sands are tested (Ishihara, 1993).

Conventionally, the mean effective stress within the soil targets is calculated as follows

$$p'_{0j} = \sigma'_v (1 + 2K_{oj}) / 3 \quad (5.7)$$

using the formulation of Jaky (1944) with $K_{oj} = 1 - \sin \phi'$. However, for densified sands, Sherif et al. (1984) state, that horizontal stresses occurring during the compaction remain in the sample and are superimposed on stresses due to gravity effects as locked-in stresses, thus yielding higher passive earth pressures at rest (and consequentially confining stress) after:

$$p'_{0s} = \sigma'_v (1 + 2 \cdot (K_{oj} + K_{os})) / 3 \quad (5.8)$$

with $K_{os} = (\rho_d / \rho_{d(\min)} - 1) \cdot 5.5$ as coefficient of locked-in at-rest earth pressure. The effective stresses have been calculated assuming a hydrostatic pore water pressure distribution.

One-dimensional compression testing and data analysis has been carried out according to DIN18135 with two-way drainage using oedometer equipment with the R_4 samples (Table 5.2). From these tests, the compression index C_c , the swelling index C_s , as well as the c_v and the oedometer modulus E_s were determined. The latter are given for a specific load step (100–200 kPa), after the $\sqrt{t_{90}}$ -method (see e.g. Budhu, 2010) to assess drainage conditions during penetration.

The state parameter ψ (Been and Jefferies, 1985) serves as a measure to describe sand behavior in terms of e and p' in relation to a the steady state reference condition and is therefore defined as the void ratio difference of a consolidated soil volume e_c to the locus of the steady state line (SSL) in $e - \ln(p')$ -space (e_{ss}):

$$\psi = e_c - e_{ss} \quad (5.9)$$

The parameters governing the SSL (M , λ , κ) were determined from the geotechnical tests. The parameter e_Γ has been calculated by application of the Modified Cam Clay Model (e.g. Muir Wood, 1990) to the test data (see Dev et al. (2003) for details) as follows:

$$e_\Gamma = e_N + (\lambda - \kappa) \ln \left(\frac{M^2 + \eta_{K_o}^2}{M^2} \right) - (\lambda - \kappa) \ln 2 \quad (5.10)$$

with e_N as void ratio of the Normal Consolidation Line (NCL) at $p'=1$,

$$\eta_{K_o} = \frac{3(1 - K_o)}{1 + 2K_o} \quad (5.11)$$

and K_o as earth pressure coefficient at rest after Sherif et al. (1984), see also Eq. 5.8. The parameters e_Γ , M , λ , κ , e_N , and K_o are given in Table 5.2. The state parameter is used to back-calculate q_c profiles with depth following the approach of Been et al. (1987):

$$q_c = k \exp(-m \cdot \psi) p' + p \quad (5.12)$$

with coefficients $m = 8.1 - \log \lambda$ and $k = 8 + 0.55 \cdot 1/(\lambda - 0.01)$. The penetrators, which were used to determine this relationship in combination with calibration chambers were standard 60 ° cones (Been et al., 1986). The typical penetration velocity in calibration chamber testing is 0.02 m/s (Kim et al., 2010).

5.3 Results

5.3.1 Impact penetrometer testing

Results of impact penetrometer testing are shown in Fig. 5.4A–D in dependency of sediment type and penetration depth. Fig. 5.4E shows the correlation between directly measured cone resistance and cone resistance inferred from acceleration measurement.

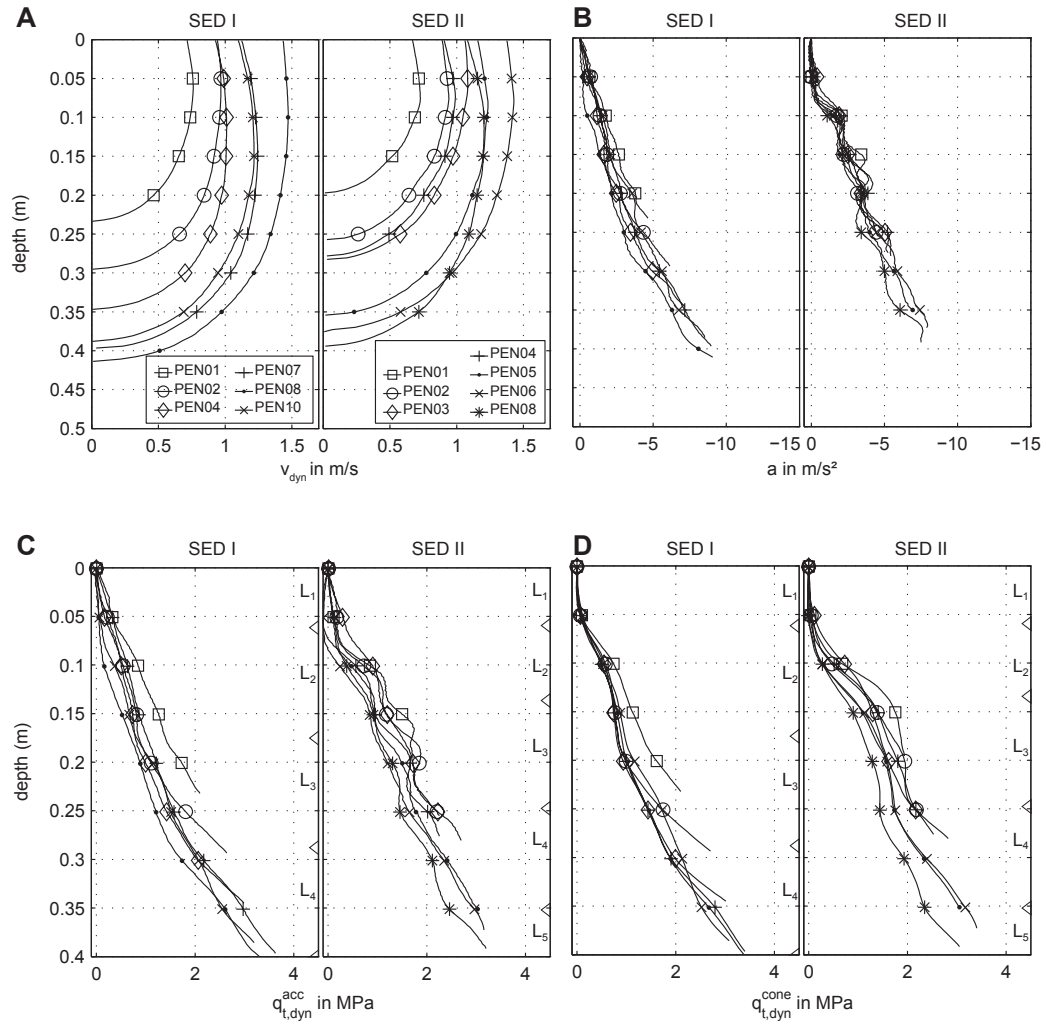
The impact velocity (Fig. 5.4A) decreases with depth, which is due to the sediment resistance force and the associated deceleration of the mLIRmeter. The penetration depth ranges between 0.24 m and 0.42 m for SED I and between 0.20 m and 0.40 m for SED II. The achieved penetration depth is linked to the impact velocity v_i (see e.g. SED I-PEN07 and SED I-PEN10) and to m_{bal} (see e.g. SED I-PEN02 and SED I-PEN04). The impact velocities range between 0.7 and 1.5 m/s for SED I and between 0.7 and 1.4 m/s for SED II.

Fig. 5.4B shows the acceleration during penetration in dependency of penetration depth. Acceleration at impact a_i has been subtracted, thus all acceleration-depth series start at 0 m/s² (cf. Table 5.4 for a_i). An increase in velocity is observable for some penetrations in the first 0.05 m, because the instrument is still accelerating in that depth range. The penetration depth of SED II-PEN08 is higher than the penetration depth of SED II-PEN05 and SED II-PEN06, although v_i is lower for SED II-PEN08. Instead, for this penetration, values for m_{bal} and acceleration at impact a_i were higher (see Table 5.4 for values). Due to friction in the system, the value of a_i is slightly below the theoretical value calculated after Eq. 5.2. The maximum deceleration during penetration reaches between 4.60 and 9.08 m/s² for SED I, and between 3.68 and 7.96 m/s² for SED II.

The acceleration records of both sediments show regular undulations, which are more pronounced in SED II than in SED I. The depth of these undulations is constant throughout all measurements for a specific sediment sample and correspond in the cone resistance measurements to stepwise increases in cone resistance. See e.g. SED II-PEN01 between 0.1 and 0.15 m penetration depth, Fig. 5.4D.

The dynamic cone resistance, deduced from acceleration measurement is shown in Fig. 5.4C. For both sediment types, $q_{t,\text{dyn}}^{\text{acc}}$ shows an increase with penetration depth. The undulations, observable in the acceleration record (esp. for SED II) likewise transfer into $q_{t,\text{dyn}}^{\text{acc}}$. The average increase in $q_{t,\text{dyn}}^{\text{acc}}$ amounts to 7.28 ± 0.23 MPa/m for SED I and 8.07 ± 0.10 MPa/m for SED II (see also Fig. 5.8). The directly acquired cone resistance $q_{t,\text{dyn}}^{\text{cone}}$ is shown in Fig. 5.4D. The average gradient of $q_{t,\text{dyn}}^{\text{cone}}$ amounts to 7.44 ± 0.14 MPa/m for SED I, and to 8.01 ± 0.11 MPa/m for SED II. The data from the cone resistance sensor show steeper increases at the layer boundaries followed by moderate increases throughout the respective layer, thus showing a stepwise pattern.

Fig. 5.4E shows the correlation between $q_{t,\text{dyn}}^{\text{acc}}$ and $q_{t,\text{dyn}}^{\text{cone}}$ for both sediment types. The cone resistance, determined from acceleration measurement reproduces the simultaneously but independently acquired cone resistance from direct measurement to a high degree, which is expressed as a linear function



The Figure is continued on the next page.

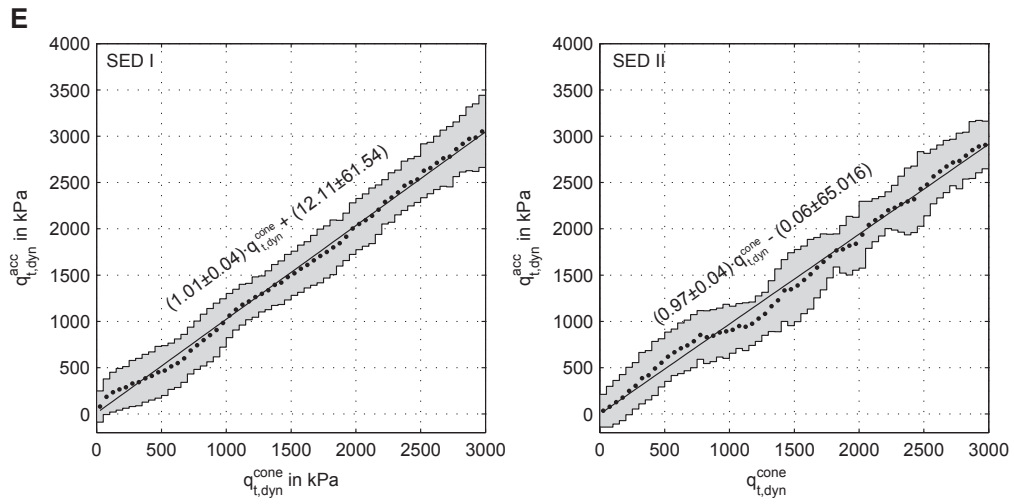


Figure 5.4 – A–D: Results of impact penetrometer testing in dependency of sediment type and depth, see A for a legend of all graphs in A–D. Balanced mass and velocity at impact are shown in Table 5.4. A: Dynamic velocity during impact v_{dyn} in dependency of penetration depth. B: Acceleration during penetration a . C: Dynamic cone resistance, deducted from acceleration measurement $q_{t,dyn}^{acc}$, open triangles: layer boundaries during target construction. D: Dynamic cone resistance, direct measurement $q_{t,dyn}^{cone}$, open triangles: layer boundaries during target construction. E: $q_{t,dyn}^{acc}$ in dependency of $q_{t,dyn}^{cone}$. Data from $q_{t,dyn}^{acc}$ are averaged in intervals of 50 kPa. Shaded area: 2σ -deviation of the intervals. Weighted linear fit is calculated on the basis of the standard deviation of each interval. The standard deviations of the fit coefficients (σ_m , σ_b in kPa) are given in the respective annotation.

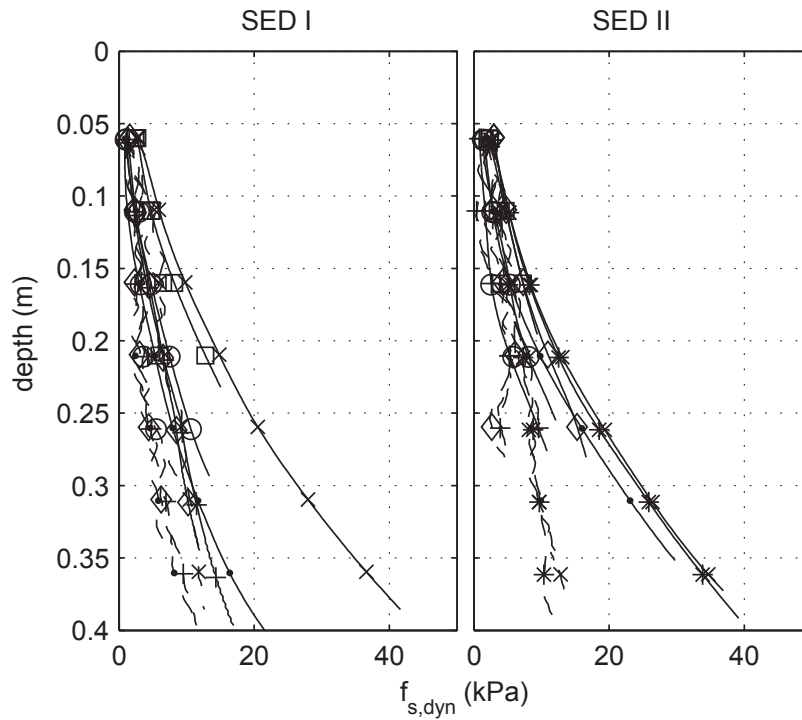


Figure 5.5 – Dashed lines: Dynamic sleeve friction data from the load cell. Solid lines: Total friction along the rod. Data begins at 0.051 m, since the friction sleeve was not fully embedded for shallower depths. Symbols: See Fig 5.4.

with a slope of 1.01 ± 0.04 for SED I and 0.97 ± 0.04 for SED II. The deviation of the averaged $q_{t,dyn}^{acc}$ values from the linear fit is high in the cone resistance ranges, where undulations occur. This is at 500 kPa or 0.05 – 0.10 m for SED I, and 1300 kPa (0.15 – 0.2 m) for SED II (see Fig. 5.4C).

The dynamic sleeve friction $f_{s,dyn}$ as a function of penetration depth is shown in Fig. 5.5 alongside the total friction along the rod for both sediment types. The total friction along the rod increases with depth, due to the increasing interface area with depth and reaches values of up to 40 kPa. The values of $f_{s,dyn}$ show a tendency to increase as well and reach up to 13 kPa for SED I and SED II.

5.3.2 Geotechnical soil testing

The results of the CIU test series are shown for both sediment types in Fig. 5.6. Deviatoric stress and evolution of pore pressure as function of axial strain are shown in Fig. 5.6A, effective stress paths (ESPs) and steady state lines are shown in Fig. 5.6B. The ESPs show a tendency to converge at higher deviatoric stresses. The envelope of the converged stress paths indicates steady state conditions resulting in $M = 1.41$ for SED I and $M = 1.39$ for SED II, corresponding to $\phi' = 34.7^\circ$ and $\phi' = 34.3^\circ$, respectively. However, as shown in Fig. 5.6A, steady state has not been attained during testing. The tests were carried out until the limit of the internal force sensor was reached, which corresponds to $\sim 10\%$ axial strain for samples R_1 and $\sim 5\%$ axial strain for samples R_2 and R_3 .

The results of one-dimensional compression testing are shown in Table 5.2. From these results, the SSL and the loci of the consolidated samples R_1 to R_3 are shown in Fig. 5.7. The values for the mean state parameter for both sediment types are given in Table 5.2. The consolidated samples lie below the SSL in $e - \ln(p')$ -space. The state parameter is used to back-calculate the cone resistance q_c in dependency of p' (see Equation 5.12), resulting in q_c -gradients of 2966 kPa/m for SED I and 3024 kPa/m for SED II. The coefficient of consolidation (see Table 5.2) is used as controlling factor for the determination whether drained or undrained conditions prevail during impact penetrometer testing (see Fig. 5.3).

5.4 Discussion

5.4.1 Geotechnical testing and soil behavior

The initial void ratios e_i achieved by compaction with the proctor method lie below the minimum void ratio e_{\min} , obtained from the test for maximum unit weight (after DIN18126, see Table 5.3 for values). This is owed to the fact, that the minimum void ratio is dependent on the compaction method (see also Blaker et al. (2015) on this topic). Moreover, platy-shaped grains, show a susceptibility in compression characteristics, depending on the compaction method (Castro and Poulos, 1977). Therefore, void ratios were used in favor to relative densities. The separate construction of soil targets and reference samples has been favored over direct sampling the soil target, which could have been done either prior or after penetration testing. This has been done to assure undisturbed reference samples and to maintain the integrity of the soil target.

The mean effective stress within SED II- T is higher with soil depth than

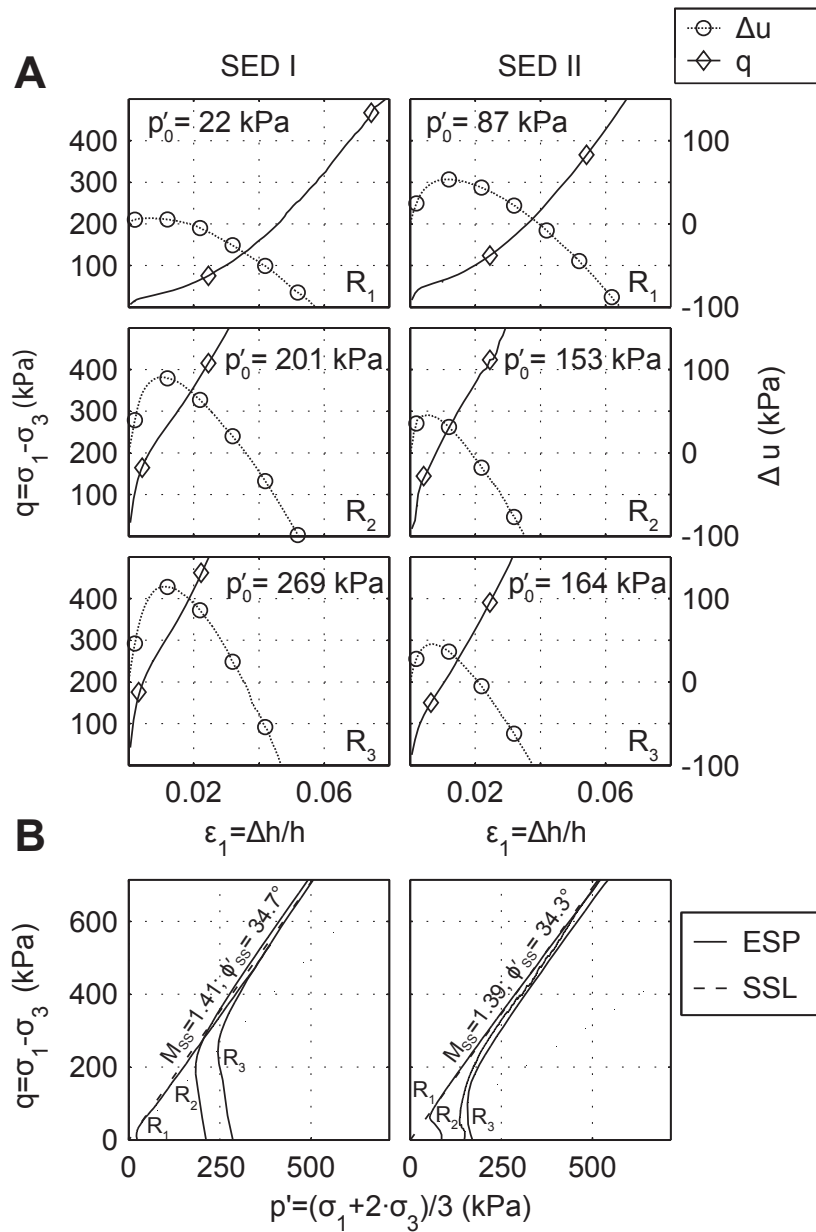


Figure 5.6 – Results of the CIU triaxial testing. A: deviatoric stress (left scale, solid line with open diamonds) and pore pressure change (right scale, dotted line with open circles) in dependency of axial strain. B: Effective stress paths (solid lines). Critical state lines for steady state conditions (inferred, widely spaced dashed lines).

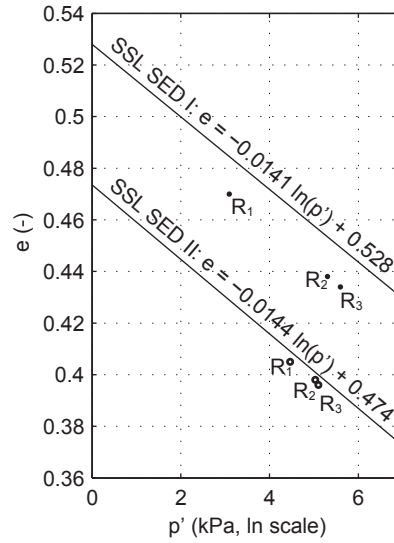


Figure 5.7 – Steady State Lines for SED I and SED II in $e - \ln(p')$ -space. The loci of consolidated samples R_1 to R_3 are shown with closed circles for SED I and with open circles for SED II.

for SED I- T (compare axes in Fig. 5.8), which is due to the higher dry density ρ_d , achieved during compaction. However, although the dry densities differ, the SSLs of SED I and SED II have nearly the same slope in $\ln(p') - e$ -space, and in $p' - q$ -space (see Fig. 5.7 and Table 5.2). Since the material composing the coarse grained matrix and the constitution procedures are the same for both sediment types, the higher density of SED II is attributed nearly exclusively to the fines content. This can be shown by calculating the granular void ratios e_G (Ni et al., 2004; Georgiannou et al., 1990), which amount to 0.683 and 0.684 for SED I and SED II, respectively. The granular void ratio considers the volume of the fines as additional void space. With e_G being nearly the same for SED I and SED II, the ρ_d difference of 90 kg/m^3 between SED I and SED II is to be accounted to the increased fines content. Moreover, it may be deduced that the different fine contents of $c_c = 10$ and 15% used in this study have a limited influence on the compression index of the samples, since they occupy less than the total available volume of voids. Moreover, Mitchell and Soga (2005) state, that for sediment mixtures, where free void space is present, the mechanical characteristics are dominated by the coarse matrix (see also Thevanayagama and Martin, 2002).

The triaxial tests show strictly increasing deviatoric stresses with strain

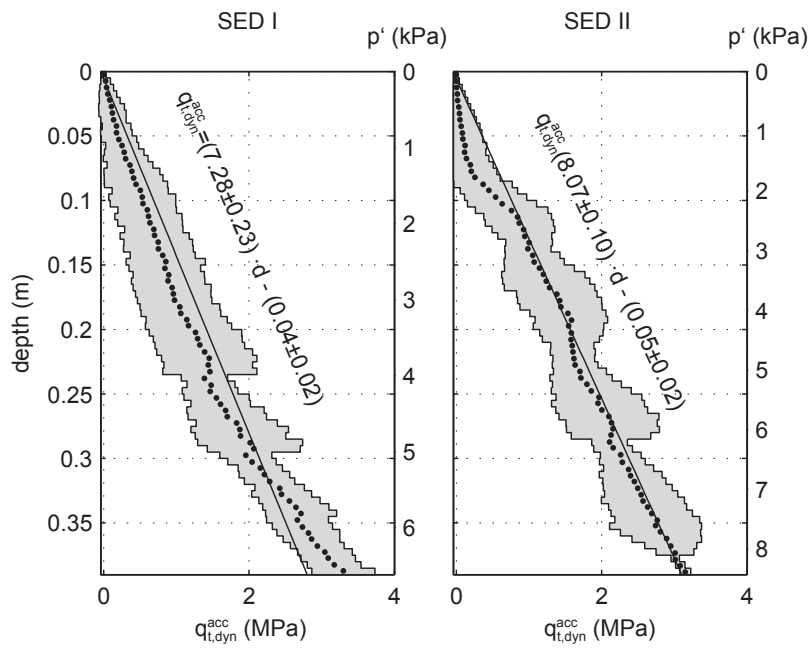


Figure 5.8 – Dynamic total cone resistance from acceleration measurement in dependency of soil depth. Averaged data from Fig. 5.4. The linear regression (line) has been calculated for mean values (dots). The errors of the fit were calculated from the 2σ standard deviation of the means, which is given by the gray bars.

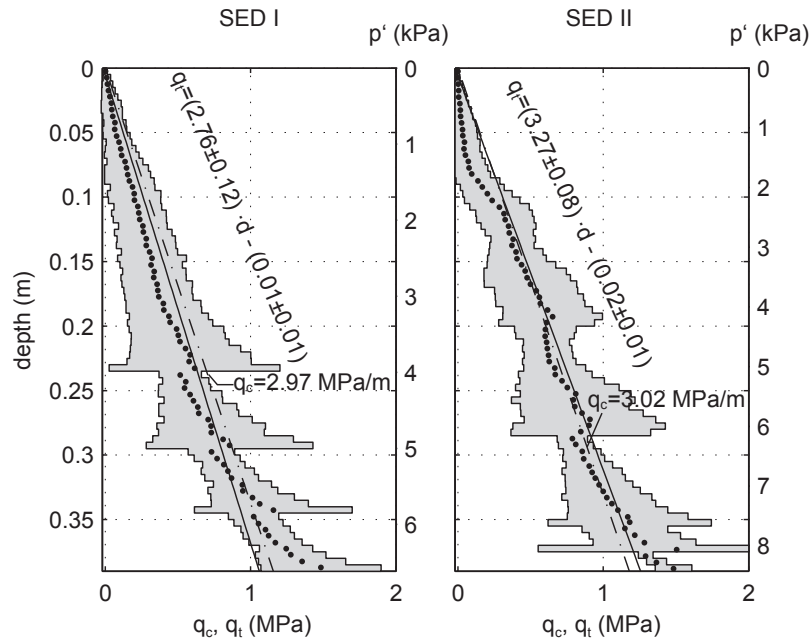


Figure 5.9 – Rate corrected total cone resistance for both resistance sensors and sediment types ($K_{rate} = 1$). See Fig. 5.8 for more information on the data. The back-calculated soil resistance profile (dash/dotted line) serves as a reference and was determined from the state factor and results of the geotechnical tests.

(see Fig. 5.6A). Also, the excess pore pressures become negative after an initial increase. Thus, the soils exhibit dilative behavior and steady state would be reached at large strains and high deviatoric stresses, which normally exceed the capacity of the testing equipment (Castro, 1969). The dilative behavior is confirmed by the location of the consolidated states of SED I and SED II below their respective SSL (Been and Jefferies, 1985; Castro and Poulos, 1977). Hence, ψ is negative. The linkage between *in situ* tests and sediment state (Kramer, 1996; Been et al., 1987) has also been used within this study to back-calculate the q_c profiles within the soil targets. See also Fig. 5.9 and Eq. 5.12.

The state parameter is susceptible to the determination of void ratios and the back-calculated cone resistance is susceptible to changes in the state parameter, and to the slope of the SSL. Carrying out a sensitivity analysis using values for λ and ψ with values within the range of the results from the geotechnical tests, it becomes evident, that the determined q_c is to a higher

degree dependent on λ , than to the state parameter ψ due to the low value of λ in Eq. 5.12. Caeteris paribus, a 10 % change in λ causes a 24 % change in q_c , whereas a 10 % change in ψ causes just 2 % change in q_c .

Admittedly, it must be considered (i) that the state parameter relationship is based on empirical data, which does not cover such dense, mixed sediments (ii) there are uncertainties in the governing parameters of Equation 5.12, which are hardly quantifiable, (iii) it could not be verified due to instrumental limitations, whether or not the sediment targets were completely saturated after construction and (iv) that the soil resistance may not increase linearly with penetration depth. However, the q_c from the state parameter relationship may serve as a reasonable first approximation of the true cone resistance within the soil targets.

5.4.2 Deployment apparatus

The performance of the deployment apparatus is assessed comparing the measured velocity to estimated velocities at impact, which can be calculated using Eq. 5.2. Theoretical and measured values are shown in Fig. 5.10. The measured values lie consistently below the theoretical values, which is attributed to the friction of the tether, bearings and the guidance rails, and to the rotational inertia of the deflection rollers, which are not accounted for by estimations after Eq. 5.2. The deviation of impact velocity is in the range of 16-28 % from the theoretical value. The scatter of the measured impact velocities is in the range of 1.7 – 2.7 % of the mean velocity for a respective fall height/mass configuration. The precision of the apparatus ensures therefore reproducible testing conditions. The friction and inertia in the system have an effect on both the lowering phase and the penetration phase. However, these effects are difficult to account for, since they are velocity dependent.

For the penetration tests, it was not important to accurately reproduce the theoretical impact velocity, since the kinematics of the penetrometer were anyhow recorded directly. Therefore, frictional and inertial forces may be neglected during the lowering phase.

During the penetration phase, frictional and inertial of the apparatus have an impact on the acceleration, as well as on the cone resistance measurement since they superimpose on the soil resistance force. Both measurements are still comparable, since they are exerted to the same external influences. However, the correlation to reference profiles does not account for the external influences. Therefore, values may be overpredicted. This is a common problem to impact penetration testing. Under marine conditions, e.g. hydrodynamic drag and drag within the soil complicate the interpretation of measurements (O'Loughlin et al., 2013; Hossain et al., 2015).

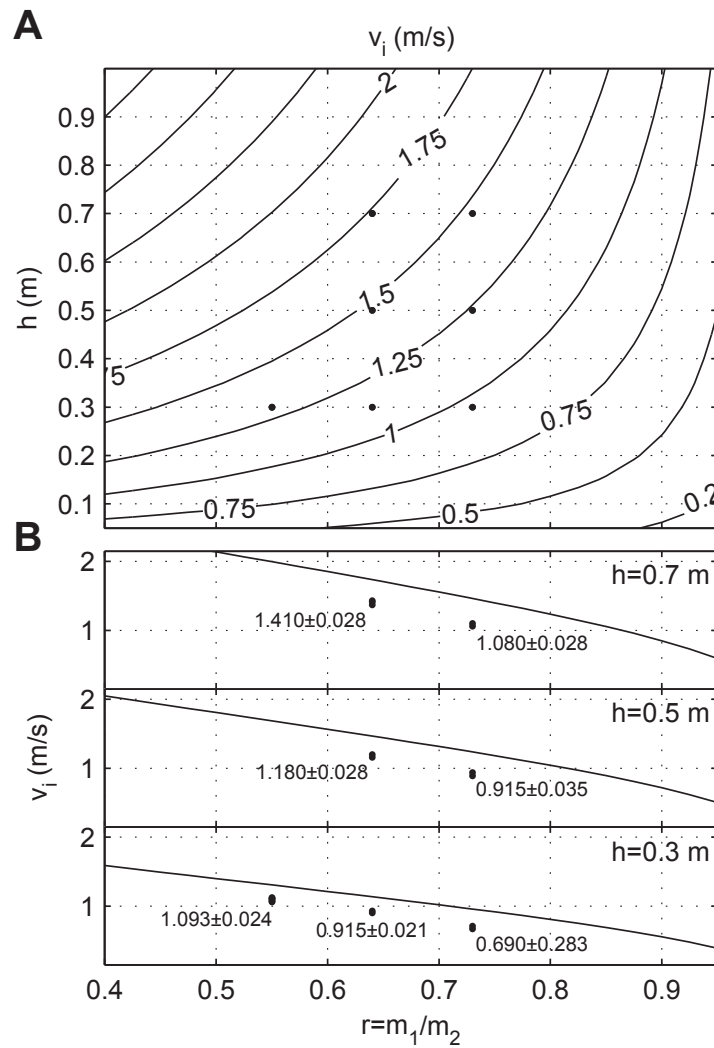


Figure 5.10 – Precision and accuracy of the deployment apparatus. A: Measured (circles) and calculated impact velocities (lines, after Eq. 5.2) in dependency of fall height and mass configuration. B: Impact velocities (lines: predicted; circles: measured, annotated with mean and standard deviation) in dependency of mass ratio for different fall heights.

5.4.3 Penetration data

The results of different mass and fall height configurations confirm, that $q_{t,\text{dyn}}^{\text{acc}}$ correlate to the dynamic cone resistance data of the cone resistance sensor $q_{t,\text{dyn}}^{\text{cone}}$ to a very high degree for both sediment types. See also Fig. 5.4E.

The undulations in acceleration data are more pronounced in the more compacted SED II (cf. Fig. 5.4C). In total, four of these undulations are distinguishable in SED II and three in SED I. The undulations coincide with the layer-boundaries during construction of the samples. The compaction procedure during sample constitution is comparable to the moist-tamping method, which is applied to construct dense sand specimen (Ladd, 1974). This method has been critically assessed by Frost and Park (2003). The authors conclude, that the moist tamping technique is susceptible to produce non-uniform specimen, which exhibit a saw tooth-like compaction profile with an increase in density around layer boundaries and at the rigid bottom platen of the compaction mold. However, averaged relative densities varied within 10 % between the layers.

As denser material causes an increase in deceleration, nonuniformities at the layer boundaries transfer into the penetrometer data with an increase in deceleration followed by a decrease in the less dense material in the lower part of the layer. The difference of stepwise increase of the tip sensor and the undulation of the acceleration sensor data may indicate, that the tip sensor is less sensitive to density changes, than the accelerometer. However, the acceleration record is also subjected to the sleeve friction, which does not affect the tip sensor. The different behavior at the layer boundaries is also expressed in the correlation between the both sensors (Fig. 5.4E) with deviations from the linear transfer function, when layer boundaries are passed. Moreover, entrapped air might be present within the soil targets, contributing to inhomogeneities, which additionally affect the penetration resistance.

For further investigations, data from $q_{t,\text{dyn}}^{\text{acc}}$ is chosen to be representative of both sensor datasets. A linear regression of $q_{t,\text{dyn}}^{\text{acc}}$ in dependency of soil depth has been calculated for all penetrations shown in Fig. 5.4C and D. Therefore, data were averaged to 0.005 m intervals (see Fig. 5.8). The errors of the fit through the mean values were calculated based on the variance of the data (Bevington and Robinson, 2003).

The tests with deep penetrations (esp. SED I-PEN04, 05, 06) might be influenced by the rigid base of the testing container, therefore yielding higher cone resistance values due to potentially greater stress concentrations (Been et al., 1986). Extensive stresses at the rigid base are moreover promoted by the sample construction procedure (Frost and Park, 2003).

Abelev et al. (2009a) report an extent of plastic deformation around FFP impact locations of $2 \cdot D$ on the basis of numerical simulations using a fully dynamic, elastic-perfectly-plastic soil model with an van Mises yield criterion. Lu et al. (2004) report an extent of the radial plastic zone between $2 \cdot D$ and $2 \cdot D$ for very soft sediments. Calibration chamber testing in dense sand is carried out with a single test per target and rod diameter to chamber diameter-ratios of 50 and more (Parkin and Lunne, 1982). The first penetrations (PEN01) were located in the center of the soil target. These penetrations show cone resistances in the upper range of the spectrum. Subsequent testing shows lower cone resistance. This might be attributed to soil weakening due to nearby penetration holes.

The sleeve friction f_s has low values throughout the whole penetration processes (< 20 kPa), which is a fraction (~ 0.7 %) of the cone resistance values. The total friction along the rod increases with depth and reaches values < 40 kPa (see Fig. 5.5), while dynamic tip resistance reaches values of up to 4 MPa. A significant contribution of overall rod friction to the deceleration of the instrument would affect the transfer function between $q_{t,dyn}^{acc}$ and $q_{t,dyn}^{cone}$, since the tip measurement is not affected by rod friction. However, the signals correlate without any scaling factor. Therefore, rod friction is neglected for the processing of acceleration data. This finding is concordant to observations of Dayal (1974), who conducted similar tests in non-cohesive sediments.

5.4.4 Rate correction of penetration data

The rate correction of the dynamic penetration data was carried out by using Eq. 5.1. Thereby, v_{ref} has been defined as the standard penetration velocity of 0.02 m/s, which is used in field tests (Lunne et al., 1997), as well as in calibration chamber testing (Kim et al., 2010). The penetration data were rate-corrected and averaged (compare Fig. 5.8 for the statistics). Between the dynamic, not rate corrected, and the reference data q_c , which has been determined from the triaxial tests and the state parameter relationship, there is a misfit in tip resistance gradients accounting to a factor of 4.52 for SED I and 4.8 for SED II. The penetration velocities range over two orders of magnitude, compared to the reference velocity $v_{ref} = 0.02$ m/s. An optimal K_{rate} has been back-fitted ($K_{rate} = 1.0$) to match averaged strain rate corrected penetration data. Thereby, K_{rate} was chosen to be equal for SED I and SED II. Data of q_t^{acc} are shown in Fig. 5.9. The gradient for SED I (2.76 ± 0.12 MPa/m) slightly underpredicts the values of q_c , where the gradient for SED II (3.27 ± 0.12 MPa/m) slightly overpredict the respective q_c values. However, considering the aforementioned sensitivities of q_c to a

change in λ and the uncertainties regarding the state of T , the gradients for q_t^{acc} are matching the reference profiles well. The standard deviation has a Christmas tree-like structure, since it is based on the penetration datasets, which become more sparse with increasing penetration depth.

The applicability of a rate correction for tests in non-cohesive sediments is a controversial issue. Dayal (1974) concluded from laboratory tests with free-fall penetrometers, that measurements in non-cohesive sediments were not susceptible to the impact velocity. However, Geuze (1953) and Kérisel (1961) observed rate dependencies in penetration resistance for penetrometers and piles in sandy soils. Moreover, rate-correction was necessary for a variety of field and laboratory tests (see Table 5.5) to produce satisfactory results. Since the correction model is highly dependent on the factor K_{rate} , it is not only the sediment type, which influences the factor, but also e.g. the strain rate range, where tests are performed (Dayal, 1974). However, setting K_{rate} to 0, as done in Dayal (1974), contradicts findings of this and other studies (Stoll et al., 2007; Stark et al., 2009b; Stephan et al., 2011).

The reference profile overpredicts the measured q_t^{acc} especially for SED II within the first 0.05 m (see Fig. 5.4C). The overestimation is attributed to the fact, that the penetrometer is still accelerating during that phase (see positive accelerations in Fig. 5.4B and velocity increases in Fig. 5.4A), because it has not reached its terminal velocity. The minimal sediment resistance in the uppermost layer does not suffice to change the mLIRmeter from accelerating to decelerating. Compare also the $q_{t,\text{dyn}}^{\text{cone}}$ in Fig. 5.4D, which is nearly 0 in that depth range. Therefore, negative F_{res} occur after Eq. 5.3 and result consequentially in negative q_t^{acc} . Moreover, the rate correction itself, as a model of soil behavior, might inherently over or underpredict soil behavior in dependency of velocity.

Both sediment types show similar reference profiles although their void ratio is different. The void ratio is an important parameter affecting the strength of sands (Yoshimine et al., 1999). Since both sediment types vary besides void ratio, solely regarding their fines content c_c , a compensation of lower void ratio seems to be attributed to the higher c_c of SED II. To attribute an apparent reduction of q_c to an increased c_c , additional measurements (e.g., pore pressure during and after penetration) would be necessary. However, this is beyond the scope of this study.

5.4.5 Penetration velocities and drainage conditions during penetration

Fig. 5.3A shows the normalized velocity at a given penetration velocity in dependency of sediment type. The distribution of penetration velocities is shown in Fig. 5.3B for all penetrations. The main population of penetration velocities ranges between 0.1 and 2 m/s, which yield undrained conditions for both sediment types under conservative assumptions of $V > 30$ for undrained conditions and $V < 0.01$ for drained conditions (Finnie and Randolph, 1994). Penetration at v_{ref} yield undrained conditions for SED II and partially drained conditions for SED I, which means, that drainage conditions between the reference profiles q_c and the rate corrected penetration data are comparable for SED II and SED I with $v_{\text{dyn}} < 0.1$ m/s. For higher impact velocities in SED I, undrained conditions would be predicted. However, uncertainties in the determination of c_v exist and are hardly quantifiable. Moreover, the location of thresholds between drained, partially drained and undrained conditions was chosen based on conservative estimates. Setting the threshold between partially drained and undrained conditions to 10, which is still within the range of published values (Kim et al., 2008), all penetration velocities would yield undrained conditions. Therefore, from a standpoint of drainage conditions, it might be argued, that the correlation of q_c and q_t^{acc} is also valid for SED I and velocities over 0.1 m/s.

5.5 Conclusions

Remolded soil targets and reference samples, consisting of dense sand mixed with amounts of cohesive fines, were constructed in a reproducible manner. The reference samples were investigated with geotechnical tests. Undrained triaxial compression tests showed dilative behavior of the samples. One-dimensional compression tests showed very low coefficients of consolidation. From these results, profiles of cone resistance were successfully deduced on the basis of state-parameter relationships.

Dynamic impact penetrometer tests were carried out on the soil targets. The impact penetrometer measurements show an excellent correlation in dynamic cone resistance from cone- and acceleration measurement, encouraging the application of acceleration sensors as supplementary, or even replacement of tip sensors in impact penetrometers, due to their advantages regarding sensitivity, robustness, and protection against external influences, such as hydrostatic and excessive pore pressures. Acceleration sensors already proved to be suited for use in impact penetrometers in combination with other sed-

iment types e.g. Stephan et al. (2015) for clay, e.g. Stark et al. (2009b) for quartz and carbonate sand, and O’Loughlin et al. (2014) for calcareous silt.

The results of the dynamic penetration tests needed to be adjusted using an established correction model for impact velocity. The soil- and instrument-specific constants of that model were back-fitted using the cone resistance profiles, deduced from the geotechnical tests, as a reference. The resulting rate-corrected cone resistance profiles from acceleration measurement match the reference profiles in a reasonable manner. The successful application of state parameter relationships to impact penetrometer data showed to be a promising, alternative, approach for the interpretation of dynamic penetration data from testing of uncohesive sediments with low amounts of plastic fines.

This study supplements earlier work on that topic (Stephan et al., 2011, 2012, 2015; Fabian et al., 2008; Stark et al., 2009a,b) and enlarges the range of application of impact penetrometers to dense sands with low amount of cohesive fines, which are prominent sediments in coastal areas, e.g. the German Bight sector of the North Sea (Zöllmer and Irion, 1996).

Acknowledgements The main author has received funding by RWE Dea AG and RWE Innogy GmbH in equal parts for conduction of this study. The authors would like to recognize the exhaustive support of Daniel Otto during the geotechnical testing campaign, as well as the dedication of Bernd Heesemann during the design of the scaled mLIRmeter and the conduction of the impact penetrometer tests. The instrumented cone, which has been provided by Fugro enabled the assessment of the acceleration sensors performance and is herewith gratefully acknowledged. The grain-size analyses were conducted by Nele Lampig. The authors thank Sylviane Stephan for the translation of the abstract into French.

Chapter 6

Conclusions

A measurement system has been developed within this study, which has proven to be suitable to determine the total cone resistance of a variety of marine sediments. From these data, undrained geotechnical properties can be determined, like from e.g. static velocity CPT. The approach of deducting cone resistance through MEMS accelerometer measurement has proven to be very robust and reproducible in conjunction with the deployment strategy of the LIRmeter.

The strategy allows thus a rapid mapping progress through pogo-style measurements in water depths of up to 4500 m, while handling requirements are comparable to those of small gravity corers. The main advantages of using acceleration sensors lie in their insensitivity to hydrostatic pressure, and in their high tolerance to shock loads. The high speed, high precision data acquisition system of the LIRmeter has proven to be reliable (see Chapter 3) and user friendly to operate through the graphical user interface.

The current design allows measurement durations of up to 14 hours, while no sensor calibration or any user intervention is needed along the way. This renders the instrument ideal for use on vessels of opportunity with non-specialized operating personnel. The ability to perform pogo-style measurements (i.e. multipenetration profiles without completely retrieving the instrument Hyndman et al., 1979) allows a rapid mapping of whole areas. Since different measurement ranges are covered by multiple acceleration sensors, even a sudden change in sedimentary conditions is mappable within a single campaign.

Field trials and laboratory analyses showed excellent repeatability among measurements and that directly acquired cone resistance is reproduced by the acceleration measurements to a very high degree. Thus, it is possible to interchange these data, e.g. when directly acquired cone resistance data are unavailable or deficient. However, for sediments exhibiting a high frictional

resistance, rod friction needs to be accounted for in the acceleration data analysis. Moreover, dynamic effects like fluid or soil drag need to be assessed ideally. When no reference measurements, such as static CPT, are available, dynamic effects need to be estimated. However, rod friction can be reduced by using a tip with a larger diameter than the rod, as currently employed within the LIRmeter.

The dynamic nature of the penetration process requires a correction for rate effects using common rate correction approaches. It has been found, that strain rate corrections are required for cohesive and as well for uncohesive sediments (with low amount of cohesive fines) within the typical range of impact velocities between 0.02 and 5 m/s. To perform a rate correction, knowledge of soil components is required to select a suitable rate parameter. If reference measurements are available, it is possible to back-fit rate parameters.

The total cone resistance, which has been derived from acceleration measurement and which has been rate corrected, is suited to conduct soil classification using well established classification schemes (e.g. Robertson, 1990), see also Chapter 4. Moreover, it is possible to determine the undrained shear strength of cohesive sediments by back-fitting a cone factor N_{kt} (see Section 2.2.2). Additionally, it has been shown, that the state parameter relationship also applies for impact penetration measurements (see Chapter 5). Thus, enabling the determination of void ratios of uncohesive sediments and uncohesive sediments with low amounts of fines.

Since the presented data analyses which establishes on (total) cone resistance – such as soil classification after Robertson (1990), the state parameter relationship after Been et al. (1987), or the determination of undrained shear strength for cohesive sediments – are founded on a broad empirical background, it must be considered that they are solely verified within the bounds of the underlying data. Moreover, it is not possible to quantify geotechnical properties solely from deceleration data of impact penetrometers since corrections and empirical relations incorporate fitting parameters, which depend on the sediment properties. These can be obtained through reference measurements or laboratory tests, as shown in Chapters 4 and 5.

Regarding the applicability of acceleration based impact penetrometer measurements, such as carried out with the LIRmeter, it may be therefore be concluded, that surveys exclusively conducted with such instruments will yield qualitative results. Such qualitative results could be obtained in the German Bight (see Chapter 3). Though, if reference data from cores or static velocity CPT are present or sediment parameters may be estimated in a reasonable way, it is feasible to obtain quantitative geotechnical properties.

The advantages of the LIRmeter regarding a rapid measurement propa-

gation and the low requirements regarding handling render the intermediary-sized penetrometer as an ideal instrument to supplement geotechnical investigations regarding their spatial extension. Such a survey has been conducted in the Southern North Sea within the frame of instrument evaluation tests (see Section 4). It was possible to classify near-surface sediments on the basis of LIRmeter measurements and draw conclusions regarding the geological setting.

The aims of this study were to develop an instrument, which is suitable to determine geotechnical properties of near-surface sediments. Requirements were defined fulfilled by the LIRmeter. Field testing showed excellent performance of the LIRmeter and the chosen measurement approach. Moreover, the quantification of geotechnical properties from kinematic LIRmeter data was herein achieved. The positive results of the field- and laboratory trials indicate that application of the LIRmeter outside the framework of instrument validation studies, e.g., for investigation of questions within a geotechnical, geoscientific, or civil engineering context. Especially the time and hence cost saving operation, as well as its reliability, render the instrument favorable for high-resolution surveys in combination with established testing methods, such as CPT.

Chapter 7

Outlook

This thesis covers several aspects on the development and evaluation of a marine penetrometer, as well as on data interpretation schemes. The original aim of developing such an instrument and being able to derive geotechnical parameters in a quantitative way was reached. Therefore, the LIRmeter is considered applicable for scientific and engineering applications.

However, during the course of the investigations, new questions arose, which may be addressed in future studies. Ideally, these problems should be addressed under controlled conditions, such as laboratory tests. To increase the accuracy of laboratory testing, the deployment apparatus should be used in combination with CPT calibration chambers to maintain control over border conditions, such as the stress distribution within the sediment target. The resulting testing data could add to the empirical evidence found within this study and could further promote the state parameter relationship for impact penetration testing.

Further improvements of the lances used in combination with the instrument, would allow for the determination of qualitative properties of both, extremely hard or extremely soft sediment.

Numerical modeling can be undertaken to supplement the findings from controlled laboratory tests as material parameters can be, therein, easily altered. By using results from laboratory tests as benchmark experiments, it would be possible to extend the empirical evidence through more refined numerical models.

7.1 Laboratory analyses and field tests

The results of the laboratory study serve as a good basis for further studies. The deployment system has proven able to deliver a high degree of repro-

ducibility, which is needed to conduct further test series. The investigation of the following questions are envisioned:

- What effect does the sample preparation technique have on the test results?
- Which volumetric content of fine material is critical with regard to the interpretation of impact penetrometer tests?
- What is the range of rate parameters over a broad range of soil types?
- What exact effect does a tip diameter larger than the rod diameter have on the friction between rod and soil?
- What is the influence of hydrodynamic drag during the penetration process?
- What role do relative density, grain size, and grain shape of cohesionless sediments play in impact penetrometer tests?

Tests would be carried out preferably on cohesionless sediments, such as quartz or carbonate sands. Such test series would on one hand, complement the laboratory tests conducted within the framework of this thesis (see Section 5). On the other hand, laboratory impact penetrometer tests are, until now, mainly conducted in cohesive sediments, such as kaolin clay. Data from additional tests in cohesionless sediment would, therefore, serve as a broad data basis for further evaluation of quantitative interpretation approaches.

It is desirable to conduct laboratory penetration tests under higher confining pressures due to better compliance in testing conditions to reference tests, such as triaxial or one dimensional compression tests. Therefore, a CPT calibration chamber could be used in conjunction with the developed deployment system (see Fig. 7.1). Moreover, using such a chamber would offer the possibility to obtain static velocity data from a pushed cone as reference data set. Additionally, it would be beneficial to conduct fewer tests on a single soil sample to avoid interference with previous penetration locations and boundary effects.

Laboratory tests on cohesive sediments would allow the determination of an empirical cone factor N_k or N_{kt} to derive undrained shear strength directly from rate corrected cone resistance data (see Section 2.2.2). However, N_k is instrument specific and would need to be determined separately for each cone employed with the LIRmeter.

The LIRmeter could be modified with regard to field tests in very dense sands. The studies showed that penetration depth were limited to ~ 0.2 m,

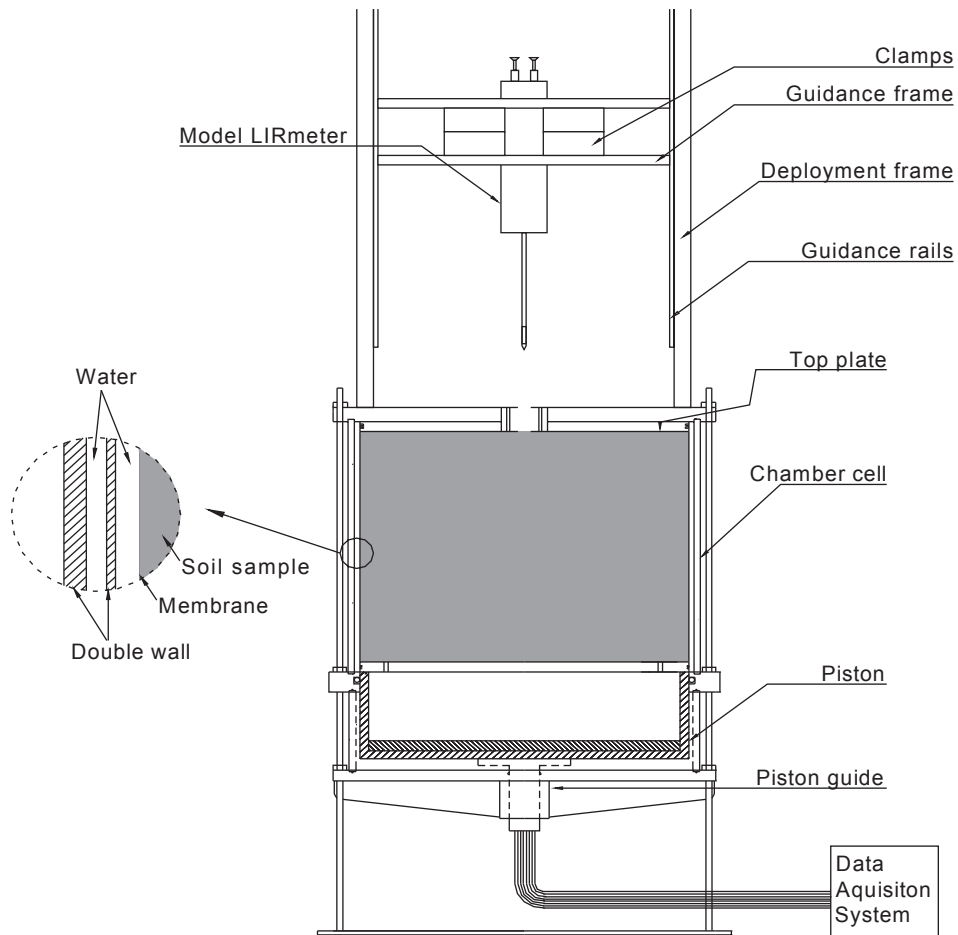


Figure 7.1 – Impact penetrometer testing with the deployment apparatus (see Section 5.2) mounted on top of a calibration chamber. Chamber sketch modified after Kim et al. (2010).

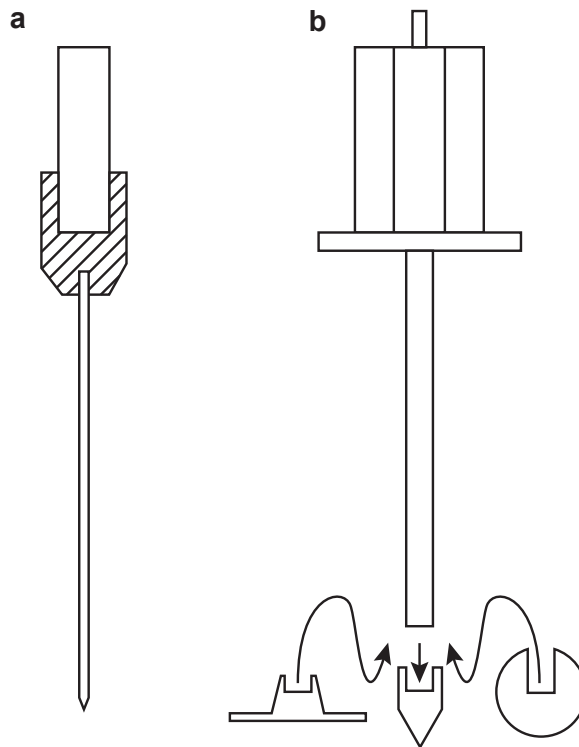


Figure 7.2 – Possible modifications for extreme sediment types. **a** The smaller diameter rod with a design allowing fast interchange in case of bending for hard sediments **b** different tip designs (plate or ball shaped) as substitutes for the conical tip to increase the sensitivity when extremely soft sediments are tested.

even with application of additional weights (total mass of the instrument: ~ 500 kg) while using the 45 or 66 cm² tips (see Chapter 3). Laboratory tests in dense sands with the model penetrometer showed penetration depths of more than 0.4 m with significantly fewer weights. Therefore, it is suggested to adapt a measurement lance with a similar rod diameter as the model lance (0.011 m) and a length of up to 2 m for the testing of dense sands (see 7.2a). Since the suggested low-diameter rod is exposed to bending stresses during penetration and retrieval, it is suggested to incorporate a mechanism for rapid interchange of the testing rod. This adaptation would enable the acquisition of penetration data at greater depths; however, if such a setup is used in very soft sediments, such as, e.g., high-porosity deposits, the sensitivity of the instrument would not suffice to determine the interface between water and sediment (mud line).

Extremely hard sediments, such as dense sands, impose a challenge on the design of the measurement lance and extremely soft sediments (such as harbor mud or deep sea sediments) are, likewise, challenging to measure with the current lance configuration (45 or 66 cm² tips). For such sediments, a different tip configuration (ball or plate, see Fig. 7.2b) would be suggested to increase the sensitivity to viscosity changes near the mud line of such sediments. However, using non-standard tips (i.e., not conical) generate challenges in data interpretation, since empirical data is predominantly gathered for conical tips.

The hydrodynamic drag during penetration exerts a resistance force on impact penetrometers. This might be important to be considered especially for sediments with a low strength. Since the drag is velocity-dependent, this force changes during the penetration process. Knowing the hydrodynamic properties (i.e., the hydrodynamic drag coefficient) of the instrument would allow a correction for this effect, as, e.g., shown in Equation 2.4 or in (O’Loughlin et al., 2009).

7.2 Numerical modeling of penetration processes

The governing variables of a constitutive model, which is numerically implemented to calculate deformation and stresses within a finite element domain, can be easily adapted to simulate a wide range of physical properties. After calibration of the model to experimental results, numerical modeling can extend the informational value of measured laboratory or field penetration data over a broader and more finely distinguished range of sediments.

Pilot experiments were undertaken with regards to numerical modeling of penetration processes. However, the task of realistically modeling a penetration process is far beyond the scope of this thesis. Ideally, numerical models would simulate both cohesive and non-cohesive sediment types, as well as consider pore water pressure distribution within the sample during the penetration process. The ultimate aim would be to numerically reproduce the laboratory experiments serving as benchmarks, and to then transfer the findings to field measurements.

7.2.1 Method

The penetration process has been implemented using the commercially available finite element code of the finite element analysis software ABAQUS (ABAQUS 6.12.1) by Dassault Systèmes. The penetrometer and the soil

specimen are modeled in an axisymmetric setup (rotational symmetry) with the penetrometer as an analytically rigid element and the soil specimen as a deformable body constrained at its outer dimensions. A mass is assigned to the penetrometer (see Table 7.1), which is placed at certain heights above the soil specimen. The analysis is carried out in two steps: a gravitational field is applied to the model setup causing the build up of stresses within the soil specimen. In a second step, the penetrometer is accelerated towards the soil by the gravitational field and subsequently penetrates the target due to the gathered momentum causing deformation of the soil target.

Table 7.1 – Model dimensions.

Parameter	Unit	Value
Penetrometer		
Mass	kg	10
Radius d	m	5.60E-03
Length	m	0.5
Apex	o	60
Soil		
Radius D	m	0.2
Height H	m	0.5
Elements (horizontal)		32
Elements (vertical)		80

The finite element method requires the components to be discretized into elements with finite size. Elements are interconnected with nodes (see Figs. 7.3 and 7.5). The deformation of the elements is governed by the constitutive laws of the material that has been assigned to them.

Since the penetration process is a nonlinear structural mechanics problem, the explicit solution scheme was used to solve the problem since large deformations occur at a high rate. Under these conditions, explicit solving is advantageous because the increment size can be adapted to the problem resulting in small increments with relatively low computational cost since computation of displacement is carried out nodal-wise. Implicit solution, in contrast, would require solving the equilibrium equations simultaneously to obtain the displacements of all nodes in the model resulting in a higher computational cost.

The mesh defining elements and nodes of the finite element analysis become severely distorted during the simulation of the penetration problem. This leads to errors while finding a solution for the respective time increments and results in abortion of the explicit iterative solution process.

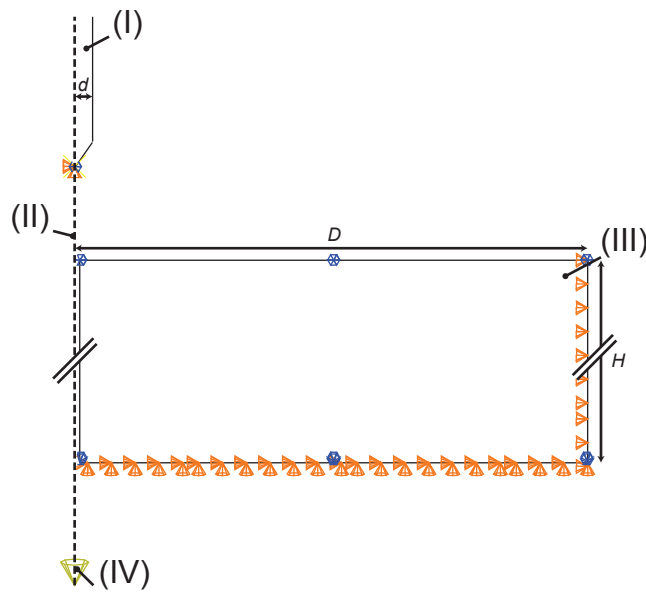


Figure 7.3 – Schematic representation of the model geometry, boundary conditions and external loads. (I): Penetrometer, (II) Axis of symmetry, (III): Soil specimen, (IV) External load (gravity). The boundary conditions are indicated by orange triangles limiting translational nodal movements and blue circles limiting rotational nodal movements. The vertical movement constraint of the penetrometer tip is removed during analysis.

The software package offers the possibility to implement an adaptive technique that updates the mesh, if certain thresholds are reached. Arbitrary Lagrangian-Eulerian (ALE) meshing is implemented for each time increment. The ALE technique allows the mesh to move independently from the material. The mesh will be detached from the material when excessive distortions occur. After a re-discretization, the newly generated mesh will be remapped onto the material and nodal, as well as element properties, will be reassigned from the material on the basis of the nodes and elements new positions. This approach maintains a numerically stable mesh with a constant number of nodes and elements.

The critical state model has been chosen to represent the soil specimen. The critical state model describes the plastic material behavior. Elastic material behavior is modeled using a linear-elastic formulation. A critical state model, which is implemented in ABAQUS is the “Cam Clay” plasticity model (named after the river “Cam” sediment, the model was formulated with Schofield and Wroth, 1968). The Cam Clay model can simulate the soil strength as a function of mean effective stress and predict strains that occur during shearing. Depending on mean effective stress and critical state friction angle, strains result in volume changes.

7.2.2 First results

A numerical model has been set up using ABAQUS. The mesh was discretized using the axisymmetric elements with four integration points CAX4R. The mesh is formed by 2560 elements and 2673 nodes ($32 \cdot 80$ elements). The dimensions of the model are given in Table 7.1 The critical state and elastic material parameters are given in Table 7.2. Contact is modeled using a frictionless pure master-slave condition, where nodes of the slave surface are on the side of the soil domain and the surface of the penetrometer constitutes the master domain.

The penetration of the soil causes the penetrometer to decelerate. The deceleration and the velocity of the penetrometer are shown in Figure 7.4. After the fall height of 0.27 m, the penetrometer decelerates until it reaches its final embedment depth of 0.55 m. The peak velocity during free fall under gravitational acceleration reaches 2.5 m/s. Pressures in the soil are given in Fig. 7.5 for two instances in time. Peak pressure is around 2 MPa.

7.2.3 Further studies

Using the established model, it is possible to study the dependency of penetration behavior on

Table 7.2 – Material parameters for the critical state model. β and K are defined as 1 as a symmetrical yield surface is defined.

Parameter	Unit	Value
Plasticity		
Stress ratio M		0.577
Initial volumetric plastic strain ϵ^p		0.002
Flow stress ratio β		1
Wet yield surface size K		1
Elasticity		
Youngs modulus E	Pa	1.30E+08
Poisson ratio ν		0.3
Density		
Mass density ρ	kgm ⁻³	2560

- changes in material properties, such as density, elasticity and plasticity parameters, as well as
- different penetrometer configurations regarding dimensions, mass, and
- deployment characteristics, such as impact velocity.

Further modifications of the model regarding the consideration of a two-phase soil system consisting of soil grains and water as pore fluid would allow further analysis regarding effective stresses within the material as the penetration process usually takes place under undrained conditions. However, the element formulation does not allow pore fluid behavior to be investigated with explicit solving techniques. Therefore, it is envisaged to set-up an implicit model. Moreover, a model with material laws for non-cohesive sediments should also be established.

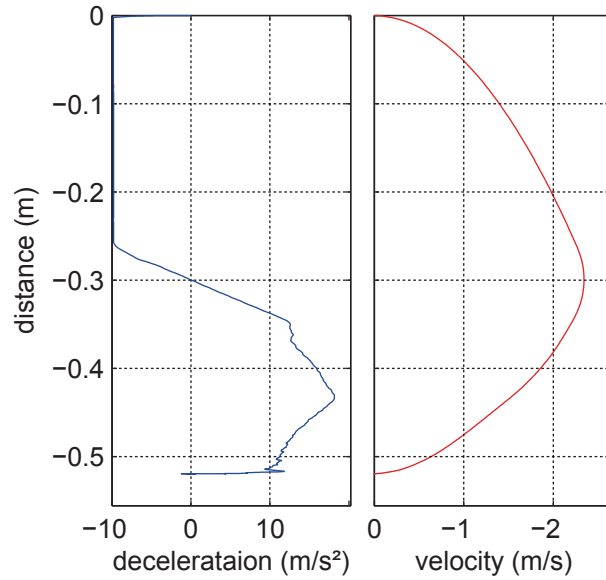


Figure 7.4 – Left: deceleration versus penetration distance. Right: penetration velocity vs. penetration distance for the conditions given in Table 7.1 and 7.2.

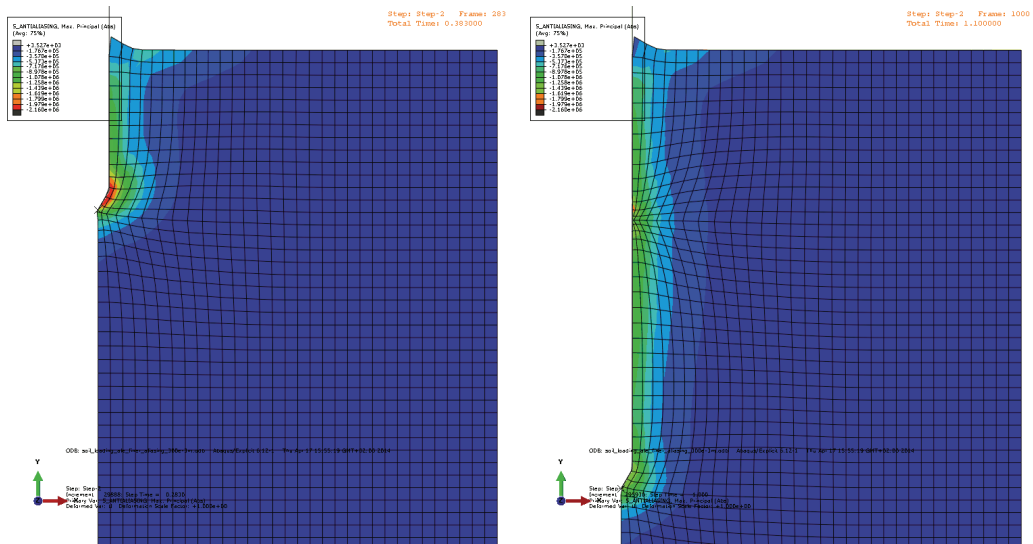


Figure 7.5 – Pressure in the material given for an intermediate and the final time step under the conditions given in Table 7.1 and 7.2.

Danksagung

Mein ganz besonderer Dank gilt Prof. Dr. Heinrich Villinger für die Betreuung und Beguachtung dieser Arbeit. Ihm möchte ich insbesondere für das mir entgegengebrachte Vertrauen und die daraus resultierenden Freiheiten in der Umsetzung der Arbeiten danken.

Prof. Dr. Achim Kopf gilt mein Dank für die sofortige Bereitschaft zur Anfertigung eines zweiten Gutachtens für diese Arbeit.

Ein besonderer Dank gilt Bernd Heesemann für die Unterstützung in jenen technischen Belangen, die meinen Horizont überstiegen. Sein anhaltender Enthusiasmus, selbst in turbulenten Zeiten, war mir stets eine große Motivation für die Durchführung der Arbeitspakete dieses Projekts. Ein Dank gilt auch Dr. Norbert Kaul für die Unterstützung in administrativen Dingen, sowie dafür, dass er mir stets ein offenes Ohr für ad-hoc aufgetretene Probleme geschenkt hat. Auch möchte ich Arne Schwab für die Zusammenarbeit während der Tüftelei an der Signalverarbeitungseinheit danken. Ein besonderer Dank gilt ebenfalls Daniel Otto und Dr. Stefan Kreiter für die Unterstützung während der geotechnischen Laborversuche.

Ich möchte weiterhin den aktuellen und ehemaligen Mitgliedern des Fachgebiets Meerestechnik und Sensorik danken, mit denen ich in einer kollegialen und freundschaftlichen Atmosphäre eine gute Zeit verbracht habe. Insbesondere danke ich auch Martina Braun für die administrative Arbeit hinter den Kulissen.

Ohne den finanziellen Rahmen wäre dieses Projekt nicht möglich gewesen. Daher gilt mein Dank an dieser Stelle dem Förderprogramm „Angewandte Umweltforschung“ der Initiative „Umwelt Unternehmen Bremen“ für die Förderung des ersten Abschnitts dieses Projekts. Der zweite Abschnitt wurde zu gleichen Teilen durch die RWE Dea AG und die RWE Innogy GmbH gefördert. Hier gilt mein Dank insbesondere Dr. Christian Buecker (RWE Dea) und Daniel Bartminn (RWE Innogy) für das Vertrauen in diese Arbeit.

Durch Bestrebungen von Dr. Klaus Michels (Fugro OSAE GmbH) war es mir möglich, Offshore-Messungen in Zusammenarbeit mit Fugro N.V. (Niederlande) durchzuführen. Insbesondere die Ergebnisse aus dieser Zusammen-

arbeit stellen einen wesentlichen Teil dieser Arbeit dar. Daher sei an dieser Stelle für die Unterstützung gedankt. Gleichmaßen gilt mein Dank den Mitarbeitern von Fugro (Niederlande). Insbesondere Joek Peuchen und Peter Looijen sei dafür gedankt, dass sie an den „SeaDART“ geglaubt haben und so vieles auf unkonventionelle Art ermöglichten. Dave Ruijtenbeek sei an dieser Stelle ebenfalls für die ausgeklügelten technischen Lösungen gedankt, die während der Erprobung wesentlich zum Erfolg der Messungen beigetragen haben.

Neben der beruflichen Unterstützung möchte ich meiner Familie für Beistand, Unterstützung und Zuversicht danken. Ohne diese Hilfe wäre es mir nicht möglich gewesen, diese Arbeit anzufertigen.

Meiner Frau Friederike gilt mein größter Dank an dieser Stelle dafür, dass sie es zu jeder Zeit schaffte mich zu motivieren, obgleich die Last in den arbeitsreichen Phasen dies unmöglich erscheinen ließ.

References

- Abelev, A, Simeonov, J, Valent, P (2009a), Numerical investigation of dynamic free-fall penetrometers in soft cohesive marine sediments using a finite element approach. In: *OCEANS 2009, MTS/IEEE Biloxi - Marine Technology for Our Future: Global and Local Challenges*, 2626–2633.
- Abelev, A, Tubbs, K, Valent, P (2009b), Numerical investigation of dynamic free-fall penetrometers in soft cohesive marine sediments using a finite difference approach. In: *OCEANS 2009, MTS/IEEE Biloxi - Marine Technology for Our Future: Global and Local Challenges*, 2616–2625.
- de Aguiar, CS, de Sousa, JRM, Ellwanger, GB, de Campos Porto, E, Fernandes, JVV, Henriques, PRD, Jr., Costa, RGB (2011), Numerical simulation of installed torpedo anchors embedded in cohesive soil. In: *Proceedings of the ASME 2011 30th International Conference on Ocean, Offshore and Arctic Engineering OMAE2011*, vol. 7, 939–949, doi: [10.1115/OMAE2009-79465](https://doi.org/10.1115/OMAE2009-79465).
- de Aguiar, CS, de Sousa, JRM, Ellwanger, GB, de Campos Porto, E, de Medeiros, CJ, Jr., Foppa, D (2009), Undrained load capacity of torpedo anchors in cohesive soils. In: *Proceedings of the ASME 2009 28th International Conference on Ocean, Offshore and Arctic Engineering*, vol. 7, 253–265, doi: [10.1115/OMAE2009-79465](https://doi.org/10.1115/OMAE2009-79465).
- Akal, T, Stoll, RD (1995), An expendable penetrometer for rapid assessment of seafloor parameters. In: *OCEANS '95. MTS/IEEE. Challenges of Our Changing Global Environment. Conference Proceedings.*, vol. 3, 1822–1826, doi: [10.1109/OCEANS.1995.528858](https://doi.org/10.1109/OCEANS.1995.528858).
- Allan, R, Airey, D, Carter, J (2007), Undrained strength from free falling penetrometer tests. In: Ameratunga, J, Taylor, B, Patten, M (eds.), *Common Ground Proceedings 10th Australia New Zealand Conference on Geomechanics Brisbane*, vol. 2, 456–461, ASTM.

- Analog Devices (2010a), ADXL203: Precision ± 1.7 g dual-axis iMEMS accelerometer. Online Datasheet, URL http://www.analog.com/static/imported-files/data_sheets/ADXL103_203.pdf, Accessed 24 Feb 2012.
- (2010b), ADXL325: Small, low power, 3-axis ± 5 g accelerometer. Online Datasheet, URL http://www.analog.com/static/imported-files/data_sheets/ADXL325.pdf, Accessed 24 Feb 2012.
- (2010c), ADXL335: Small, low power, 3-axis ± 3 g accelerometer. Online Datasheet, URL http://www.analog.com/static/imported-files/data_sheets/ADXL335.pdf, Accessed 24 Feb 2012.
- Applied Geomechanics (2000), User's manual series 755, 756 and 757 miniature tilt sensors. Manual.
- de Araujo, JB, Machado, RD, de Medeiros, CJ, Jr. (2004), High holding power torpedo pile – results for the first long term application. In: *Proceedings of OMAE04 23rd International Conference on Offshore Mechanics and Arctic Engineering*, vol. 1, 417–421, doi: [10.1115/OMAE2004-51201](https://doi.org/10.1115/OMAE2004-51201).
- ASTM (2000), Standard test method for laboratory miniature vane shear test for saturated fine-grained clayey soils. ASTM D 4648, American Society for Testing and Materials, West Conshohocken.
- (2007), Standard test methods for laboratory compaction characteristics of soil using standard effort (12 400 ft-lbf/ft³ (600 kn-m/m³)). ASTM D 698 07, American Society for Testing and Materials, West Conshohocken.
- (2012), Standard test method for electronic friction cone and piezocone penetration testing of soils. ASTM D 5778 12, American Society for Testing and Materials, West Conshohocken.
- Atturio, JM, Valent, PJ (1977), High-capacity, deep-water, free-fall anchor. In: *OCEANS '77 Conference Record*, 592–596, doi: [10.1109/OCEANS.1977.1154324](https://doi.org/10.1109/OCEANS.1977.1154324).
- Aubeny, CP, Shi, H (2006), Interpretation of impact penetration measurements in soft clays. *Journal of Geotechnical and Environmental Engineering*, 132(6):770–777, doi: [10.1061/\(ASCE\)1090-0241\(2006\)132:6\(770\)](https://doi.org/10.1061/(ASCE)1090-0241(2006)132:6(770)).
- Audibert, JME, Movant, MN, Jeong-Yun, W, Gilbert, RB (2006), Torpedo piles: Laboratory and field research. In: *The Sixteenth International Offshore and Polar Engineering Conference*, vol. 2, 462–468.

- Baldi, G, Bellotti, R, Ghionna, N, Jamilokowski, M, Pasqualini, E (1986), Interpretation of CPT's and CPTU's. 2nd part: Drained penetration of sands. In: Broms, BB (ed.), *Fourth International Geotechnical Seminar*, 134–156.
- Baligh, MM (1975), Theory of deep site static cone penetration resistance. Technical Report R75-56, Massachusetts Institute of Technology, Cambridge.
- (1985), Strain path method. *Journal of Geotechnical Engineering*, 111(9):1108–1136, doi: [10.1061/\(ASCE\)0733-9410\(1985\)111:9\(1108\)](https://doi.org/10.1061/(ASCE)0733-9410(1985)111:9(1108)).
- Bayne, JM, Tjelta, TI (1987), Advanced cone penetrometer development for in-situ testing at gullfaks c. In: *Offshore Technology Conference*, doi: [10.4043/5420-MS](https://doi.org/10.4043/5420-MS).
- Beard, RM (1976), Expendable Doppler Penetrometer: Interim report. Technical Note N-1435, Civil Engineering Laboratory, Naval Construction Battalion Center, Port Hueneme, URL <http://www.biodiversitylibrary.org/item/102113#page/1/mode/1up>.
- (1977), Expendable Doppler Penetrometer: A performance evaluation. Technical Report R 855, Civil Engineering Laboratory Naval Construction Battalion Center, Port Hueneme, URL <http://www.dtic.mil/dtic/tr/fulltext/u2/a043912.pdf>.
- (1981), A penetrometer for deep ocean seafloor exploration. In: *OCEANS 81*, 668–673, doi: [10.1109/OCEANS.1981.1151586](https://doi.org/10.1109/OCEANS.1981.1151586).
- (1984), Expendable Doppler Penetrometer for deep ocean sediment strength measurements. Technical Report R-905, Civil Engineering Laboratory, Port Hueneme, URL <http://www.dtic.mil/dtic/tr/fulltext/u2/a142011.pdf>.
- (1985), Expendable doppler penetrometer for deep ocean sediment measurements. In: Chaney, RC, Demars, KR (eds.), *Strength Testing of Marine Sediments: Laboratory and In-Situ Measurements*, vol. 883 of *STP*, 101–124, ASTM, doi: [10.1520/STP36332S](https://doi.org/10.1520/STP36332S).
- Been, K, Crooks, JHA, Becker, DE, Jefferies, MG (1986), The cone penetration test in sands: Part I, state parameter interpretation. *Géotechnique*, 36(2):239–249, doi: [10.1680/geot.1986.36.2.239](https://doi.org/10.1680/geot.1986.36.2.239).

- Been, K, Jefferies, MG (1985), A state parameter for sands. *Géotechnique*, 35(2):99–112, doi: [10.1680/geot.1985.35.2.99](https://doi.org/10.1680/geot.1985.35.2.99).
- Been, K, Jefferies, MG, Crooks, JHA, Rothenburg, L (1987), The cone penetration test in sands: Part II, general inference of state. *Géotechnique*, 37(3):285–299, doi: [10.1680/geot.1987.37.3.285](https://doi.org/10.1680/geot.1987.37.3.285).
- Beliveau, A, Spencer, GT, Thomas, KA, Roberson, SL (1999), Evaluation of MEMS capacitive accelerometers. *IEEE Design & Test of Computers*, 16(4):48–56, doi: [10.1109/54.808209](https://doi.org/10.1109/54.808209).
- Bevington, PR, Robinson, DK (2003), *Data Reduction and Error Analysis for the Physical Sciences*. McGraw-Hill Higher Education, New York, 3 edn., 320 pp.
- Bhattacharya, S, Murali Krishna, A, Lombardi, D, Crewe, A, Alexander, N (2012), Economic MEMS based 3-axis water proof accelerometer for dynamic geo-engineering applications. *Soil Dynamics and Earthquake Engineering*, 36:111–118, doi: [10.1016/j.soildyn.2011.12.001](https://doi.org/10.1016/j.soildyn.2011.12.001).
- BIPM (2006), *The International System of Units (SI)*. Bureau International des Poids et Mesures, Organisation Intergouvernementale de la Convention du Mètre, Paris, 8 edn., 142-143 pp., URL <http://www.bipm.org/en/publications/si-brochure/>.
- Biscontin, G, Pestana, JM (2001), Influence of peripheral velocity on vane shear strength of an artificial clay. *Geotechnical Testing Journal*, 24(4):423–429, doi: [10.1520/GTJ11140J](https://doi.org/10.1520/GTJ11140J).
- Bishop, RF, Hill, R, Mott, NF (1945), The theory of indentation and hardness tests. *Proceedings of the Physical Society*, 57(3):147–159, doi: [10.1088/0959-5309/57/3/301](https://doi.org/10.1088/0959-5309/57/3/301).
- Blaker, Ø, Lunne, T, Vestgården, T, Krogh, L, Thomsen, NV, Powell, JJM, Wallave, CF (2015), Method dependency for determining maximum and minimum dry unit weights of sands. In: Meyer, V (ed.), *Frontiers in Off-shore Geotechnics III*, 1159–1166, doi: [10.1201/b18442-174](https://doi.org/10.1201/b18442-174).
- BODC (2009), GEBCO gridded global bathymetry data. GEBCO_08 grid, British Oceanographic Data Centre, Liverpool.
- Bouma, AH, Boerma, JAK (1968), Vertical disturbances in piston cores. *Marine Geology*, 6(3):231–241, doi: [10.1016/0025-3227\(68\)90032-7](https://doi.org/10.1016/0025-3227(68)90032-7).

- Bowen, DQ (1999), The Geological Society special report. In: Gregory, FJ (ed.), *A revised correlation of Quaternary deposits in the British Isles*, vol. 23, Geological Society Publishing House, Bath.
- Brandão, FEN, Henriques, CCD, Araujo, JB, Ferreira, OCG, dos Santos Amaral, C (2006), Albacora Leste field development - FPSO P-50 mooring system concept and installation. In: *Offshore Technology Conference*, vol. 3, 1443–1452, doi: [10.4043/18243-MS](https://doi.org/10.4043/18243-MS).
- Briaud, JL, Garland, E, Felio, G (1984), Rate of loading parameters for vertically loaded piles in clay. In: *Sixteenth Annual Offshore Technology Conference*, vol. 1.2 of 407-412, doi: [10.4043/4694-MS](https://doi.org/10.4043/4694-MS).
- Buckley, DE, MacKinnon, WG, Cranston, RE, Christian, HA (1994), Problems with piston core sampling: Mechanical and geochemical diagnosis. *Marine Geology*, 117(1-4):95–106, doi: [10.1016/0025-3227\(94\)90008-6](https://doi.org/10.1016/0025-3227(94)90008-6).
- Budhu, M (2010), *Soil mechanics and foundations*. Wiley, New York, 3 edn.
- Buhler, RL, Audibert, JME (2012), Rate-effect correction methods for free-fall CPT data in deepwater Gulf of Mexico - an operator's perspective. In: *Offshore Site Investigation and Geotechnics*, 187–194.
- Burns, RE (1966), Free-fall behavior of small, light-weight gravity corers. *Marine Geology*, 4(1):1–9, doi: [10.1016/0025-3227\(66\)90033-8](https://doi.org/10.1016/0025-3227(66)90033-8).
- Caffisch, RE (1998), Monte carlo and quasi-monte carlo methods. *Acta Numerica*, 1998:1–49, doi: [10.1017/S0962492900002804](https://doi.org/10.1017/S0962492900002804).
- Cameron, TDJ (1992), *United Kingdom Offshore Regional Report: the Geology of the Southern North Sea*. H.M.S.O. for the British Geological Survey, London.
- Cameron, TDJ, Laban, C, Mesdag, C, Schüttenhelm, RTE (1986), Indefatigable sheet/kaartblad 53 °N–02 °E. Quaternary geology/geologie von het Kwartair.
- Cameron, TDJ, Laban, C, Schüttenhelm, RTE (1989a), *The Quaternary and Tertiary geology of the Southern Bight, North Sea*, chap. Upper Pliocene and lower Pleistocene stratigraphy in the Southern Bight of the North Sea, 97–110. Belgian Geological Survey, Brussel.
- Cameron, TDJ, Schüttenhelm, RTE, Laban, C (1989b), *The Quaternary and Tertiary geology of the Southern Bight, North Sea*, chap. Middle and upper

- Pleistocene and Holocene stratigraphy in the Southern North Sea between 52 ° and 54 °N, 2 ° to 4 °E, 119–135. Belgian Geological Survey, Brussel.
- Cameron, TDJ, Stoker, MS, Long, D (1987), The history of Quaternary sedimentation in the UK sector of the North Sea Basin. *Journal of the Geological Society*, 144(1):43–58, doi: [10.1144/gsjgs.144.1.0043](https://doi.org/10.1144/gsjgs.144.1.0043).
- Carr, S (1999), The micromorphology of last glacial maximum sediments in the Southern North Sea. *Catena*, 35(2-4):123–145, doi: [10.1016/S0341-8162\(98\)00097-6](https://doi.org/10.1016/S0341-8162(98)00097-6).
- Carr, SJ, Holmes, R, van der Meer, JJM, Rose, J (2006), The Last Glacial Maximum in the North Sea Basin: Micromorphological evidence of extensive glaciation. *Journal of Quaternary Science*, 21(2):131–153, doi: [10.1002/jqs.950](https://doi.org/10.1002/jqs.950).
- Carter, JP, Booker, JR, Yeung, SK (1986), Cavity expansion in cohesive frictional soils. *Géotechnique*, 36(3):349–358, doi: [10.1680/geot.1986.36.3.349](https://doi.org/10.1680/geot.1986.36.3.349).
- Caruthers, C, Hartsfield, R, Young, AG, Spikula, D, Dobias, J, Fitzpatrick, M, Remmes, B (2014), Case study of geotechnical site investigation using a seafloor drilling unit, large-diameter cores, and coring-vessel-deployed cone penetration tests in the Gulf of Mexico. In: *Offshore Technology Conference*, vol. 4, 3127–3138, doi: [10.4043/25378-MS](https://doi.org/10.4043/25378-MS).
- Casagrande, A, Shannon, WL (1949), Strength of soils under dynamic loads. *Transactions, ASCE*, 114(1):755–772.
- Castro, G (1969), Liquefaction of sands. In: *Harvard Soil Mechanics Series*, vol. 81, Harvard University, Cambridge, Massachusetts.
- Castro, G, Poulos, SJ (1977), Factors affecting liquefaction and cyclic mobility. *Journal Of The Geotechnical Engineering Division*, 103(6):501–516.
- Chakrabarti, S, Halkyard, J, Capanoglu, C (2005), *Handbook of Offshore Engineering*, chap. Chapter 1 - Historical Development of Offshore Structures, 1 – 38. Elsevier, London, doi: [10.1016/B978-008044381-2.50004-7](https://doi.org/10.1016/B978-008044381-2.50004-7).
- Chari, TR, Smith, WG, Chaudhuri, SN (1981), Development of the free-fall penetrometer. In: *OCEANS 81*, 678–682, doi: [10.1109/OCEANS.1981.1151560](https://doi.org/10.1109/OCEANS.1981.1151560).
- Chari, TR, Smith, WG, Zielinski, A (1978), Use of free fall penetrometer in seafloor engineering. In: *OCEANS '78*, 686–691, doi: [10.1109/OCEANS.1978.1151162](https://doi.org/10.1109/OCEANS.1978.1151162).

- Chow, SH (2013), *Free falling penetrometer tests in clay*. Ph.D. thesis, The University of Sydney, Sydney.
- Chow, SH, Airey, DW (2011a), *Deformation Characteristics of Geomaterials*, chap. Rate effects in free falling penetrometer tests, 592–599. IOS Press, Amsterdam, doi: [10.3233/978-1-60750-822-9-592](https://doi.org/10.3233/978-1-60750-822-9-592).
- (2011b), Soil strength estimation using free falling penetrometers. *Journal and News of the Australian Geomechanics Society*, 46(1):105–112.
- (2013), Soil strength characterisation using free-falling penetrometers. *Géotechnique*, 63(13):1131–1143, doi: [10.1680/geot.12.P.129](https://doi.org/10.1680/geot.12.P.129).
- (2014), Free-falling penetrometers: A laboratory investigation in clay. *Journal of Geotechnical and Geoenvironmental Engineering*, 140(1):201–214, doi: [10.1061/\(ASCE\)GT.1943-5606.0000973](https://doi.org/10.1061/(ASCE)GT.1943-5606.0000973).
- Chow, SH, O’Loughlin, CD, Randolph, MF (2014), Soil strength estimation and pore pressure dissipation for free-fall piezocone in soft clay. *Géotechnique*, 64(10):817–827, doi: [10.1680/geot.14.P.107](https://doi.org/10.1680/geot.14.P.107).
- Chu, PC, Chenwu, F (2007), Mine-impact burial model (IMPACT35) verification and improvement using sediment bearing factor method. *IEEE Journal of Oceanic Engineering*, 32(1):34–48, doi: [10.1109/JOE.2007.890942](https://doi.org/10.1109/JOE.2007.890942).
- Chung, SF, Randolph, MF (2004), Penetration resistance in soft clay for different shaped penetrometers. In: Viana da Fonseca, A, Mayne, PW (eds.), *Geotechnical and geophysical site characterization*, Proceedings of the 2nd International Conference on Site Characterization, ISC’2, Porto, 671–677.
- Colliat, JL (2002), Anchors for deepwater to ultradeepwater moorings. In: *Offshore Technology Conference*, vol. 3, 2561–2569, doi: [10.4043/14306-MS](https://doi.org/10.4043/14306-MS).
- Colp, J, Caudle, W, Schuster, C (1975), Penetrometer system for measuring in situ properties of marine sediment. In: *OCEANS 75 Conference*, 405–411, doi: [10.1109/OCEANS.1975.1154127](https://doi.org/10.1109/OCEANS.1975.1154127).
- Creutzberg, F, Postma, H (1979), An experimental approach to the distribution of mud in the Southern North Sea. *Netherlands Journal of Sea Research*, 13(1):99–116, doi: [10.1016/0077-7579\(79\)90036-X](https://doi.org/10.1016/0077-7579(79)90036-X).

- Cyr, R (1990), Sea bed sampling with an expendable acoustic penetrometer system. In: Arduś, DA, Champ, MA (eds.), *Ocean Resources*, vol. 2, 45–56, Springer Netherlands, doi: [10.1007/978-94-009-2133-7_6](https://doi.org/10.1007/978-94-009-2133-7_6).
- Danziger, FAB, Lunne, T (2012), Rate effect on cone penetration test in sand. *Geotechnical Engineering Journal of the SEAGS & AGSSEA*, 43(4):72–81.
- Das, B (2001), *Principles of Geotechnical Engineering*. Thomson Press, Toronto, 5 edn., 608 pp.
- Dayal, U (1974), *Instrumented impact cone penetrometer*. Ph.D. thesis, Memorial University of Newfoundland, St. John's, URL http://research.library.mun.ca/1036/1/Dayal_Umesh.pdf.
- (1980), Free fall penetrometer: A performance evaluation. *Applied Ocean Research*, 2(1):39–43, doi: [10.1016/0141-1187\(80\)90046-2](https://doi.org/10.1016/0141-1187(80)90046-2).
- (1981), Analysis of free-fall penetrometer data. In: *OCEANS 81*, 683–687, doi: [10.1109/OCEANS.1981.1151505](https://doi.org/10.1109/OCEANS.1981.1151505).
- Dayal, U, Allen, JH (1973), Instrumented impact cone penetrometer. *Canadian Geotechnical Journal*, 10(3):397–409, doi: [10.1139/t73-034](https://doi.org/10.1139/t73-034).
- (1975), The effect of penetration rate on the strength of remolded clay and sand samples. *Canadian Geotechnical Journal*, 12(3):336–348, doi: [10.1139/t75-038](https://doi.org/10.1139/t75-038).
- Dayal, U, Allen, JH, Jones, JM (1973), Marine impact cone penetrometer. Technical Report IO 73-662/01, Memorial University of Newfoundland, St. John's.
- (1975), Use of an impact penetrometer for the evaluation of the in-situ strength of marine sediments. *Marine Geotechnology*, 1(2):73–89, doi: [10.1080/10641197509388155](https://doi.org/10.1080/10641197509388155).
- Denness, B, Berry, A, Darwell, J, Nakamura, T (1981), Dynamic seabed penetration. In: *OCEANS 81*, 662–667, doi: [10.1109/OCEANS.1981.1151564](https://doi.org/10.1109/OCEANS.1981.1151564).
- Dev, KL, Rakesh, JP, Robinson, RG (2003), Estimation of critical state parameters from one-dimensional consolidation and triaxial compression tests. *Indian Geotechnical Journal*, 43(3):229–237, doi: [10.1007/s40098-013-0063-5](https://doi.org/10.1007/s40098-013-0063-5).

- DiamondSystems (2011), Helios Single Board Computer. Online Manual, URL <http://www.diamondsystems.com/files/binaries/Helios%20User%20Manual.pdf>, Accessed 24 Feb 2012.
- Diesing, M, Ware, S, Foster-Smith, B, Stewart, H, Long, D, Vanstaen, K, Forster, R, Morando, A (2009), Understanding the marine environment: Seabed habitat investigations of the Dogger Bank. Report 429, Joint Nature Conservation Committee, Peterborough, URL <http://core.ac.uk/download/pdf/54760.pdf>.
- DIN (1990), Baugrund, Versuche und Versuchsgeräte - Bestimmung der Scherfestigkeit - Triaxialversuch. DIN 18137 Teil 2:1990-12, Deutsches Institut für Normung, Berlin.
- (1996), Baugrund, Untersuchung von Bodenproben - Bestimmung der Dichte nichtbindiger Böden bei lockerster und dichtester Lagerung. DIN 18126 1996-11, Deutsches Institut für Normung, Berlin.
- (2012a), Baugrund, Untersuchung von Bodenproben - Eindimensionaler Kompressionsversuch. DIN 18135:2012-04, Deutsches Institut für Normung, Berlin.
- (2012b), Baugrund, Untersuchung von Bodenproben - Proctorversuch. DIN 18127:2012-09, Deutsches Institut für Normung, Berlin.
- Douglas, BL, Wapner, MP (1996), Test results of the doppler penetrometer seafloor sediment profiling system. In: *OCEANS '96. MTS/IEEE. Prospects for the 21st Century. Conference Proceedings*, vol. 2, 722–727, doi: [10.1109/OCEANS.1996.568316](https://doi.org/10.1109/OCEANS.1996.568316).
- Duncan, CC (1969), Plowing cables under the sea. *IEEE Transactions on Communication Technology*, 17(1):74–82, doi: [10.1109/T-COM.1969.1090047](https://doi.org/10.1109/T-COM.1969.1090047).
- Durgonoglu, HT, Mitchell, JK (1975), Static penetration resistance of soils: I - analysis. In: *Proceedings of the conference of in situ measurement of soil properties*, vol. 1, 151–171.
- Edrington, TS, Calloway, TM (1984), Sound speed and attenuation measurements in gassy sediments in the Gulf of Mexico. *Geophysics*, 49(3):297–299, doi: [10.1190/1.1441662](https://doi.org/10.1190/1.1441662).
- Ehlers, CJ, Young, AG, Chen, JH (2004), Technology assessment of deepwater anchors. In: *Offshore Technology Conference*, vol. 3, 2105–2121, doi: [10.4043/16840-MS](https://doi.org/10.4043/16840-MS).

- Einav, I, Randolph, MF (2005), Combining upper bound and strain path methods for evaluating penetration resistance. *International Journal for Numerical Methods in Engineering*, 63:1991–2016, doi: 10.1002/nme.1350.
- Elsworth, D, Lee, DS (2005), Indentation of a free-falling lance penetrometer into a poroelastic seabed. *International Journal for Numerical and Analytical Methods in Geomechanics*, 29(2):141–162, doi: 10.1002/nag.408.
- Eyring, H (1936), Viscosity, plasticity, and diffusion as examples of absolute reaction rates. *The Journal of Chemical Physics*, 4:283–291, doi: 10.1063/1.1749836.
- Fabian, M, Kaul, N, Gmeinder, T (2008), The Bremen Lance Insertion Retardation (LIR) Meter to assess sea floor stability. *Sea Technology*, 49(10):10–13.
- Figge, K (1981), *Karte zur Sedimentverteilung im Bereich der Deutschen Bucht im Maßstab 1: 250000*. Deutsches Hydrographisches Institut, Hamburg.
- Finnie, IMS, Randolph, MF (1994), Punch-through and liquefaction induced failure of shallow foundations on calcareous sediments. In: Chryssostomidis, C (ed.), *Seventh International Conference on the Behaviour of Off-shore Structures*, vol. 1, 535–540.
- Fitch, S, Thomson, K, Gaffney, V (2005), Late Pleistocene and Holocene depositional systems and the palaeogeography of the Dogger Bank, North Sea. *Quaternary Research*, 64(2):185–196, doi: 10.1016/j.yqres.2005.03.007.
- Flemming, BW, Nyandwi, N (1994), Land reclamation as a cause of fine-grained sediment depletion in backbarrier tidal flats (Southern North Sea). *Netherland Journal of Aquatic Ecology*, 28(3-4):299–307, doi: 10.1007/BF02334198.
- Folk, RL, Ward, WC (1957), Brazos river bar: A study in the significance of grain size parameters. *Journal of Sedimentary Petrology*, 27(1):3–26, doi: 10.1306/74D70646-2B21-11D7-8648000102C1865D.
- Freeman, TJ, Burdett, JRF (1986), Deep ocean model penetrator experiments. Report CD-NA-10-502-EN-C, Directorate-General for Science, Research and Development, Brussels, URL <http://bookshop.europa.eu/en/deep-ocean-model-penetrator-experiments-report-pbCDNA10502/>.

- Freeman, TJ, Murray, CN, Francis, TJG, McPhail, SD, Schultheiss, PJ (1984), Modelling radioactive waste disposal by penetrator experiments in the abyssal Atlantic Ocean. *Nature*, 310:130–133, doi: [10.1038/310130a0](https://doi.org/10.1038/310130a0).
- Freeman, TJ, Schüttenhelm, RTE (1990), *Geotechnical Engineering of Ocean Waste Disposal*, vol. 1087 of *ASTM STP*, chap. A Geotechnical Investigation of a Deep Ocean Site, 255–275. American Society for Testing and Materials, Philadelphia, doi: [10.1520/STP17240S](https://doi.org/10.1520/STP17240S).
- Frost, JD, Park, JY (2003), A critical assessment of the moist tamping technique. *Geotechnical Testing Journal*, 26(1):57–70, doi: [10.1520/GTJ11108J](https://doi.org/10.1520/GTJ11108J).
- Furlong, A, Osler, J, Christian, H, Cunningham, D, Pecknold, S (2006), The Moving Vessel Profiler (MVP)-a rapid environmental assessment tool for the collection of water column profiles and sediment classification. Technical report, Defense Research and Development Canada, Ottawa, URL <http://cradpdf.drdc-rddc.gc.ca/PDFS/unc59/p527475.pdf>.
- Gaudin, C, O’Loughlin, CD, Hossain, MS, Zimmerman, EH (2013), The performance of dynamically embedded anchors in calcareous silt. In: Ferrant, P (ed.), *Proceedings of the ASME 2013 32nd International Conference on Ocean, Offshore and Arctic Engineering*, vol. 6, V006T1OA006–1–8, doi: [10.1115/OMAE2013-10115](https://doi.org/10.1115/OMAE2013-10115).
- Geirnaert, K, Staelens, P, Deprez, S (2011), System and method for sand detection. Patent US20110313685A1.
- Geirnaert, K, Staelens, P, Deprez, S, Noordijk, A, Van Hassent, A (2014), Innovative free fall sediment profiler for preparing and evaluating dredging works and determining the nautical depth. In: *20th World Dredging Congress and Exhibition (WODCON XX)*, vol. 1, 169–179.
- Georgiannou, VN, Burland, JB, Hight, DW (1990), The undrained behaviour of clayey sands in triaxial compression and extension. *Géotechnique*, 40(3):431–449, doi: [10.1680/geot.1990.40.3.431](https://doi.org/10.1680/geot.1990.40.3.431).
- Germaine, JT, Germaine, AV (2009), *Geotechnical laboratory measurements for engineers*. Wiley, New York.
- Geuze, ECWA (1953), Résultats d’essais de pénétration en profondeur et de mise en charge de pieux-modèle. *Annales de l’Institut Technique du Bâtiment et des Travaux Publics*, 63-64:313–319.

- Ghodssi, R, Lin, P (2011), *MEMS materials and processes handbook*. Springer, New York, doi: [10.1007/978-0-387-47318-5](https://doi.org/10.1007/978-0-387-47318-5).
- Gilbert, RB, Morvant, M, Audibert, J (2008), Torpedo piles joint industry project – model torpedo pile tests in kaolinite test beds. Technical Report 02/08B187, Minerals Management Service, Washington, D. C., URL <http://www.bsee.gov/Technology-and-Research/Technology-Assessment-Programs/Reports/500-599/575AA/>.
- Glasstone, S, Laidler, KJ, Eyring, H (1941), *The theory of rate processes*. McGraw-Hill Book Company, Inc., New York.
- Gogoi, BP, Mladenovic, D (2002), Integration technology for MEMS automotive sensors. In: *28th Annual Conference of the Industrial Electronics Society*, vol. 4, 2712–2717, doi: [10.1109/IECON.2002.1182823](https://doi.org/10.1109/IECON.2002.1182823).
- Graham, AGC, Stoker, MS, Lonergan, L, Bradwell, T, Stewart, MA (2011), Chapter 21 - the Pleistocene glaciations of the North Sea Basin. In: Ehlers, J, Gibbard, PL, Hughes, PD (eds.), *Quaternary Glaciations - Extent and Chronology – A Closer Look*, vol. 15 of *Developments in Quaternary Sciences*, 261–278, Elsevier, Amsterdam, doi: [10.1016/B978-0-444-53447-7.00021-0](https://doi.org/10.1016/B978-0-444-53447-7.00021-0).
- Graham, J, Crooks, JHA, Bell, ALL (1983), Time effects on the stress-strain behaviour of natural soft clays. *Géotechnique*, 33(3):327–340, doi: [10.1680/geot.1983.33.3.327](https://doi.org/10.1680/geot.1983.33.3.327).
- Green, AW (1984), Bulk dynamics of the expendable bathythermograph (XBT). *Deep Sea Research Part A Oceanographic Research Papers*, 31(4):415–426, doi: [10.1016/0198-0149\(84\)90093-1](https://doi.org/10.1016/0198-0149(84)90093-1).
- Hansbo, S (1957), A new approach to the determination of the shear strength of clay by the fall-cone test. In: *Swedish geotechnical Institute; Proceedings*, vol. 14, 1–48.
- Harris, MM, Avera, WE, Abelev, A, Bentrem, FW, Bibee, LD (2008), Sensing shallow seafloor and sediment properties, recent history. In: *OCEANS 2008*, 146–156, doi: [10.1109/OCEANS.2008.5289424](https://doi.org/10.1109/OCEANS.2008.5289424).
- Harrison, D, Laban, C, Schüttenhelm, RTE (1987), Indefatigable sheet/kaartblad 53 °N–02 °E. Sea bed sediments & Holocene / Holocene en oppervlaktensedimenten.

- Hauser, GC, Hickerson, J (1988), An explosive acoustic telemetry system for seabed penetrators. Technical Report SAND87-0952, Sandia National Laboratories, Albuquerque, URL <http://prod.sandia.gov/techlib/access-control.cgi/1987/870952.pdf>.
- Hazell, E (2008), *Numerical and experimental studies of shallow cone penetration in clay*. Ph.D. thesis, University of Oxford, Oxford, URL www.eng.ox.ac.uk/civil/publications/theses/hazell.pdf.
- Hefer, PA, Peuchen, J, Adrichem, J (2005), Practice notes on push-in penetrometers for offshore geotechnical investigation. In: Cassidy, M, Gourvenec, S (eds.), *Frontiers in Offshore Geotechnics*, 973–979, doi: 10.1201/NOE0415390637.ch117.
- Heffler, D (1991), Piston corer dynamics. In: *OCEANS '91*, 1587–1591, doi: 10.1109/OCEANS.1991.606532.
- Hembise, O, Guevel, P, Bardey, PR, Viaud, JL, Boisson, JY (1987), Identification of marine soils by ballistic penetrometry. In: Chung, JS (ed.), *Proceedings of the Sixth International Offshore Mechanics and Arctic Engineering Symposium*, vol. 1, 395–401.
- Hembise, O, Guevel, P, Bardey, PR, Viaud, JL, Boisson, JY, Vacherand, F (1990), Identification of marine soils by ballistic penetrometry. *Journal of Offshore Mechanics and Arctic Engineering*, 112(4):277–284, doi: 10.1115/1.2919867.
- Hickerson, J (1988), FREEFALL: A seabed penetrator flight code. Technical Report SAND87-0951, Sandia National Laboratories, Albuquerque, URL <http://prod.sandia.gov/techlib/access-control.cgi/1987/870951.pdf>.
- Hickerson, J, Freeman, TJ, Boisson, JY, Murray, CN, Gera, F, Nakamura, H, Nieuwenhuis, JD, Schaller, KH (1988), Engineering. In: de Marsily, G (ed.), *Feasibility of disposal of high-level radioactive waste into the seabed*, vol. 4, Nuclear Energy Agency, URL http://www.iaea.org/inis/collection/NCLCollectionStore/_Public/20/049/20049719.pdf.
- Hollocher, D, Zhang, X, Sparks, A, Bart, S, Sawyer, W, Narayanasamy, P, Pipitone, C, Memishian, J, Samuels, H, Ng, SL, Mhatre, R, Whitley, D, Sammoura, F, Bhagavat, M, Tsau, C, Nunan, K, Judy, M, Farrington, M, Yang, K (2009), A very low cost, 3-axis, MEMS accelerometer for consumer applications. In: *IEEE Sensors*, 953–957, doi: 10.1109/ICSENS.2009.5398189.

- Hossain, MS, Kim, Y, Gaudin, C (2014), Experimental investigation of installation and pullout of dynamically penetrating anchors in clay and silt. *Journal of Geotechnical and Geoenvironmental Engineering*, 140(7):04014026–1–13, doi: [10.1061/\(ASCE\)GT.1943-5606.0001100](https://doi.org/10.1061/(ASCE)GT.1943-5606.0001100).
- Hossain, MS, Kim, Y, Wang, D (2013), Physical and numerical modelling of installation and pull-out of dynamically penetrating anchors in clay and silt. In: Ferrant, P (ed.), *Proceedings of the ASME 2013 32nd International Conference on Ocean, Offshore and Arctic Engineering*, vol. 6, V006T10A019–1–10, doi: [10.1115/OMAE2013-10322](https://doi.org/10.1115/OMAE2013-10322).
- Hossain, MS, O’Loughlin, CD, Kim, Y (2015), Dynamic installation and monotonic pullout of a torpedo anchor in calcareous silt. *Géotechnique*, 65(2):77–90, doi: [10.1680/geot.13.P.153](https://doi.org/10.1680/geot.13.P.153).
- Howell, JL, Shackelford, CD, Amer, NH, Stern, RT (1997), Compaction of sand-processed clay soil mixtures. *Geotechnical Testing Journal*, 20(4):443–458, doi: [10.1520/GTJ10411J](https://doi.org/10.1520/GTJ10411J).
- Huuse, M, Lykke-Andersen, H (2000), Overdeepened Quaternary valleys in the eastern Danish North Sea: Morphology and origin. *Quaternary Science Reviews*, 19(12):1233–1253, doi: [10.1016/S0277-3791\(99\)00103-1](https://doi.org/10.1016/S0277-3791(99)00103-1).
- Hyndman, RD, Davis, EE, Wright, JA (1979), The measurement of marine geothermal heat flow by a multipenetration probe with digital acoustic telemetry and insitu thermal conductivity. *Marine Geophysical Researches*, 4(2):181–205, doi: [10.1007/BF00286404](https://doi.org/10.1007/BF00286404).
- IAEA (1999), Inventory of radioactive waste disposals at sea. Technical Report IAEA-TECDOC-1105, International Atomic Energy Agency, Toronto, URL http://www-pub.iaea.org/MTCD/publications/PDF/te_1105_prn.pdf.
- IMO (1993), Sixteenth consultative meeting of contracting parties to the convention on the prevention of marine pollution by dumping of wastes and other matter. Report LC 16/14, International Maritime Organization, London, URL http://www.imo.org/KnowledgeCentre/ReferencesAndArchives/IMO_Conferences_and_Meetings/London_Convention/LCandLDCReports/Documents/Report%20of%20LC%2016%20November%201993.pdf.
- Ingram, C (1982), Expendable penetrometer for seafloor classification. *Geo-Marine Letters*, 2(3-4):239–241, doi: [10.1007/BF02462771](https://doi.org/10.1007/BF02462771).

- Ishihara, K (1993), Liquefaction and flow failure during earthquakes. *Géotechnique*, 43(3):351–415, doi: [10.1680/geot.1993.43.3.351](https://doi.org/10.1680/geot.1993.43.3.351).
- ITelegance BVBA (2010a), System and method for sand detection. Patent WO2010076295A2.
- (2010b), System and method for sand detection. Patent GB246673A.
- Jaeger, RA, DeJong, JT, Boulanger, RW, Low, HE, Randolph, MF (2010), Variable penetration rate CPT in an intermediate soil. In: *2nd International Symposium on Cone Penetration Testing*, Paper 2-50, URL http://www.cpt10.com/PDF_Files/2-50Jaevpr.pdf.
- Jaky, J (1944), The coefficient of earth pressure at rest. *Journal of the Society of Hungarian Architects and Engineers*, 78(22):355–358.
- James, LT, Calloway, TM (1983), Initial field tests of ISP-1 and ISP-2 - systems that extend the technology of instrumented seabed penetrators. In: *OCEANS '83*, 608–612, doi: [10.1109/OCEANS.1983.1152133](https://doi.org/10.1109/OCEANS.1983.1152133).
- James, LT, Edrington, TS, Reis, GE, Suazo, JE (1981), Development of a gun-launched; instrumented seabed penetrator system. In: *OCEANS 81*, 656 – 661, doi: [10.1109/OCEANS.1981.1151492](https://doi.org/10.1109/OCEANS.1981.1151492).
- Jansen, JHF, van Weering, TCE, D., E (1979), *Acta Universitatis Upsalien-sis, Annum Quingentesimum Celebrantis*, vol. 2, chap. Late Quaternary sedimentation in the North Sea, 175–187. Almquist & Wiksell International, Uppsala.
- Janszen, A (2012), *Tunnel valleys: Genetic models, sedimentary infill and 3D architecture*. Ph.D. thesis, TU Delft, Delft, URL <http://repository.tudelft.nl/assets/uuid:b2897176-e66d-4dfe-b8c1-26fa9b280d9c/Thesis.pdf>.
- Jeanjean, P, Spikula, D, Young, A (2012), Technical vetting of free-fall cone penetrometer. In: *Offshore Site Investigation and Geotechnics*, 179–186.
- Jeffery, D, Frantsen, P, Laban, C, Schüttenhelm, RTE (1989), Silver Well sheet/kaartblad 54 °N–02 °E. Quaternary geology / geologie von het Kwartair.
- Jeffery, D, Laban, C, Niessen, A, Schüttenhelm, RTE (1988), Silver Well sheet/kaartblad 54 °N–02 °E. Sea bed sediments & Holocene / Holocene en oppervlakesedimenten.

- Jelgersma, S, Oele, E, A., W (1979), *Acta Universitatis Upsaliensis, Annum Quingentesimum Celebrantis*, vol. 2, chap. Depositional history and coastal development in The Netherlands and the adjacent North Sea since the Eemian, 115–142. Almqvist & Wiksell International, Uppsala.
- Jeong, SW, Leroueil, S, Locat, J (2009), Applicability of power law for describing the rheology of soils of different origins and characteristics. *Canadian Geotechnical Journal*, 49(9):1011–1023, doi: [10.1139/T09-031](https://doi.org/10.1139/T09-031).
- Jorat, ME, Mörz, T, Schunn, W, Kreiter, S, Moon, V, de Lange, W (2014a), Geotechnical Offshore Seabed Tool (GOST): A new cone penetrometer. In: *3rd International Symposium on Cone Penetration Testing*, Paper 1–04, URL <http://www.cpt14.com/cpt14-papers>.
- (2014b), Geotechnical Offshore Seabed Tool (GOST): CPTu measurements and operations in New Zealand. In: *3rd International Symposium on Cone Penetration Testing*, Paper 1–04a, URL <http://www.cpt14.com/cpt14-papers>.
- Kelleher, PJ, Randolph, MF (2005), Seabed geotechnical characterisation with a ball penetrometer deployed from the Portable Remotely Operated Drill. In: Gouvernec, S, Cassidy, M (eds.), *Frontiers in Offshore Geotechnics*, 365–371, doi: [10.1201/NOE0415390637.ch35](https://doi.org/10.1201/NOE0415390637.ch35).
- Kérisel, J (1961), Fondations profondes en milieux sableux: Variation de la force portante limite en fonction de la densité, de la profondeur, du diamètre et de la vitesse d'enfoncement. In: *Comptes rendus du cinquième Congrès International de Mécanique des Sols et des Travaux de Fondations*, vol. 2, 73–83.
- Kerner, M (2007), Effects of deepening the Elbe estuary on sediment regime and water quality. *Estuarine, Coastal and Shelf Science*, 75(4):492–500, doi: [10.1016/j.ecss.2007.05.033](https://doi.org/10.1016/j.ecss.2007.05.033).
- Kim, K, Prezzi, M, Salgado, R, Lee, W (2008), Effect of penetration rate on cone penetration resistance in saturated clayey soils. *Journal of Geotechnical and Geoenvironmental Engineering*, 134(8):1142–1153, doi: [10.1061/\(ASCE\)1090-0241\(2008\)134:8\(1142\)](https://doi.org/10.1061/(ASCE)1090-0241(2008)134:8(1142)).
- (2010), Penetration rate effects on cone resistance measured in a calibration chamber. In: *2nd International Symposium on Cone Penetration Testing*, vol. 2, Paper 2–03, URL http://www.cpt10.com/PDF_Files/2-03Kimpred.pdf.

- Kopf, A, Stegmann, S, Delisle, G, Panahi, B, Aliyev, CS, Guliyev, I (2009), In situ cone penetration tests at the active Dashgil mud volcano, Azerbaijan: Evidence for excess fluid pressure, updoming, and possible future violent eruption. *Marine and Petroleum Geology*, 26(9):1716–1723, doi: [10.1016/j.marpetgeo.2008.11.005](https://doi.org/10.1016/j.marpetgeo.2008.11.005).
- Kopf, A, Stegmann, S, Krastel, S, Förster, A, Strasser, M, Irving, M (2007), Marine deep-water free-fall CPT measurements for landslide characterisation off Crete, Greece (Eastern Mediterranean Sea) part 2: Initial data from the Western Cretan Sea. In: *Submarine Mass Movements and Their Consequences; 3rd International Symposium*, 199–208, Springer, doi: [10.1007/978-1-4020-6512-5_21](https://doi.org/10.1007/978-1-4020-6512-5_21).
- Kosters, EC, VanMierlo, BEJM, Verbeek, NH, Posthumus, BJ, McGee, TM, Brouwer, J (1992), Late Quaternary stratigraphic signature, offshore from the Dutch barrier shoreline. *Sedimentary Geology*, 80(3-4):199–212, doi: [10.1016/0037-0738\(92\)90041-O](https://doi.org/10.1016/0037-0738(92)90041-O).
- Kramer, SL (1996), Geotechnical earthquake engineering. In: Hall, WJ (ed.), *Prentice-Hall Series International Series in Civil Engineering and Engineering Mechanics*, Prentice-Hall.
- Kreiter, S, Moerz, T, Strasser, M, Lange, M, Schunn, W, Schlue, BF, Otto, D, Kopf, A (2010), Advanced dynamic soil testing—introducing the new MARUM dynamic triaxial testing device. In: Mosher, DC, Shipp, RC, Moscardelli, L, Chaytor, JD, Baxter, CDP, Lee, HJ, Urgeles, R (eds.), *Submarine Mass Movements and Their Consequences*, vol. 28 of *Advances in Natural and Technological Hazards Research Volume*, 31–41, Springer, doi: [10.1007/978-90-481-3071-9_3](https://doi.org/10.1007/978-90-481-3071-9_3).
- Kuhn, MR (1987), *Micromechanical aspects of soil creep*. Ph.D. thesis, University of California, Berkeley, URL <http://search.proquest.com/docview/303496848>.
- Kulhawy, FH, Mayne, PW (1990), Manual on estimating soil properties for foundation design. Technical Report EL-6800, Electric Power Research Institute, Palo Alto, URL <http://www.geoplanning.it/test/wp-content/uploads/2012/02/manual-on-estimating-soil-properties-for-foundation-design.pdf>.
- Kullenberg, B (1947), *The piston core sampler*, vol. 1 of *Svenska Hydrografisk Biologiska Kommissionens Skrifter*. Svenska Hydrografisk-Biologiska Kommissionen, Göteborg.

- Ladd, RS (1974), Specimen preparation and liquefaction of sands. *Journal of the Geotechnical Engineering Division*, 100(10):1180–1184.
- (1978), Preparing test specimens using undercompaction. *Geotechnical Testing Journal*, 1(1):16–23, doi: [10.1520/GTJ10364J](https://doi.org/10.1520/GTJ10364J).
- de Lange, M (2011), Conducting site surveys for offshore wind farms. *Sea Technology*, 52(9):25–29.
- Lee, D, Elsworth, D (2004), Indentation of a free-falling sharp penetrometer into a poroelastic seabed. *Journal of Engineering Mechanics*, 130(2):170–179, doi: [10.1061/\(ASCE\)0733-9399\(2004\)130:2\(170\)](https://doi.org/10.1061/(ASCE)0733-9399(2004)130:2(170)).
- Lehane, BM, O’Loughlin, CD, Gaudin, C, Randolph, MF (2009), Rate effects on penetrometer resistance in kaolin. *Géotechnique*, 59(1):41–52, doi: [10.1680/geot.2007.00072](https://doi.org/10.1680/geot.2007.00072).
- Levacher, D (1985), Pénétrromètre à chute libre: Impact et pénétration dans des argiles reconstituées. *Canadian Geotechnical Journal*, 22(1):129–135, doi: [10.1139/t85-012](https://doi.org/10.1139/t85-012).
- Lieng, JT, Hove, F, Tjelta, TI (1999), Deep Penetrating Anchor: Subseabed deepwater anchor concept for floaters and other installations. In: *Proceedings of the Ninth International Offshore and Polar Engineering Conference*, vol. 1, 613–619.
- Lieng, JT, Kavli, A, Hove, F, Tjelta, TI (2000), Deep Penetrating Anchor: Further development, optimization and capacity verification. In: *Proceedings of the Tenth International Offshore and Polar Engineering Conference*, vol. 2, 410–416.
- Lieng, JT, Tjelta, TI, Skaugset, K (2010), Installation of two prototype deep penetrating anchors at the Gjøa Field in the North Sea. In: *Offshore Technology Conference*, 1999–2007, doi: [10.4043/20758-MS](https://doi.org/10.4043/20758-MS).
- Lister, CRB (1964), On the vertical motion of equipment lowered by wire into the deep sea. *Buletinul Institutului Politehnic din Iași*, 10(14):87–97.
- Litkouthi, S, Poskitt, TJ (1980), Damping constants for pile driveability calculations. *Géotechnique*, 30(1):77–86, doi: [10.1680/geot.1980.30.1.77](https://doi.org/10.1680/geot.1980.30.1.77).
- Lorenz, RD, Bannister, M, Daniell, PM, Krysiniski, Z, Leese, MR, Miller, RJ, Newton, G, Rabbetts, P, Willett, DM, Zarnecki, JC (1994), An impact penetrometer for a landing spacecraft. *Measurement Science and Technology*, 5(9):1033–1041, doi: [10.1088/0957-0233/5/9/001](https://doi.org/10.1088/0957-0233/5/9/001).

- Lott, DF, Poeckert, RH (1996), Extending cooperative research. *Sea Technology*, 37(9):56–61.
- Low, HE, Lunne, T, Andersen, KH, Sjursen, MA, Li, X, Randolph, MF (2010), Estimation of intact and remoulded undrained shear strengths from penetration tests in soft clays. *Géotechnique*, 60(11):843–859, doi: [10.1680/geot.9.P.017](https://doi.org/10.1680/geot.9.P.017).
- Low, HE, Randolph, MF, DeJong, JT, Yafrate, NJ (2008), Variable rate full-flow penetration tests in intact and remoulded soil. In: Huang, AB, Mayne, PW (eds.), *Geotechnical and geophysical site characterization*, Proceedings of the 3rd International Conference on Site Characterization, ISC'3, Taipei, 1087–1092.
- Lu, Q, Randolph, MF, Hu, Y, Bugarski, IC (2004), A numerical study of cone penetration in clay. *Géotechnique*, 54(4):257–267, doi: [10.1680/geot.2004.54.4.257](https://doi.org/10.1680/geot.2004.54.4.257).
- Lunne, T (2010), The CPT in offshore soil investigations - a historic perspective. In: *2nd International Symposium on Cone Penetration Testing*, KN 4, URL http://www.cpt10.com/PDF_Files/KN4Luntci.pdf.
- (2012), The fourth James K. Mitchell Lecture: The CPT in offshore soil investigations - a historic perspective. *Geomechanics and Geoengineering*, 7(2):75–101, doi: [10.1080/17486025.2011.640712](https://doi.org/10.1080/17486025.2011.640712).
- Lunne, T, Kleven, A (1981), Role of CPT in North Sea foundation engineering. In: Norris, GM, Holtz, RD (eds.), *Cone Penetration Testing and experience*, 76–107.
- Lunne, T, Robertson, PK, Powell, JJM (1997), *Cone penetration testing in geotechnical practice*. Taylor & Francis, London.
- Masson, D, Harbitz, C, Wynn, R, Pedersen, G, Løvholt, F (2006), Submarine landslides: Processes, triggers and hazard prediction. *Philosophical Transactions of the Royal Society of London A: Mathematical, Physical and Engineering Sciences*, 364(1845):2009–2039, doi: [10.1098/rsta.2006.1810](https://doi.org/10.1098/rsta.2006.1810).
- Maxim Integrated Products (1999), MAXIM 8th-order, lowpass, butterworth, switched-capacitor filter. Online Datasheet, URL <http://datasheets.maxim-ic.com/en/ds/MAX7480.pdf>, Accessed 24 Feb 2012.

- McCarty, JL, Brooks, GW, Beswick, AG (1964), Application of penetrometers to the study of physical properties of lunar and planetary surfaces. Technical Note TN D-2413, National Aeronautics and Space Administration, Washington, D. C., URL <http://catalog.hathitrust.org/Record/011433883>.
- McCarty, JL, Carden, HD (1962), Impact characteristics of various materials obtained by an acceleration-time-history technique applicable to evaluating remote targets. Technical Report D-1269, National Aeronautics and Space Administration, Langley Station, URL <http://babel.hathitrust.org/cgi/pt?id=uiug.30112106593285>.
- (1968), Response characteristics of impacting penetrometers appropriate to lunar and planetary missions. Technical Report D-4454, National Aeronautics and Space Administration, Langley Station, URL <http://books.google.de/books?id=A9YB1K7z00oC>.
- McCoy, FW (1980), Photographic analysis of coring. *Marine Geology*, 38(1–3):263–282, doi: 10.1016/0025-3227(80)90063-8.
- (1985), Mid-core flow-in; implications for stretched stratigraphic sections in piston cores. *Journal of Sedimentary Research*, 55(4):608–610.
- McCoy, FW, Von Herzen, RP (1971), Deep-sea corehead camera photography and piston coring. *Deep Sea Research and Oceanographic Abstracts*, 18(3):361–373, doi: 10.1016/0011-7471(71)90041-6.
- de Medeiros, CJ, Jr. (2001), Torpedo anchor for deep water. In: *Pathways to ultra deepwater opportunities: deep offshore technology*, DOT.
- (2002), Low cost anchor system for flexible risers in deep waters. In: *Offshore Technology Conference*, vol. 2, 1267–1271, doi: 10.4043/14151-MS.
- van der Meer, JJM, Laban, C (1990), Micromorphology of some North Sea till samples, a pilot study. *Journal of Quaternary Science*, 5(2):95–101, doi: 10.1002/jqs.3390050202.
- Melton, JS, Clausner, JE, Christian, H, Furlong, A (2000), Use of dynamic penetrometers to determine fluid mud properties. In: Pederson, J, Adams, EE (eds.), *Dredged material management: options and environmental considerations*, 58–63.

- Meunier, J, Sultan, N, Jegou, P, Harmegnies, F (2004), First tests of penfeld: A new seabed penetrometer. In: *The Fourteenth International Offshore and Polar Engineering Conference*, 338-345.
- Meyerhof, GG (1951), The ultimate bearing capacity of foundations. *Géotechnique*, 2(4):301–332, doi: 10.1680/geot.1951.2.4.301.
- (1953), The bearing capacity of foundations under excentric or inclined loads. In: *Proceedings of the 3rd International Conference on Soil Mechanics and Foundation Engineering*, vol. 1, 440–445.
- (1961), The ultimate bearing capacity of wedge shaped foundations. In: *Proceedings of the 5th International Conference on Soil Mechanics and Foundation Engineering*, vol. 2, 105–109.
- Migliore, HJ, Lee, HJ (1971), Seafloor penetration tests: Presentation and analysis of results. Technical Note N-1178, Naval Civil Engineering Laboratory, Port Hueneme, URL <http://www.dtic.mil/get-tr-doc/pdf?AD=AD0732367>.
- Mitchell, JK (1964), Shearing resistance of soils as a rate process. *Journal of the Soil Mechanics and Foundations Division*, 90(SM1):29–61.
- Mitchell, JK, Soga, K (2005), *Fundamentals of soil behavior*. Wiley, New York, 3 edn.
- Mosher, DC, Christian, H, Cunningham, D, MacKillop, K, Furlong, A, Jarrett, K (2007), The Harpoon free fall cone penetrometer for rapid offshore geotechnical assessment. In: *Offshore site investigation and geotechnics*, 185–202.
- Muir Wood, D (1990), *Soil Behavior and Critical State Soil Mechanics*. Cambridge University Press, Cambridge, 462 pp.
- Mulhearn, PJ (2002), Influences of penetrometer probe tip geometry on bearing strength estimates for mine burial prediction. Technical Report DSTO-TR-1285, Defence Science & Technology, Victoria, URL <http://www.dtic.mil/get-tr-doc/pdf?AD=ADA402610>.
- (2003), Influences of penetrometer tip geometry on bearing strength estimates. *International Journal of Offshore and Polar Engineering*, 13(1):73–78.

- Mulukutla, GK, Huff, LC, Melton, JS, Baldwin, KC, Mayer, LA (2011), Sediment identification using free fall penetrometer acceleration-time histories. *Marine Geophysical Research*, 32(3):397–411, doi: [10.1007/s11001-011-9116-2](https://doi.org/10.1007/s11001-011-9116-2).
- Murray, C, Visintini, L (1985), Parametric analysis of performances of free-fall penetrators in deep-ocean sediments. *IEEE Journal of Oceanic Engineering*, 10(1):38–49, doi: [10.1109/JOE.1985.1137416](https://doi.org/10.1109/JOE.1985.1137416).
- dotOcean N. V. (2012), Determination of a waterway characteristic. Patent EP2460939A1.
- Nazem, M, Carter, JP, Airey, DW, Chow, SH (2012), Dynamic analysis of a smooth penetrometer free-falling into uniform clay. *Géotechnique*, 62(10):893–905, doi: [10.1680/geot.10.P.055](https://doi.org/10.1680/geot.10.P.055).
- Ni, Q, Tan, TS, Dasari, GR, Hight, DW (2004), Contribution of fines to the compressive strength of mixed soils. *Géotechnique*, 54(9):561–569, doi: [10.1680/geot.2004.54.9.561](https://doi.org/10.1680/geot.2004.54.9.561).
- O’Loughlin, CD, Gaudin, C, Morton, JP, White, DJ (2014), MEMS accelerometers for measuring dynamic penetration events in geotechnical centrifuge tests. *International Journal of Physical Modelling in Geotechnics*, 14(2):31–39, doi: [10.1680/ijpmg.13.00020](https://doi.org/10.1680/ijpmg.13.00020).
- O’Loughlin, CD, Randolph, MF, Richardson, M (2004), Experimental and theoretical studies of deep penetrating anchors. In: *Offshore Technology Conference*, 2122–2132, doi: [10.4043/16841-MS](https://doi.org/10.4043/16841-MS).
- O’Loughlin, CD, Richardson, MD, Randolph, MF (2009), Centrifuge tests on dynamically installed anchors. In: *Proceedings of the ASME 2009 28th International Conference on Ocean, Offshore and Arctic Engineering*, vol. 7, 391–399, Ocean, Offshore, and Arctic Engineering Division, ASME, doi: [10.1115/OMAE2009-80238](https://doi.org/10.1115/OMAE2009-80238).
- O’Loughlin, CD, Richardson, MD, Randolph, MF, Gaudin, C (2013), Penetration of dynamically installed anchors in clay. *Géotechnique*, 63(11):909–919, doi: [10.1680/geot.11.P.137](https://doi.org/10.1680/geot.11.P.137).
- Orenberg, P, True, D, Bowman, L, Herrmann, H, March, R (1996), Use of a dropped dynamic penetrometer in cohesionless soil. In: *28th Annual Offshore Technology Conference*, vol. 1, 639–648, doi: [10.4043/8027-MS](https://doi.org/10.4043/8027-MS).

- Osler, J, Furlong, A, Christian, H (2006a), A sediment probe for the rapid assessment of seabed characteristics. In: *Acoustic sensing techniques for the shallow water environment*, 171–181, Springer, doi: [10.1007/978-1-4020-4386-4_13](https://doi.org/10.1007/978-1-4020-4386-4_13).
- Osler, J, Furlong, A, Christian, H, Lamplugh, M (2006b), The integration of the Free Fall Cone Penetrometer (FFCPT) with the Moving Vessel Profiler (MVP) for the rapid assessment of seabed characteristics. In: *Proceedings of the Canadian Hydrographic Conference*, URL http://www.brooke-ocean.com/document/ffcpt_paper_osler_chc2006.pdf.
- (2006c), The integration of the Free Fall Cone Penetrometer (FFCPT) with the Moving Vessel Profiler (MVP) for the rapid assessment of seabed characteristics. *International Hydrographic Review*, 7(3):45–53.
- Parker, WR, Sills, GC (1990), Observation of corer penetration and sample entry during gravity coring. *Marine Geophysical Researches*, 12(1-2):101–107, doi: [10.1007/BF00310566](https://doi.org/10.1007/BF00310566).
- Parkin, A, Lunne, T (1982), Boundary effects in the laboratory calibration of a cone. In: Verruijt, A (ed.), *European Symposium on Penetration Testing (ESOPT II)*, vol. 2, 761–768.
- Perlow, M, Richards, AF (1977), Influence of shear velocity on vane shear strength. *Journal of the Geotechnical Engineering Division*, 103(GT1):19–32.
- Peuchen, J, Mayne, P (2007), Rate effects in vane shear testing. In: *Offshore site investigation and geotechnics*, 187–194.
- Poorooshasb, F, James, RG (1989), Centrifuge modelling of heat-generating waste disposal. *Canadian Geotechnical Journal*, 26(4):640–652, doi: [10.1139/t89-077](https://doi.org/10.1139/t89-077).
- Power, PT, Geise, JM (1994), Offshore soil investigation techniques and equipment for the next century. In: Chryssostomidis, C (ed.), *Seventh International Conference on the Behaviour of Offshore Structures*, vol. 1, 97–109.
- Prandtl, L (1921), Über die Eindringungsfestigkeit (Härte) plastischer Baustoffe und die Festigkeit von Schneiden. *Zeitschrift für Angewandte Mathematik und Mechanik*, 1(1):15–20, doi: [10.1002/zamm.19210010102](https://doi.org/10.1002/zamm.19210010102).

- Preslan, WL (1969), Accelerometer-monitored coring. In: *Civil Engineering in the Oceans II*, 655–687.
- Raie, MS, Tassoulas, JL (2009), Installation of torpedo anchors: Numerical modeling. *Journal of Geotechnical and Geoenvironmental Engineering*, 135(12):1805–1813, doi: [10.1061/\(ASCE\)GT.1943-5606.0000159](https://doi.org/10.1061/(ASCE)GT.1943-5606.0000159).
- Randolph, MF (2004), Characterisation of soft sediments for offshore applications. In: Viana da Fonseca, A, Mayne, PW (eds.), *Geotechnical and geophysical site characterization*, Proceedings of the 2nd International Conference on Site Characterization, ISC'2, Porto, 209–231.
- Randolph, MF, Gaudin, C, Gourvenec, SM, White, DJ, Boylan, N, Cassidy, MJ (2011), Recent advances in offshore geotechnics for deep water oil and gas developments. *Ocean Engineering*, 38(7):818–834, doi: [10.1016/j.oceaneng.2010.10.021](https://doi.org/10.1016/j.oceaneng.2010.10.021).
- Rattley, MJ, Richards, DJ, Lehane, BM (2008), Uplift performance of transmission tower foundations embedded in clay. *Journal of Geotechnical and Geoenvironmental Engineering*, 134(4):531–540, doi: [10.1061/\(ASCE\)1090-0241\(2008\)134:4\(531\)](https://doi.org/10.1061/(ASCE)1090-0241(2008)134:4(531)).
- Richards, AF, McDonald, VJ, Olson, RE, Keller, GH (1972), *Underwater soil sampling, testing and construction control*, vol. 501 of *ATSM STP*, chap. In-Place Measurement of Deep Sea Soil Shear Strength, 55–68. American Society for Testing and Materials, Philadelphia, doi: [10.1520/STP38793S](https://doi.org/10.1520/STP38793S).
- Richards, AF, Zuidberg, H (1985), In situ testing and sampling offshore in water depths exceeding 300 m. In: *Offshore site investigation*, 129–163.
- Richardson, MD (2008), *Dynamically installed anchors for floating offshore structures*. Ph.D. thesis, The University Of Western Australia, Crawley, URL http://repository.uwa.edu.au:80/R/-?func=dbin-jump-full&object_id=10597&silolibrary=GEN01.
- Richardson, MD, O'Loughlin, CD, Randolph, MF, Cunningham, TJ (2006), Drum centrifuge modelling of dynamically penetrating anchors. In: Ng, CWW (ed.), *Proceedings of the Sixth International Conference on Physical Modelling in Geotechnics*, 673–678, doi: [10.1201/NOE0415415866.ch96](https://doi.org/10.1201/NOE0415415866.ch96).
- Richardson, MD, O'Loughlin, CD, Randolph, MF, Gaudin, C (2009), Setup following installation of dynamic anchors in normally consolidated clay. *Journal of Geotechnical and Geoenvironmental Engineering*, 135(4):487–496, doi: [10.1061/\(ASCE\)1090-0241\(2009\)135:4\(487\)](https://doi.org/10.1061/(ASCE)1090-0241(2009)135:4(487)).

- Rijsdijk, KF, Passchier, S, Weerts, HJT, Laban, C, van Leeuwen, RJW, Ebbing, JHJ (2005), Revised Upper Cenozoic stratigraphy of the Dutch sector of the North Sea Basin: Towards an integrated lithostratigraphic, seismostratigraphic and allostratigraphic approach. *Netherlands Journal of Geosciences*, 85(2):129–146.
- Robertson, PK (1990), Soil classification using the cone penetration test. *Canadian Geotechnical Journal*, 27(1):151–158, doi: [10.1139/t90-014](https://doi.org/10.1139/t90-014).
- Roddy, DJ, Rittenhouse, JB, Scott, RF (1963), Dynamic penetration studies in crushed rock under atmospheric and vacuum conditions. *AIAA Journal*, 1(4):868–873, doi: [10.2514/3.1656](https://doi.org/10.2514/3.1656).
- Salgado, R, Mitchell, JK, Jamilokowski, M (1997), Cavity expansion and penetration resistance in sand. *Journal of Geotechnical and Geoenvironmental Engineering*, 123(4):344–354, doi: [10.1061/\(ASCE\)1090-0241\(1997\)123:4\(344\)](https://doi.org/10.1061/(ASCE)1090-0241(1997)123:4(344)).
- Sanglerat, G (1972), Developments in geotechnical engineering. In: Sanglerat, G (ed.), *The penetrometer and soil exploration*, vol. 1, Elsevier, Amsterdam, doi: [10.1016/B978-0-444-40976-8.50006-8](https://doi.org/10.1016/B978-0-444-40976-8.50006-8).
- Schlue, BF, Moerz, T, Kreiter, S (2010), Influence of shear rate on undrained vane shear strength of organic harbor mud. *Journal of Geotechnical and Geoenvironmental Engineering*, 136(10):1437–1447, doi: [10.1061/\(ASCE\)GT.1943-5606.0000356](https://doi.org/10.1061/(ASCE)GT.1943-5606.0000356).
- Schmid, WE (1969), Penetration of objects into the ocean bottom. Technical Report CR 69.030, Naval Civil Engineering Laboratory, Port Hueneme, URL www.dtic.mil/cgi-bin/GetTRDoc?AD=AD0695434.
- Schofield, A, Wroth, P (1968), *Critical state soil mechanics*. McGraw-Hill, London, URL <http://www.geotechnique.info/CSSM>.
- Schroot, BM, Schüttenhelm, RTE (2003), Expressions of shallow gas in the Netherlands North Sea. *Netherlands Journal of Geosciences*, 82(1):91–106.
- Scott, RF (1967), In-place soil mechanics measurements. In: Richards, AF (ed.), *Proceedings of the International Research Conference on Marine Geotechnique*, 264–273.
- (1970), In-place ocean soil strength by accelerometer. *Journal of the Soil Mechanics & Foundations Division*, 96(1):199–211.

- Scourse, JD, Ansari, MH, Wingfield, RTR, Harland, R, S., BP (1998), A middle Pleistocene shallow marine interglacial sequence, Inner Silver Pit, Southern North Sea: Pollen and dinoflagellate cyst stratigraphy and sea-level history. *Quaternary Science Reviews*, 17(9-10):871–900, doi: [10.1016/S0277-3791\(98\)00023-7](https://doi.org/10.1016/S0277-3791(98)00023-7).
- Seifert, A, Stegmann, S, Mörz, T, Lange, M, Wever, T, Kopf, A (2008), In situ pore-pressure evolution during dynamic CPT measurements in soft sediments of the western Baltic Sea. *Geo-Marine Letters*, 28(4):213–227, doi: [10.1007/s00367-008-0102-x](https://doi.org/10.1007/s00367-008-0102-x).
- Seyb, SM, Hammond, SR, Gilliard, T (1977), A new device for recording the behavior of a piston corer. *Deep Sea Research*, 24(10):943–950, doi: [10.1016/0146-6291\(77\)90564-1](https://doi.org/10.1016/0146-6291(77)90564-1).
- Sheahan, TC, Ladd, CC, Germaine, JT (1996), Rate-dependent undrained shear behavior of saturated clay. *Journal of Geotechnical Engineering*, 122(2):99–108, doi: [10.1061/\(ASCE\)0733-9410\(1996\)122:2\(99\)](https://doi.org/10.1061/(ASCE)0733-9410(1996)122:2(99)).
- Shelton, JT (2007), OMNI-MaxTM anchor development and technology. In: *OCEANS 2007*, 1990–1999, IEEE, doi: [10.1109/OCEANS.2007.4449415](https://doi.org/10.1109/OCEANS.2007.4449415).
- Sherif, MA, Fang, YS, Sherif, RI (1984), K_a and K_o behind rotating and non-yielding walls. *Journal of Geotechnical Engineering*, 110(1):41–56, doi: [10.1061/\(ASCE\)0733-9410\(1984\)110:1\(41\)](https://doi.org/10.1061/(ASCE)0733-9410(1984)110:1(41)).
- Skinner, LC, McCave, IN (2003), Analysis and modelling of gravity- and piston coring based on soil mechanics. *Marine Geology*, 199(1-2):181–204, doi: [10.1016/S0025-3227\(03\)00127-0](https://doi.org/10.1016/S0025-3227(03)00127-0).
- Soga, K, Mitchell, JK (1996), *Measuring and Modeling Time Dependent Soil Behavior*, chap. Rate-dependent deformation of structured natural clays, 243–257. ASCE, New York.
- de Sousa, JRM, de Aguiar, CS, Ellwanger, GB, Porto, EC, Foppa, D, de Medeiros, CJ (2011), Undrained load capacity of torpedo anchors embedded in cohesive soils. *Journal of Offshore Mechanics and Arctic Engineering*, 133(2):021102–1–12, doi: [10.1115/1.4001953](https://doi.org/10.1115/1.4001953).
- Spohn, T, Knollenberg, J, Ball, AJ, Banaszkiwicz, M, Benkhoff, J, Grott, M, Grygorczuk, J, Hüttig, C, Hagermann, A, Kargl, G, Kaufmann, E, Kömle, N, Kührt, E, Kossacki, KJ, Marczewski, W, Pelivan, I, Schrödter,

- R, Seiferlin, K (2015), Thermal and mechanical properties of the near-surface layers of comet 67P/Churyumov-Gerasimenko. *Science*, 349(6247), doi: [10.1126/science.aab0464](https://doi.org/10.1126/science.aab0464).
- Spohn, T, Seiferlin, K, Hagermann, A, Knollenberg, J, Ball, AJ, Banaszkiwicz, M, Benkhoff, J, Gadowski, S, Gregorczyk, W, Grygorczuk, J, Hlond, M, Kargl, G, Kührt, E, Kömle, N, Krasowski, J, Marczewski, W, Zarnecki, JC (2007), Mupus – a thermal and mechanical properties probe for the rosetta lander Philae. *Space Science Reviews*, 128(1-4):339–362, doi: [10.1007/s11214-006-9081-2](https://doi.org/10.1007/s11214-006-9081-2).
- Spooner, IS, Williams, P, Martin, K (2004), Construction and use of an inexpensive, lightweight free-fall penetrometer: Applications to paleolimnological research. *Journal of Paleolimnology*, 32(3):305–310, doi: [10.1023/B:JOPL.0000042997.78454.e2](https://doi.org/10.1023/B:JOPL.0000042997.78454.e2).
- Stark, N (2010), *Geotechnical investigation of sediment remobilization processes using dynamic penetrometers*. Ph.D. thesis, Universität Bremen, Bremen, URL <http://elib.suub.uni-bremen.de/edocs/00101886-1.pdf>.
- Stark, N, Coco, G, Bryan, KR, Kopf, A (2012a), In-situ geotechnical characterization of mixed-grain-size bedforms using a dynamic penetrometer. *Journal of Sedimentary Research*, 82(7):540–544, doi: [10.2110/jsr.2012.45](https://doi.org/10.2110/jsr.2012.45).
- Stark, N, Hanff, H, Kopf, A (2009a), Nimrod: A tool for rapid geotechnical characterization of surface sediments. *Sea Technology*, 50(4):10–14.
- Stark, N, Hanff, H, Svenson, C, Ernstsens, VB, Lefebvre, A, Winter, C, Kopf, A (2011), Coupled penetrometer, MBES and ADCP assessments of tidal variations in surface sediment layer characteristics along active subaqueous dunes, Danish Wadden Sea. *Geo-Marine Letters*, 31(4):249–258, doi: [10.1007/s00367-011-0230-6](https://doi.org/10.1007/s00367-011-0230-6).
- Stark, N, Hay, AE, Trowse, G (2014a), Cost-effective geotechnical and sedimentological early site assessment for ocean renewable energies. In: *Oceans-St. John's, 2014*, 183–190, doi: [10.1109/OCEANS.2014.7003004](https://doi.org/10.1109/OCEANS.2014.7003004).
- Stark, N, Kopf, A (2011), Detection and quantification of sediment remobilization processes using a dynamic penetrometer. In: *OCEANS'11 MT-S/IEEE KONA*, 938–946, IEEE.
- (2013), In-situ geotechnical investigation of sediment remobilization processes. *Sea Technology*, 54(2):53–59.

- Stark, N, Kopf, A, Hanff, H, Stegmann, S, Wilkens, R (2009b), Geotechnical investigations of sandy seafloors using dynamic penetrometers. In: *OCEANS 2009, MTS/IEEE Biloxi - Marine Technology for Our Future: Global and Local Challenges*, 114–123.
- Stark, N, Le Dantec, N, Corella, JP, Barry, DA, Lemmin, U, Girardclos, S, Kopf, A (2013), Deployment of a dynamic penetrometer from manned submersibles for fine-scale geomorphology studies. *Limnology and Oceanography: Methods*, 11(10):529–539, doi: [10.4319/lom.2013.11.529](https://doi.org/10.4319/lom.2013.11.529).
- Stark, N, Staelens, P, Hay, AE, Hatcher, B, Kopf, A (2014b), Geotechnical investigation of coastal areas with difficult access using portable free-fall penetrometers. In: *3rd International Symposium on Cone Penetration Testing*, Paper 1–06, URL <http://www.cpt14.com/cpt14-papers>.
- Stark, N, Wever, T (2009), Unraveling subtle details of expendable bottom penetrometer (xbp) deceleration profiles. *Geo-Marine Letters*, 29(1):39–45, doi: [10.1007/s00367-008-0119-1](https://doi.org/10.1007/s00367-008-0119-1).
- Stark, N, Wilkens, R, Ernstsen, VB, Lambers-Huesmann, M, Stegmann, S, Kopf, A (2012b), Geotechnical properties of sandy seafloors and the consequences for dynamic penetrometer interpretations: Quartz sand versus carbonate sand. *Geotechnical and Geological Engineering*, 30(1):1–14, doi: [10.1007/s10706-011-9444-7](https://doi.org/10.1007/s10706-011-9444-7).
- Stegmann, S (2007), *Design of a free-fall penetrometer for geotechnical characterisation of saturated sediments and its geological application*. Ph.D. thesis, Universität Bremen, Bremen, URL <http://elib.suub.uni-bremen.de/diss/docs/00011220.pdf>.
- Stegmann, S, Kopf, A (2007), Marine deep-water free-fall CPT measurements for landslide characterisation off Crete, Greece (Eastern Mediterranean) - part 1: A new 4000 m cone penetrometer. In: Lykousis, V, Sakellariou, D, Locat, J (eds.), *Submarine Mass Movements and Their Consequences*, vol. 27 of *Advances in Natural and Technological Hazards Research*, 171–177, Springer Netherlands, doi: [10.1007/978-1-4020-6512-5_18](https://doi.org/10.1007/978-1-4020-6512-5_18).
- Stegmann, S, Mörz, T, Kopf, A (2006a), Initial results of a new free fall-cone penetrometer. *Norwegian Journal of Geology*, 86(3):199–208.
- Stegmann, S, Strasser, M, Anselmetti, F, Kopf, A (2007), Geotechnical in situ characterization of subaquatic slopes: The role of pore pressure transients versus frictional strength in landslide initiation. *Geophysical Research Letters*, 34(7):L07607–1–5, doi: [10.1029/2006GL029122](https://doi.org/10.1029/2006GL029122).

- Stegmann, S, Villinger, H, Kopf, A (2006b), Design of a modular, marine free-fall cone penetrometer. *Sea Technology*, 47(2):27–33.
- Steiner, A (2013), *Sub-seafloor characterization and stability of submarine slope sediments using dynamic and static piezocone penetrometers*. Ph.D. thesis, Universität Bremen, Bremen, URL <http://elib.suub.uni-bremen.de/edocs/00103577-1.pdf>.
- Steiner, A, Kopf, AJ, L’Heureux, JS, Kreiter, S, Stegmann, S, Hafidason, H, Moerz, T (2014), In situ dynamic piezocone penetrometer tests in natural clayey soils – a reappraisal of strain-rate corrections. *Canadian Geotechnical Journal*, 51(3):272–288, doi: [10.1139/cgj-2013-0048](https://doi.org/10.1139/cgj-2013-0048).
- Steiner, A, L’Heureux, JS, Kopf, A, Vanneste, M, Longva, O, Lange, M, Hafidason, H (2012), An in-situ free-fall piezocone penetrometer for characterizing soft and sensitive clays at Finneidfjord (Northern Norway). In: Yamada, Y, Kawamura, K, Ikehara, K, Ogawa, Y, Urgeles, R, Mosher, D, Chaytor, J, Strasser, M (eds.), *Submarine Mass Movements and Their Consequences*, vol. 31 of *Advances in Natural and Technological Hazards Research*, 99–109, Springer, doi: [10.1007/978-94-007-2162-3_9](https://doi.org/10.1007/978-94-007-2162-3_9).
- Stephan, S, Kaul, N, Stark, N, Villinger, H, Wever, T (2011), LIRmeter: a new tool for rapid assessment of sea floor parameters. bridging the gap between free-fall instruments and frame-based CPT. In: *OCEANS’11 MT-S/IEEE KONA*, 952–961.
- Stephan, S, Kaul, N, Villinger, H (2012), The Lance Insertion Retardation meter (LIRmeter): An instrument for in situ determination of sea floor properties—technical description and performance evaluation. *Marine Geophysical Research*, 33(3):209–221, doi: [10.1007/s11001-012-9156-2](https://doi.org/10.1007/s11001-012-9156-2).
- (2015), Validation of impact penetrometer data by cone penetration testing and shallow seismic data within the regional geology of the Southern North Sea. *Geo-Marine Letters*, 35(3):203–219, doi: [10.1007/s00367-015-0401-y](https://doi.org/10.1007/s00367-015-0401-y).
- Stewart, DP, Randolph, MF (1991), A new site investigation tool for the centrifuge. In: Ko, HY, McLean, FG (eds.), *Centrifuge 91*, 531–538.
- Stoker, MS, Balson, PS, Long, D, Tappin, DR (2011), An overview of the lithostratigraphical framework for the Quaternary deposits on the United Kingdom continental shelf. Research Report RR/11/03, British Geological Survey, Keyworth, URL <https://www.bgs.ac.uk/downloads/start.cfm?id=2084>.

- Stoll, RD (2004), Measuring sea bed properties using static and dynamic penetrometers. In: *Civil engineering in the Oceans VI*, 386–395, doi: [10.1061/40775\(182\)31](https://doi.org/10.1061/40775(182)31).
- Stoll, RD, Akal, T (1997), Probe for evaluating seafloor geoaoustic and geotechnical properties. Patent US5681982.
- (1999), XBP - tool for rapid assessment of seabed sediment properties. *Sea Technology*, 40(2):47–51.
- Stoll, RD, Sun, YF, Bitte, I (2007), Seafloor properties from penetrometer tests. *IEEE Journal of Oceanic Engineering*, 32(1):57–63, doi: [10.1109/JOE.2007.890943](https://doi.org/10.1109/JOE.2007.890943).
- Strasser, M, Stegmann, S, Bussmann, F, Anselmetti, FS, Rick, B, Kopf, A (2007), Quantifying subaqueous slope stability during seismic shaking: Lake lucerne as model for ocean margins. *Marine Geology*, 240(1-4):77–97, doi: [10.1016/j.margeo.2007.02.016](https://doi.org/10.1016/j.margeo.2007.02.016).
- Sturm, H, Andresen, L (2010), Large deformation analysis of the installation of dynamic anchor. In: Benz, T, Nordal, S (eds.), *7th European Conference on Numerical Methods in Geotechnical Engineering (NUMGE'10)*, 255–260, doi: [10.1201/b10551-47](https://doi.org/10.1201/b10551-47).
- Talbert, DM (1980), Subseabed radioactive waste disposal feasibility program: Ocean engineering challenges for the 80's. Technical report SAND-80-0304C, Sandia National Labs, Albuquerque, URL <http://www.osti.gov/scitech/servlets/purl/5168453>.
- Teh, CI (1987), *An analytical study of the cone penetration test*. Ph.D. thesis, University of Oxford, Oxford, URL <http://www.eng.ox.ac.uk/civil/publications/theses/teh.pdf>.
- Terzaghi, K (1943), *Theoretical Soil Mechanics*. John Chapman and Hall Ltd, London, 528 pp.
- Thevanayagama, S, Martin, GR (2002), Liquefaction in silty soils—screening and remediation issues. *Soil Dynamics and Earthquake Engineering*, 22(9-12):1035–1042, doi: [10.1016/S0267-7261\(02\)00128-8](https://doi.org/10.1016/S0267-7261(02)00128-8).
- Thompson, D, March, R, Herrmann, H (2002), Groundtruth results for dynamic penetrometers in cohesive soils. In: *OCEANS '02 MTS/IEEE*, vol. 4, 2117–2123, IEEE, doi: [10.1109/OCEANS.2002.1191958](https://doi.org/10.1109/OCEANS.2002.1191958).

- Trabant, PK (1984), *Applied high-resolution geophysical methods: Offshore geoengineering hazards*, chap. Marine geotechnique, an overview, 25–42. Springer, Dordrecht, doi: [10.1007/978-94-009-6493-8_3](https://doi.org/10.1007/978-94-009-6493-8_3).
- True, DG (1976), *Undrained vertical penetration into ocean bottom soils*. Ph.D. thesis, University of California, Berkeley, URL <http://search.proquest.com/docview/302795036>.
- Šuklje, L (1957), The analysis of the consolidation process by the isotaches method. In: *Proceedings of the Fourth International Conference on Soil Mechanics and Foundation Engineering*, vol. 1, 200–206.
- Vanneste, M, Sultan, N, Garziglia, S, Forsberg, CF, L’Heureux, JS (2014), Seafloor instabilities and sediment deformation processes: The need for integrated, multi-disciplinary investigations. *Marine Geology*, 352:183–214, doi: [10.1016/j.margeo.2014.01.005](https://doi.org/10.1016/j.margeo.2014.01.005).
- Vesic, AS (1975), *Foundation engineering handbook*, chap. Bearing capacity of shallow foundations, 121–147. van Nostrand, New York, 1 edn.
- Villinger, H, Alexandrakis, E, Alt-Epping, P, Becke, R, Dziadek, R, Enneking, K, Fleischmann, T, Gaida, K, Heesemann, B, Janßen, C, Kaul, N, Pichler, T, Ruiz, M, Schmidt-Schierhorn, F, Schwab, A, Stephan, S, Zwick, M (2010a), Report and preliminary results of R/V Sonne cruise SO207, Caldera-Caldera, 21 June–13 July, 2010. Seamountflux: Efficient cooling in young oceanic crust caused by circulation of seawater through seamounts (Guatemala Basin, East Pacific Ocean). Report 276, Fachbereich Geowissenschaften, Universität Bremen, Bremen, URL <http://elib.suub.uni-bremen.de/edocs/00102553-1.pdf>.
- Villinger, H, Bach, W, Biddle, J, Blazejak, A, Edwards, K, Ferdelman, T, Heesemann, B, Heuer, V, Kaul, N, Kellermann, M, Knab, N, McManus, J, Muratli, J, Picard, A, Polster, A, Schippers, A, Schmidt-Schierhorn, F, Schwab, A, Stephan, S, Teske, A, Ziebis, W (2010b), Mid-Atlantic Ridge site surveys of sediments and basement in North Pond. Maria S. Merian Berichte Fahrtbericht 11-1, Leitstelle Deutsche Forschungsschiffe, Institut für Meereskunde der Universität Hamburg, Hamburg, URL http://www.geo.uni-bremen.de/FB5/Sensorik/publikationen/Fahrtbericht_MSM11_1.pdf.
- Villinger, H, Grigel, J, Heesemann, B (1999), Acceleration-monitored coring revisited. *Geo-Marine Letters*, 19(4):275–281, doi: [10.1007/s003670050119](https://doi.org/10.1007/s003670050119).

- Villinger, HW, Tréhu, AM, Grevemeyer, I (2010c), *Geophysical Characterization of Gas Hydrates*, chap. Seafloor Marine Heat Flux Measurements and Estimation of Heat Flux from Seismic Observations of Bottom Simulating Reflectors, 279–300. Society of Exploration Geophysicists, Tulsa, doi: [10.1190/1.9781560802197.ch18](https://doi.org/10.1190/1.9781560802197.ch18).
- Watson, PG, Newson, TA, Randolph, MF (1998), Strength profiling in soft offshore soils. In: Robertson, PK, Mayne, PW (eds.), *Geotechnical site characterization*, vol. 2, 1389–1394.
- Weaver, PPE, Schultheiss, PJ (1983), Detection of re-penetration and sediment disturbance in open-barrel gravity cores. *Journal of Sedimentary Petrology*, 53(2):649–654.
- Wentworth, CK (1922), A scale of grade and class terms for clastic sediments. *The Journal of Geology*, 30(5):377–392, doi: [10.1086/622910](https://doi.org/10.1086/622910).
- Wessel, P, Smith, WHF (1991), Free software helps map and display data. *Eos, Transactions American Geophysical Union*, 72(41):441–448, doi: [10.1029/90EO00319](https://doi.org/10.1029/90EO00319).
- Wessel, P, Smith, WHF, Scharroo, R, Luis, J, F., W (2013), Generic mapping tools: Improved version released. *Eos, Transactions American Geophysical Union*, 94(45):409–410, doi: [10.1002/2013EO450001](https://doi.org/10.1002/2013EO450001).
- Winters, WJ (1987), Embedment, penetration, hole closure, and related geotechnical tests associated with subseafloor nuclear waste disposal. Technical Report 87-256, Woods Hole Oceanographic Institution, Woods Hole, URL <http://pubs.usgs.gov/of/1987/0256/report.pdf>.
- Winterwerp, JC (2005), Reducing harbor siltation. I: Methodology. *Journal of Waterway, Port, Coastal, and Ocean Engineering*, 131(6):258–266, doi: [10.1061/\(ASCE\)0733-950X\(2005\)131:6\(258\)](https://doi.org/10.1061/(ASCE)0733-950X(2005)131:6(258)).
- Yoshimine, M, Robertson, PK, Wride, CE (1999), Undrained shear strength of clean sands to trigger flow liquefaction. *Canadian Geotechnical Journal*, 36(5):891–906, doi: [10.1139/t99-047](https://doi.org/10.1139/t99-047).
- Young, AG, Bernard, BB, Remmes, BD, Babb, LV, Brooks, JM (2011), “CPT Stinger” - an innovative method to obtain CPT data for integrated geoscience studies. In: *Offshore Technology Conference*, vol. 2, 1509–1518, doi: [10.4043/21569-MS](https://doi.org/10.4043/21569-MS).

- Yu, HS, Houlsby, GT (1991), Finite cavity expansion in dilatant soils: Loading analysis. *Géotechnique*, 41(2):173–183, doi: [10.1680/geot.1991.41.2.173](https://doi.org/10.1680/geot.1991.41.2.173).
- Zagwijn, WH (1974), The palaeogeographic evolution of the Netherlands during the Quaternary. *Geologie en Mijnbouw*, 53(6):369–385.
- Zarnecki, JC, Leese, MR, Hathi, B, Ball, AJ, Hagermann, A, Towner, MC, Lorenz, RD, McDonnell, JAM, Green, SF, Patel, MR, Ringrose, TJ, Rosenberg, PD, Atkinson, KR, Paton, MD, Banaszekiewicz, M, Clark, BC, Ferri, F, Fulchignoni, M, Ghafoor, NAL, Kargl, G, Svedhem, H, Delderfield, J, Grande, M, Parker, DJ, Challenor, PG, Geake, JE (2005), A soft solid surface on Titan as revealed by the Huygens Surface Science Package. *Nature*, 438:792–795, doi: [10.1038/nature04211](https://doi.org/10.1038/nature04211).
- Zhou, H, Randolph, MF (2009), Resistance of full-flow penetrometers in rate-dependent and strain-softening clay. *Géotechnique*, 59(2):79–86, doi: [10.1680/geot.2007.00164](https://doi.org/10.1680/geot.2007.00164).
- Zhu, H, Randolph, MF (2011), Numerical analysis of a cylinder moving through rate-dependent undrained soil. *Ocean Engineering*, 38(7):943–953, doi: [10.1016/j.oceaneng.2010.08.005](https://doi.org/10.1016/j.oceaneng.2010.08.005).
- Zimmerman, EH (2010), Proven high efficiency anchor for harsh cyclonic environments. In: *OCEANS 2010 IEEE - Sydney*, 1–4, doi: [10.1109/OCEANSSYD.2010.5603797](https://doi.org/10.1109/OCEANSSYD.2010.5603797).
- Zimmerman, EH, Smith, MW, Shelton, JT (2009), Efficient gravity installed anchor for deepwater mooring. In: *Offshore Technology Conference*, vol. 3, 1773–1781, doi: [10.4043/20117-MS](https://doi.org/10.4043/20117-MS).
- Zöllmer, V, Irion, G (1996), *Tonminerale des Nordseeraumes: Ihr Verteilungsmuster in kreidezeitlichen bis pleistozänen Sedimentabfolgen und in den Oberflächensedimenten der heutigen Nordsee*, vol. 190 of *Courier Forschungsinstitut Senckenberg*. Schweizerbart Science Publishers, Stuttgart.
- Zuidberg, HM (1972), *Seabed penetrometer tests*. Fugro Symposium on Penetration testing, Fugro, The Hague.
- (1975a), Seacalf: A submersible cone-penetrometer rig. *Marine Geotechnology*, 1(1):15–32, doi: [10.1080/10641197509388150](https://doi.org/10.1080/10641197509388150).

- (1975b), Use of static cone penetrometer testing in the North Sea. In: Verruijt, A (ed.), *Proceedings of the European Symposium on Penetration Testing*, 433–436.

Appendix A

Conference contribution to the OCEANS 2011

LIRmeter: A new tool for rapid assessment of sea floor
parameters. Bridging the gap between free-fall
instruments and frame-based CPT

Stephan, S¹ ✉ and Kaul, N¹ and Stark N² and Villinger, H¹ and Wever, T³

Published in: *OCEANS'11 MTS/IEEE KONA*; Received: 20 April 2011 /
Accepted: 12 June 2011 / Published online: December 2011

Citation: Stephan, S, Kaul, N, Stark N, Villinger, H, Wever, T (2011).
LIRmeter: A new tool for rapid assessment of sea floor parameters. Bridging
the gap between free-fall instruments and frame-based CPT. In: *OCEANS'11
MTS/IEEE KONA*, 952–961.

¹Universität Bremen
Department of Geosciences
28359 Bremen, Germany
sstephan@uni.bremen.de

²Universität Bremen
MARUM - Zentrum für Marine
Umweltwissenschaften
28359 Bremen, Germany

³Forschungsbereich für Wasserschall und Geophysik
(Wehrtechnische Dienststelle für Schiffe und Marinewaffen, Maritime
Technologie und Forschung)
24148 Kiel, Germany

Abstract Physical and geotechnical parameters of marine sediments are of vital interest to fields like foundation planning of offshore structures, surveying of cable routes, sediment dynamics, sediment manipulation (dredging, plowing), ground truthing of acoustical surveys, risk assessment and mine burial predictions. Therefore, characterization of geotechnical *in situ* parameters with dynamic penetrometers is of interest for research, consulting and the offshore industry, because *in situ* methods, and especially dynamic tests, are generally less time consuming than static tests or measurements on samples. In addition, recovery of sediment samples from the seafloor may alter the sediment characteristics (pressure decrease, temperature change) and limits the information value. To date, the determination of fundamental parameters like shear strength, bearing capacity or grain size is predominantly done *ex situ*. However, *in situ* assessment of these parameters leads to a better characterization of marine sediments due to direct measurement under field conditions.

In this paper, we present the technical specifications and performance of a newly developed dynamic penetrometer. The penetrometer, named Lance Insertion Retardation Meter (LIRmeter), is a winch lowered device which can be used in a pogo style fashion to make multi penetration measurements. The observed parameter is the deceleration during penetration. The probe consists of a lance of four meter length equipped with electronics to record the deceleration during penetration, and is aimed to bridge the gap between lightweight free falling systems and sophisticated static CPT. The LIRmeter weighs about 400 kg in water and can achieve penetration depths up to four meters in cohesive sediments in its current configuration.

Signals from analog MEMS acceleration sensors of different ranges of 1.7, 3.5 and 6 g are converted using a 16-bit/16-channel ADC. Data is sampled at rates of typically 500 Hz per channel assuring a high data density even at short penetrations. Ambient pressure, inclination and temperature are also recorded as secondary parameters. Power supply is provided by a 20 Ah lithium polymer battery, allowing an operation time of 14 h. Charging of

The final publication is available at IEEE via <http://ieeexplore.ieee.org/xpl/login.jsp?tp=&arnumber=6106973>

the battery takes about four hours. Data acquisition, as well as communication is controlled by a rugged, low power industrial PC/104-system running GNU/Linux. Charging and communication can be done without needing to open the pressure case. Data can be downloaded via Ethernet interfaces.

The recorded time series of deceleration during sea floor penetrations can be integrated once and twice to obtain time series of velocity and penetration depth. Thus, a relationship between deceleration and penetration depth can be established. The justification for this approach is provided by a common and well accepted premise that stiff to hard sediments cause a high deceleration during penetration, whereas soft sediments lead to lower peak deceleration of a probe during penetration. By using state of the art methods, geotechnical parameters can be deduced from this relationship, and estimates on grain size can be made.

Calculating sediment physical and geotechnical parameters from deceleration measurements is not yet common, but represents an up and coming field of research. Different approaches (momentum based, empirical relations and numerical experiments) exist and have mainly been adopted for lightweight free falling penetrometers in the context of sediment mobilization and burial predictions. Some of the theoretical approaches appear to be suitable for penetrometers like the LIRmeter. Here, we show results of an adaptation of these approaches.

Data were collected in (a) the eastern part of the German Bight (North Sea) and (b) the western part of the German Bight. The variety of sediment types ranges from muddy sediments to sandy sediments with different grain sizes and a varying amount of mud. The deceleration of the probe is in the range of about 3 m/s^2 for deep sea ooze, $10\text{-}20 \text{ m/s}^2$ for sediments with a higher amount of mud and over 35 m/s^2 for sandy sediments. Samples of these sediments were taken and analyzed with respect to grain size in the laboratory. Supplemental information has been provided by the German North Sea geoscientific database "Geopotenzial Deutsche Nordsee" (GPDN).

The system has proven failsafe operation, regardless of the regime, soil and weather. These conditions ranged from shallow seas to ocean depth (in other surveys), from gravel to deep sea ooze and from calm to stormy seas.

The first deployments show excellent data quality and operational performance of the LIRmeter. It can be observed that the achieved penetration depth is affected by the amount of mud content in the sediment. A high amount of mud leads to deeper penetration of the probe. Especially the research areas in the North Sea show a high variability in mud content. Hence, special attention is paid on these sediments. Results of different approaches are presented and discussed in context of grain size and measurements with other penetrometers.

A.1 Introduction

Marine penetrometers and especially dynamic penetrometers are an up and coming field of application in industry and research, as they are easy to handle and fast to deploy. In recent years the development of dynamic penetrometers has been accelerated by new sensors like micro electro mechanical systems (MEMS) or new developments in high speed and low power data acquisition systems. These new techniques allow the development of robust and high performing systems.

Dynamic marine penetrometers are used for the characterization of soils regarding their geotechnical and sedimentological properties. The parameters, which are deducted from penetrometer measurements, are first order descriptors like shear strength (Aubeny and Shi, 2006; Ingram, 1982; Fabian et al., 2008; Harris et al., 2008; Osler et al., 2006a; Spooner et al., 2004), undrained shear strength (Beard, 1981; Aubeny and Shi, 2006; Chari et al., 1978; Douglas and Wapner, 1996; Akal and Stoll, 1995), bearing capacity (Akal and Stoll, 1995; Dayal and Allen, 1975; Stark et al., 2009b; Mulhearn, 2003; Lee and Elsworth, 2004; Elsworth and Lee, 2005; Chari et al., 1978), dynamic shear modulus (Akal and Stoll, 1995) and grain sizes (Mulukutla et al., 2011; Osler et al., 2006a). Second order descriptors, derived from marine penetrometer measurements are parameters like sediment resistance (Chari et al., 1981; Colp et al., 1975), granularity (Akal and Stoll, 1995), burial prediction (Aubeny and Shi, 2006; Murray and Visintini, 1985), core compaction (Villinger et al., 1999) and sea floor stability (Fabian et al., 2008).

Especially soil mechanical parameters like shear strength or bearing capacity are of vital importance to plan the embedment of marine high voltage cables or pipelines. Marine penetrometers are also used for ground truthing (Stoll et al., 2007), risk assessment (Stegmann et al., 2007), (mine-)burial (Stoll et al., 2007; Beard, 1981), for foundation engineering (Raie and Tsoulas, 2009) and to assess sediment dynamics like scouring, erosion or sediment morphodynamics (Stark et al., 2011; Seifert et al., 2008).

We developed a marine penetrometer called “Lance Insertion Retardation Meter” (LIRmeter) with a penetration depth of up to four meters and for ocean depths of up to 4500 m. The new device was developed to fill the gap between small and lightweight (free fall) penetrometers and frame based Cone Penetration Tests (CPT). Especially the penetration depth range of 0 to 4 m is of interest for cable- and pipeline laying. A tethered marine penetrometer, which is easy to handle and capable to penetrate the desired depth range, could be a new approach to assess sediment properties in the planning phase of such projects.

The instrument has been deployed during two research cruises in the German Bight (North Sea) area. There, the sediment ranged from coarse grained material (coarse sand, gravel) to very fine grained material with cohesive properties (silty and muddy grain sizes). The probe was able to penetrate over the whole range of grain sizes. The resulting data is described in a qualitative and quantitative way. For the quantification of geotechnical and sedimentological properties, links are drawn to results in similar sediments with other penetrometers.

The aims of this projects were to conduct extensive field tests under real conditions with a coverage of a broad spectrum of marine sediments. This is necessary to establish a solid database for further studies on the estimation of quantitative geotechnical parameters from these measurements and to evaluate the performance of the newly developed instrument.

A.2 Material and method

The LIRmeter measures the deceleration during penetration with MEMS sensors. The penetrometer is a tethered and winch lowered device, which can operate autonomously in a pogo style to perform multi penetration measurements. The measurement takes place during the embedment of the probe and hence delivers *in situ* information on sediment properties.

The LIRmeter consists of a weight stand, a rod and an interchangeable conical tip. Two cones with an apex of 60° and a penetration surface of 45 or 60 cm² are currently available. An adaptation of tips with other shapes (cylindrical or spherical) is easily possible and depends on the investigation area. The rod has an effective length of 4 m and a diameter of 65 mm. Due to the fact, that the diameter of the tips are larger than the diameter of the rod, friction along the rod is considered to be reduced. This leads to a design resembling a full-flow penetrometer (see Fig. A.1). Both the rod and the tips are made of high grade stainless steel. The weight stand consists of three mounting tubes for housing the electronics, whereby only one of them is used

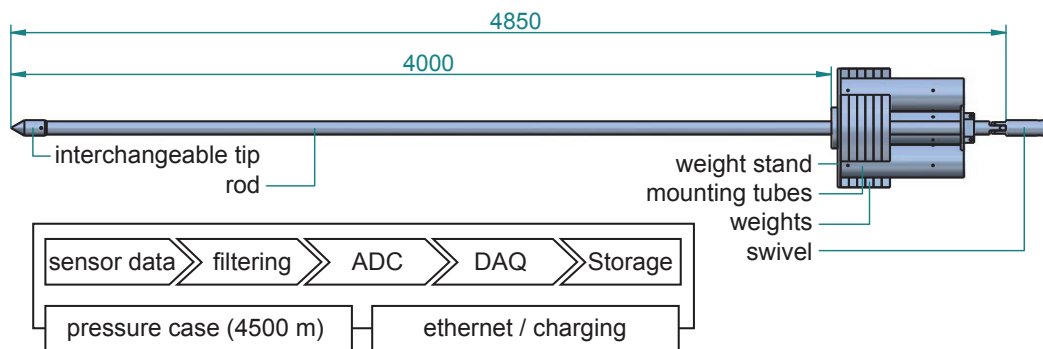


Figure A.1 – Schematics of the lance (lengths in mm) and diagram of signal processing and acquisition process. The electronics are mounted in a pressure case, which fits into the mounting tubes in the weight stand. Communication on deck is realized via Ethernet.

by the LIRmeter in its current configuration. The device is mounted to the wire of the winch with a swivel. The whole lance has a mass of 300 kg and up to 500 kg with additional weights for a deeper embedment. These weights can be mounted between the tubes for the electronics (see Fig. A.1). The maximum operating depth of the system depends on the pressure housing of the electronics and is currently limited to 5000 m water depth. The system has been operated in water depths of up to 4300 m.

A.2.1 Electronics and data acquisition

The instrument consists of a high resolution data acquisition (DAQ) system and sensors providing data of acceleration and ambient water pressure. The DAQ is capable of sampling 16 analog sensors at a rate of 500 Hz per channel simultaneously. The DAQ consists of a PC/104-type microcomputer with integrated 16-channel/16-bit Analog to Digital converter (ADC). The microcomputer has common interfaces like Ethernet, RS-232, PS/2, IDE, as well as digital in/out and analog in/out provided by the ADC. The analog data is filtered before digitalization. Therefore a switched capacitor low-pass butterworth filter (8th Order) at a user selectable corner frequency of (100 Hz typical) is used. The ADC buffers the converted voltages to an on board FPGA, which allows high speed data acquisition. Interrupt routines are provided to read data from the FPGA, which reduces the polling frequency for the logging routine. The PC/104 runs with Debian GNU/Linux and DAQ and logging is controlled via a self written C routine. During a measurement campaign all data is stored autonomously and in a continuous

way on a CompactFlash drive (4 GB). The acquisition process is controlled with a user interface. This interface is based on a dynamic web application running on a webserver. The user has the possibility to set start- and endtimes, schedule sampling jobs and set the sampling rates for each individual channel. It is also possible to maintain the system (halt, reboot, set date/time) and to use a network time server over the network time protocol (NTP) for adequately accurate time synchronisation. Data download is realized via http or ftp. Acceleration data is currently delivered by three micro electro mechanical sensors (MEMS) with different ranges and sensitivities. The resulting resolution of the recorded acceleration data varies with these properties from 38 to 219 μg for a set of sensors covering the range from ± 1 to ± 5 g.

A.2.2 Handling of the instrument

The LIRmeter can be deployed from any vessel with an appropriate winch. The lance is lowered typically with speeds of 1.5 - 2 m/s, depending on sedimentary conditions, water depth and swell. The lance penetrates marine sediments due to its own momentum. A typical measurement has a duration of up to 2 seconds and additionally the time, it takes to lower the device to the sea floor (a set of three measurements in the North Sea at water depths of 35 m took 5 minutes). Hence, a rapid spatial propagation is possible.

A.2.3 Data processing and methods for the determination of sea floor strength

Acceleration-time series during a sea floor penetration indicate the acceleration or deceleration of the probe penetrating the sediment. The measured vertical deceleration is a function of the soil resistance. This soil resistance depends on different parameters such as grain size, unit weight, porosity, permeability, pore pressure or shear strength.

The measuring axes of the vertical and horizontal acceleration sensors are orientated parallel and perpendicular to the rod and measure acceleration or deceleration during a penetration process and the inclination of the probe after its final arrest, respectively. Numerical integration over time for the former acceleration-time-series leads to velocity-time series, another integration step leads to distance over time (Eq. A.2 and A.2).

$$v(t) = \int_0^t a(t)dt = at + v_0 \quad (\text{A.1})$$

$$d(t) = \int_0^t v(t)dt = \frac{a}{2}t^2 + v_0t + d_0 \quad (\text{A.2})$$

The integration is done reversely, so that the starting point for the integration is the point of final rest and the integration ends with the impact on the sea floor. An error in the starting value reproduces as a linear trend after the first integration and as a quadratic trend after the second integration. The optimal starting value is found by a Monte Carlo integration routine, selecting a starting value which provokes a minimal linear trend after the first integration.

Methods for an interpretation of deceleration-depth or deceleration-time series resulting from penetrometer measurements are described by Beard (1981), Stark et al. (2009b) and Mulukutla et al. (2011). The first two approaches are based on the Newtonian laws; the latter author developed a classification scheme. The approaches of Stark et al. (2009b) and Mulukutla et al. (2011) are used here to estimate quantitative parameters.

A.2.4 Site description and deployments

Data has been collected at four sites in the German Bight (North Sea) during two cruises. The first two sites (Amrumbank and Helgoland) are east of Helgoland. These sites were investigated in November 2010 during a cruise with RV PLANET. The third site is located near the wind energy research field “alpha ventus” (approximately 40 nm off shore). The fourth site is situated approximately 60 nm north of the island Borkum. The third and fourth site were investigated during Heincke cruise HE-347 in Feb. 2011 (see Fig. A.3 for the locations).

Besides the penetrometer measurements with the LIRmeter, other penetrometers like the FF-CPT (Stegmann et al., 2006b) and NIMROD (Stark et al., 2009a) were deployed. Sidescan Sonar, multibeam echosounding and coring or grab sampling were also carried out at both locations. The dataset is supplemented by archive data from the North-Sea Geoscientific Database “Geopotenzial Deutsche Nordsee” (GPDN, <http://www.gpdn.de>) providing grain size analyses and core descriptions over the last decades.

A.2.5 Pitfalls

The penetration behavior of the lance can be influenced by the movement of the platform, especially under heavy sea conditions, or if the driving heave

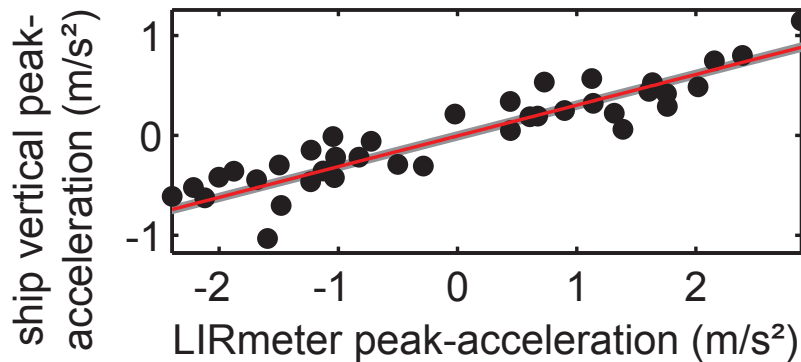


Figure A.2 – Amplification of ship movement over the deep sea wire. Black dots: cross correlated peak accelerations of ship- and instrument movement during a no lowering phase in the water column at 4300 m. Red line: fit through data, grey area: 1σ error of the fit.

frequency of the suspension point lies near the momentary resonance frequency of the wire/instrument-system. An upward movement during the penetration process is a clear indicator for such a disturbance. Another way to verify the quality of a penetration dataset is to estimate if at each time step of the penetration, the instrument is moving slower than the wire of the winch with added heave movement (relative to the sea floor). A loose connection between instrument and cable exists if the cable is moving faster. Hence, the penetration can be considered as undisturbed or “free fall”. If the instrument moves slower relative to the sea floor than the cable, the penetration process should be considered as potentially disturbed. This behavior is predominantly observed at deep sea deployments, where the elastic properties of the cable have a high influence on a possible amplification of the heave movement (Figure A.2) In most cases, the initial deceleration of the probe is so high, that an upward movement of the cable has no effect on the further downward movement of the probe.

A.2.6 Grain size analysis

Analysis of surficial sediments has been done for samples collected during cruise HE-347 and a PLANET cruise in Nov./Dec. 2010, as well as for archive data from the GPDN database. The grain size distribution was analyzed to generate a classification after [Wentworth \(1922\)](#) for the mean grain size of each individual sample.

The grain size distribution of homogeneous and fine grained sediment

samples was generated using a laser diffractometer, whereas grain size distributions of inhomogeneous samples or datasets from the database were generated from sieving experiments. In total 950 datasets were analyzed following the scheme of Folk and Ward (1957) to determine the mean grain size (see Eq. A.3) in terms of diameter (classification in φ -units after Wentworth (1922)).

$$M_z = \frac{\varphi_{16} + \varphi_{50} + \varphi_{84}}{3} \quad (\text{A.3})$$

With M_z as mean grain size and φ_{xx} as grain size, representing 16, 50 or 84 percent of the total fraction.

A.3 Results

A.3.1 Grain size distribution

The variability of the mean grain sizes in the research areas Kaikas, Innogy and Amrumbank is in the range of sandy sediments. In contrast, the research area Helgoland provides a broader spectrum ranging from gravel to silty sediments (see Figure A.3). The standard deviation after Folk and Ward (1957) shows that mostly all of the samples are very well sorted. Hence, the value of the mean grain size gives a good representation of all sediment fractions in each sample.

The spacing of the sample locations is at most 0.5 nautical miles. Thus, data was easily interpolated to generate maps of grain size of surficial sediments for each research area. The maps with the locations for samples and penetrations are shown in Fig. A.5. Due to the fact, that the majority of the samples lie in the range from 0 to 4 ϕ (see Figure A.3), the limits of the spatial representation of grain size were selected by this range.

A.3.2 Penetration types

Due to the length of the rod and the mass of the lance, different types of results can be expected. The first type is a more or less parabolic shaped deceleration curve (see Figure A.4). This occurs if the system is solely decelerated by mechanically hard sediment (Fig. A.6, c). The other type occurs if the lance is first decelerated by the impact to the sea floor, but afterwards gains on velocity and then switches several times between deceleration and acceleration until its final embedment (Figure A.6, LIR1002). This behavior is an evidence for a sea bed that cannot withstand the load applied by

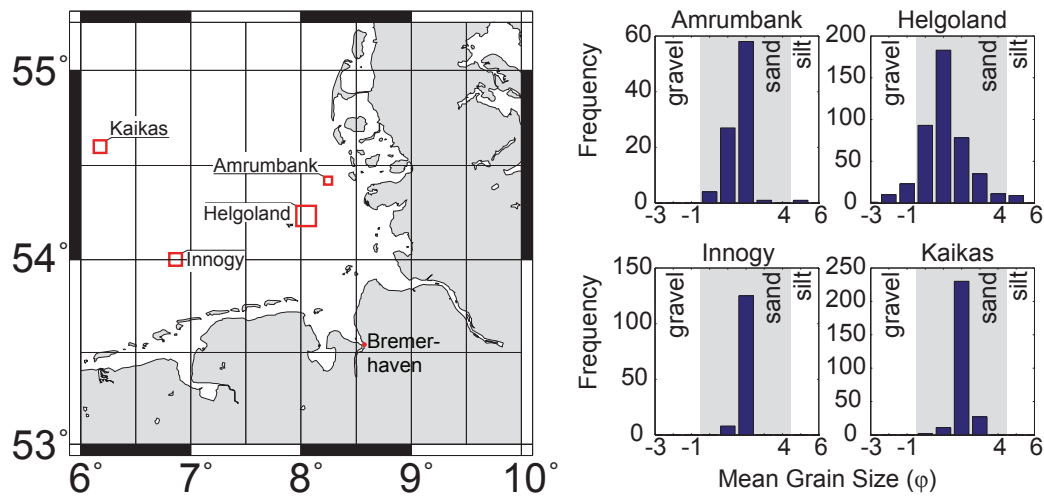


Figure A.3 – Left: Working areas in the German Bight. Map is annotated with Latitude/Longitude (degrees, WGS84) Right: Histograms of the grain sizes. The gray area delimits the range of the most prominent grain sizes discussed in this paper. This range is used as minimum and maximum values for the scale of Fig. A.5.

the probe and has likely several layers. A possible classification scheme of embedments is by normalizing the embedment depth to the probes diameter z/D . After Mulukutla et al. (2011) a shallow penetration has a normalized depth of $z/D \leq 5$, an intermediate penetration has a normalized depth of $5 < z/D \leq 20$ and a deep penetration has a normalized depth of $z/D > 20$.

A.3.3 Acceleration measurements

The positions of the penetrometer deployments are marked in Fig. A.5 as black, filled circles. A representative dataset for each research area is shown in this study (see Fig. A.5, white circles for locations and Fig. A.6 for data.).

In general, the reproducibility of a penetration measurement at the same location is good to very good. The penetration depths can be reproduced with a range of 0.1 m in most of the cases. The general deceleration depth patterns of the independent penetrations at one location are very similar (see i.e. Figure A.6 LIR1002, LIR1011 or LIR1105-STAT092).

The penetration behavior varies with the properties of the sediment. In areas with a very narrow grain size spectrum, such as Amrumbank (LIR1011 and LIR1015), Innogy or Kaikas, the penetration depth varies within a range of less than 0.1 m. In contrast, the grain size distribution in the Helgoland

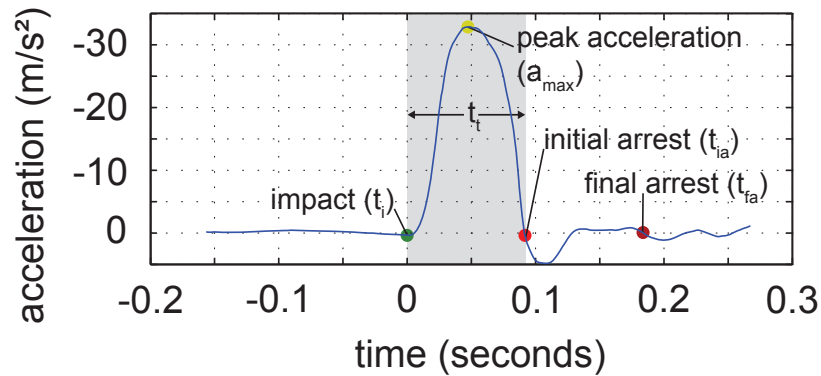


Figure A.4 – Time series of a shallow embedment. The acceleration signal is parabolically shaped. Events are marked with colored circles.

area is very heterogeneous. In this area, the achieved penetration depth varies from 0.1 m to nearly the maximum depth of 4.0 m. The heterogeneity is also visible in the peak decelerations. The measured peak deceleration is high ($> 15 \text{ m/s}^2$), if a fine sand is penetrated and low ($< 15 \text{ m/s}^2$), if finer grained sediments (very fine sand, or finer) occur. The values for a_{\max} (see Figure A.4 for a definition) are also dependent on the impact velocity v_i .

The impact velocities vary, as different winch or lowering strategies were used during each survey. Moreover, the heave induced movement of the vessel influences the impact velocity of the probe. In most cases, the impact velocity lies above 1.0 m/s. The total duration of a penetration varies with sediment properties.

A.3.4 Research area Amrumbank

In the research area Amrumbank, the grain size distribution is homogeneous. Database samples and samples recently taken on the surveys show a very good correlation. Five locations have been investigated in this area; three of them are shown in this paper. The grain size spectrum of the locations LIR1011 and LIR1015 is in the range of fine sand (2 to 3 φ), the location LIR1014 lies in the range of fine to very fine sand (3 to 4 φ). This value is confirmed by two database samples and a grain size sample directly at the location. Data (Fig. A.6, a) of the locations LIR1011 and LIR1015 show very similar behavior. There, the penetration depth is in the range of 0.08 to 0.1 m. The peak decelerations indicate a mechanically hard sediment with values for $a_{\max} \sim 25 - 40 \text{ m/s}^2$. The penetration in the area of fine to very fine sand (LIR1014) yields penetration depths of around 0.5 m.

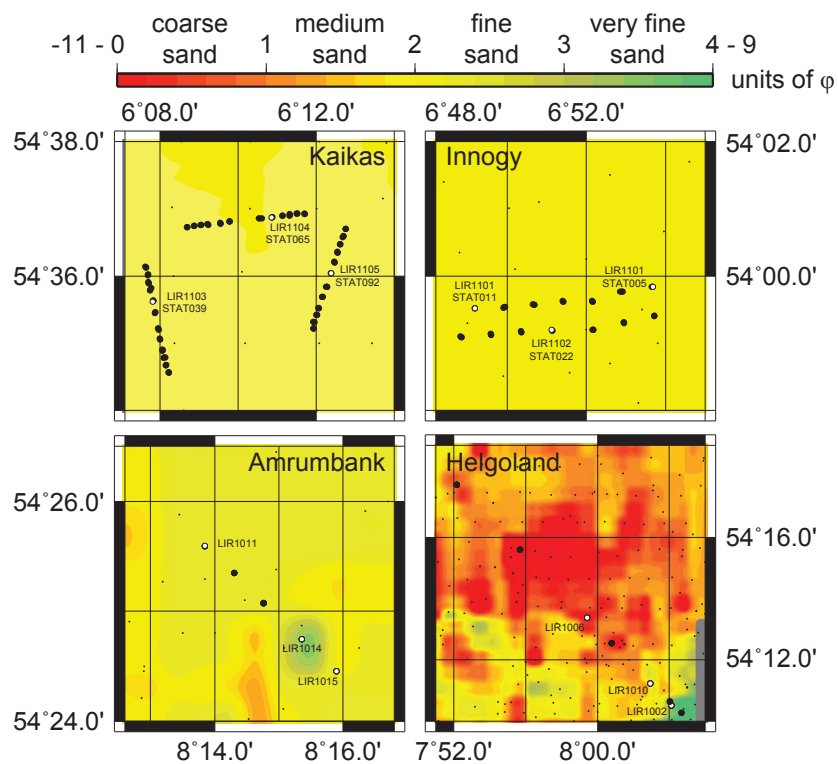


Figure A.5 – Grain size distribution in the working areas. The grain size classes in units of ϕ are indicated by the color coded background. The positions of grain size samples are shown by very small crosses, the positions of penetrations are shown by dots. Distances in Map: 1' (lat) \sim 1855 m, 1' (lon) \sim 1093 m (WGS 84).

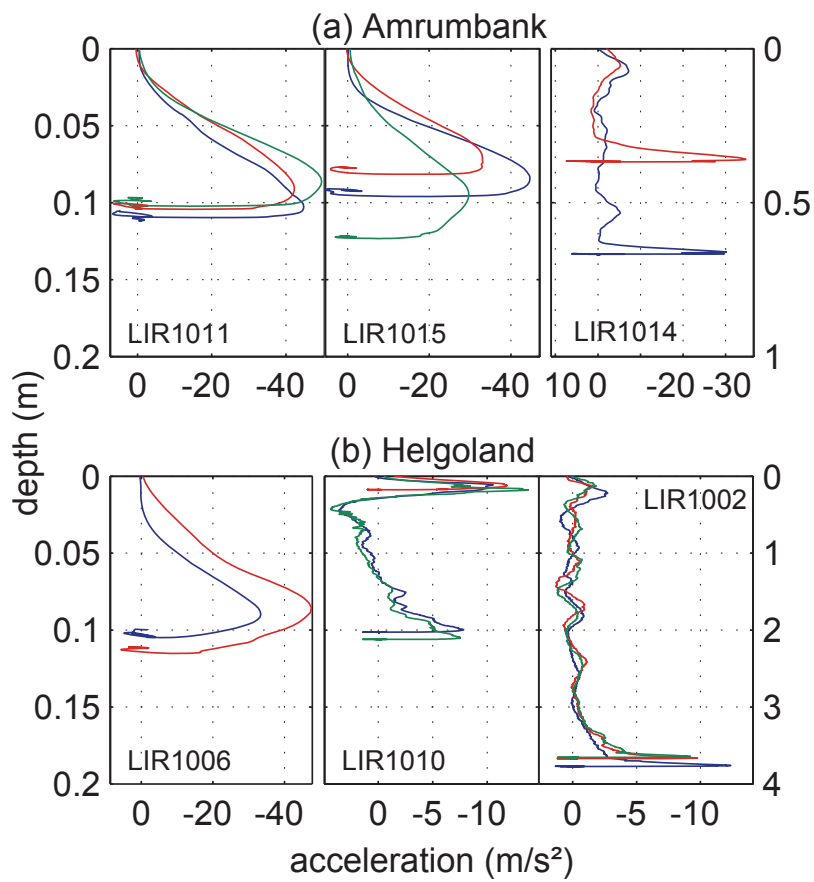
The different penetration depths are a result of different impact velocities (1.83 and 1.41 m/s).

A.3.5 Research area Helgoland

The research area Helgoland is characterized by a very heterogeneous grain size distribution and a very broad grain size spectrum. Eight locations were investigated. The prominent grain size ranged from very coarse material to very fine sand. The location LIR1006 lies in an area with very coarse sand, LIR1010 in an intermediate area with fine sand and LIR1002 in an area with very fine sand. The measured deceleration profiles are shown in Fig. A.6 b. At location LIR1006, we find a similar behavior as at the research area Amrumbank. The peak deceleration lies in the range of 30 m/s^2 and the achieved penetration depth are around 0.1 m. The penetration at the location with very fine sediment (LIR1002) yields penetration depths of nearly four meters. The acceleration develops an alternating pattern ranging from negative to positive values until final arrest. This type is described as a deep penetration or deep embedment. The three independent measurements reproduce very well at this location. At site LIR1010, two penetrations show nearly the same behavior (with penetration depths of 2 m), whereas one penetration yields a significantly lower penetration depth (0.1 m). The three penetrations match very well within the range from 0 to 0.1 m. The deeper penetrations show the behavior observed at station LIR1002 with a change of deceleration to acceleration with depth. As the grain size information is coming from surficial sediments and is mainly generated from box corer samples, it is only valid for the uppermost centimeters. The measurements of station LIR1010 suggest a two layer setting with a weaker (or finer grained) layer beneath the top layer being significantly harder.

A.3.6 Research area Innogy

The research area Innogy is an area, where the installation of an offshore wind energy field is planned. In the North Sea, it is common practice to establish these wind energy fields in areas which are dominated by a uniform sedimentation of sand. Thus, it is not surprising, that the recorded deceleration depth profiles show a typical parabolically shaped deceleration curve. Two profiles with a total of 14 stations were carried out in this area. Three of them are shown here (Fig. A.6, c). The stations LIR1101-STAT005 and STAT011 show penetration depths of up to 0.08 m and peak decelerations of 10 to 20 m/s^2 . The prominent grain size class (2 to 3 φ) suggests fine sand in this area. Hence, peak decelerations are expected to be in the range



The Figure is continued on the next page.

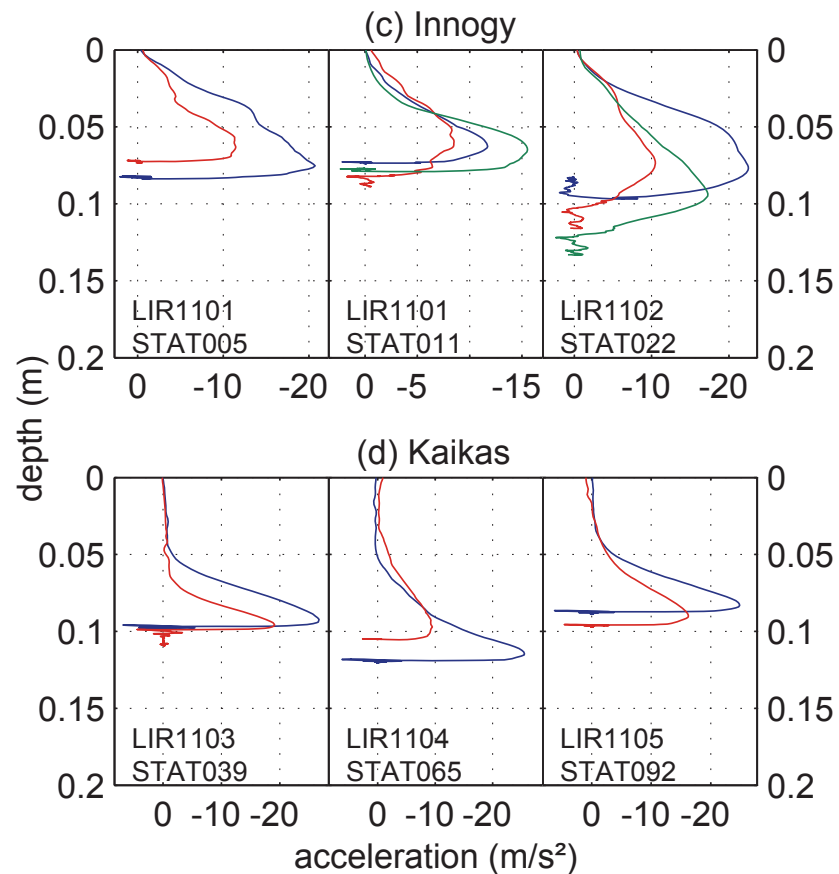


Figure A.6 – Deceleration vs. depth for selected locations in the four working areas. Each row represents one location. The different colors show repetition measurements at each location. If the diagrams are not connected (see row 1, 2 - Areas Amrumbank and Helgoland), a different scaling of the y-axis has been applied.

of 30 to 40 m/s² (see Amrumbank A.6, a). The lower peak decelerations can be explained with lower impact velocities (factor of 0.5 in comparison to Amrumbank area) due to another instrumentation on the vessel. The station LIR1102-STAT022 yields higher peak decelerations and slightly deeper penetrations, as the weight of the lance was raised from 280 to nearly 500 kg.

A.3.7 Research area Kaikas

Like the research area Innogy, the Kaikas area is also a designated offshore wind energy field. In this region, three profiles with a total of 36 stations were conducted. Three stations are shown here. The penetration depth ranges around 1.0 m and the penetration depth profiles in the Kaikas area show the characteristic bell-shaped deceleration curve. Peak decelerations are ranging from around 15 m/s² to a maximum of around 25 m/s². The grain size distribution in this area is very homogeneous and in the range of fine sand (2 to 3 φ). The penetration depth is around 0.1 m. The slope of deceleration increases after 5 cm of the total penetration depth. The behavior during penetration is very similar among the three selected stations.

A.3.8 Quantitative analysis of the datasets

The bell-shaped deceleration profiles can be used to establish a normalization of peak acceleration (a_{\max}) by total time of embedment (t_t) and impact velocity (v_i). This has been described for a general penetrometer capable to penetrate different materials in McCarty et al. (1964). Recently, this approach is used for marine penetrometers and water saturated soils by Mulukutla et al. (2011). The authors describe a firmness factor, formulated as follows:

$$F_f = \frac{a_{\max}}{v_i g t_t} \quad (\text{A.4})$$

with g as gravitational acceleration. A double logarithmic relationship between firmness-factor and normalized embedment depth yields groups of penetration events which can be assigned to a grain size spectrum (see Mulukutla et al., 2011).

In this paper, the approach is used for measurements with the LIRmeter. The diameter of tip and shaft of the lance, as well as the impact velocities are smaller by a factor of 2.5 to 5, compared to the Free Fall Cone Penetrometer (FFCPT; Osler et al., 2006a) sold by ODIM Brooke Ocean Inc, Canada (<http://www.brooke-ocean.com>) (see also Mulukutla et al., 2011), whereas the total weight of the LIRmeter is higher. The grain size spectrum in the

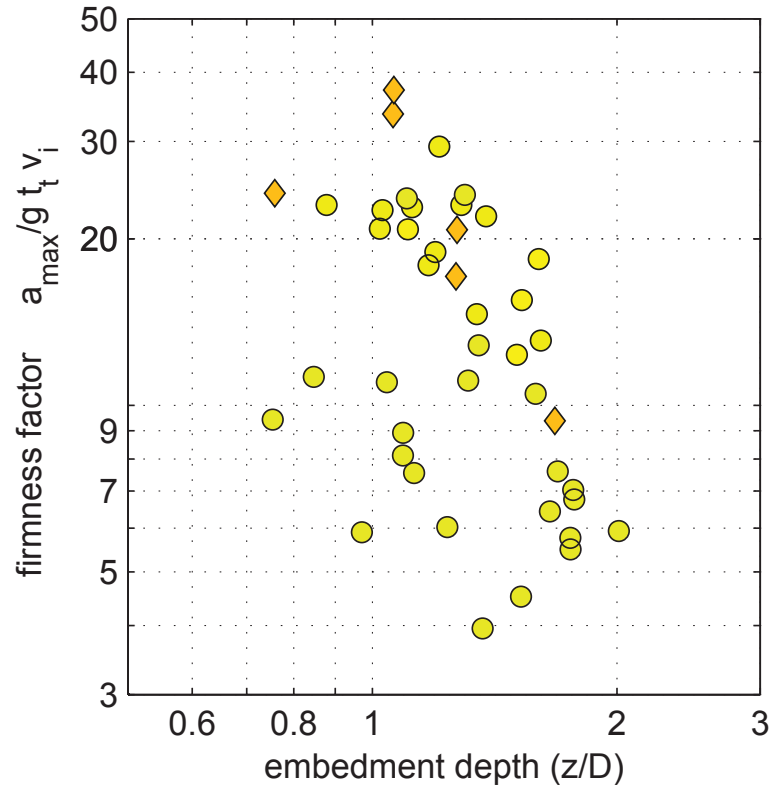


Figure A.7 – Firmness factor vs. normalized embedment depth. Grain size classes are indicated by symbols: diamonds for medium sand and circles for fine sand. The grain size classes are color coded by steps of 0.2φ according to the color scale of Fig. A.5.

investigated research areas where bell-shaped, shallow penetrations occur, is limited to the range of fine sand (between 1.5 and 2.5φ). Hence, the grain size classification, by the method presented in [Mulukutla et al. \(2011\)](#), has to be done for this narrow spectrum. Therefore a higher resolution was selected, yielding grain size classes of 0.2φ . The allocation of grain sizes is, where possible, done by selecting direct samples at the penetration position. Otherwise the grain size information is derived from database values. A classification is shown in Fig. A.7 for eligible penetrations.

The distribution of grain size classes indicates an accumulation of coarser classes in the upper right section (medium sand and low- φ fine sand) and finer grain sizes (fine sand and high- φ fine sand) in the lower left section shown in Fig. A.7.

Another approach was published by Stark et al. (2009b) and is based on investigations by Aubeny and Shi (2006). The bearing capacity formulation by Terzaghi (1943) is used to estimate bearing strength for the penetrations in sandy soils. According to Newtonian laws, the soil resistance force is proportional to the measured deceleration by the device. The soil resistance force is simplified to the shearing resistance force (F_s , Eq. A.5), neglecting external forces like buoyancy and friction and inertial forces (see Stark et al., 2009b). The dynamic penetration velocity is transformed to a quasi static penetration velocity of typically 0.02 m/s (see Stark et al., 2009b; Stoll, 2004; Dayal and Allen, 1975) using a strain rate factor (f_{ac} , Eq. A.7). The factor K is sediment type dependent and ranges between 1 and 1.5 (see Stoll et al., 2007; Dayal and Allen, 1975)). This leads to a quasi static resistance force F_{qsr} (Eq. A.8). The quasi static resistance force would exist between the soil and the cross sectional area of the probe, if the probe was inserted with a constant velocity into the sediment. This pressure can cause the soil to fail and is defined as quasi static bearing capacity $q_{u(q)}$ (Stark et al., 2009b) in Eq. A.8.

$$F_{sr} = m \cdot a_{dec} \quad (\text{A.5})$$

$$f_{ac} = 1 + K \cdot \log\left(\frac{v}{v_0}\right) \quad (\text{A.6})$$

$$F_{qsr} = \frac{F_{sr}}{f_{ac}} \quad (\text{A.7})$$

$$q_{u(q)} = \frac{F_{qsr}}{A} \quad (\text{A.8})$$

with m as mass, a_{dec} as deceleration, K as an empirical strain rate factor (Stoll, 2004; Dayal and Allen, 1975), v_i as impact velocity, v_0 as quasi static velocity and A as penetration surface of the probe.

The result for this type of analysis is shown for four locations of the research area Amrumbank (see Fig. A.8). For this analysis, the strain rate factor K was set to 1.5, other constraints such as weight and cross sectional area of the probe were given by the mechanics of the probe. For the locations LIR1011, LIR1013 and LIR1015, the estimated maximum quasi static bearing capacity ranges between 400 and 600 kPa and gains on strength with depth. The change of the slope of the bearing capacity-curve is reproduced very well between the measurements (see i.e. Fig. A.8: LIR1012 red, green or LIR1015 red, green). At station LIR1012 (Fig. A.8: LIR1012 red, green), two penetrations ranged to depths of 12 cm whereas two penetrations reached depth of 14 to 16 cm (Fig. A.8: LIR1012 blue, brown). The deeper penetrations of station LIR1012 show an increase in bearing capacity after an

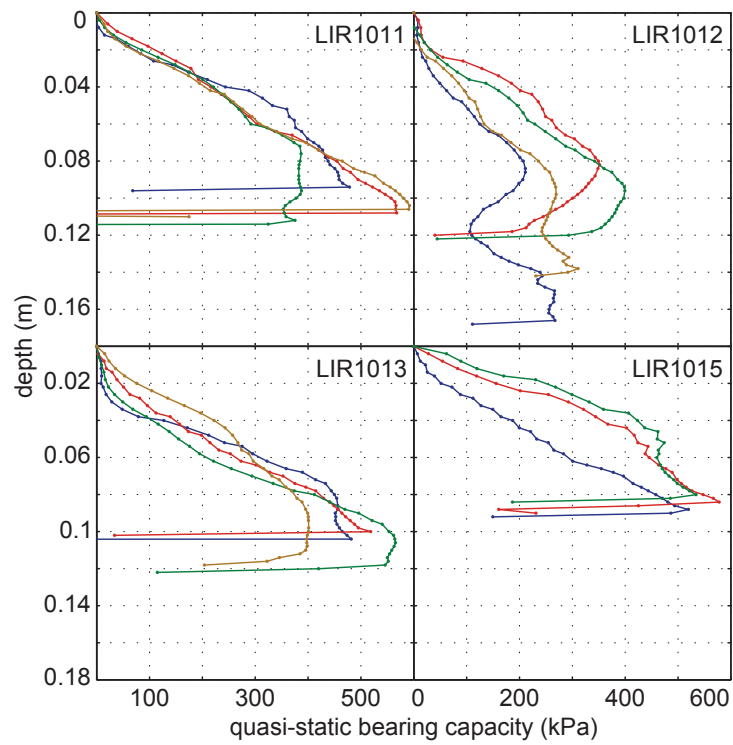


Figure A.8 – Result of the quasi static bearing capacity analysis. Four locations of research area Amrumbank (see Fig A.5). At each location, three or more repetition measurements were done (indicated by coloured lines).

initial drop at 12 cm. This could be an evidence for a two layer system with different bearing capacities.

A.4 Discussion

The results suggest that grain size is an important factor for the penetration behavior of a dynamic penetrometer like the LIRmeter. Different processing schemes deliver information on grain size and estimate geotechnical properties like bearing capacity. In this section we (a) discuss qualitative results in the geological context and (b) compare quantitative results to results from other penetrometers.

Grain size and content of cohesive material in the sediment

The research area Helgoland has a broad grain size spectrum and a high spatial variability in terms of grain size distribution. Penetrations were made over the whole spectrum of sediments ranging from coarse sand (and even coarser material) to very fine sand (and finer). The resulting penetration depths range from 0.1 m to 4 m, whereas the shallow penetrations (≤ 0.2 m) lie in areas with coarse, medium and fine sand. Penetrations in areas with a mean grain size of very fine sand achieve penetration depths in the range of (≥ 3 m). A compilation of grain size and amount of cohesive material for the German Bight was done by Figge (1981) resulting in a map with a grain size classification and a quantification of cohesive sediments. The amount of cohesive material is described as fraction of the sediment smaller than 0.063 mm or smaller than 4φ . The classification from Figge (1981) has been applied on the grain size data of the Helgoland area (see Fig. A.9).

On the one hand, grain size is an important factor to control the penetration behavior of the lance, but on the other hand, the amount of cohesive material in the sediment is crucial for the mechanical stability and hence the bearing capacity or the ability to decelerate a penetrometer. The relative amount of fine grained sediments ($\varphi \geq 4$) is very high in the south eastern corner of the research area (station LIR1002: amount of cohesive material is over 50 %). In this part of the area, the achieved penetration depth lie in the range of ≥ 2 m, whereas the achieved penetration depth in the north westerly part of the profile is at around 2 m to 0.1 m (no cohesive material, fine sand).

The penetration behavior at station LIR1010 in the Helgoland area (see Fig. A.6) shows two penetrations (green, blue curves) with penetration

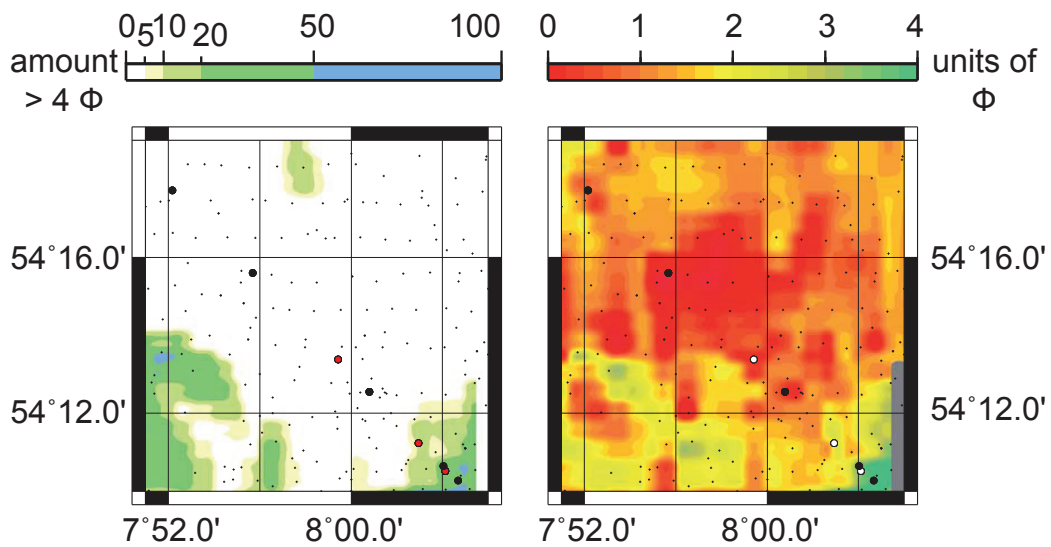


Figure A.9 – Left: Amount of fine grained sediment (≤ 0.063 mm) in percent of the total sediment fraction. Right: mean grain size after Folk and Ward (1957) in classes of ϕ .

depths of up to 2 m, whereas one penetration (red curve) is in the range of 0.2 m. Here, the amount of cohesive sediments is between 20 and 50 %, and penetration depths are high (≥ 2 m) in two cases. A visual description of a grab sample, which was taken at the exact penetration location, yields a layer of shell fragments in the uppermost zone of the sample. The matrix of the sediment was described as fine sand. Laboratory experiments confirm the mean grain size in the range of fine sand and indicate an amount of fine grained sediment (silt, mud) of 28 %. The shell fragment layer seems to have a very pronounced influence to the total penetration depth and provokes a very prominent peak in deceleration at a depth of 0.2 m (see Fig. A.6, b, middle). Such features in the deceleration-depth profiles of dynamic penetrometers were observed before in areas characterized by a surficial shell layer and described by Stark and Wever (2009). The slow increase in deceleration at the stations LIR1103, 04, 05 (see Fig. A.6 d) is a clear indication for a very soft upper zone, laying on a harder, sandy sediment layer. This upper layer could be interpreted as bedload (mobile sediment) as seen in Stark et al. (2011).

A.4.1 Grain size classification from penetrometer measurements

As stated earlier, the penetration depth and total time of embedment is related to sediment properties, and in particular, to grain size (see [Mulukutla et al., 2011](#)). The grain size is used as a first order approximation for the complex system of material properties, describing marine sediments. The authors of [Mulukutla et al. \(2011\)](#) suggest a relation between normalized peak acceleration and normalized penetration depth. This analysis was also carried out for LIRmeter data (shallow embedments in sandy sediments). In this section, LIRmeter data from the research area Amrumbank is compiled with literature values from [Mulukutla et al. \(2011\)](#), gathered with the FFCPT instrument (see Fig. A.10).

The grain size spectrum of the LIRmeter dataset is very limited, as only sediments in the range of medium to fine sand could be selected, due to the present material and achieved embedment depth ratios (z/D). Sediments with finer grain sizes lead to higher penetration depths and thus to intermediate or deep embedment depths, where the sediment identification model presented by [Mulukutla et al. \(2011\)](#) is not valid. The mechanical difference between the probes (mainly different masses and different tip shapes) can be the reason for a very narrow, grouped distribution of LIRmeter data in contrast to FFCPT data. The typical impact velocity of the LIRmeter is in the range of 1 to 2 m/s, whereas the FFCPT has a typical impact velocity of 5 to 9 m/s. The valid range for the classification by [Mulukutla et al. \(2011\)](#) is between 1.3 and 5.3 φ for impact velocities above 4.8 m/s and an FFCPT type penetrometer. Although data is normalized by the impact velocity, the penetration process remains a dynamic process in a two-phase-system and dilative/displacement effects are not considered here. The impact-velocity is likely to be the controlling factor, causing a build up of pore water pressure in the near field of the penetration, and thus generating a higher resistance to the probe.

A.4.2 Quasi-static bearing capacity: comparison to a lightweight, free fall penetrometer

The results from a lightweight free fall penetrometer (NIMROD) show a similar penetration behavior to the measurements with the LIRmeter regarding the estimated quasi static bearing capacities in relation to peak acceleration and impact velocity (see Table A.1).

The penetration depths of NIMROD deployments are in the range from 0.04 to 0.06 m, whereas the penetration depths of LIRmeter deployments lie

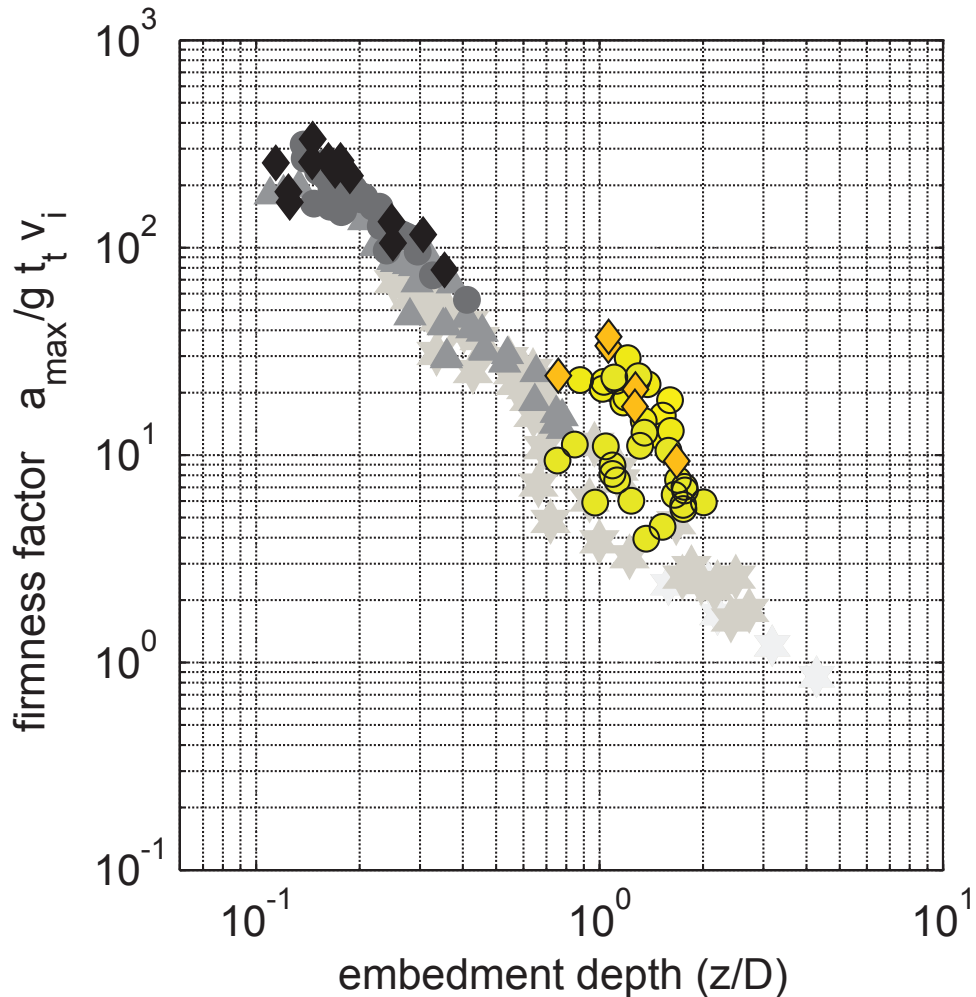


Figure A.10 – Colored data: LIRmeter measurements, black/white data: FFCPT measurements in the Bering Sea (modified after [Mulukutla et al. \(2011\)](#)). All grain sizes as medium grain size after [Folk and Ward \(1957\)](#). Stars (light gray): coarse and very coarse silt, triangles (gray): very fine sand, circles (dark gray): fine sand, diamonds (black): medium sand. Circles (yellow): fine sand, diamonds (orange): medium sand. The amount of greenish color indicates a tendency to very fine sand for the LIRmeter dataset.

Table A.1 – Mean values for quasi static bearing capacity $q_{u(q)}$, impact velocity v_i , penetration depth z and peak deceleration a_{peak} . Data from NIMROD: Stark, pers. comm.

Station	NIMROD				LIRmeter			
	$q_{u(q)}$ kPa	v_i m/s	z m	a_{peak} m/s ²	$q_{u(q)}$ kPa	v_i m/s	z m	a_{peak} m/s ²
11	130	4.9	0.05	660	503	2	0.10	37
13	108	4.5	0.06	540	487	1.9	0.11	36
15	149	4.6	0.04	700	545	1.7	0.08	36

in the range of 0.08 to 0.11 m. The estimated quasi static bearing capacity shows a similar relation between the stations for the two methods, but the absolute values differ significantly. This leads to the observation, that the processing of penetrometer data regarding $q_{u(q)}$ is strongly instrument specific, because due to the different designs, the instruments achieve different penetration depths. The penetration depth is an important factor for an estimation of ultimate bearing capacity (Das, 2001). As a result of higher bearing capacities with depth peak decelerations also differ significantly. Another factor influencing the penetration depth is the kinetic energy, which is predominantly influenced by the impact velocity (in case of NIMROD), in contrast to the kinetic energy of the LIRmeter, which is predominantly influenced by the mass of the instrument. The kinetic energy of the LIRmeter is, for typical impact velocities, by the factor of ~ 4 higher than the kinetic energy of a NIMROD type penetrometer.

A.5 Conclusion

One aim of the research project was the development and establishment of a new method for sea floor classification for a sediment depth in the range of 0 to 4 meters. The instrument has proven a failsafe and robust operation during two research cruises under harsh weather conditions in the North Sea. The system has now reached a mature state in development and is ready to conduct numerous surveys to establish a borad database on penetrations in sediments with different properties.

The first results show, that straight forward approaches work for the instrument, deeper penetrations however still need further research. Especially, penetrations to depth of 2 m or more are very complex to describe due to sediment-physical effects like a potential buildup of pore water pressure especially in fine grained or cohesive sediments.

Nevertheless, the deceleration of the probe can be broken down to first order sediment descriptors like grain size for shallow penetrations. From a pragmatic point of view, a qualitative estimation of the firmness can be established on the basis of deceleration-depth curves. Hence, a rapid classification in hard, intermediate or soft sediment is possible by simply assessing the raw acceleration data. Even an interpretation regarding mobile sediments is possible. From an academic point of view, the penetration process itself is of interest. The highly complex two phase or even three phase system (if gas is present) influences the penetration process of the lance. Geotechnical parameters like shear strength or porosity/permeability are the main variables in this system. To promote further research on the penetration behavior of the LIRmeter in marine sediments, several options arise:

- More tests under well known and stable conditions. Especially fine grained sediments, which allow deep embedments should be investigated.
- Inclusion of hydro acoustical datasets. The acoustical strength of sea floor or sub bottom reflections could correlate with the penetrometer measurements.
- Numerical modeling of a simple case (i.e., one layer case) and comparison to field measurements matching the constraints of the model.
- Laboratory experiments with a scaled-down version of the lance and artificial sediment having well known properties, and perhaps, in a second step, comparison to numerical modeling results.

Acknowledgements We acknowledge the Senator for Environment, Construction and Transport of Bremen, Germany for funding within the framework of the research transfer program “Angewandte Umweltforschung”, funded by the European Union, “European Regional Development Fund - Investing In Your Future”, Funding-# FV204A. We would like to thank the crews of WFES Planet and FS Heincke for their tireless effort and support during the field measurements. The cooperation with the project “Geo-scientific Potentials of the German North Sea” (GPDN) is highly appreciated, especially the cooperation with M. Naumann (LBEG), C. Thürnagel (BGR) and W-U. Laurer (BSH). A special thank goes to Prof. A. Kopf for providing lab time and A. Steiner for conducting experiments on grain size.